Engineering Department

Doctoral Programme in Energy Engineering

Integrated Experimental and Numerical Analysis of System Performance and Product Freezing in a Vapor Injection Seafood Freezing System

Doctor of Philosophy (PhD):

Hamed Jafargholi

Supervisor:

Prof. Domenico Panno

Academic Year 2024–2025

Dedication

To my beloved parents,

whose endless love, unwavering support, and boundless sacrifices have been the guiding light of my life. Every achievement I have reached, and every dream I dare to pursue, is rooted in the values you have instilled in me.

This work is as much yours as it is mine.

With deepest gratitude and all my heart.

Acknowledgements

I would like to express my profound gratitude to Professor Domenico Panno, whose exceptional guidance, thoughtful advice, and unwavering encouragement have been instrumental throughout the entirety of my doctoral journey. His profound expertise and constructive criticism not only shaped the direction of this research but also enriched my academic growth in immeasurable ways.

I am sincerely indebted to Professor Massimo Morale for granting me access to the refrigeration laboratory facilities, without which the experimental investigations of this work could not have been accomplished.

My heartfelt appreciation also goes to Professor Pietro Catrini, whose steady support and kind companionship during my doctoral studies created an atmosphere of motivation and collaboration that I will always value.

List of Tables

List of Figures

Nomenclature

$\dot{m}_{inj}$	Injection Mass Flowrate (kg/h)	η_{is}	Isentropic Efficiency
$\dot{m}_{suc}$	Suction Mass Flowrate (kg/h)	ρ	Density (kg/m^3)
Q_{main}	Rejected Heat (kJ/h)	Q''	Specific Heat Flux (W/m^2)
Q_{inj}	Injected Heat (kJ/h)	C	Specific Heat (kJ/kg. K)
h_1	Inlet Compressor Enthalpy (kJ/kg)	U	Internal Energy (kJ/kg)
h_2	Outlet Compressor Enthalpy (kJ/kg)	c_a	Apparent Specific Heat (kJ/kgK)
h_3	Inlet Condenser Enthalpy (kJ/kg)	c_f	Specific Heat of Fully Frozen Food (Typically at –40 °C) (kJ/kgK)
h_4	Outlet Condenser Enthalpy (kJ/kg)	M_s	Relative Molecular Mass of Soluble Solids, (kg/kmol)
h_5	Inlet Evaporator Enthalpy (kJ/kg)	t_0	Freezing Point of Water = 0 °C
h_6	Outlet Evaporator Enthalpy (kJ/kg)	t_f	Initial Freezing Point of Fish (°C)
h_7	Inlet Evaporator (After Lamination) Enthalpy (kJ/kg)	t	Fish Temperature (°C)
h_8	Outlet Evaporator Enthalpy (kJ/kg)	L_0	Latent Heat of Fusion of Water = 333.6 (kJ/kg)
h_9	Inlet Economizer (from Condenser) Enthalpy (kJ/kg)	x_{ice}	Ice Fraction
h_{10}	Outlet Economizer (vs Compression Injection) Enthalpy (kJ/kg)	x_{wo}	Unfrozen Water Fraction
h_{12}	Internal (vs Compression Injection) Enthalpy of Refrigerant (kJ/kg)	x_w	Unfrozen Water Fraction
h_{13}	Internal (vs Inlet Compressor) Enthalpy of Refrigerant (kJ/kg)	x_p	Protein Fraction
W	Compressor Work (kW)	x_f	Fat Fraction
Q_{evp}	Absorbed Heat by Evaporator (kW)	x_a	Ash Fraction
x	Quality	ρ_{ice}	Ice Density (kg/m^3)
m_5	Mass of Refrigerant in Two-Phase (kg)	ρ_w	Water Density (kg/m^3)
x_b	Bound Water Fraction	ρ_f	Fat Density (kg/m^3)
$x_{w,freezable}$	Freezable Water Fraction	ρ_p	Protein Density (kg/m^3)
x_s	Solids Mass Fraction	ρ_a	Ash Density (kg/m^3)
$x_{w,liq}$	Remaining Water Fraction	$k_\perp$	Perpendicular Thermal Conductivity (W/m. K)
T_0	Freezing Point of Water in 273.2 K	$k_\parallel$	Parallel Thermal Conductivity (W/m. K)
c_w	Water Specific Heat (kJ/kg. K)	α	Thermal Diffusivity (mm^2/s)
c_{ice}	Ice Specific Heat (kJ/kg. K)	T_{cell}	Cell Temperature (°C)
c_f	Fat Specific Heat (kJ/kg. K)	$T_{cw,in}$	Inlet Coolant Water (°C)
c_p	Protein Specific Heat (kJ/kg. K)	$T_{core,fish}$	Fish Core Temperature (°C)

$\mathbf{c_a}$	Ash Specific Heat (kJ/kg. K)	$\mathbf{T_{surf,fish}}$	Fish Surface Temperature (°C)
$\mathbf{k_w}$	Water Thermal Conductivity (W/m. K)	$\mathbf{P_{EVP}}$	Evaporating Temperature (°C)
$\mathbf{k_{ice}}$	Ice Thermal Conductivity (W/m. K)	$\mathbf{P_{CND}}$	Condensing Pressure (bar)
$\mathbf{k_p}$	Protein Thermal Conductivity (W/m. K)	$\mathbf{Q_{cnd}}$	Rejected Heat by Condenser (kW)
$\mathbf{k_f}$	Fat Thermal Conductivity (W/m. K)	$\mathbf{T_{chamber}}$	Chamber Temperature (°C)
$\mathbf{k_a}$	Ash Thermal Conductivity (W/m. K)	$\mathbf{x_i^v}$	Volume Fraction of Component i
$\mathbf{R}$	Universal Gas Constant (kJ/kg. mol. K)	$\mathbf{u_{rel}}$	Relative Standard Uncertainty
$\mathbf{\Delta h_{evp}}$	Evaporator Specific Enthalpy Difference	$\mathbf{u\left(\Delta h_{evp}\right)}$	Standard Uncertainty of Evaporator Specific Enthalpy Difference
$\mathbf{w_{eq}}$	Equivalent Specific Compressor Work	$\mathbf{u\left(w_{eq}\right)}$	Standard Uncertainty of Equivalent Specific Compressor Work
$\mathbf{u\left(Q_{evp}\right)}$	Standard Uncertainty of Absorbed Heat by Evaporator	$\mathbf{u\left(W\right)}$	Standard Uncertainty of Compressor Work
$\mathbf{u\left(COP\right)}$	Standard Uncertainty of Coefficient of Performance	$\mathbf{Q_{evp}}$, $\mathbf{Q_{evp,min}}$	Minimum Absorbed Heat by Evaporator in Steady-state Window (kW)
$\mathbf{Q_{evp,max}}$	Maximum Absorbed Heat by Evaporator in Steady-state Window (kW)	$\mathbf{Q_{evp,mean}}$	Average Absorbed Heat by Evaporator in Steady-state Window (kW)
$\mathbf{W_{min}}$	Minimum Compressor Work in Steady-state Window (kW)	$\mathbf{W_{mean}}$	Maximum Compressor Work in Steady-state Window (kW)
$\mathbf{W_{max}}$	Average Compressor Work in Steady-state Window (kW)	$\mathbf{COP_{min}}$	Minimum COP in Steady-state Window
$\mathbf{COP_{max}}$	Maximum COP in Steady-state Window	$\mathbf{COP_{mean}}$	Average COP in Steady-state Window

Abbreviations

GWP	Global Warming Potential
HFC	Hydrofluorocarbon
HFO	Hydrofluoroolefin
HC	Hydrocarbon
ODP	Ozone Depletion Potential
SCVI	Scroll Compressor Vapor Injection
ASHP	Air Source Heat pump
VCRC	Vapor Compression Refrigeration Cycle
HVAC	Heating, Ventilation, and Air Conditioning
VCC	Vapor Compression Cycle
COP	Coefficient of Performance
CND	Condenser
EVP	Evaporator
CMP	Compressor
Surf	Surface

Table of Contents

Chapter 1

Introduction

1 Introduction

1.1 Background and Motivation

Distinctive features of aquatic animal product trade are the increasing prevalence of processed products, other than live and fresh whole aquatic animals. In 2022, 92 percent of aquatic animal products, measured in live weight equivalent, were processed items. Processing methods have evolved with increasing adoption of freezing. As a result, frozen products in 2022 constituted 44 percent of the total traded quantity, a significant increase from the 22 percent recorded in 1976. This expansion was made possible through the adoption of innovative technologies in chilling, packaging and distribution. These new technologies also facilitated growth of trade in fresh processed products such as fresh fillets.

In 2022, of the 165 million tonnes destined for human consumption, live, fresh or chilled accounted for about 43 percent. This continues to represent the preferred and most high-priced form of aquatic food products, followed by frozen (35 percent), prepared and preserved (12 percent) and cured (10 percent). Freezing is the main method of preserving aquatic foods, accounting for 62 percent of the 93 million tonnes of processed aquatic animal production for human consumption (i.e. excluding life, fresh or chilled).

In general, aquatic species are highly perishable and several chemical and biological changes take place immediately after harvest; this can result in spoilage and food safety risks if good handling and preservation practices are not applied at harvesting and all along the supply chain. These practices are based on temperature reduction (chilling and freezing), heat treatment (canning, boiling and smoking), reduction of available water (drying, salting and smoking) and changing of the storage environment (vacuum packaging, modified atmosphere packaging and refrigeration). Aquatic food products also require special facilities such as cold storage and refrigerated transport, and rapid delivery to consumers. [1]. The IIR estimated that 19% of fish and seafood produced for human consumption in 2017 was lost due to lack of refrigeration, particularly in Africa (47%) and Latin America (38%) [2]. Frozen food is a method of preserving products that offers a convenient and affordable way to consume safe and nutrient-rich fruit and vegetables. For example, vegetables are usually frozen shortly after harvest, minimizing nutritional loss [3]. Frozen food may also help consumers reduce food waste by offering the opportunity for scheduled consumption, as it extends the product shelf life compared with similar chilled products. [4], though food cold chains are a considerable source of greenhouse gas emissions from both indirect (energy-related) and direct (refrigerant leakage) sources. Most commercial and industrial freezers available today continue to utilize high-GWP (Global Warming Potential) refrigerants such as R404A, which are being phased out under international agreements like the Kigali Amendment to the Montreal Protocol, along with the EU's F-Gas Regulation [5], [6].

Here, the current study is powered by the twin imperative of enhancing energy efficiency and environmental performance in seafood freezing systems. It deals specifically with the combination of a low-GWP refrigerant, R448A, and a vapor injection scroll compressor—a novel technology that improves system performance at high compression ratios. The research seeks to contribute to the development of sustainable refrigeration solutions that are adapted to present-day governance and functional requirements, and more specifically in the seafood industry.

1.2 Importance of Freezing in Seafood Preservation

In recent times, the fishery industry has attracted increasing attention, more than ever. Technically, economically, and environmentally, it is a critical sector for global sustainability. Water and energy resources are driving factors in seafood production activities, which lie mainly in the areas of production and distribution.

Figure 1 describes the seafood system via a schematic framework, depicting the flow of resources into and out of the system. The system is organized around two main areas: production and supply chain activities. In the production sector, seafood is derived from three major sources; natural fisheries, marine aquaculture, and overseas imports. A fraction of the catch is allocated to non-food uses such as pharmaceutical products, fish oil, or animal feed, with the remainder going to human consumption after preliminary handling and storage (HS). These are energy- and water-demanding activities dependent on large water and energy inputs and produce environmental outputs in the form of greenhouse gas emissions and wastewater. The retail and distribution chain consists of four linked phases: HS, processing and packaging (PP), distribution and marketing (DM), and ultimate consumption. Some of the processed products are exported, while the rest cater to domestic markets. Each activity in this chain adds to resource use and the consequent production of waste and emissions [7]. Such processes are classified into nine core categories, as shown in Table 1, for specific subsectors of the food and beverage industry [8].

Category	Description	Examples
Materials Reception and Preparation	The receipt, unpacking, and storage of raw materials, byproducts and waste	Conveyer belts that receive vegetables, screw conveyors for rice, or pumps for wine
	Sorting and screening	Human inspection and grading of products, de-hulling of corn, trimming of vegetable stalks, peeling
	Washing	Removing, often via sedimentation, unwanted components such as dirt, brine, salt, or microorganisms

	Thawing	Removing, often via sedimentation, unwanted components such as dirt, brine, salt, or microorganisms
Size reduction, mixing and forming	Size reduction	Cutting, chopping, slicing, mincing or pressing food materials
	Mixing and blending	Combining different materials or obtaining a more even particle size by blending
	Grinding, milling and crushing	Reducing the size of solid materials e.g. flour milling, animal feed, brewing, dairy and sugar
	Forming, molding and extruding	Properly shaping foodstuffs such as bread, biscuits, chocolate, pies, sausages and starch-based snacks
Separation techniques	Extraction	Recovering soluble components from raw materials e.g. sugar from beets or sugarcane, caffeine from coffee beans, essential oils, etc.
	Centrifugation and sedimentation	Separating solids from liquids, e.g. oils and fats, cocoa butter, dairy
	Filtration	Using screens and filters to retain solids and allow liquids to pass through, e.g. beer, wine, fruit juices
	Distillation	Separating liquid mixtures by partial vaporization, especially for alcohol and spirits
Product processing technologies	Soaking	Adjusting water levels or temperature to moisten or soften grains or seeds
	Fermentation	Utilizing microorganisms to alter the texture of foods or aid in preservation
Heat processing	Pasteurization	A controlled heating process to remove microorganisms
	Baking	Use of baking ovens to make food more edible
Concentration by heat	Evaporation	Partial removal of water from a liquid by boiling
	Drying	Applying heat to remove water from liquid foods
	Freeze drying	Preserving food such as coffee extracts, spices, soup vegetables, fish and meat that cannot be dried by evaporation
Chilling and freezing	Refrigeration	Walk-in cold rooms or standalone refrigerators used to cool and store food products
	Cooling or chilling	Reducing the temperature of food from one processing temperature to another
	Freezing	Reducing the temperature of food below the freezing point, especially for pizza or ice cream
Post processing operations	Packing and filling	Placing food into wood, metal, glass, plastic, paper or cardboard packages, often in a vacuum or modified atmosphere

	Gas flushing	Storing meat, bakery products and wine in an artificially produced atmosphere
Utility processes	Cleaning and disinfecting	Removing product remnants and contaminants via cleaning in place or cleaning out of place
	Water	The movement and utilization of water for food processing, cleaning, washing, and boiling
	Vacuums	Reducing processing temperatures and extending the preservation of food
	Compressed air	Generated to run simple tools or pneumatic controls

Table 1 Nine Categories of Energy Intensive Processes for Food and Drinks Manufacturing

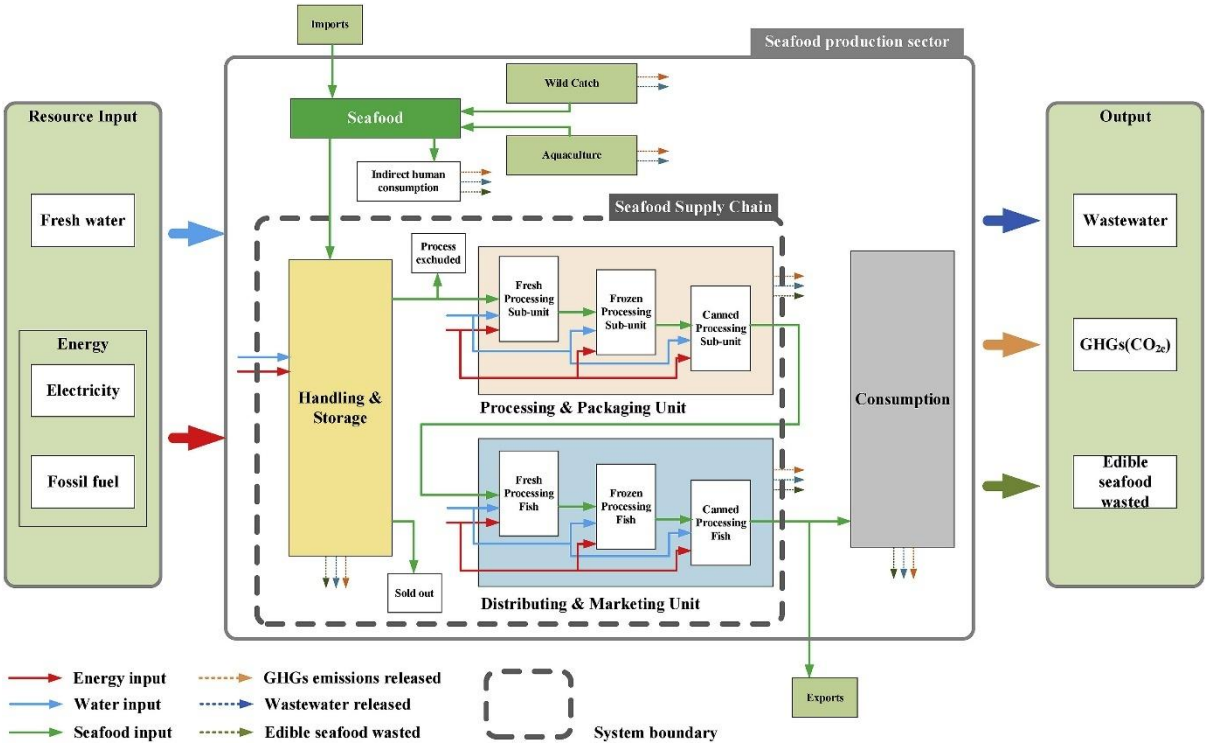

Figure 1 A Framework of Seafood, Energy and Water Nexus

Freezing stands as the most effective and commonly used preservation method for seafood products. The perishable nature of fish and other marine products requires freezing as an essential method to preserve their quality and safety because these products spoil quickly after harvesting through enzymatic and microbial activities. Freezing the product below its freezing point stops microbial growth and slows down enzymatic reactions and substantially decreases biochemical breakdown. The preservation effects are essential for maintaining food safety while extending the storage and transportation period of seafood products. Freezing stands as one of the most energy-intensive procedures used in seafood handling and processing operations. The substantial energy requirements for refrigeration and freezing systems create economic and environmental problems mainly through carbon emissions and reduced energy efficiency. The European seafood industry

along with other modern seafood systems have started to adopt sustainable technologies and low-energy solutions for their cold chain logistics operations. The main objective of innovative solutions aims to reduce environmental impact without compromising product quality.

1.3 Role of low-GWP refrigerants and R448A

The rising awareness about climate change and synthetic refrigerant environmental effects drives the market demand for low-GWP alternatives in refrigeration and air conditioning systems. R448A stands out as a promising replacement for high-GWP refrigerants such as R404A because it delivers equivalent thermodynamic performance while minimizing environmental impact. R448A functions as a non-ozone-depleting HFO/HFC blend, which helps achieve international regulatory targets, including the Kigali Amendment, while supporting the development of sustainable cooling technologies. This section examines low-GWP refrigerants and their functional and environmental aspects, with particular attention to R448A properties and applications in contemporary refrigeration systems (Figure 2).

Multiple working fluids have been used throughout refrigeration history in vapor compression cycles. Ether was the first refrigerant adopted and then naturally occurring substances like carbon dioxide (CO_2), ammonia (NH_3), and hydrocarbons (HCs) emerged as prominent alternative solutions [9]. According to Calm [10] refrigerants have developed through four distinct generations. The first generation consisted mostly of natural fluids, which included those previously mentioned. Safety concerns about toxic and flammable early refrigerants led researchers to find alternative refrigerants that were less dangerous and more stable.

The development of second-generation refrigerants occurred due to the need for safer CFCs and HCFCs which provided superior chemical stability during operational use. The synthetic compounds substituted natural refrigerants and became the dominant selection for commercial and industrial applications.

The development of second-generation refrigerants occurred due to the need for safer CFCs and HCFCs which provided superior chemical stability during operational use. The synthetic compounds substituted natural refrigerants and became the dominant selection for commercial and industrial applications. Scientists later discovered that CFCs and HCFCs created substantial environmental problems because they had both high ozone depletion potential (ODP) and GWP. The third generation of refrigerants emerged during the 1990s because international regulatory efforts such as the Montreal Protocol (1987) mandated ozone-depleting substances phase-out. Mainstream adoption of hydrofluorocarbons (HFCs) occurred because they did not harm the ozone layer while serving as a safer temporary solution.

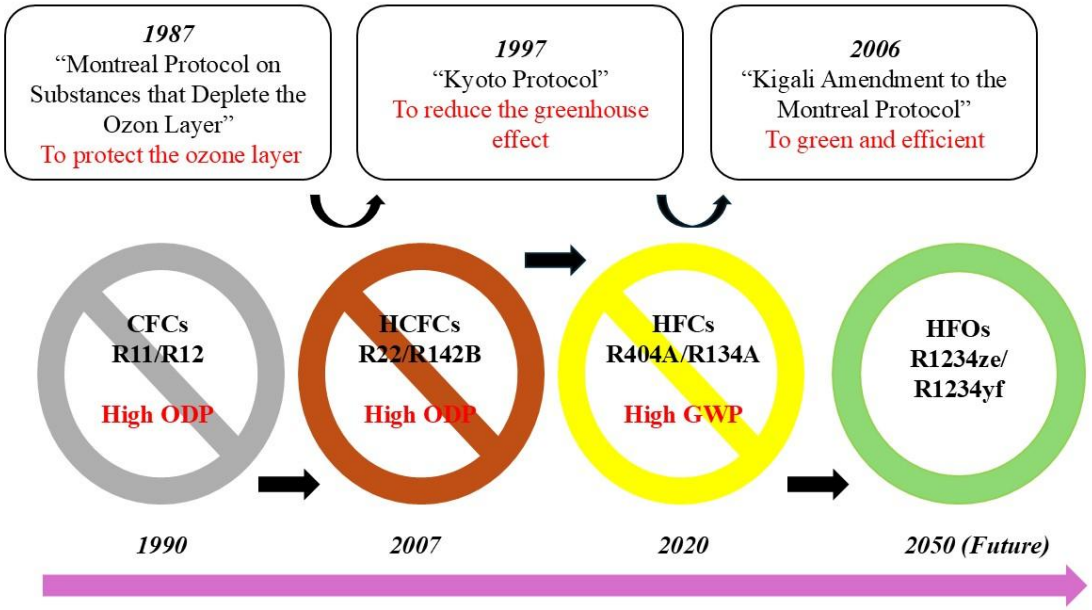

Figure 2 Development of Refrigerants Since 1990's

The absence of ODP in HFCs did not stop them from becoming major greenhouse gas contributors because of their high GWP values. The establishment of the United Nations Framework Convention on Climate Change (UNFCCC) in 1992 took place during the time HFCs gained popularity. It became clear that finding a long-term sustainable solution needed refrigerants that both eliminated ODP and minimized GWP. The Kyoto Protocol (1997) included HFCs as controlled greenhouse gases before the Kigali Amendment to the Montreal Protocol formally adopted their phase-down in 2016 [9], [11], [12].

HFOs entered the market as the fourth generation of refrigerants during the early part of the twenty-first century because of expanding environmental and regulatory demands [13], [14], [15]. The compounds demonstrate low GWP values together with zero ozone depletion potential and desirable thermodynamic properties, which make them suitable for domestic refrigeration and automotive air conditioning systems [16], [17].

The heating, air conditioning, and refrigeration (HACR) industry relies on the hydrofluorocarbons R134a, R404A, R407C and R410A but these compounds present high global warming potential which demands researchers to find new refrigerant alternatives. The hydrofluoroolefin R1234yf stands as an environmentally beneficial alternative refrigerant to traditional HFCs. The refrigerant blend R448A functions as an emerging alternative to replace traditional HACR refrigerants R404A and R22. The complete assessment of these alternatives needs to include multiple performance and environmental standards [18].

The researchers tested various low-GWP refrigerants for performance evaluation as R404A alternatives through theoretical methods which included cooling capacity and volumetric flow rate

and COP assessment [19]. The performance evaluation of R448A and R404A took place through laboratory testing of the refrigeration system. The cooling capacity of R448A remained lower than R404A yet it used less energy and provided better COP performance. The adoption of R448A as a refrigerant produced a 70% reduction in overall environmental impact through global warming potential reduction [20].

R404A serves numerous refrigeration applications across supermarkets and transport refrigeration systems because of its extensive market adoption. Several environmental regulations both in the United States and Europe have set targets to reduce R404A usage because it exhibits a high global warming potential of 3943. The researchers tested R448A and R455A as two potential refrigerant alternatives with minimal GWPs of 1273 and 146 respectively. The researchers performed experimental testing using a commercial self-contained freezer which operated on R404A. Both R448A and R455A maintained compressor operating times like R404A because they possessed identical cooling performance. The 24-hour operation showed R448A consumed 9% less compressor energy than R404A while R455A consumed 6% less energy. A commercial walk-in freezer/cooler operated with R448A provided equivalent cooling performance but achieved improved efficiency through a 4% to 8% enhancement. Both R448A and R455A show promise to decrease the emissions generated by refrigeration systems through direct and indirect means. The transition from R404A to R448A in real-world supermarket refrigeration systems resulted in energy savings ranging from 9% to 20% based on outdoor ambient temperatures [21].

1.4 Use of Vapor Injection Scroll Compressor in Low-Temperature Applications

The efficiency of single-stage vapor compression refrigeration and heat pump systems decreases substantially when there exists a wide temperature difference between evaporator and condenser units. The following list presents several disadvantages of these systems:

I. The compressor produces high discharge temperatures which create negative effects on the thermal stability of lubrication oil.
II. The system capacity decreases because the compressor volumetric efficiency drops when pressure ratios increase.
III. Heat pumps become less competitive than traditional heating boilers because both Carnot and compressor efficiencies decrease dramatically at high temperature differentials.
IV. The decrease in volumetric efficiency at elevated pressure ratios requires compressors to become larger to achieve the same output which increases equipment costs.

Two-stage compression with vapor injection represents a common solution to handle these problems. The method of injecting refrigerant vapor into an intermediate port of the compressor provides multiple essential advantages.

I. The system provides enhanced performance during heating operations at subzero temperatures and cooling operations above 35 degrees Celsius.
II. The system output becomes flexible through vapor mass flow rate adjustments which helps decrease energy consumption by reducing compressor cycling.
III. The compressor discharge temperature remains lower than what traditional single-stage systems produce [22], [23].

The use of vapor-injection scroll compressors (SCVIs) is a strong solution for improving refrigeration and heat pump system performance at low temperature operation. Technology involves injecting vapor into compression stages to reduce discharge temperatures while at the same time improving heating and cooling performance which translates to better COP.

The technology enables system capacity modulation by means of vapor injection mass flow rate adjustments. Flexible operation of the system saves power consumption and lowers compressor start-stop cycles which translates to extended equipment expected lifespan. Compactness and smaller external heat exchange surface area as well as greater volumetric efficiency of SCVIs render them appropriate for severe climate and variable load applications over two-stage reciprocating compressors.

The combination of mechanical simplicity and reliable low-temperature performance and improved energy efficiency make vapor injection in scroll compressors a reliable solution. Technology stands as the preferred choice for advanced refrigeration systems and modern heat pumps that need to operate efficiently across diverse demanding environmental conditions.

1.5 Research Objectives

The study aims to conduct experimental testing of a seafood freezing refrigeration system which employs a vapor injection scroll compressor and operates with R448A as its low-GWP refrigerant. The research has three main goals:

1. To compare the thermodynamic performance of R448A in low-temperature seafood freezing processes through the analysis of cooling capacity, COP, compressor electric power consumption and discharge temperature.
2. To investigate how cooling water inlet temperature of the condenser would affect the performance and energy efficiency of the system under varying operating conditions.

3. To determine the efficiency of the vapor injection, scroll compressor technology based on the system performance when it was compared to the traditional single-stage and two-stage refrigeration benchmarks.
4. To develop and assess numerical and data-driven models capable of describing and estimating key performance indicators within the investigated experimental range.
5. To offer viable information on the use of low-GWP refrigerants and innovative compressor technologies in commercial seafood freezing systems.

1.6 Scope and Limitations

This study focuses on the experimental and theoretical assessment of a vapor injection refrigeration system using R448A for seafood freezing. It does not address the microbiological or nutritional quality of seafood after freezing. Experimental assessment is limited to steady-state operation under controlled environments, with transient behaviors, defrost cycles, and long-term reliability studies falling outside its scope.

While R448A is the main refrigerant studied, the findings might not be directly applicable to other low-GWP refrigerants, which have different thermodynamic properties. The compressor model studied is that of a particular commercial unit, and differences in performance may result with other brands or configurations.

1.7 Thesis Structure

This thesis is organized into six chapters:

Chapter 1 presents the background of the research, motivation, study goals, and scope.

Chapter 2 is a literature review of technologies in seafood freezing, low-GWP refrigerants, and vapor injection scroll compressor systems.

Chapter 3 outlines the experimental design, methods of measurement and the test procedures of study.

Chapter 4 introduces the methods of numerical and data-driven modeling used to analyze and describe system performance and freezing behavior.

Chapter 5 covers the experimental and simulation findings with the focus on energy performance and important operating parameters.

Chapter 6 concludes and presents the key findings of the thesis and the future research directions and contributions.

Chapter 2

Literature Review

2. Literature Review

2.1 Refrigeration Technologies in Seafood Industry

The choice of freezing equipment for a specific food product is influenced by numerous parameters, including the product's sensitivity, physical dimensions and geometry, required end-product quality, production throughput, spatial limitations, budgetary constraints, and the nature of the refrigerant employed [24]. Accordingly, freezing systems are categorized based on different operational principles, as outlined below:

1. Equipment Based on Direct Contact with a Cold Surface

In these systems, the food—either packaged or unpackaged—comes into direct contact with a cooled metal surface during freezing. This category includes plate freezers and scraped surface freezers.

2. Equipment Using Air as the Cooling Agent

In this type, cold air serves as the refrigerant. Systems in this group include still air freezers, air blast tunnels, belt freezers, spray freezers, fluidized bed freezers, and impingement freezers.

3. Equipment Utilizing Liquid Coolants

Here, extremely cold liquids are either sprayed onto the product or used to immerse it directly. Systems under this classification encompass immersion-type and cryogenic freezers.

A comprehensive understanding of the functional characteristics of each system is crucial for selecting suitable equipment.

2.2 Freezers Classifications

2.2.1 Direct Contact Freezers with Cold Surfaces

2.2.1.1 Plate Freezers

These systems employ metal plates as a thermal barrier between the refrigerant and the product. In the case of packaged items, the packaging film introduces additional thermal resistance. Plate freezers can feature either double or multi-plate configurations. The plates, which are internally hollow, house cooling agents either via coil circulation or complete flooding. These plates are enclosed in insulated chambers, and heat transfer primarily occurs through conduction. In double plate systems (Figure 3A), freezing progresses from both sides. Air films or gaps between food and plates impede heat transfer. To address this, multi-plate designs apply light pressure—less than one bar—on the plates (Figure 3C), which enhances contact and minimizes thermal resistance. Caution is necessary to avoid damaging packages; spacers are often employed to prevent deformation. In loosely packed items, stagnant air inside the packaging adds to thermal resistance. Plate configurations may be horizontal (Figure

3C) for uniformly shaped products or vertical (Figure 3B) for non-packaged, pliable items like meat or fish. Vertical plate systems also accommodate semi-liquid and liquid products. Depending on system capacity, up to 20 plates may be used. Common applications include freezing packaged vegetables, fish, ice cream, and meat. Plate freezers offer high freezing rates, compact designs, and efficient space utilization, outperforming air blast systems in throughput per unit volume.

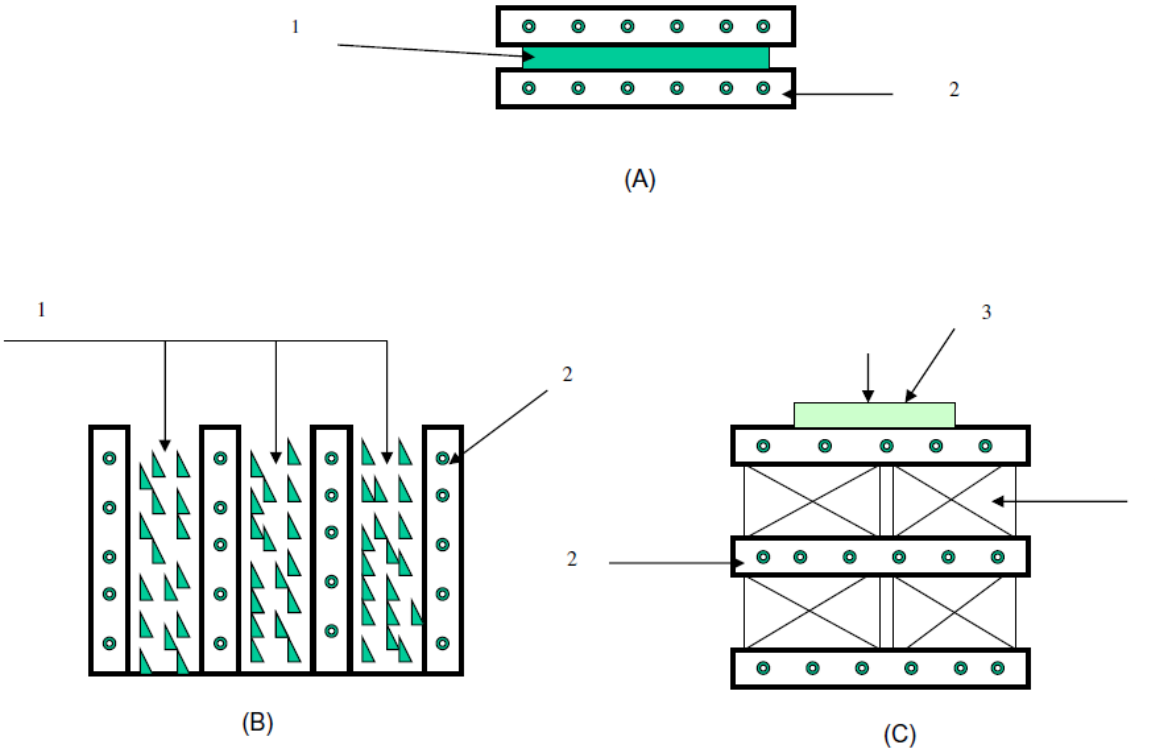

1–Food, 2–plate with cooling coils, 3–pressure plate

Figure 3 Plate Freezers: (A) Double Plate, (B) Vertical Plate, and (C) Horizontal Plate with Press

2.2.1.2 Scraped Surface Freezers

Primarily used for freezing liquids and semi-solids (with or without particulates), these systems comprise two concentric cylinders: an insulated outer shell and an inner cylinder containing food. Refrigerant circulates in the annular space, while a scraper inside the inner cylinder continuously removes frozen layers from the wall (Figure 4). This ensures clean surfaces and efficient heat transfer. Operable in batch or continuous mode, these freezers facilitate rapid freezing, resulting in fine ice crystal formation. They are widely adopted in ice cream production.

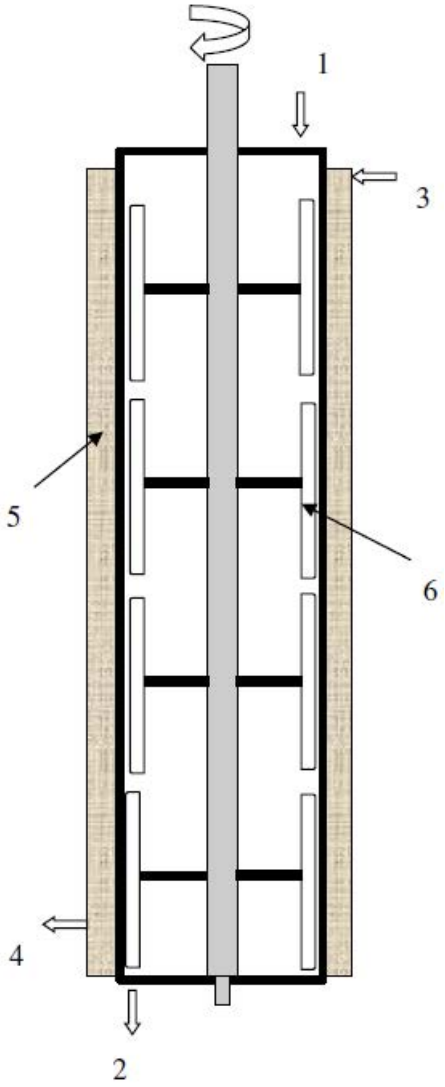

1–Product in, 2–product out, 3–freezing medium in, 4–freezing medium out, 5–insulation, 6–scrapper

Figure 4 Scraped Surface Freezer

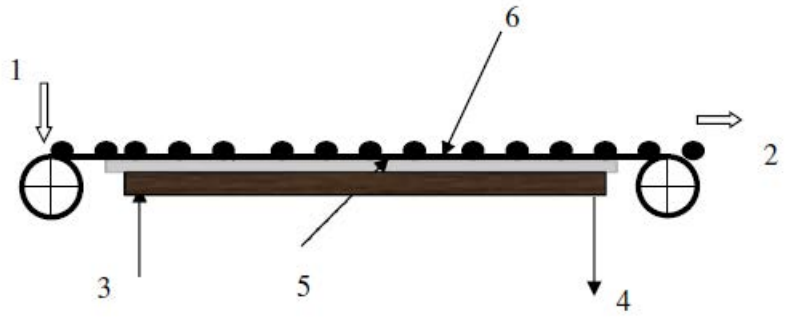

1–Product in, 2–product out, 3–freezing medium in, 4–freezing medium out, 5–steel plate, 6–nonstick belt

Figure 5 Contact Belt Freezer

2.2.1.3 Contact Belt Freezers

Ideal for sticky, moist, and delicate unpackaged items (e.g., fish fillets, yolk, fruit pulp), this system uses a moving non-stick belt placed over a refrigerated plate or drum (Figure 5). Food travels along this belt, undergoing conduction-based freezing. These systems are particularly suited for pre-hardening the base of irregularly shaped foods—like poultry—prior to complete freezing, helping maintain product form.

2.2.2 Freezers Utilizing Air as the Cooling Medium

2.2.2.1 Still Air Freezers

Functionally akin to cold storage rooms, these large units offer both freezing and storage. Refrigerant coils are positioned on one side, with air moving at minimal velocities. Due to low convective heat transfer coefficients, freezing is slow, often resulting in the formation of large ice crystals, which may degrade product quality. Prolonged exposure to air leads to moisture loss, particularly in unwrapped goods. Despite limitations, these systems remain popular due to affordability and versatility.

2.2.2.2 Air Blast Tunnel Freezers

High-velocity cold air circulation in these freezers occurs through insulated tunnels that use fans. Products enter either batch (Figure 6A) or continuous (Figure 6B) tunnels after being placed on trolleys, conveyors or hooks. These systems utilize moving conveyors which operate with either co-current or counter-current airflow, so the latter system produces better heat transfer because of its increased temperature gradient. The equipment functions between −30 °C to −40 °C while operating at 3–6 m/s air speeds to process different product sizes and shapes. These flexible systems suffer from uneven airflow and low heat transfer efficiency together with notable moisture loss from products without packaging [25].

2.2.2.3 Belt Freezers

Belt systems use a continuous moving belt which operates as a straight (Figure 7A–C) or spiral (Figure 7D) unit inside an insulated chamber. Solid products benefit from heat transfer when air passes through perforated belts because this creates partial lifting of the items. Air velocities typically range from 1–6 m/s. Frozen products exit either by being scraped off or by detaching naturally due to brittleness. Both conduction and convection play a role in heat exchange. High-capacity operations benefit from using cryogenic gas sprays which include liquid nitrogen. Spiral belts maintain longer exposure durations which makes them suitable for processing both bulkier and packaged products [26].

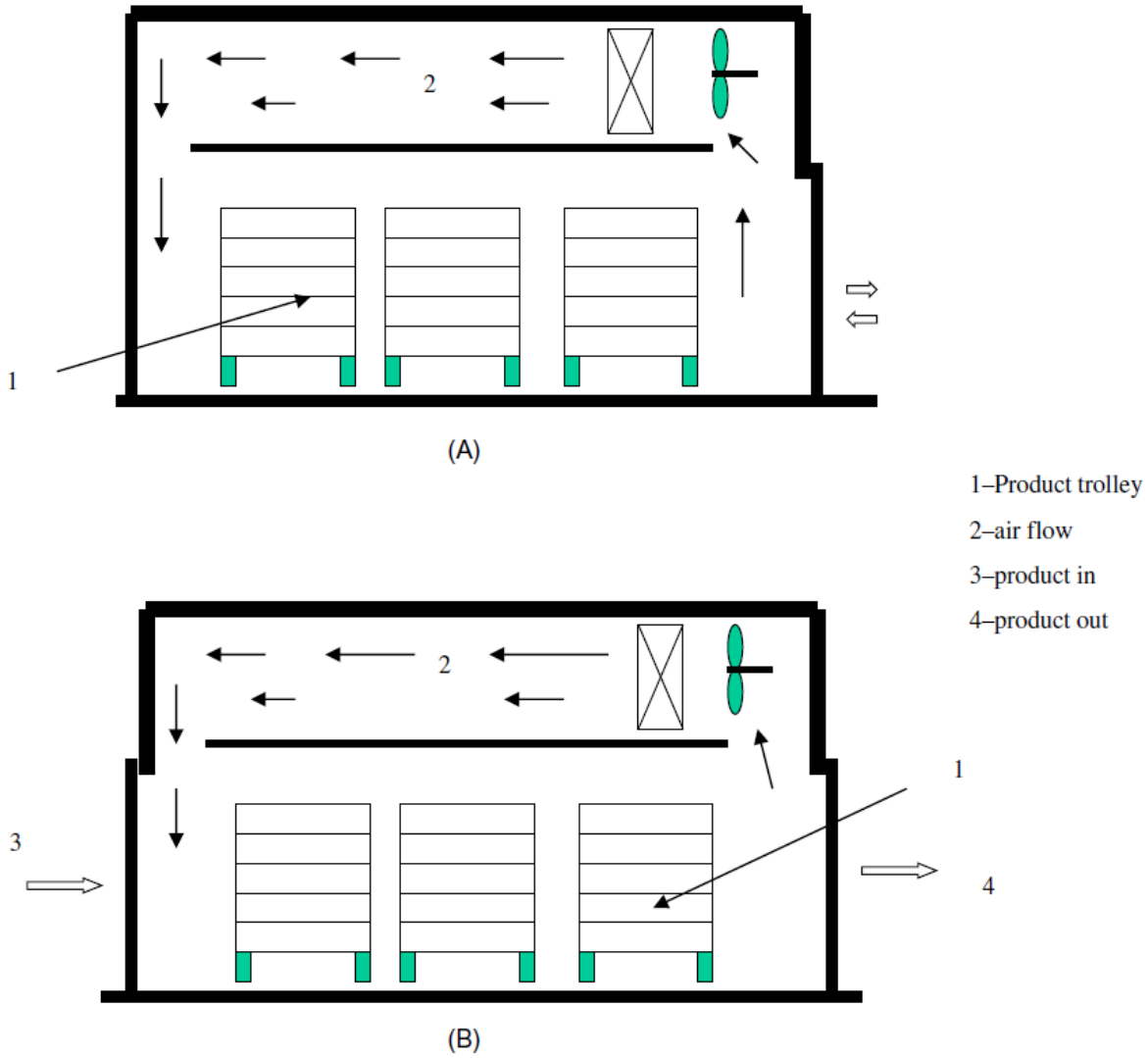

Figure 6 Air Blast Freezers: (A) Batch Type and (B) Continuous Type

2.2.2.4 Fluidized Bed Freezers

The freezing system uses a perforated base to support food particles while blowing high-velocity air through it. The increase in air velocity eventually produces a fluidized state through which heat transfer becomes highly efficient. Typical air temperatures are around −40 °C. The heat transfer occurs through product-air convection and base-particle conduction. Product discharge is often aided by vibration or inclined plates. The length of time products stay in the freezer depends on both the feed rate and the bed volume. Small uniform items including diced vegetables and peas are the best candidates for fluidized beds while this method also supports individual quick freezing (IQF) [27]. The moisture loss from this method remains at approximately 2%. Fluidized systems achieve heat transfer coefficients two to three times greater than forced air systems yet internal product resistance could become the rate-limiting factor. The evaluation of optimal convective coefficients must be performed for different products [28].

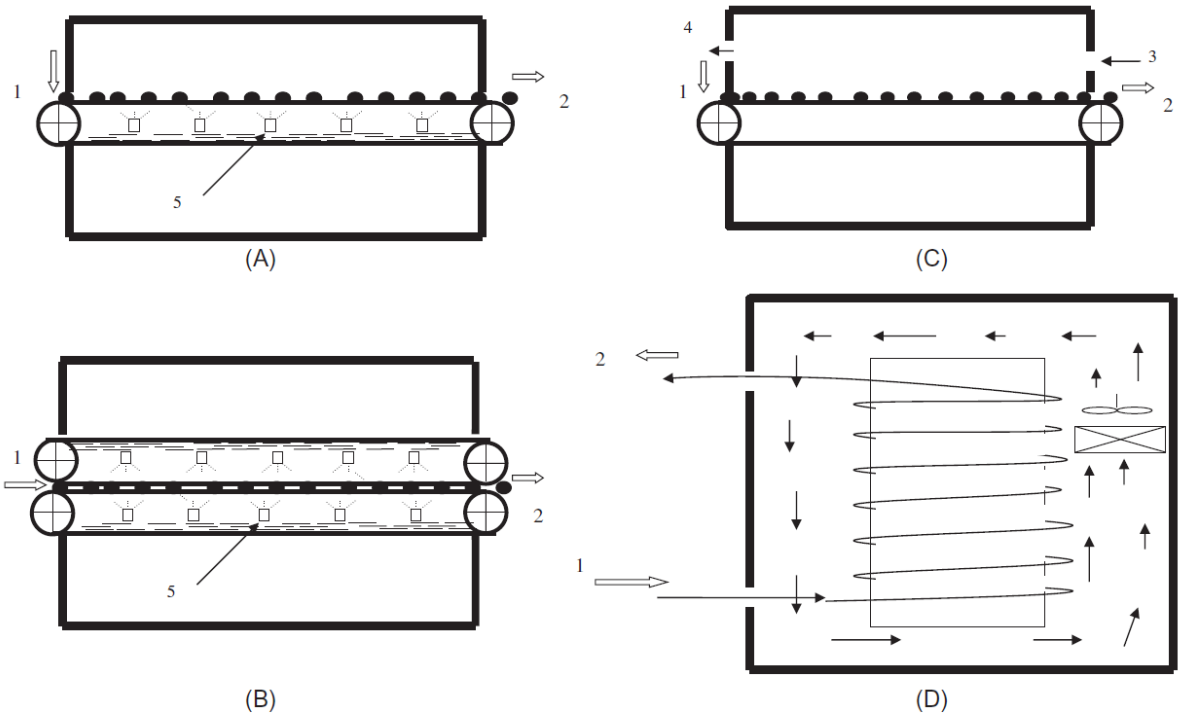

1–Product in, 2–product out, 3–air in, 4–air out, 5–liquid coolant spray

Figure 7 Belt Freezers: (A) Liquid Spray, (B) Twin Belt Liquid spray, (C) Air Cooling, and (D) Spiral Belt

2.2.2.5 Impingement Freezers

The traditional air blast systems experience reduced convective heat transfer because boundary layers form during operation. The solution to boundary layer issues in traditional air blast systems is achieved by using high-speed cold air jets that strike the product from above or below or both directions to break up boundary layers thus enhancing heat transfer. This freezer method proves successful for freezing bakery products and confectioneries and fish on board ships [29]. This system works effectively with bread dough and chicken and meat as its appropriate products. Various types of nozzles such as orifices or jet tubes dispense air jets to achieve shorter processing times along with higher throughputs and minimal weight loss.

2.2.3 Freezers Operating with Liquid Coolants

2.2.3.1 Immersion Systems

The freezing method requires packaging of items to be submerged in brine, glycol, or propylene glycol–water solutions which serve as cold liquids. All product surfaces experience rapid and efficient freezing because they directly contact the coolant. Certain arrangements involve placing liquid food products on corrugated belts through which refrigerant sprays from beneath. The belts can pass through coolant baths, but the product stays partially exposed to the fluid surface. Safety evaluations need to be

performed before selecting freezing media and the product density must exceed that of the liquid to avoid floating [30]. The freezing method has decreased in usage since recent years.

2.2.3.2 Cryogenic Freezers

Cryogenic systems emerged during the 1960s to utilize refrigerants that include liquid nitrogen with a boiling point at −196 °C and liquid carbon dioxide with a boiling point at −79 °C. The odorless inert liquids demonstrate superior heat transfer properties through their high temperature differentials and large enthalpies which amount to 228.7 kJ/kg for nitrogen and 310.3 kJ/kg for CO_2. A standard cryogenic freezer design features insulated tunnels that contain a metal belt structure with three distinct sections for precooling immersion/spray and equilibration.

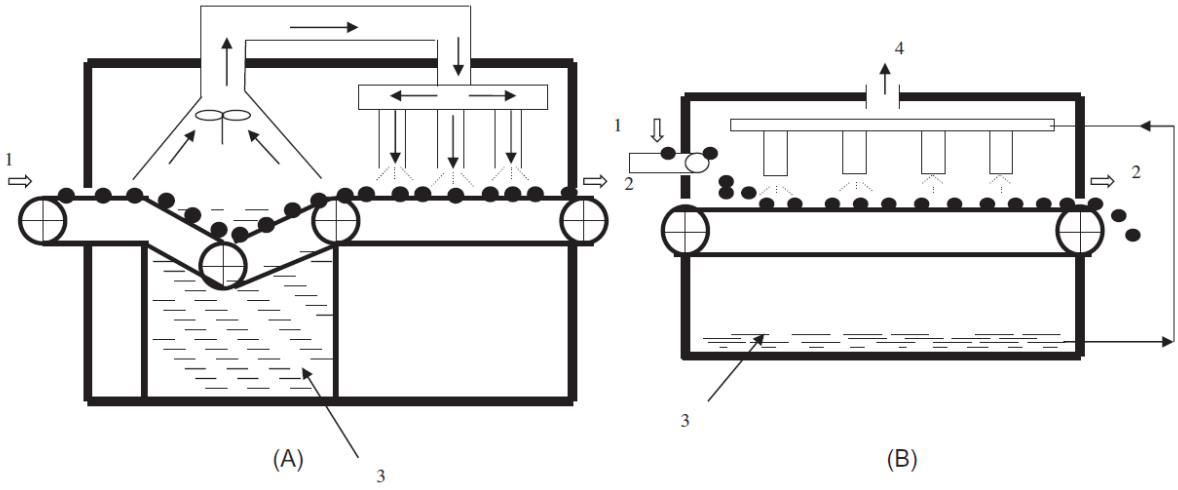

1–Product in, 2–product out, 3–cooling medium, 4–vapor out

Figure 8 Cryogenic Freezers: (A) Immersion Type and (B) Spray Type

The precooling area lowers product temperatures down to approximately −70 °C which helps prevent the formation of freeze cracks when products face direct freezing. The immersion/spray zone of liquid nitrogen decreases product temperature to approximately −190 °C. CO_2 systems use high-pressure liquid which transforms into vapor and dry ice at the tunnel entrance while coolant is sprayed to overcome sublimation delays. Figure 8A and B depict these systems. The combination of high-speed air jets with cryogenic systems produces cryogenic impingement freezers which achieve excellent results with products that have extensive surface areas [31], [32]. Specialized versions for liquid foods like yogurt and flavored ice creams have also been patented [33]. Modern technology has brought about the development of cryomechanical freezers which unite cryogenic and mechanical freezing methods. The cryogenic section starts the freezing process by achieving 25–50% completion before the mechanical stage using spiral, belt or spray finishes the freezing operation. The vapor

produced during cryogenic cooling enables better cooling of the mechanical stage which results in enhanced efficiency together with improved product quality and higher throughput and reduced weight loss and processing duration [34], [35].

Additionally, new technologies have emerged, and several of them will be discussed further.

2.2.4 Advanced Freezing Technologies (AFTs)

2.2.4.1 Radiofrequency-Assisted Freezing (RFAF)

Radiofrequency (RF) technology, which has long been used in the food industry for heating applications, has more recently been recognized for its potential in freezing operations. RF heating, unlike traditional heating methods, provides rapid, uniform, and volumetric thermal distribution. Because of its longer wavelength compared to microwave energy, RF waves have a deeper penetration into food matrices, which enables more uniform internal heating and temperature profiles. This technology usually works within a frequency range of 300 kHz to 300 MHz, which corresponds to wavelengths of 1 mm to 1000 km [36]. Industrially accepted frequencies that are normally utilized are 13.56 MHz ± 6.68 kHz, 27.12 MHz ± 160.00 kHz, and 40.68 MHz ± 20.00 kHz, and their applications extend to scientific, industrial, and medical fields [37].

In RF-assisted freezing, an RF generator creates an alternating electric field between two electrodes, where the food is placed. The field makes polar molecules—primarily water molecules in food tissues—orient and rotate back and forth quickly, creating frictional heat. The molecular agitation promotes the nucleation of ice and results in smaller ice crystals [38]. The smaller the crystals, the less the mechanical damage to cell structures, therefore maintaining the texture and quality of the frozen product [39], [40].

When used in freezing, RF technology can actively affect ice nucleation by breaking up larger crystal formations into smaller ones. RF fields' torque on water molecules changes equilibrium conditions within ice clusters, allowing for precise management of crystal size. A study conducted by Hafezparast-Moadab et al. [41] compared the effects of air-blast freezing and RFAF on rainbow trout fillet post-thaw quality. The results emphasized that RFAF-treated samples showed less structural damage, less drip loss, and improved texture retention. Ice crystals in RFAF samples were much smaller and better distributed (13.19 ± 2.25 to 31.14 ± 4.88 μm) in comparison with control samples (52.02 ± 7.16 μm), suggesting greater water retention and reduced cell rupture. The improved nucleation rate in RF-treated products is due to water molecules' rapid rotational movement, a phenomenon also confirmed by Manzocco et al. [40], who noticed improved preservation of meat microstructure and reduced myofibrillar degradation in samples treated with low-voltage RF in combination with different freezing approaches.

Although it has advantages, RFAF can be affected by non-uniform thermal distribution. The coupling of the electric field with food constituents can lead to hotspots at geometrically complicated edges and corners, thus producing thermal runaways. To alleviate this, several solutions have been suggested, including immersing samples in thermal mediums [42], using dielectric-matching materials surrounding the product [43], or intermittently repositioning samples halfway through the process [44].

2.2.4.2 High Pressure-Assisted Freezing (HPAF)

High-pressure processing (HPP), at pressures of 100 to 800 MPa, has been shown to be effective in the deactivation of microbial contaminants such as bacteria, yeasts, and viruses [45]. When combined with freezing, termed High Pressure-Assisted Freezing (HPAF), the method greatly inhibits the growth and size of ice crystals, thereby reducing structural damage due to crystallization-induced volume expansion [46], [47]. Critical operational parameters like pressure intensity, duration, and freezing temperature have significant impacts on process efficiency [48].

HPAF works in the same way as traditional freezing (CF) but at high pressures. First, the food sample is compressed to a desired pressure and cooled. When enough supercooling is reached, ice nucleation is induced, and phase transition occurs under pressure [49]. Fernández et al. [50] classified HPAF into three classes: high-pressure freezing (HPF), in which crystallization occurs under fixed pressure; high-pressure shift freezing (HPSF), in which pressure is abruptly released to induce freezing; and high-pressure induced freezing (HPIF), in which rising pressure induces and maintains the freezing phase.

HPF initiates freezing from the surface layers inwards, as in CF, and is expected to create ice only on surfaces in contact with the coolant [51]. By contrast, HPSF consists of sample compression (typically to ~200 MPa), quick cooling to a subzero setpoint, followed by sudden depressurization. This induces uniform nucleation throughout the food matrix to create fine ice crystals and release latent heat, thus increasing the sample temperature to the freezing point [50], [52]. HPIF, by contrast, consists of a two-stage compression: initially to moderate pressure without freezing, followed by pressure increase to initiate freezing under isobaric conditions [53], [54].

Of these, HPSF has been the most promising because of the deep supercooling it produces. Fernández et al. [50] found more rapid nucleation and more homogeneous ice formation in HPSF than in HPF. Under depressurization, the quick temperature decrease allowed fast crystallization, with phase transition times of 5.9–13.7 minutes (HPSF) versus 14.1–23.1 minutes (HPF). Comparable observations were reported by Su et al. [55], who worked with shrimp muscle and pork liver at various pressures and temperatures. HPSF produced numerous, well-distributed microcrystals because of considerable supercooling (6.5–16.8 °C).

Aside from improvements in quality, HPAF is also beneficial regarding energy consumption. Li et al. [56] made comparisons on the energy consumption of atmospheric freezing and HPAF and noted that HPAF consumed merely 68,980 kJ, while conventional freezing needed 280,260 kJ.

Despite its efficacy, HPAF is still bound by economic and technical limitations. Elevated equipment expenses—attributable to the requirement for strengthened pressure vessels and accurate control systems—and poor scalability limit most uses to laboratory or pilot environments [57].

2.2.4.3 Magnetic Field-Assisted Freezing (MFAF)

Water's dipolar character, resulting from its asymmetrical molecular shape, renders it responsive to magnetic fields [58]. Under the influence of magnetic fields, water molecules try to align along field lines, disrupting hydrogen bonding networks and inducing changes in water structure and mobility. Exposure can create ring-shaped electric currents by altering hydrogen-bonded chains, which in turn influence water cluster dynamics. Smaller water clusters, established via bond weakening or reorientation, can act as nucleation sites, inducing quicker and more uniform ice formation [59]. Sun et al. [60] studied, magnetic fields can tighten or break up hydrogen bonds, thus altering water molecule clustering and enlarging the ratio of non-freezable water, improving quality preservation.

There are four magnetic field modalities commonly applied in freezing: Static (SMF), Alternating (AMF), Oscillating (OMF), and Pulsed Magnetic Fields (PMF) [61].

Wei et al. [62] investigated the impact of SMF (60 mT) under sub-zero temperatures on Pacific white shrimp and concluded that SMF at −35 °C decreased the total freezing time to 380 seconds—22.7% lower than conventional immersion freezing. The treatment also reduced the phase change time and led to finer, more uniform ice crystal distribution.

With the freezing temperature rising, ice crystals became bigger; yet magnetic fields restricted their growth through the disturbance of hydrogen bonds. This probably accelerated the frequency of nucleation, thus reducing the activation energy for crystallization. Ye et al. [63] studied AMF (50–250 Hz) actions on tilapia fillets and found a non-linear impact on freezing time and textural quality. This can be explained by resonance coupling between field frequency and molecular movements, which could be modulated by ionic components in the sample. Fractal analysis indicated that microstructural responses had no consistent tendency.

Tang et al. [64] also studied SMF (2–20 mT) and AMF (0.05–1.74 mT at 50 Hz) on cherries. They reported shorter phase change times—13.24 min (SMF at 10 mT) and 11.69 min (AMF at 1.74 mT)—than the control (15.50 min). Drip loss was also lower for both SMF (4.79%) and AMF (4.64%) compared to freeze-dried samples (10.39%). Ice crystal sizes were noticeably smaller, with AMF having the lowest mean area (1220.5 ± 16 μm²).

2.2.4.4 High-Voltage Electrostatic Field-Assisted Freezing (HVEFAF)

High-voltage electric fields (HVEF) are a non-thermal preservation method, which is renowned for preserving food quality with less nutrient deterioration [65]. HVEF systems utilize corona discharge to produce an "electric wind." As air is ionized between needle-plate electrodes, ion momentum is transferred to neutral air molecules, propelling airflow towards the food surface [66]. HVEF technologies are divided into Static Electric Fields (SEF) and High-Voltage Electrical Discharges (HVED), based on whether the field is constant or goes beyond breakdown voltage levels [67].

In High-Voltage Electrostatic Field-Assisted Freezing (HVEFAF), food is positioned between electrodes where a direct current creates a high-voltage electric field [66]. Polarization and orientation of water molecules are induced by this field, which increases nucleation and decreases supercooling. Jia et al. [68] showed that 10 kV HVEF treatment resulted in smaller ice crystal areas in pork tenderloin. Hu et al. [69] tested different electric (10–50 kV/m) and magnetic field (2–8 mT) intensities. The most favorable results—reduction of freezing time by ~40%, reduction of thawing loss to 1.7% (from 5.7%)—were achieved at 30 kV/m electric and 2 mT magnetic field intensities.

2.2.4.5 Dehydrofreezing (DF)

Dehydrofreezing (DF) entails partial removal of moisture prior to freezing to avert structural damage from crystallization. Pre-drying treatments such as air-drying or osmotic dehydration deplete water content to an optimum [70], [71], [72]. Water in plant tissues is intracellular (cytosol, vacuoles) and extracellular. Freezing typically starts outside the cells, where there are fewer solutes, thus higher freezing points. Ice formation external to cells draws out intracellular water, resulting in huge extracellular crystals that distort tissues [73]. Quick freezing restricts this by producing smaller, more evenly distributed crystals. Noestroys membranes through abrupt water expansion [70]. DF seeks to reduce this damage. Ben Haj Said et al. [71] evaluated freezing of apples at various water contents and freezing rates. Apples with high moisture content took longer to freeze (86–329 min), yielding greater thaw exudate, whereas samples of lower moisture content froze more quickly (32 min) with reduced damage. Schudel et al. [70] also noted better firmness and reduced drip loss in carrots, bell peppers, and cucumbers when DF was compared with traditional freezing.

2.3 Studies on Vapor Compression Refrigeration System with Vapor Injection Scroll Compressors

The following section provides an extensive explanation of the vapor compression refrigeration cycle. The diagram in Figure 9 demonstrates the four essential components of the cycle which connect the evaporator to the compressor and condenser and expansion device.

The working fluid moves counterclockwise through the components following the sequence shown in the figure. The components connect through pipes and tubes which extend between their respective inlets and outlets.

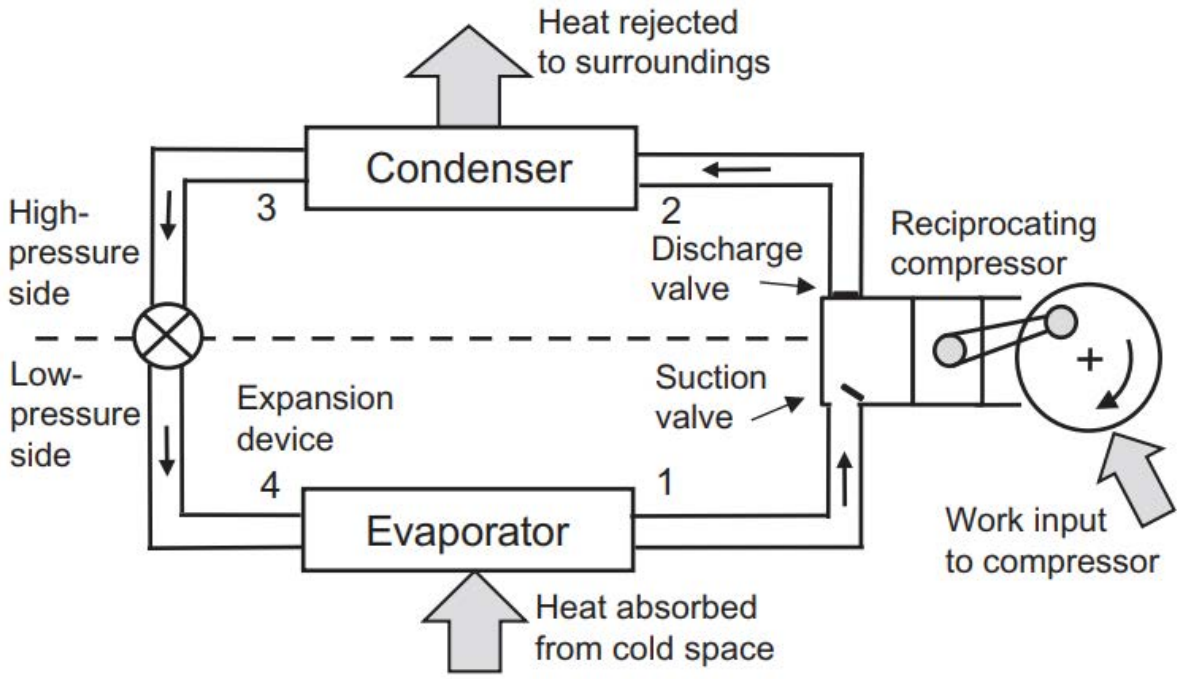

Figure 9 Schematic Diagram Showing the Basic Four Components of an Ideal Vapor Compression Refrigeration Cycle

The evaporator receives heat from the cold environment through a phase transition of liquid refrigerant to vapor. The condenser rejects heat to the environment through the process of refrigerant condensation. The refrigeration effect requires the evaporator refrigerant temperature to remain below cold space temperature so heat can transfer into the fluid. The condenser requires refrigerant temperatures above ambient conditions to transfer heat to the environment.

The expansion device functions to rapidly reduce refrigerant pressure which produces temperatures below the cold space temperature. The compressor increases the pressure of refrigerant vapor from the evaporator to reach temperatures above ambient conditions which enables heat rejection and vapor condensation. The expansion device and compressor operate together to establish an effective separation between the high-pressure and low-pressure regions of the vapor compression refrigeration cycle.

Vapor compression refrigeration systems (VCRs) function as the dominant technology in worldwide refrigeration operations because they represent 80% of all industrial and domestic and commercial and cold-chain logistics applications. The extensive use of these systems results in substantial energy

consumption which makes up 15% of global electricity usage while generating 10% of greenhouse gas emissions. Commercial freezing and refrigeration applications predominantly choose electrically powered VCRs among various available technologies.

Cascade refrigeration systems serve as the standard technology for storing biological specimens at ultra-low temperatures (e.g., −80 °C). The complicated setup of these systems leads to reduced energy efficiency and operating stability. The Global Cooling Corporation conducted research in the United States where they studied two refrigeration systems which operated at −90 °C temperatures near the minimum level achievable by the system: dual-stage cascade and Stirling cryocooler systems. The evaluation demonstrated that the cascade system reached a COP of 0.25 yet the Stirling system surpassed this with a COP of 0.39.

The Stirling refrigeration cycle has developed into a standard small cryogenic system through extensive improvements. The system delivers high operational stability and deep-freezing performance which positions it as a future development direction for sub-zero refrigeration technology.

A comparison of the principal technical characteristics of vapor compression, Stirling, and absorption refrigeration techniques is given in Table 2.

Vapor compression refrigeration systems require high-quality electricity to generate low-temperature cooling which results in low energy efficiency, but absorption cooling technology offers a viable alternative. This system cuts down electricity requirements through low-grade heat source utilization and produces substantial cooling effects. The system operates using environmentally friendly refrigerants.

The operational performance of absorption units depends on the thermal and mass transfer properties of their working fluids because these characteristics significantly influence their operation according to Jiang et al. (2022) [74].

System Type	Characteristics	Strengths	Weaknesses
Vapor compression refrigeration system	Uses a compressor, condenser, expansion valve, and evaporator for the cycle	High efficiency; Wide applicability; Rapid cooling; Easy to control; Technically mature; High reliability; Suitable for various scales of application [75].	Requires electric power; Potential environmental impact; High maintenance and operating costs; Compressor noise and vibration; high initial investment cost [76], [77]
Stirling refrigeration system	Based on the Stirling cycle, uses gas as the	Efficient and quiet; Can use various gases	Complex structure; High initial cost; Not

	working medium, achieving refrigeration through gas expansion and compression	as the working medium; Does not require electricity, can be driven by thermal energy [78], [79]	suitable for all types of refrigeration needs
Absorption refrigeration system	Uses thermal chemical reactions between an absorbent and a refrigerant, driven by thermal energy	Energy-saving and environmentally friendly; Almost no noise and vibration; Suitable for remote or off-grid locations [80].	Lower efficiency; Requires a large amount of thermal energy; high maintenance costs [81]

Table 2 Comparison of Refrigeration Systems

2.4 Vapor Compression Refrigeration System Components

2.4.1 Classification of Compressors

The main function of compressors in vapor compression systems involves raising both pressure and temperature levels of the working fluid. The classification of compressors occurs through their operational principles and construction methods and performance characteristics. The two primary compressor types include positive displacement compressors which mechanically reduce vapor volume to compress it and dynamic compressors which use kinetic energy for compression. The selection of compressor types depends on application needs because each compressor type provides unique benefits for specific requirements including capacity and efficiency and operating conditions and noise levels. The following section explains the main compressor types which operate in refrigeration and heat pump systems through detailed classification and description (Figure 10).

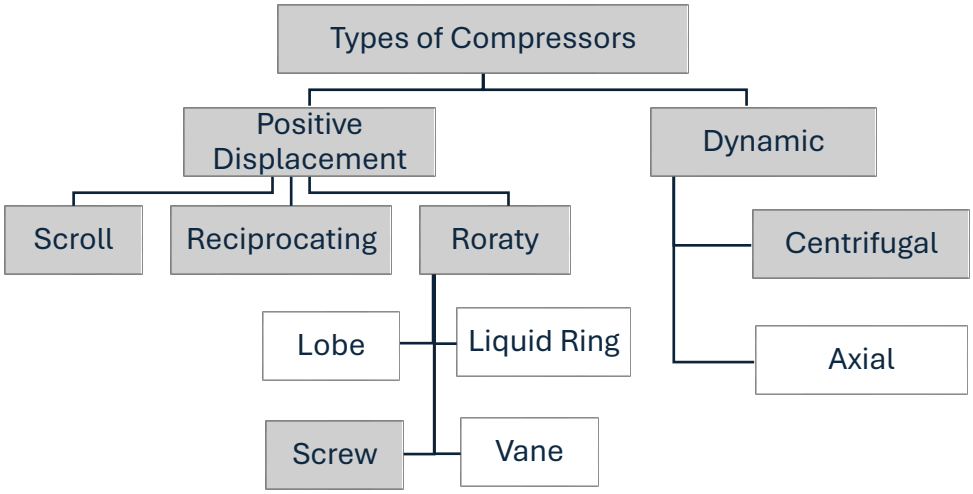

Figure 10 Classification of Compressors [82]

2.4.1.1 Reciprocating Compressors

Reciprocating compressors are a type of positive displacement compressor that work on a repetitive cycle of suction, compression, and discharge of the working fluid—usually water vapor. This is achieved by the back-and-forth (reciprocating) movement of a piston within a sealed cylinder, which produces changes in vapor volume.

One of the characteristics of this type of compressor is the crankshaft that transforms rotary drive shaft motion into linear piston motion. To improve efficiency, two-step capacity control has been implemented by varying the dead volume of the cylinder (Figure 11).

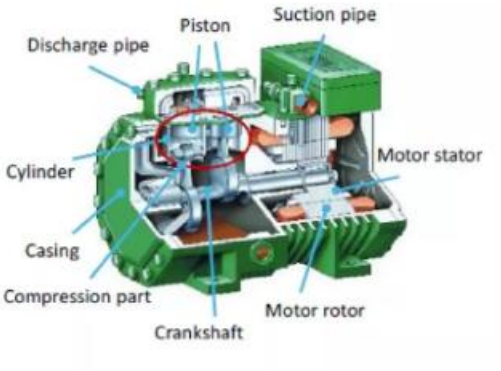

(a)

View of a Reciprocating Compressor

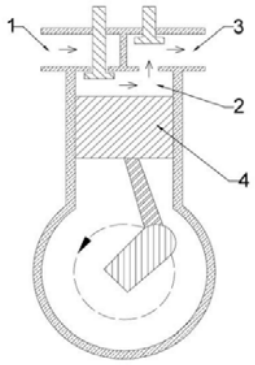

(b)

Simplified Diagram of a Reciprocating Compressor:
1 - Compressor Suction Area
2 - Working Area
3 - Pressure Area
4 - Piston of Compressor

Figure 11 Schematic and Color-Coded Cutaway View of a Reciprocating Compressor

The reciprocating compressors can be categorized based on several criteria:

- configuration and number of valves
- arrangement and quantity of cylinders,
- construction of the compressor casing,
- number of stages of compression, and
- the type of refrigerant used [83].

2.4.1.2 Rotary Compressors

Rotary compressors are also positive displacement. Compression in these systems is obtained through a rotating piston in the cylinder. The design can be more compact and is much quieter during operation than reciprocating types because it does not have a crankshaft.

The piston is eccentrically mounted, and a spring-loaded blade is pressed against it, separating the internal space into compression and suction areas. The blade allows continuous compression as the piston continues to rotate. The schematic of a common rotary compressor is in Figure 12 [83].

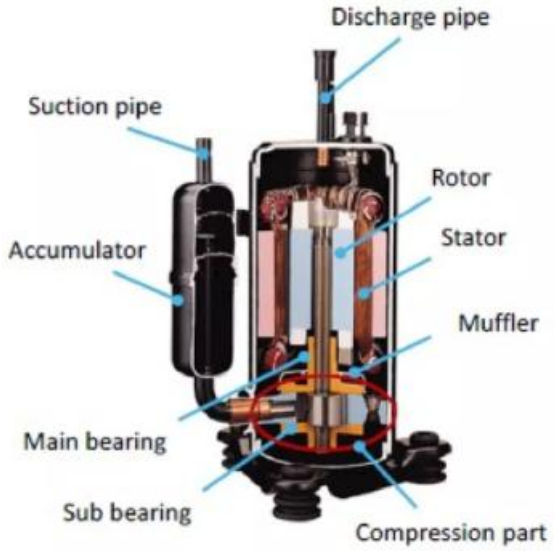

Simplified schematic and color-coded cutaway view of a rotary compressor (a)

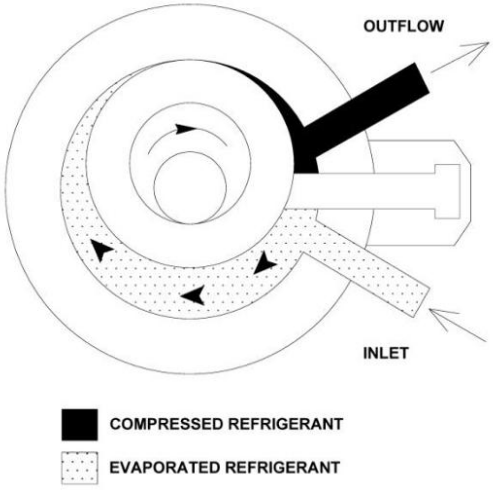

Schematic diagram of a rotary compressor (b)

Figure 12 Rotary Compressor

2.4.1.3 Scroll Compressors

Scroll compressors are yet another type of positive displacement device. They use two spiral elements (scrolls): one is fixed while the other orbits in a planetary motion. As the orbital movement continues, the volume between the scrolls is slowly reduced from the outer suction area toward the center discharge point, compressing the gas in the process.

Figure 13 demonstrates the operation principle of a scroll compressor. There are three pressure areas—low, medium, and high—localized close to the center. One of the significant benefits compared to reciprocating compressors is the lack of residual volume ("dead space"), which makes volumetric efficiency much higher—up to 100% or so.

A very thin lubricant film serves as a sealant medium among the scrolls. The orbiting scroll is attached to a shaft on an eccentric drive, and the fixed scroll contains the discharge port.

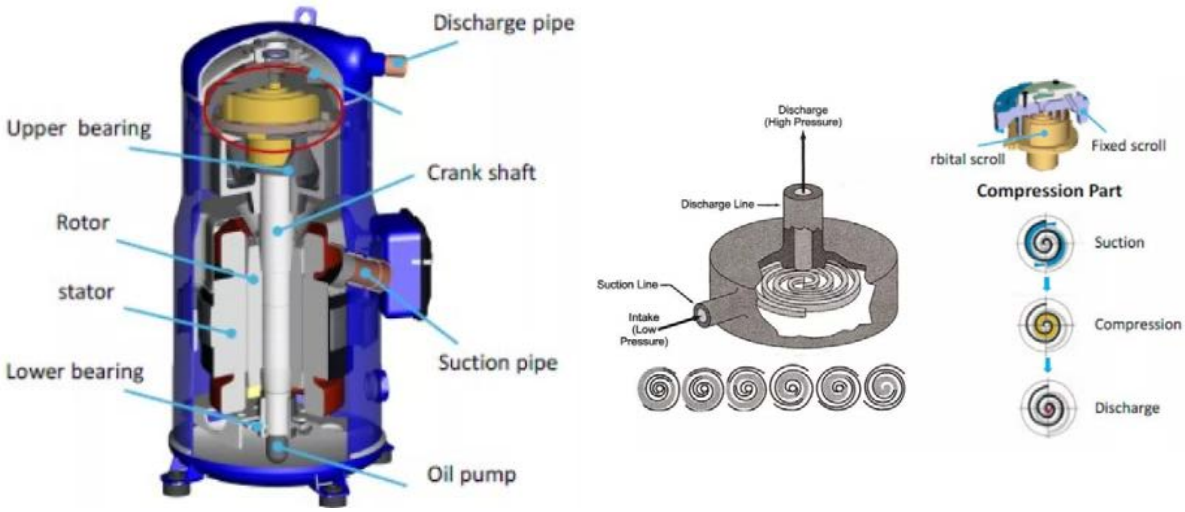

Schematic and cutaway view of a scroll compressor and showing suction, compression (a)

Operation of the scroll compressor (b)

Figure 13 Scroll Compressor

The radius of orbiting motion is one of the key design parameters [84]. Scroll compressors have several benefits over reciprocating models:

- fewer moving parts
- decreased size because of the removal of crank mechanisms,
- greater resistance to water hammer,
- reduced dynamic load variations on the motor shaft
- less vibration, and
- longer operational lifespan [83].

2.4.1.4 Rotary Screw Compressors

Rotary screw compressors are also positive displacement machines. They are made up of two helical rotors with intermeshing lobes and grooves, set in parallel in a closed casing. In operation, a thin film of lubricants provides the required clearance (backlash) between rotors and housing.

The working fluid is sucked in through the suction port and compressed as it travels along the length of the rotors toward the discharge port at the other end. Figure 14 shows a schematic diagram of a screw compressor.

The process of compression is carried out in four steps:

- suction
- transportation of the refrigerant toward the discharge side,
- compression
- and discharge.

Compared to reciprocating compressors, screw compressors offer several benefits:

- continuous pulsation-free flow
- no need for inlet and outlet valves
- resistance to water hammer,
- and the capability to adjust heating output over a broad range (20–100% of full capacity).

In the past, these compressors had been applied mostly in high-capacity heat pumps. They can be found as single-stage and multistage compressors; the latter being favored for use in high pressure ratio applications. Multistage compressors are especially difficult to optimize because geometry, operating conditions, and interstage pressures must be fine-tuned [85].

A more recent innovation, the "miniscrew" compressor, has been added for capacities over 125 kW. These smaller units are the benefactors of the advantages of large screw compressors: few moving parts, accurate capacity control, and minimal vibration.

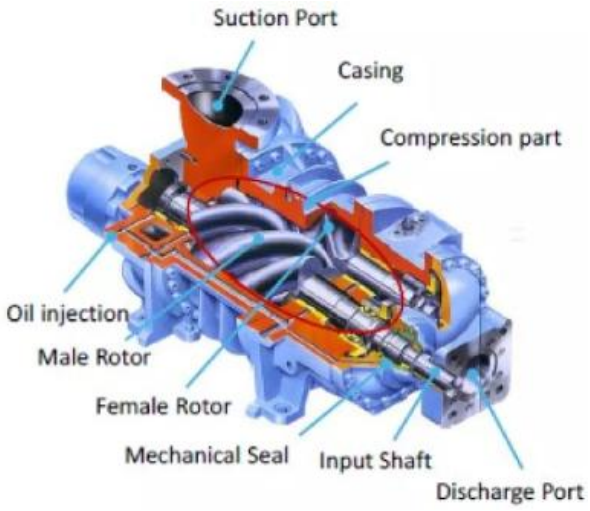

Schematic Diagram of a Screw Compressor (a)

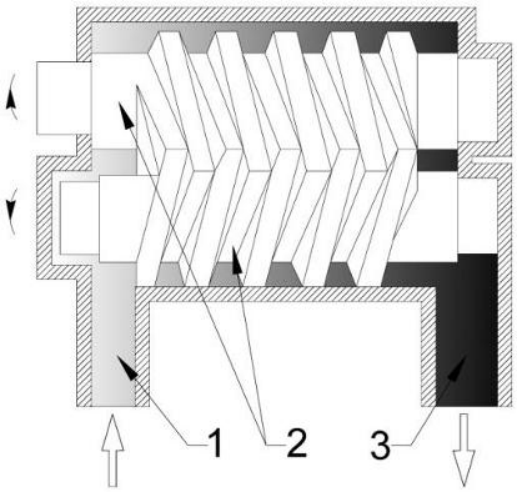

Diagram of Rotary Screw Compressor (b)
1 - Compressor Suction Area
2 - Screw Compressor Rotors
3 - Pressure Area

Figure 14 Screw Compressor

2.4.1.5 Centrifugal (Dynamic) Compressors

Centrifugal compressors use dynamic compression by centrifugal force to push the refrigerant out. A diffuser is also employed to reduce the flow velocity and to convert the kinetic energy into static pressure rise. Guide vans may be included to direct the direction of flow. Based on flow direction, centrifugal compressors may be either radial or axial, but radial configurations are most typical in heat pump applications. These compressors are specifically applicable to high-capacity systems since high efficiency demands a minimum of 0.2–0.3 m^3/s refrigerant vapor flow rate and 83.5–167 s^{-1} rotational speeds. One of their key design benefits is the elimination of gear trains, which minimizes the number of bearings and the complexity of the lubrication system. The result is fewer mechanical losses and improved reliability in operation (Figure 15) [83].

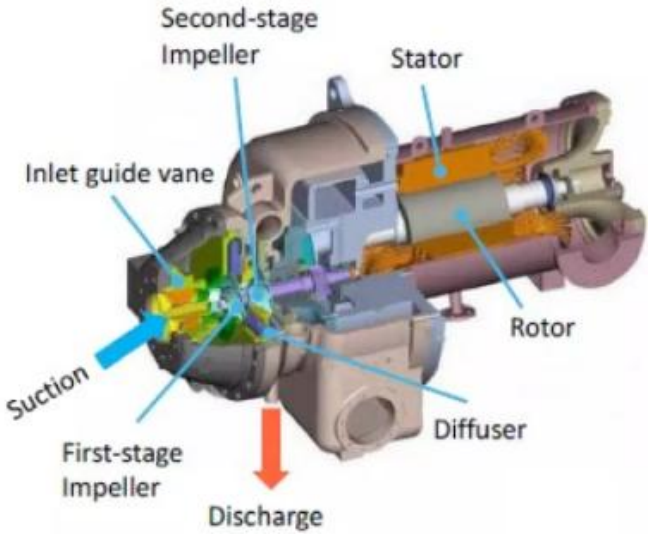

Figure 15 Simplified Schematic and Color-Coded Cutaway View of a Centrifugal Compressor

2.4.1.6 Vapor Injection Scroll Compressor

One way to improve heat pump performance and dependability, particularly in harsh working environments, is through refrigerant injection. At a midpoint in the compression process, the procedure entails rerouting a part of the refrigerant from the condenser outlet back into the compressor. Several advantages for heat pumps might result from doing this, firstly, A higher mass flow rate at discharge. Higher heating capacity can be attained by increasing the condenser's refrigerant circulation. Furthermore, convective heat transfer coefficients may rise with increased refrigerant mass flows, improving the efficiency of the heat exchange process. Secondly, less effort was made on compression. Less compression effort is needed than with a non-injected compressor producing the same flow rate because some of the refrigerant is injected into the compressor at an intermediate pressure. Thirdly, Lowering the discharge temperature. Elevated discharge temperatures have the potential to negatively impact the dependability of the compressor by causing overheating and eventual malfunction. Injecting refrigerant can lower the compressor's discharge temperature.

Three forms of refrigerant injection have been identified via significant research:

(i) liquid Injection (LI) involves injecting liquid-phase refrigerant from the condenser outlet directly into the compressor. Ayub, S et al conducted the research. They explore the use of liquid refrigerant injections in scroll compressors to manage high discharge temperatures during operations at elevated compression ratios, common in refrigeration and heat pump applications. Through both thermodynamic analysis and laboratory testing, the study evaluated how liquid injection impacts compressor capacity, efficiency, and discharge temperature. The findings confirmed that liquid refrigerant injections effectively reduce discharge temperatures, improving the compressor's reliability. Both injecting into the suction flow and directly into the compression pocket were tested, with similar success in temperature reduction and no major differences in performance [86].

Winandy, Eric L. and Lebrun, J investigated the performance of hermetic scroll compressors using various injection methods, including no injection, vapor injection, and liquid injection. The study aimed to assess how these methods influence compressor behavior and efficiency. Experimental tests were conducted on different compressor configurations, and a simplified model was developed to simulate the effects of heat transfers and injection processes. The results showed that liquid injection significantly reduced discharge temperatures, lowering them by about 1.2 K for each 1% increase in injection ratio. The model also effectively predicted key variables such as mass flow rate, power consumption, and discharge temperature, aligning well with the experimental data [87].

Cho, H et al examined how liquid refrigerant injection impacts the performance of an inverter-driven scroll compressor under varying frequencies, injection pressures, and injection locations. Experimental tests measured cooling capacity, power input, and discharge temperature. The results showed that liquid injection significantly lowered discharge temperatures, particularly at high frequencies. Injection was most beneficial at higher frequencies, where efficiency improvements were noted, while at lower frequencies, increased leakage and power consumption reduced overall performance. Injection at a 180° angle performed slightly better than at 90° [88].

Lee D et al focused on analyzing the performance of a refrigeration system utilizing vapor and liquid refrigerant injections at high compression ratios to reduce excessive discharge temperatures. The experiments were conducted using a scroll compressor operating with R22 refrigerant, testing various injection ratios. The results indicated that liquid injections were more effective in controlling discharge temperatures compared to vapor injections, particularly at a 10% injection ratio. Liquid injection maintained cooling capacity and reduced compressor temperatures, while vapor injection caused a decrease in the COPat higher injection ratios [89].

Kim D et al compared the performance of two-phase, liquid, and vapor injection in scroll compressors for heat pumps using R410A refrigerant. A numerical model was developed and validated through experimental testing under various outdoor temperatures. The results revealed that two-phase injection

provided the highest COP, especially in colder conditions, while liquid injection was effective in reducing discharge temperatures. Vapor injection showed moderate performance. Overall, two-phase injections proved to be the most efficient, providing significant energy savings across varying operational conditions [90].

(ii) Two-Phase Injection (TPI) involves injecting a mixture of liquid-vapor phase refrigerant.

Lee H et al proposed a novel saturation cycle to enhance the vapor compression cycle (VCC) performance by reducing thermodynamic losses associated with gas compression and expansion. Two-phase refrigerant injections are introduced into a multi-stage cycle, and the performance of various configurations is modeled and compared under standard ASHRAE conditions. The use of low GWP refrigerants like R123 was found to be highly effective, yielding significant improvements in COP. The study also explores practical ways to implement the saturation cycle, highlighting multi-stage phase separators and alternative injection locations as key to achieving performance gains [91]. Yang M et al investigated three methods two-phase suction, liquid injection, and two-phase injection—to reduce the high discharge temperature of the R32 scroll compressor, which is known for being higher than R410A, thereby limiting its adoption. Using a modified distributed parameter model, the effectiveness of these methods in reducing discharge temperature and their impact on compressor performance are evaluated. Results show that all three methods successfully decrease discharge temperatures, with two-phase injections outperforming the other methods by improving cooling capacity by 11.8% and COP by 4.8%. The study concludes that these methods can extend the operating range of R32 scroll compressors and improve overall system reliability and performance [92].

(iii) Vapor Injection (VI) involves injecting vapor-phase refrigerant.

Ding et al studied a novel air source heat pump (ASHP) system to address the limitations of conventional ASHPs, which struggle to operate efficiently in extreme weather conditions. The improved ASHP incorporates a scroll compressor with supplementary injections and a subcooling system, designed to enhance performance in both high summer heat and cold winter temperatures. The testing revealed that the new system can operate reliably under extreme conditions, maintaining efficiency and reducing energy consumption compared to conventional ASHPs. The results demonstrate that the improved ASHP expands the operational range and efficiency, saving energy and contributing to environmental protection [93]. Ma G and Chai Q introduced an improved heat pump cycle with a scroll compressor economizer aimed at increasing the heating capacity of ASHPs in cold regions. The authors developed a prototype and conducted experiments showing that the heat pump operates effectively even at low ambient temperatures (down to -15°C), providing high heating output and water supply. The thermodynamic model developed for this system optimizes performance, demonstrating that it increases efficiency and expands the operational range of ASHPs in cold climates, addressing issues such as reduced heating capacity and increased discharge temperatures in conventional systems

[94]. Bertsch S and Groll E investigated the design, simulation, and testing of a two-stage air-source heat pump using R410A, tailored for residential heating in northern U.S. climates. The system was developed to address the challenges of decreased heating capacity and efficiency at low outdoor temperatures. Experiments were conducted at ambient temperatures as low as -30°C, demonstrating the system's ability to provide adequate heating and cooling. The results showed that second-law efficiencies of up to 45% were achieved, with a COP of 2.1 at -30°C. The study concludes that two-stage heat pumps can effectively meet heating demands in cold climates while also offering air conditioning capabilities in warmer conditions [95].

Wang X et al explored the performance of a two-stage heat pump system using R410A as a refrigerant and a vapor-injected scroll compressor. The system is tested under both flash tank and internal heat exchanger configurations, and its performance is compared with a conventional system. Experimental results show a significant improvement in cooling and heating capacities. In cooling mode, a 14% capacity gain and a 4% improvement in COP at 46.1°C were observed. In heating mode, at -17.8°C, the system exhibited a 30% increase in capacity and a 20% COP improvement. The study concludes that vapor-injection is an effective technique for enhancing the performance of heat pumps in both high and low ambient temperature conditions [96].

Heo J et al compared the heating performance of air-source heat pumps (ASHP) using different types of refrigerant injection, including flash tank and sub-cooler vapor injection cycles (FTSC and SC). The research was aimed at addressing the performance degradation of ASHPs in extreme low and high ambient temperatures. Experimental results showed that the average heating capacities of the FT, FTSC, and DESC cycles were higher by 14.4%, 6.0%, and 3.8%, respectively, compared to the SC cycle. However, the COP was similar across all cycles. The study concludes that while the FT cycle shows superior heating performance, the FTSC cycle offers a more stable and controlled system, making it an attractive alternative for applications where precise control is required [97]. Roh C and Kim M examined how intermediate pressure impacts the heating performance of a heat pump system using the R410A vapor-injection technique. The authors conducted experiments by adjusting the intermediate pressure through an additional expansion valve and evaluating the system's performance under different injection ratios and compressor frequencies. Results indicate that a lower intermediate pressure led to higher initial heating capacity and COP, but it also restricted the range of vapor injections. Conversely, higher intermediate pressure extended the available range of injections but reduced heating capacity. The study concludes that optimal performance depends on careful control of the intermediate pressure, balancing initial heating capacity with the vapor-injection range [98].

Navarro E et al focused on the performance of a vapor injection (VI) scroll compressor under varying pressures and temperature conditions. The research aimed to assess the compressor's efficiency across a wide range of operational conditions, comparing it with a non-injection compressor. Results indicated

that vapor injection significantly improves compressor efficiency and capacity, particularly under extreme temperature conditions. The study also explored the impact of intermediate pressure and superheat on the VI compressor's performance, finding that these factors are crucial in optimizing the system's cycle efficiency, particularly for applications in heat pumps and air conditioning under challenging climate conditions [99]. Dardenne L et al introduced a semi-empirical model for a variable speed scroll compressor with vapor injection, aimed at improving performance predictions for high-temperature lift applications. The model, validated through 63 experimental tests, calculates the suction and injection refrigerant mass flow rates, compressor power, and refrigerant discharge temperature. The model's predictions align well with experimental results, with 89% to 98% of the data falling within acceptable error margins. The study concludes that the semi-empirical model effectively balances computational efficiency with accuracy, making it suitable for integration into vapor compression system simulations [100]. Tello Oquendo, F M et al provided a comparative analysis between a scroll compressor with vapor injection (SCVI) and a two-stage reciprocating compressor (TSRC) under extreme conditions, focusing on efficiency, volumetric efficiency, COP, and cooling capacity using R407C refrigerant. The results show that the SCVI performs better in terms of efficiency and COP for pressure ratios below 7.5, making it suitable for air conditioning and heat pump systems in moderate climates. However, at higher pressure ratios, the TSRC exhibits superior efficiency and COP, making it more appropriate for applications like sanitary hot water systems and low temperature freezing. The seasonal performance analysis confirms that the SCVI is more efficient for heating and cooling at moderate temperatures, while the TSRC excels in harsh climates with higher pressure requirements [101]. In another research, they introduced a methodology for characterizing SCVI. The SCVI is tested in a modified calorimetric test bench that controls intermediate pressure and injection superheat. The methodology allows the prediction of compressor performance by correlating the injection mass flow rate and intermediate pressure. The findings demonstrate that the proposed model achieves less than 5% deviation in predicting intermediate pressure, mass flow rate, and compressor power input, offering an efficient approach for SCVI characterization in various operating conditions [102]. Lumpkin D et al presented experimental results and mapping correlations for a single-speed R-407C scroll compressor with two-phase injected and vapor-injected compression. The study investigates how economized vapor-injection compressors can reduce discharge temperatures and improve system efficiency in high-pressure-ratio applications, such as air conditioning in hot climates. Experimental data were collected for different injection methods, and a mapping correlation using the Buckingham-PI theorem was developed to predict the injection ratio, compressor power, and discharge temperature. Results show that two-phase injection reduces discharge temperatures and enhances cooling capacity, with the correlation successfully mapping compressor performance across various conditions [103].

Dechesne, B J et al presented an experimental study of a residential ASHP using a variable-speed scroll compressor with refrigerant injection and R410A refrigerant. The study investigates the performance

of the system under varying evaporating and condensing temperatures, compressor speeds, and superheat levels at the suction and injection ports. The results showed that reducing evaporator superheat from 15 K to 5 K increased the COP by 9.3% and heating capacity by 12.6%, while decreasing discharge temperature by 6 K. Additionally, reducing injection superheat did not affect the COP but improved heating capacity by 3.5% and further reduced discharge temperature by 7 K. The study also introduced an empirical compressor model with good accuracy in predicting mass flow rates, electrical consumption, and discharge temperature. This research highlights the potential for optimizing ASHP performance through controlled refrigerant injection and superheat adjustments [104]. Xu Q et al investigated the optimal intermediate temperature and injection pressure for refrigerant injection heat pump systems with an economizer, focusing on two-phase and vapor injection cycles. The authors use theoretical derivations based on thermodynamic properties to determine the ideal conditions for maximizing the COP. The study found that the optimal intermediate temperature is more sensitive to subcooling than suction superheat, and increasing the economizer's heat transfer efficiency improves the heating COP. Experimental validation showed the theoretical results to be in close agreement with observed data, with errors in injection pressure prediction within 3%. The research concludes that optimizing injection quality and pressure can significantly enhance the performance of heat pump systems, especially under severe operating conditions [105].

2.4.2 Expansion Device

An expansion valve is a vital and extremely effective component in refrigeration systems and heat pumps. Inadequate supply of vapor refrigerant leads to a decrease in system efficiency, while oversupply could result in compressor damage. Proper selection of expansion devices governs the refrigerant flow and level of superheat. Different types of expansion devices were employed in VCRS, including manual, automated, float, capillary tube, thermostatic, and electronic expansion valves. Each expansion valve demonstrates distinct performance characteristics in terms of cooling load, electrical consumption, and COP under different conditions.

An expansion valve is a crucial and very efficient component in refrigeration units and heat pumps. Insufficient supply of vapor refrigerant leads to decrease in system efficiency, while excessive supply might result in compressor damage. Smart choice of expansion devices governs the refrigerant flow and level of superheat. Different types of expansion devices were employed in vapor compression refrigeration systems, including manual, automated, float, capillary tube, thermostatic, and electronic expansion valves. Each expansion valve demonstrates distinct performance characteristics in terms of cooling load, electrical consumption, and COP under different conditions [106], [107].

The performance of VCRS is influenced by several key parameters, including evaporating temperature, condensing temperature, refrigerant type, equipment type, system controls, and system maintenance.

2.4.2.1 Needle Valve

A needle valve is a simple expansion device consisting of an adjustable knob, a needle, and an orifice. The refrigerant flow could be regulated by adjusting the knob. It was suitable just for the evaporator with a constant load and is unsuitable for fluctuating loads [106].

2.4.2.2 Constant Pressure Expansion Valve

The constant pressure expansion valve, or automated expansion valve, has components including an adjustable screw, spring, diaphragm, and needle with seat. The diaphragm has been shifted vertically in conjunction with a needle due to refrigerant pressure. The needle movement was used to open and close the orifices. This valve maintained a certain pressure within the evaporator by manipulating the screw, rather than loading. The experiments indicated that the refrigeration effect of the thermostatic expansion device was 13% higher to that of a constant pressure expansion valve and 20% better to that of a capillary tube. VCRs utilize two kinds of float valves: high-pressure side and low-pressure side float valves. A float is used to control refrigerant levels [108], [109].

2.4.2.3 Capillary Tube

The capillary tube is a basic and steady expansion device made of copper. The length and internal diameter correspond to the refrigeration capacity. The pressure drop depends on the length and diameter of the capillary tube [110]. It is used in residential refrigeration and air-conditioning systems due to its affordability. The capillary tube is twisted into helical or serpentine configurations to achieve a compact system. The internal diameter, gauge diameter, length, and pitch of a capillary tube are essential design factors [111].

2.4.2.4 Thermostatic Expansion Valve

The thermostatic expansion valve (TEV) is an advanced throttling device composed of a brass body, diaphragm, power cap, capillary tube, pin, superheat setting spring, and detecting bulb. If the cooling load in the evaporator increases, the refrigerant evaporates rapidly, and the bulb detects the superheat [110]. The capillary tube connected to the bulb is filled with the same refrigerant, referred to as power refrigerant, that circulates in the VCRS circuit. The pressure force traveled through the refrigerant, oscillating with a pin within the diaphragm. The valve initially remains in the open position due to the force of spring pressure, which decreases as the diaphragm goes upward. The larger the quantity of current and refrigerant sent to the evaporator as the diaphragm descends [112].

2.4.2.5 Electronic Expansion Valve

An electronic expansion valve is more advanced and precise than classic expansion valves, mostly utilized for non-flammable, non-toxic refrigerants. EEV replaces all prior varieties of expansion valves and includes a stepper motor, sensor, regulator, actuator, valve, and a microprocessor-based electronic controller. There are two distinct types of EEV valves in use: proportional and pulsating variants. In the proportional version, the refrigerant flow is controlled by the orifice. The pulsating valve is actuated by a solenoid valve, which opens and closes in response to inputs from a microprocessor controller. Fluid dynamic analysis indicates that mass flow rate is dependent on the opening status of the EEV [113]. EEV has delivered quicker responses than TEV. It enhances efficiency and decreases the system's power consumption by up to 30% [114].

2.4.3 Heat Exchangers

Condensers in all cooling systems are used to reject the heat gained during evaporation and gas compression processes of the refrigerant to the ambient air. The refrigerant changes from superheated vapor to liquid as energy is extracted from the hot refrigerant to the surroundings. There are three main types of condensers based on the cooling medium: air-cooled, water-cooled, and a combination of both types known as the evaporative cooled condenser. Condensers employed in conventional small and medium-sized refrigeration cooling systems (up to 20 TR) are mainly air-cooled constituting the primary type [115], [116], [117]. The air-cooled condensers rely on the heat transfer between the condenser coils and the surrounding airflow. Their energy performance is determined by thermodynamic properties and heat transfer with air. Consequently, the thermodynamic efficiency of cooling systems integrated with an air-cooled condenser is dependent on climatic circumstances, resulting in variable performance. Air-cooled condensers are the most common kind due to their simplicity, since they do not require a water system; nonetheless, they necessitate a high air flow rate to enhance performance, which can occasionally lead to noise issues. Air-cooled condensers have lower capital and operational costs compared to water-cooled and evaporative condensers, on one side. Conversely, the system power consumption utilizing an air-cooled condenser exceeds that of other condenser types. This is due to the air-cooled condenser necessitating condensing temperatures around 15–20 °C higher than the ambient air temperature [118]. Water-cooled condensers are the second category of condensers, wherein heat is dissipated to the surrounding cooling water, which then removes heat to the ambient air via a cooling tower [119], [120], [121]. This kind of condenser is more compact and has a greater heat transfer coefficient than air-cooled condenser; however, it incurs higher initial expenses and requires water [122], [123], [124], [125]. Consequently, a water pump is necessary for water circulation, chemical treatment is needed to minimize coil fouling, and ongoing supervision is

vital. When the distance between the compressor and the heat rejection point is too long to pump the refrigerant vapor with an acceptable pressure drop, only a water-cooled condenser is used. Water-cooled condensers are manufactured in capacities ranging from 0.5 to 10,000 TR [126].

These condensers are mainly used in heat pumps and specific applications. The third category consists of evaporative condensers. Extensive use of these systems has been made to enhance heat transfer and improve the performance of air-cooled condensers utilizing evaporative cooling, particularly in the non-residential larger tonnage market. The evaporative condenser serves as a compact heat exchanger which combines the functions of air-cooled and water-cooled condensers. Both sensible and latent heat transfers between air and water are utilized, with cooling achieved through the evaporation of water into the air stream. The airflow rate required for this type of condenser is lower than that of an air-cooled condenser, allowing for the use of a smaller fan and motor. The requirements for water pumping and chemical treatment in water-cooled condensers are decreased. Water-cooled and evaporative condensers provide condensing temperatures constrained by the ambient wet bulb temperature, which is lower than the ambient dry bulb temperature. Consequently, refrigeration systems utilizing these condensers can operate at lower condensing temperatures, thereby enhancing energy efficiency. As a result, systems employing these condensers demonstrate greater coefficients of performance and refrigeration capacities compared to those employing air-cooled condensers. The evaporative and water-cooled condensers consume equivalent water quantities per unit of refrigeration; however, the evaporative condenser contains significantly less water compared to a water-cooled condenser combined with a cooling tower. The entire water circulation system of the evaporative condenser is enclosed within the condenser casing. Additionally, the initial cost of the evaporative condenser is lower than that of the water-cooled condenser, due to the reduced space and fewer components required. While water and air-cooled condensers can be modeled with relative ease, evaporative condensers pose challenges due to the evaporation of water into the air stream [127]. Heat exchangers can be categorized according to various characteristics, as illustrated in Figure 16:

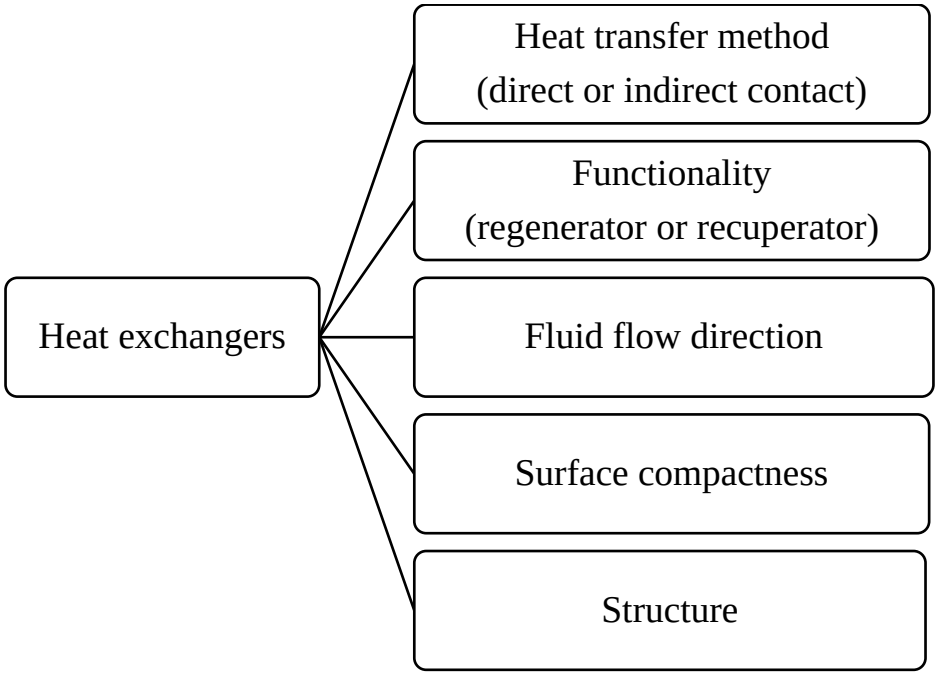

Figure 16 Classification of Heat Exchanger

While there are many other ways to classify exchangers, this part will focus on these five attributes for the sake of brevity and clarity. Each of these attributes will be briefly explained, as they will be relevant in the subsequent chapters.

2.4.3.1 Classification of Heat Exchangers Based on the Method of Heat Transfer

Regardless of whether the fluid within the exchanger a single phase or two phases is, or if the heat transfer occurs in a condenser or boiler involving a phase change, heat transfer can occur through either direct or indirect contact between two fluids. In the case of direct contact, the two fluids come into direct contact with one another. For example, mixing two fluids at different temperatures to achieve a common average temperature illustrates direct contact heat transfer. Another instance is the cooling of air in evaporative coolers, where heat is transferred directly from the air to the water, leading to a phase change in the water from liquid to vapor. Numerous such examples exist in industry. In indirect contact exchangers, the two fluids are separated by a barrier that prevents them from mixing.

2.4.3.2 Categorization of Heat Exchangers Based on Their Function

From a different perspective, heat exchangers can be divided into two types: regenerators and recuperators. At first glance, this classification might appear misleading since nearly all exchangers can serve as regenerators for capturing heat in power generation cycles. However, a regenerator in this discussion specifically denotes an exchanger that operates with periodic heat transfer rather than

continuous heat transfer. For instance, during one phase, the thermal energy from the hot fluid is accumulated within matrices or packed beds, and in the subsequent phase, the accumulated heat is conveyed to the cold fluid by moving it through these matrices or beds. Regardless of the different types of regenerators, there is always a risk of fluid leakage in these devices. In contrast, recuperators facilitate heat transfer in a continuous manner.

2.4.3.3 Categorization of Heat Exchangers Based on the Fluid Flow Direction

The orientation of hot and cold flows within an exchanger can be arranged in three ways:

I. Parallel flow (co-current)

II. Counterflow (countercurrent)

III. Crossflow

In parallel flow, the two fluids move alongside one another, with both the hot and cold fluids entering from the same end; thus, at the entry point, the cold fluid encounters the hottest fluid, and their temperatures gradually equalize along the length of the exchanger (Figure 17). In counterflow, the hot and cold fluids still run parallel, but they enter the exchanger from opposite ends. Consequently, the temperature difference between the fluids remains relatively stable throughout the length of the exchanger (Figure 17).

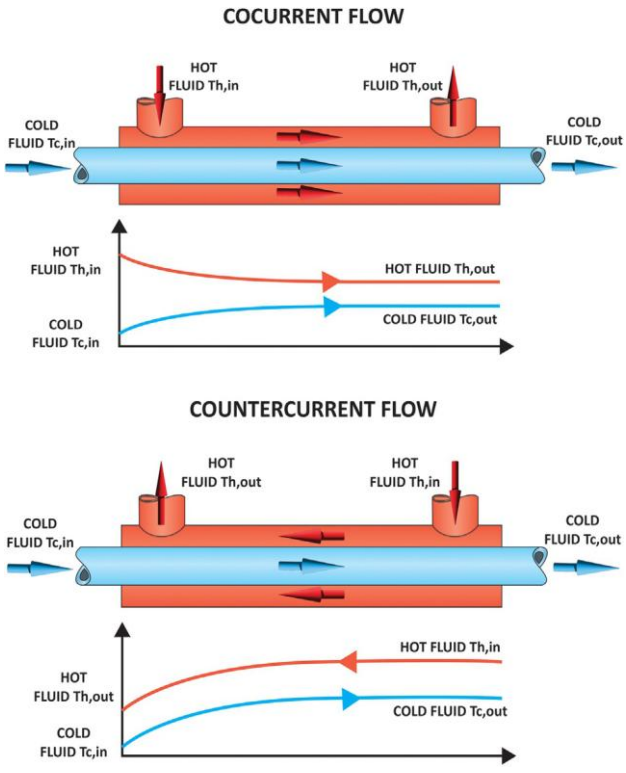

Figure 17 Cocurrent Flow and Countercurrent Flow Heat Exchangers

From a thermodynamic perspective, the most effective heat transfer occurs in a completely counterflow setup, while the least effective occurs in a fully parallel flow arrangement. Additionally, because the maximum temperature difference in counterflow is lower than that in parallel flow, the likelihood of thermal shocks (sudden fluctuations in temperature) occurring in the exchanger is reduced. Hence, it is preferable to utilize a counterflow configuration in heat exchangers whenever feasible. However, since the temperature of the separating wall is more consistently maintained in parallel flow, instances where the wall temperature needs to remain below a certain threshold should consider parallel flow options. In a crossflow arrangement, the two fluids flow perpendicularly to one another. It is important to note that in certain exchangers, such as shell-and-tube heat exchangers, both parallel and crossflow configurations may occur simultaneously, meaning flows can be parallel in some areas and crossed in others (Figure 18).

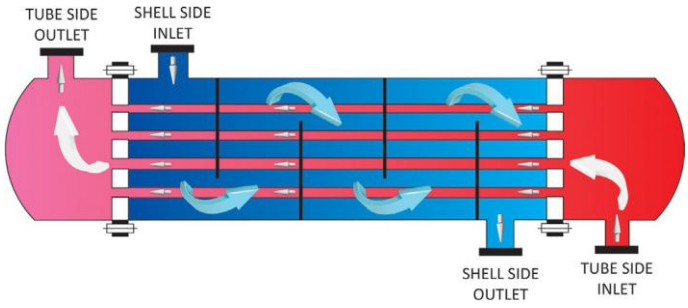

Figure 18 Shell-and-tube Heat Exchanger

Often, the fluid does not achieve the desired temperature after a single pass through the entire exchanger. Therefore, the fluid may need to circulate through the exchanger several additional times without exiting. Each complete flow of the fluid through the length of the exchanger is termed one pass. Consequently, a cross-parallel or cross-counterflow pattern is present in an exchanger with cross-flow configurations and multiple passes. In other words, if the hot and cold fluid entries are on the same side, it is classified as cross-parallel flow; otherwise, it is termed cross-counterflow (Figure 19).

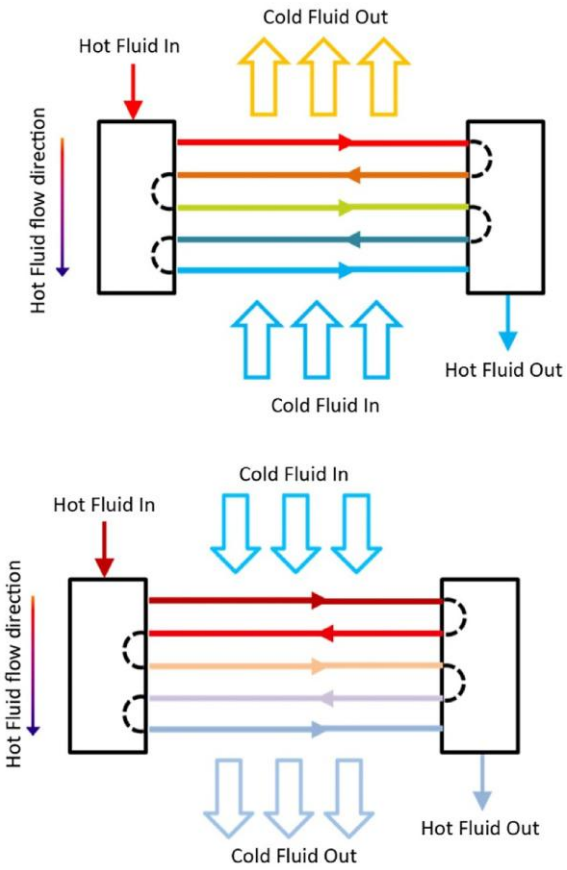

Figure 19 Cross-Counter Flow, Bottom: Cross-Parallel Flow

2.4.3.4 Classification of Heat Exchangers Based on Surface Compactness

Surface compactness is a key factor when selecting heat exchangers. The surface compactness factor in an exchanger indicates the ratio of the heat transfer area to the exchanger's volume. Consequently, a higher factor signifies that the heat exchanger will be smaller and lighter. This factor can also influence the initial manufacturing costs of an exchanger; in other words, lighter exchangers typically incur lower manufacturing expenses. It is important to highlight that when the volume or weight of the exchanger is a crucial consideration, as in the case of marine or offshore heat exchangers, evaluating surface compactness becomes essential. For exchangers with a single gaseous flow, those with a compactness exceeding 700 $m^2/_{m^3}$ are classified as compact heat exchangers. In different applications, an exchanger is deemed compact if it has a surface compactness of 400 m^2/m^3. All plate heat exchangers presented in this book fall under the category of compact exchangers. However, some commonly used heat exchangers, such as air-cooled or shell-and-tube models, do not meet the criteria for compact exchangers.

2.4.3.5 Classification of Heat Exchangers Based on Their Structure

Typically, recuperator heat exchangers can be divided into two main categories: Plate heat exchangers and Tubular heat exchangers. Plate heat exchangers are defined as the type where the barrier between the fluids consists of plates or sheets, whereas in tubular exchangers, the division is achieved using tubes. Both exchanger types may incorporate secondary surfaces like fins to enhance the total heat transfer area. Different types of plate heat exchangers are listed below:

- Gasketed plate-and-frame exchangers
- Double-wall plate exchangers
- Semi-welded plate exchangers
- Brazed plate exchangers
- Bavex exchangers
- Compabloc exchangers
- Packinox exchangers
- Lamella exchangers
- Spiral exchangers
- Plate-fin exchangers

In terms of tubular exchangers, the discussion is limited to the most common varieties, which are:

- Air-cooled exchangers
- Cooling towers
- Shell-and-tube exchangers
- Double-pipe (hairpin) exchangers
- Heat pipe exchangers [128]

2.4.3.6 Classification of Heat Exchangers Based on Their Construction

Different studies and materials have provided various classifications, with the most important one focusing on construction, as shown in Figure 20. In relation to the system under examination in this thesis, three distinct categories of heat exchangers are considered: shell and tube, plate, and fin-tube [129], [130].

i. Shell and Tube Heat Exchanger

The shell and tube heat exchanger is the most prevalent type of heat exchanger design, commonly utilized in fuel processing and energy generation. Its structure consists of a large pressure vessel (the shell) that houses tube bundles which run through it; the design may include baffles or finned tubes to

enhance the available heat transfer area. Generally, one fluid flows through the tube, while the other circulates within the shell surrounding the tubes to facilitate heat exchange [131].

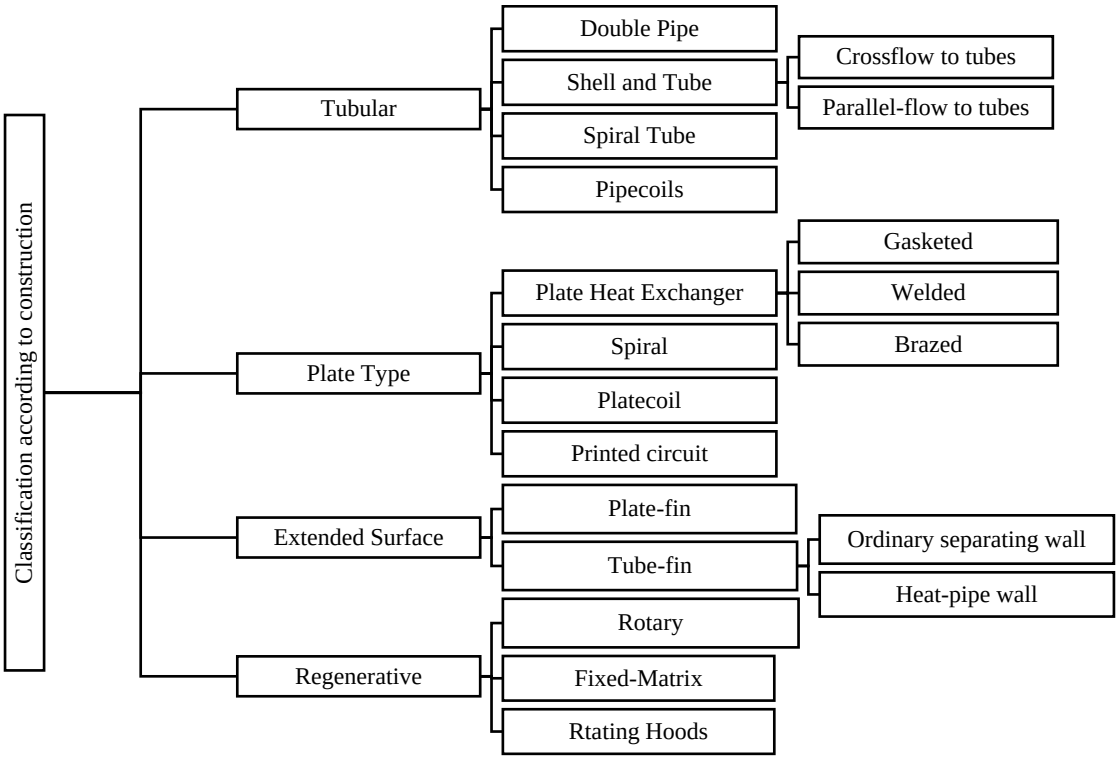

Figure 20 Heat Exchanger Classification According to Construction

The design and construction of shell and tube heat exchangers involve numerous details that affect the efficiency of the heat pipe. For example, certain configurations may incorporate baffles to enhance the available heat transfer surface while also bolstering the structural strength of the system. The design of these baffles can be optimized to facilitate sensible heat transfer or altered to support condensation. To describe the contact arrangements between the tube bundle and the shell, a specific numbering system is utilized (1-2, 1-4, 2-4, etc.). The first digit represents the numbered baffle, while the second digit denotes the quantity of tube passes. The term "pass" refers to the flow moving from one side of the heat exchanger to the other. Shell and tube heat exchangers can be designed with either fixed tube sheets or U-tube configurations.

- Fixed tube sheet

In shell and tube heat exchangers, fixed tube sheets incorporate straight tubes that are securely attached to a plenum, ensuring smooth fluid transfer between tube passes, as depicted in Figure 21. This design is widely recognized as one of the most fundamental and commonly used configurations due to its simplicity and efficiency.

However, despite its practicality, there are some important considerations. A major limitation is the inability to clean the tubes externally, which over time may lead to reduced performance and durability.

Additionally, since the tubes are rigidly affixed, they lack the flexibility to expand or contract under thermal variations, increasing the risk of structural stress and mechanical failure. Fortunately, incorporating a floating tube sheet can effectively counteract these challenges by allowing for controlled expansion, significantly enhancing both longevity and operational efficiency of the system.

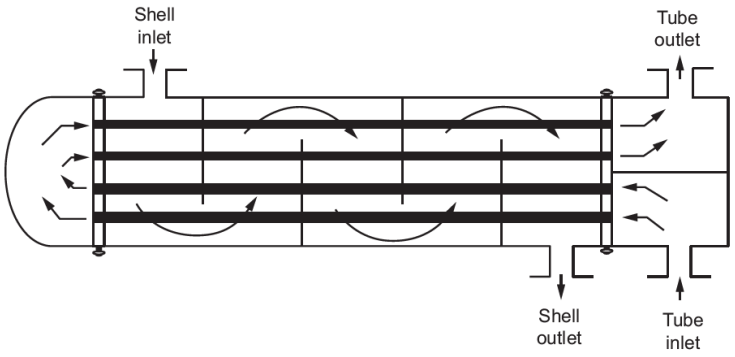

Figure 21 Shell and Tube Heat Exchanger with a Fixed and Floating Tube Sheet [132]

- U-tube arrangement

Unlike fixed tube configurations, U-tube heat exchangers derive their name from the distinct U-shaped curvature of the tubes, as illustrated in Figure 22. This design allows the tubes to bend into a U-form, enabling multiple fluid passes as needed. A key advantage of this setup is its flexibility—since the tubes are not rigidly affixed, the entire tube bundle can be removed, making mechanical cleaning and maintenance much more convenient [131].

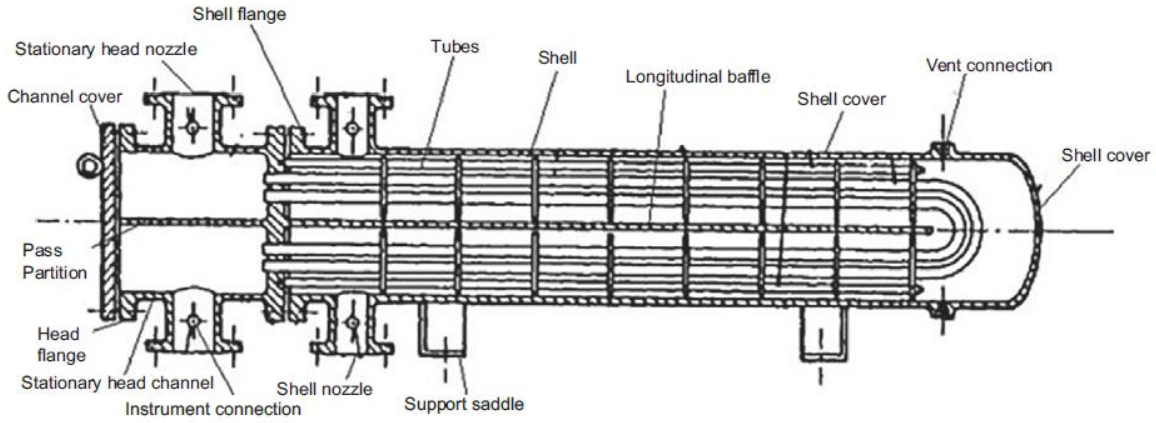

Figure 22 U-Tube Shell and Tube Heat Exchanger [133]

From a functional standpoint, because the shell essentially acts as a pressure vessel, this method has been widely adopted for industrial applications requiring high pressures (above 30 bar) and elevated temperatures (over 260°C). However, whether it can be implemented successfully depends heavily on the materials used in its construction and how well it accommodates thermal expansion and mechanical

stress. Ensuring the exchanger's structural integrity under such demanding conditions is critical for safety and long-term performance.

Recent findings suggest that this technology can also be used at lower pressures and temperatures but applying it beyond 70 bar and 550°C is generally discouraged, as it may introduce significant operational risks and compromise durability [131].

ii. Plate Heat Exchangers

Plate heat exchangers (PHEs) are widely used across various industries due to their space-saving design and excellent thermal efficiency. These systems are built using thin, corrugated metal plates that are securely assembled within a sturdy frame, as depicted in Figure 23. Their operation relies on the flow of multiple fluids through alternate plate channels, where the unique corrugated texture significantly enhances heat transfer efficiency by increasing the total surface area available for thermal exchange [132], [133], [134].

A key advantage of plate heat exchangers is their versatility—the plates can be designed in different sizes, making them suitable for a broad spectrum of low-pressure applications, including residential combination boilers. Over the years, significant advancements in PHE technology have primarily focused on enhancing thermal performance while simultaneously making the units more compact and efficient, as shown in Figure 24.

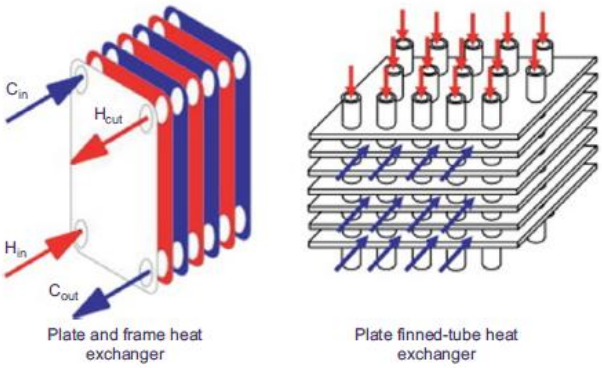

Figure 23 Plate Heat Exchanger [137]

Manufacturers have developed high-performance variants using stainless steel and titanium, allowing these systems to endure temperatures as high as 200°C and pressures up to 25 bar, with flow capacities reaching 5000 m^3/h. However, the manufacturing process plays a crucial role in determining their exact operational limits. For example, brazed plate heat exchangers can function at temperatures between 195°C and 200°C, handling pressures up to 30 bar, whereas welded plate configurations are designed for even more extreme conditions, withstanding pressures up to 60 bar and a broader temperature range [131].

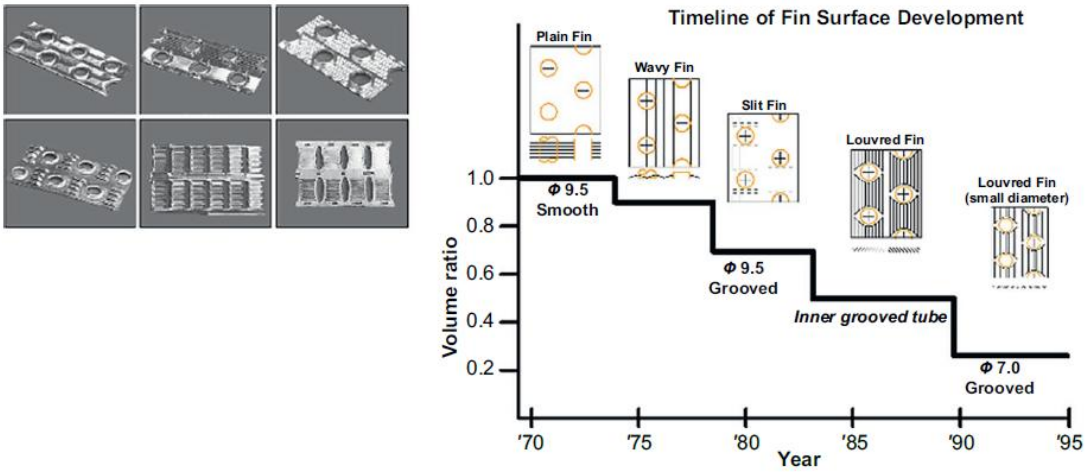

Figure 24 Development Timeline of Plate Heat Exchanger Surfaces [134]

2.4.4 An Exhaustive Analysis of the EU F-Gas Regulation

2.4.4.1 A Paradigm Shift in Cooling and Refrigeration Policies

EU F-Gas Regulation (EU) 2024/573 is a groundbreaking rule shift in the European Union's efforts to cut emissions of fluorinated greenhouse gases (F-gases). Replacing (EU) No 517/2014, it is not merely a piecemeal revision but a tactical redesign of the refrigeration and cooling industry, requiring an immediate transition from high global warming potential (GWP) refrigerants to cleaner substitutes.

Effectively, the regulation also aligns with the policies of the European Green Deal, the Kigali Amendment to the Montreal Protocol, and the overall decarbonization goals of REPowerEU. In aiming for deeper reductions in hydrofluorocarbon (HFC) quotas, total prohibitions on certain refrigerants, stronger enforcement provisions, and increased burdens on industry stakeholders, it sets the stage for a revolutionary transformation in the design, manufacture, and servicing of cooling, refrigeration, and heat pump equipment across the EU.

This update was driven by several considerations, such as the climate impact of high-global warming potential gases, the need for improved energy efficiency, the problems created by illicit trade in F-gases, and the rapid development of replacement refrigerants. The updated regulations give the industry clear direction, giving companies and researchers a vision for the future of refrigeration and air conditioning in a low-carbon world.

2.4.4.2 A Substantially Stepped-Up HFC Phase-Down Schedule

One of the most characteristic elements of the 2024 regulation is to fast-track the phase-down schedule for HFCs. The EU has pledged to cut HFC use by 80% by 2050, from 2015 levels, through further tighter quota allocations that cap the availability of high-GWP refrigerants.

HFCs have been utilized extensively in industrial cooling, commercial refrigeration, and heat pumps for many decades because they are stable, non-toxic, and simple to use. Nevertheless, they possess high GWP values, and this implies that they make a huge contribution to global warming once they leak into the atmosphere. According to the new phase-down schedule, manufacturers will hardly have access to these refrigerants, and this will compel them to switch to low-GWP alternatives much earlier than expected.

In real-world application, this means that:

- R-404A (GWP ~3922) and R-507A (GWP ~3985), traditionally the market leading supermarket refrigeration and industrial cold storage refrigerants, will no longer be acceptable in new equipment.
- In addition, R-410A (GWP ~2088), a long-established standard refrigerant for residential and commercial air conditioning, is increasingly being replaced by R-32 (GWP ~675), R-454B (GWP ~466), and hydrocarbon-based alternatives like R-290 (propane, GWP ~3).
- R-134a (GWP ~1430), the widely used medium-temperature refrigeration and automotive air conditioning refrigerant, is being replaced by R-1234yf (GWP ~1) and CO_2-based systems.

These transitions necessitate manufacturers and service providers to completely rethink refrigeration system designs to facilitate compatibility with new refrigerants, which often require diverse pressure levels, heat exchanger design, and safety protocols.

Prohibiting High-GWP Refrigerants and Compelling Natural Refrigerant Adoption

Beyond quota cuts, the 2024 rule specifically bars the use of specific refrigerants on new equipment produced, most notably those of very high GWPs. Emphasis is put on encouraging natural refrigerants and future-generation low-GWP alternatives.

2.4.4.3 Natural Refrigerants: The Future of Cooling

Natural refrigerants are significantly favored under the new regulation as they have no or near-zero GWP. They are accompanied by technical issues, most importantly flammability, toxicity, and high-pressure operation.

- CO_2 (R-744, GWP = 1) is now replacing HFCs in supermarket refrigeration, industrial refrigeration, and data center cooling. Transcritical CO_2 systems do have the drawback of needing to operate at extremely high pressures (~90 bar in supercritical mode), which creates some engineering challenges in certain applications.

- Ammonia (R-717, GWP = 0) is still the most thermodynamically effective industrial refrigerant and cold storage. Its toxicity does limit application to large, well-ventilated industrial plants, though.
- Hydrocarbons (R-290, R-600a, R-1270, GWP < 5) are increasingly used in home and light commercial refrigeration. Propane (R-290) is very promising but is classified as highly flammable (A3 refrigerant), so very strict safety provisions must be followed.

2.4.4.4 HFOs and Synthetic Blends: A Transitional Solution

Hydrofluoroolefins (HFOs) are low-GWP drop-in replacements for HFCs. A few of the most common ones are:

- R-1234yf (GWP = 1), now ubiquitous in automotive air conditioning.
- R-1234ze (GWP < 1), gaining acceptance in chillers and large cooling applications.
- HFO blends (R-454B, R-513A, R-466A), intended to replace R-410A and R-134a in certain applications.

However, although with low GWP, HFOs break down to long-lived byproducts such as trifluoroacetic acid (TFA), with associated long-term environmental issues. Due to this, the EU can further limit their use in future amendments.

2.4.4.5 Dealing with Illegal Trade, Compliance, and Workforce Issues

Illegal trade in refrigerants has been a prominent characteristic, with HFCs on the black market entering the EU beyond the quota regime. The new regulation gives customs authorities more tools to track illegal imports.

Secondly, online sales of F-gases are placed under tighter compliance obligations, eliminating unauthorized distribution.

To allow industry to transition to these changes, the regulation also establishes mandatory training and certification schemes for HVAC and refrigeration technicians. Due to the combustibility of hydrocarbons, the high-pressure handling of CO_2, and the risks of toxicity from ammonia, the technicians will be required to undertake specialized training so that they can work with these refrigerants safely.

2.4.4.6 Impact on Industry and the Research Roadmap

This regulation establishes a clear industrial and research roadmap, compelling manufacturers to:

- Redesign refrigeration systems to include low-GWP and natural refrigerants.
- Develop high-efficiency heat exchangers, compressors, and thermal management systems.
- Apply leak prevention and refrigerant recovery technologies.
- Invest in next-generation cooling technologies, such as magnetic refrigeration, ejector-based CO_2 cycles, and hybrid absorption-compression cooling systems.

The regulation also aims for circular economy principles, where refrigerants are mandated to be recovered, reclaimed, and reused, thus limiting virgin refrigerant production.

2.4.4.7 Final Considerations: The Future of Refrigeration in the EU F-Gas Regulation

EU F-Gas Regulation (EU) 2024/573 is not just an emissions-reduction strategy; it is a milestone in cooling technology evolution and governance. It forces producers to rethink the use of different refrigerants, reengineer systems, and retool technician training courses. The days of high-GWP refrigerants like R-404A and R-410A are numbered, and the next decade will be telling in a manner that decides whether the cooling industry can make the transition successfully to cleaner options without compromise in performance, safety, and cost.

With tighter regulation, faster phase-down, and a concerted drive for natural refrigerants, the EU is sending this message loud and clear: the future of refrigeration is green, and change is no longer a choice, it's a requirement [5].

2.5 Improved Design Alternatives for Conventional Vapor Compression Systems

The vapor compression refrigeration system works due to fluid thermophysical properties that contain pressure-dependent boiling point and latent heat of phase changes. The system enables heat transfer from a cold place to a warm place. The refrigerant evaporates at low pressure by taking in heat from cold places prior to compression converting it to liquid that gives out heat to warm places. The basic thermodynamic cycle sustains several uses ranging from compact air conditioners to large chilling plants. The elementary components of the vapor compression cycle (VCC) are shown in Figure 25.

The compressor is the key element of VCC systems while consuming most of electrical power. Three broad categories of compressor technologies are available despite their technological improvements. The types of compressors are Positive displacement compressors (reciprocating and linear types) and Rotary compressors (scroll, screw, roots and rolling piston models) and Kinematic compressors (centrifugal and axial-flow types). The COP improvement of the system needs approaches beyond compressor efficiency improvement. Various optimization techniques can be combined for energy recovery from expansion and refrigerant subcooling and superheating performance enhancement.

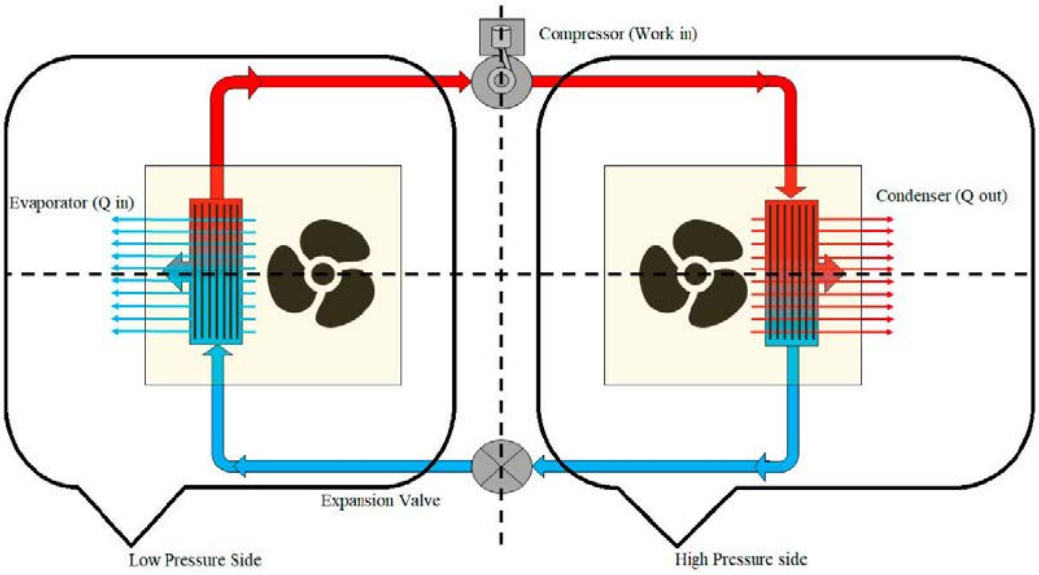

Figure 25 Main Components of a Basic Vapor Compression Cycle

The refrigerant goes through a four-stage process in the closed-loop system of the vapor compression cycle. The compressor first draws in low-pressure vapor refrigerant, then compresses it to a high-pressure gas. After condensation, the refrigerant becomes a high-pressure liquid as it gives off heat to an external fluid that flows through the opposite coil of the condenser. The refrigerant then goes through an expansion device that can be a capillary tube, orifice, thermostatic expansion valve, or electronic expansion valve, where its pressure drops significantly until it becomes a low-pressure liquid. In the evaporator, the refrigerant draws heat from the space to be cooled or from a cooling fluid, eventually becoming a superheated low-pressure vapor in the final stage. The processes of this cycle are shown in Figure 25 [135].

The vapor compression cycle (VCC) is inherently subject to thermodynamic inefficiencies compared to the ideal reversed Carnot cycle. These inefficiencies are mainly associated with the compression of single-phase vapor and the isenthalpic expansion process. The former contributes to high refrigerant discharge temperatures, higher compression work, and more heat rejection in the condenser. The latter causes high throttling losses and lower cooling capacity. To alleviate such inefficiencies, researchers investigated several advanced cycle modifications such as subcooling methods (including suction line heat exchangers, thermoelectric subcoolers, and mechanical subcoolers), expansion work recovery cycles (using expanders and ejectors), and multi-stage configurations (including vapor or liquid injection cycles, two-phase injection, and saturation cycles). This section presents a thorough review of these cycle improvements with an emphasis on performance enhancement [136].

2.5.1 Enhancement of Cycle Performance through Elevated Sub-Cooling and Superheating Levels

In conventional vapor compression systems, the refrigerant at the inlet to the expansion valve is usually in a subcooled liquid condition to maintain stable flow and controlled expansion. By providing a greater degree of subcooling, the expansion process, ordinarily isenthalpic, becomes closer to an isentropic process, as shown in Figure 26. More subcooling also increases the effect of refrigeration and can result in an increased COP. Although a variety of heat sinks at appropriate temperatures can be used for subcooling, three techniques are most widely used: suction line heat exchangers (SLHX), mechanical subcoolers, and thermoelectric subcoolers.

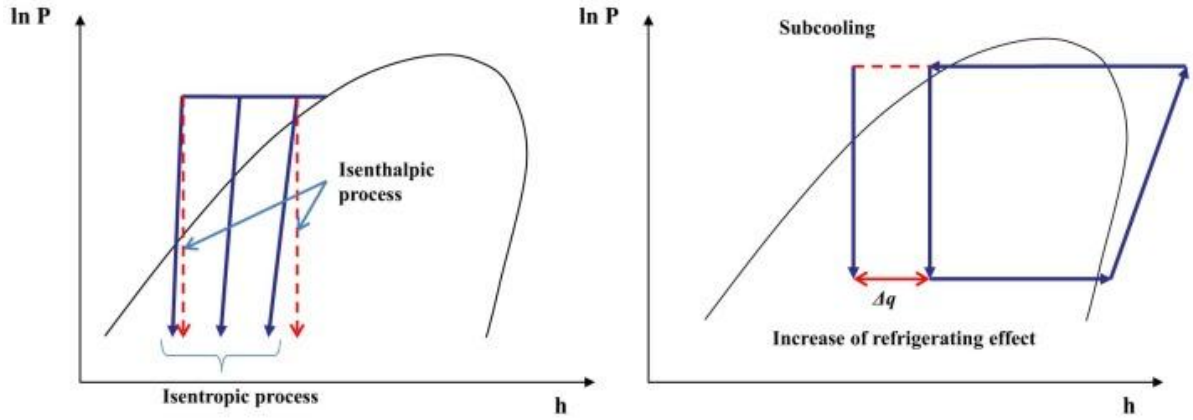

Figure 26 P–h Diagram of the Vapor Compression Cycle with Liquid Subcooling

2.5.1.1 Suction Line Heat Exchanger

The suction line heat exchanger (SLHX) or internal heat exchanger (IHX) is a common component in VCCs for system performance improvement and component protection. It is essentially used for heat exchange between the liquid refrigerant exiting the condenser and the vapor refrigerant exiting the evaporator. This has the effect of subcooling the refrigerant prior to the expansion device and superheating the vapor prior to its entry into the compressor [137]. Figure 27 shows the schematic diagram and P–h diagram of the vapor compression cycle with the SLHX.

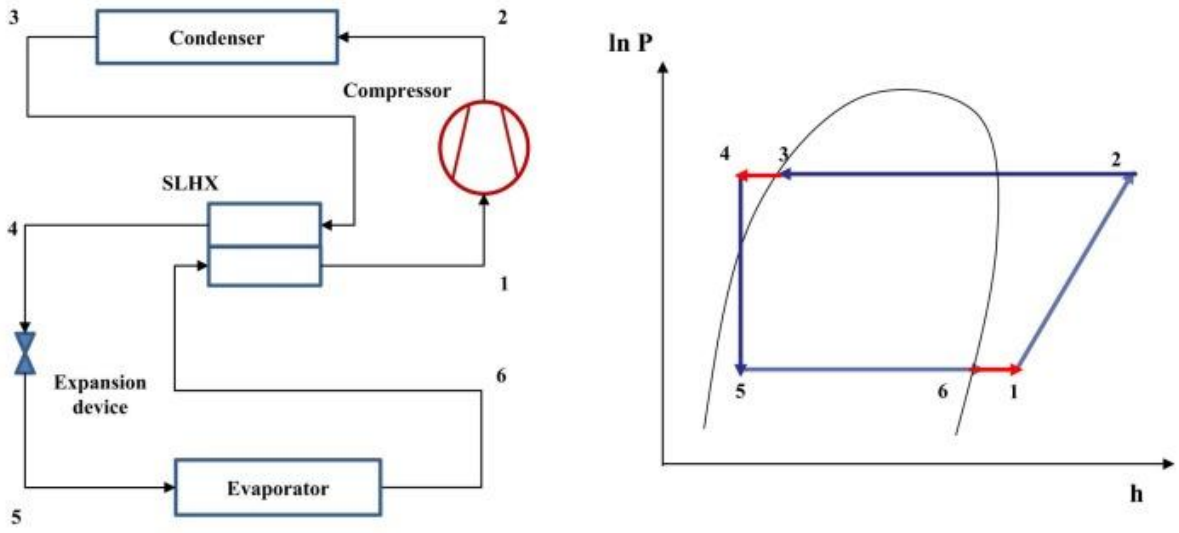

Figure 27 Schematic Diagram and P–h Diagram of the Vapor Compression Cycle with SLHX

This arrangement enhances the enthalpy difference across the evaporator and hence the system cooling capacity. At the same time, it also increases the suction temperature at the compressor inlet, which decreases the compressor volumetric efficiency and can adversely impact the system COP overall. Since this trade-off is directly related to the thermodynamic properties of the refrigerant and operating conditions, the use of SLHX must be optimized [140], [138]. Domanski et al. [140] investigated the effect of SLHXs for a range of refrigerants and operating conditions. They found that refrigerant properties have an important influence on overall benefit, especially in terms of system COP. A plot in the enthalpy-pressure diagram illustrates how the inclusion of an SLHX enhances cooling capacity for only a small decrease in volumetric efficiency [141].

Likewise, Klein et al. [139]examined SLHX performance based on a novel dimensionless parameter, which connects refrigerant thermodynamic properties and temperature lift. They concluded that SLHXs perform very well with refrigerants of lower latent heat of vaporization and specific heat capacity, particularly at high temperature lift. Based on their study, the use of SLHXs is favorable with R-410A, R-134a, R-290, and R-404A, while R-744 (CO_2) has the most promising performance. On the other hand, refrigerants R-32 and R-717 (ammonia) exhibited negative impacts when coupled with an SLHX [142]. The performance of SLHXs in CO_2 cycles has been widely investigated. For example, Hwang et al. [140] showed COP enhancements of 7% and 18% for single- and double-stage compression systems, respectively, when SLHXs were used. The better performance in two-stage systems may be a result of a greater temperature gradient over the heat exchanger, which results in more effective heat transfer. Likewise, Cho et al. [141] showed a COP increase of 8% in an R-744 cycle with a variable speed compressor, an electronic expansion valve, and a SLHX.

Automobile air conditioning systems also see substantial gains with the use of SLHX. Preissner et al. [141] experimentally tested an R-134a system at a 40 °C condenser temperature, with 5–10% COP enhancement. To be more environmentally friendly and phase out R-134a, R-1234yf was introduced as its substitute. But because of its 21–28% lower latent heat of vaporization than R-134a, its adoption results in decreased cooling capacity. SLHX efficiently eliminates these losses [142], [143]. Cho et al. [144] observed that, in the absence of a SLHX, COP and cooling capacity of R-1234yf were decreased by 4.5% and 7%, respectively, when compared to R-134a. The inclusion of SLHX reduced these losses to only 1.8% and 2.9%, respectively.

Navarro-Esbrí et al. (2013) experimentally achieved 17–25% effectiveness and 2–9% cooling capacity improvement in a tube-in-tube SLHX [146]. Pottker and Hrnjak (2015) also determined that the utilization of condenser subcooling and SLHX together resulted in better efficiency, particularly in R-1234yf systems. Their results support that SLHX effectiveness is strongly reliant on the thermophysical properties of the utilized refrigerant [145]. Aside from CO_2 and automotive uses, Prabakaran et al. [146] applied SLHXs in mobile air conditioners with R-134a. The COP improvements varied from 2.8% to 11.8%, depending on the thermostatic expansion valve (TXV) settings, highlighting that system parameters—along with refrigerant properties—play a major role in SLHX performance.

In addition, Mahdi Al-Obaidi et al. [147] investigated the SLHX in a VCC system with R-22 for changing cooling loads and noticed up to 10% enhancement in COP. They recommended that more desirable results could be obtained by incorporating an automatic equalizing thermal expansion valve and a variable speed compressor, indicating the contribution of control strategy in increasing SLHX gains. In summary, SLHX is an effective means for improving the performance of VCC systems. However, its effectiveness is not consistent and requires a case-by-case evaluation that takes into account refrigerant type, operating conditions, and system configuration. With proper optimization and correct component selection, significant energy savings and capacity improvements can be achieved, especially in new, environmentally friendly refrigerant systems.

2.5.1.2 Mechanical Subcooler

A supplementary cooling system known as mechanical sub-cooling serves to boost cooling performance by integrating a compact auxiliary cooling system. The secondary refrigeration loop in Figure 28 cools the working fluid before expansion to increase system operational efficiency. The implementation of a mechanical sub-cooling system by Thornton et al. [148] in supermarket refrigeration led to a 10% increase in COP across various operational parameters suitable for the application. Their research showed promising results, but the study did not examine the system's long-term sustainability extensively.

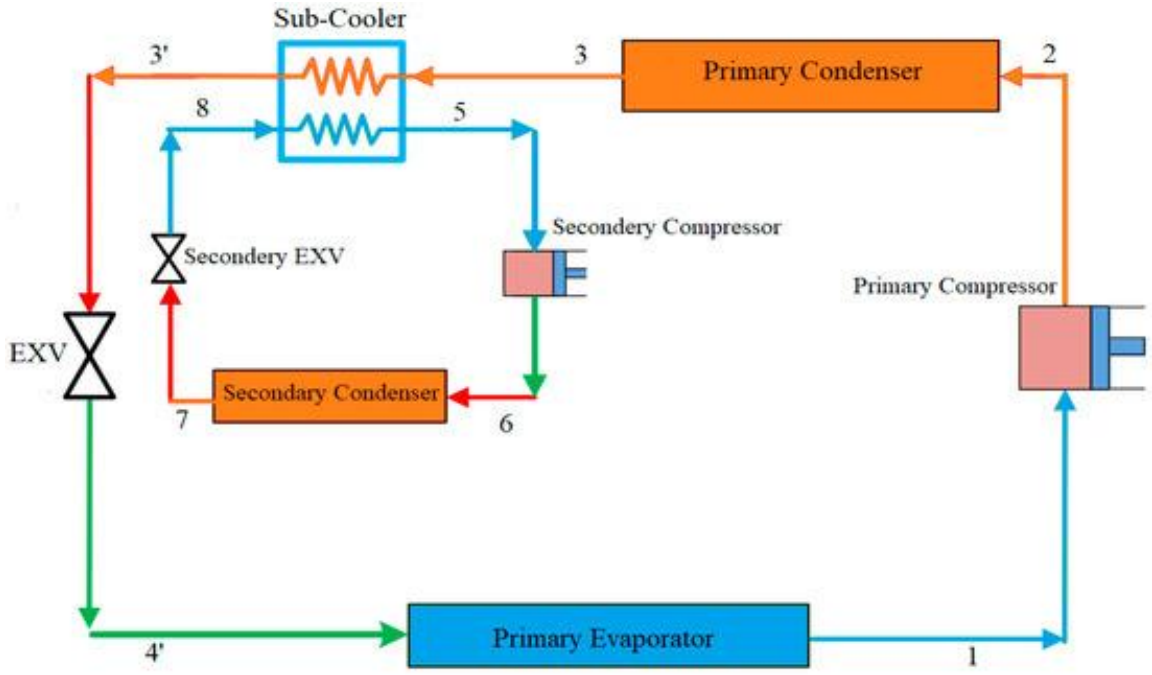

Figure 28 Schematic of the VCC with Mechanical Sub-Cooling [138]

Khan and Zubair [149] studied how mechanical sub-cooling affects the post-condenser COP of the cycle and demonstrated a 7.5% improvement. Qureshi and Zubair [150] investigated the best refrigerant pairs for main and sub-cooling cycles through a comparative study. The evaluation revealed R-134a provided the highest COP performance when used as the primary loop refrigerant. Research into additional refrigerants by the study revealed potential improved combinations might be discovered. The expander-driven sub-cooling cycle proposed by She et al. [151] achieved a 19% increase in primary system COP compared to traditional mechanical sub-cooling approaches. The design proposed R-744 as the primary cycle refrigerant while using R-12 for the sub-cooling circuit. The researchers proposed using environmentally friendly alternatives such as HFOs or natural refrigerants due to R-12's high ODP level. Research examined how CO_2, N_2O and ethane function as dedicated mechanical sub-cooling systems. The research established that all three refrigerants improved performance, yet ethane produced the greatest COP increase at 36.1% followed by CO_2 at 30.74% [152]. Chen et al. [153] studied how mechanical sub-cooling vapor compression systems respond to increased cooling capacity and sub-cooling power augmentation. The experimental research measured augmented cooling capacity to sub-cooling energy input ratios which fell between 7.5% and 50% according to compressor speed and chilled water flow rate and secondary cycle power levels.

2.5.1.3 Thermoelectric Sub-Cooling (TS)

Thermoelectric devices convert electrical energy into temperature differences through the Peltier effect without mechanical components resulting in high reliability. Their practical application remains

restricted because thermoelectric devices struggle to achieve efficient operation at high-temperature gradients [138]. The diagram in Figure 29 illustrates a vapor compression cycle system that uses thermoelectric internal heat exchangers. Winkler et al. [154] used simulation to evaluate R-744 refrigeration systems with thermoelectric sub-cooler integration which resulted in a 20% boost in cooling performance and a 16% improvement of the coefficient of performance (COP). The theoretical evaluation performed by Radermacher et al. [155] analyzed single-stage versus double-stage thermoelectric sub-cooler systems. The research proved that the double-stage setup delivered better COP enhancement. The authors failed to assess the practical challenges and system complexity enhancements between the double-stage and single-stage designs.

Schoenfeld et al. [156]conducted experimental research to study the effects of thermoelectric sub-cooling on R-744 system performance. The researchers achieved a 7.9% increase in system capacity along with a 3.3% increase in COP by using a controlled thermoelectric hybrid arrangement. Sarkar [157] executed an energy and exergy analysis simulation to enhance the performance of R-744 systems that use thermoelectric sub-coolers. The study showed that thermoelectric sub-cooling boosted COP and decreased the high-side pressure which resulted in reduced compressor pressure ratio and power consumption.

Kwan et al. [158] introduced a thermoelectric heat exchanger into transcritical cycles to improve the coefficient of performance (COP) in their recent publication. The system underwent two operational tests where it functioned as a thermoelectric generator (TEG) to generate electricity from heat and as a thermoelectric cooler to boost internal heat transfer. The simulation demonstrated that the TEG configuration reached a maximum COP boost of 5% but its performance fell below the level of direct thermoelectric cooling because thermal resistance lowered heat transfer efficiency. Using the system as a thermoelectric cooler lowered compressor power usage yet the energy expenses of the thermoelectric module partially diminished this advantage.

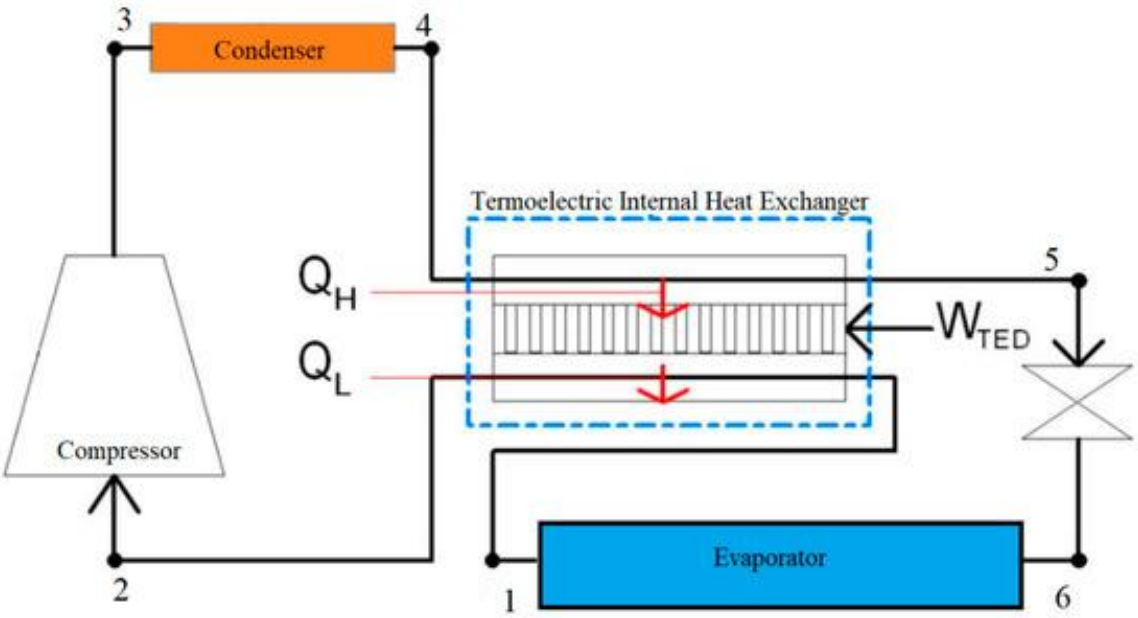

Figure 29 Schematic of the VCC with Thermoelectric Cooler

Liu et al. [159] analysed a CO_2 ejector refrigeration cycle with a thermoelectric sub-cooler through exergy-based performance assessment. The total exergy destruction reached 89.44% with the compressor and thermoelectric sub-cooler producing the most significant avoidable losses followed by the evaporator and ejector and gas cooler respectively.

Research on an actual transcritical R-744 vapor compression system that integrated a thermoelectric sub-cooler demonstrated that operating the sub-cooler with 2 V and the fan with 9 V resulted in COP enhancement by 11.3% and cooling capacity improvement by 15.3% [160].

2.5.2 Enhancing the Cycle through Recovery of Expansion Losses

Several types of expansion devices including capillary tubes orifices thermostatic expansion valves and electronic expansion valves reduce refrigerant pressure in a refrigeration cycle. The expansion process maintains constant enthalpy according to theoretical assumptions, yet real-world conditions result in energy dissipation. The energy loss can be reduced by integrating expanders or ejectors as energy recovery components [161].

2.5.2.1 Expander Cycle

The expander functions as a compact device which operates with a reverse operation to that of compressors. The device expands refrigerant through a process which transforms recovered expansion energy into kinetic energy for multiple applications particularly enhancing system COP and cooling

performance. The expander cycle diagram appears in Figure 30 [138]. Huff et al. [162] performed a performance assessment of an R-744 refrigeration cycle with positive displacement expander integration. The research findings showed substantial performance improvement because COP increased by 40-70% and cooling capacity increased by 5-15%.

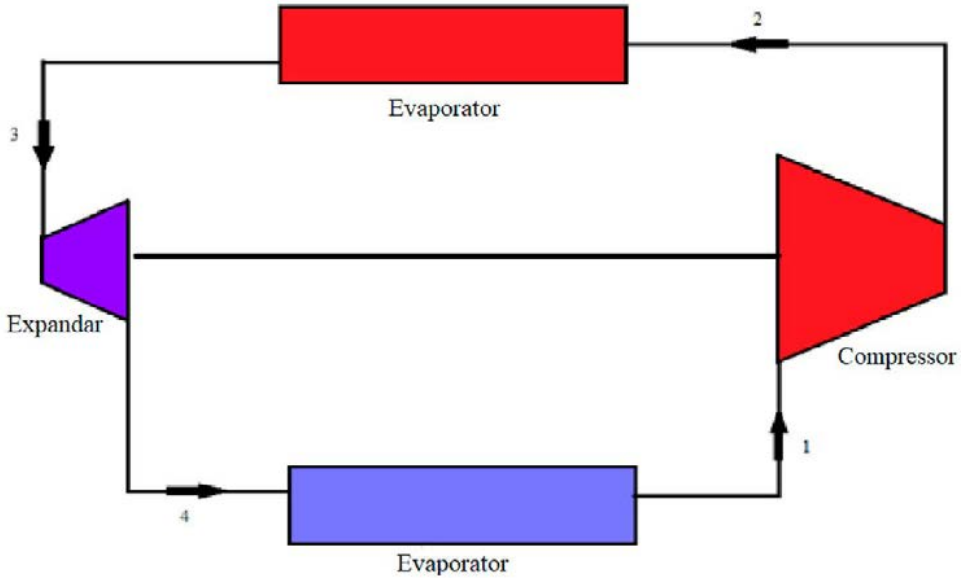

Figure 30 Expander Refrigeration Schematic Diagram [138]

The control of high-side pressure requires special attention because the expander connects directly to the compressor shaft. The circuitry options for high-side pressure control in expander systems are presented in Figure 31. The system contains an independent compressor and expander speed control through option (a). The high-side pressure adjustment in options (b) and (c) occurs through additional adjustable pressure drops that increase total flow resistance across the expansion section. Option (d) controls the expansion section flow resistance through an adjustable bypass that directs flow away from the expander. The compression process in options (e) and (f) operates through two separate sections. The operating conditions determine the speed at which the expander operates. The low stage compressor (e) or the high-stage compressor (f) operates independently from the expander speed.

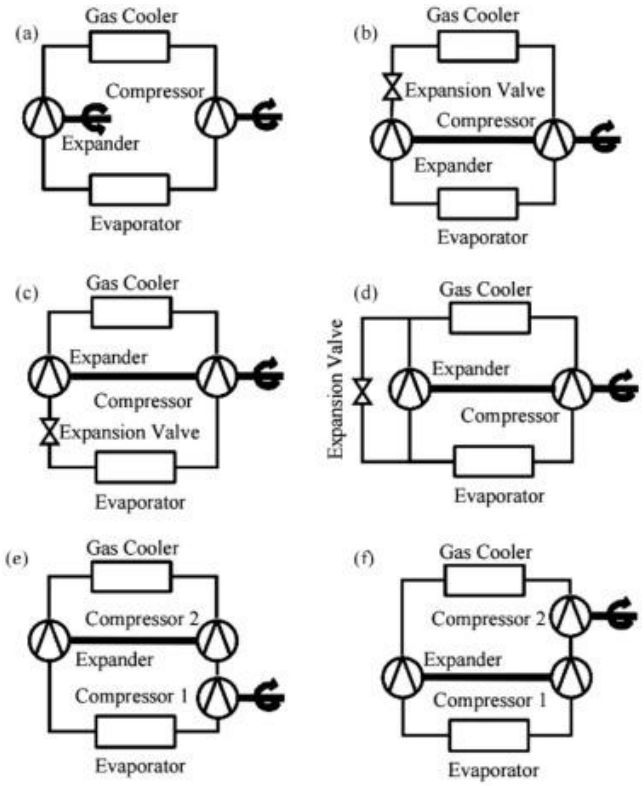

Figure 31 Configurations for High-Pressure Regulation on the High Side of Expander Circuits [166]

Nickl et al. [163] evaluated a CO_2 refrigeration system that utilized a three-stage expander system. The analysis demonstrated a 40% increase in COP while showing a decrease in main compressor discharge pressure. Wang et al. [164] performed a simulation of an R-410A refrigeration system that used a two-stage vane-type expander. The research investigation resulted in a 14.2% improvement of COP. The economic evaluation of expander implementation in medium-scale vapor compression air conditioning systems was studied by Subiantoro and Ooi [165] using 50% isentropic efficiency for the expander and 75% efficiency for the compressor. The authors presented different system arrangements which required a five-year period to recover the investment costs. Hu et al. [166] conducted experimental evaluations of an enhanced expander within a CO_2-based water-to-water heat pump system. The enhanced device outperformed the standard version by reaching 77% peak efficiency at 867 rpm while producing 242 W of maximum expansion work at 770 rpm. The authors suggested additional development because the prototype measurements failed to match the intended design specifications.

2.5.2.2 Ejector Cycle

The ejector has three essential components which include a nozzle, mixing chamber, and diffuser. The main purpose of an ejector is to combine refrigerant streams from both high- and low-pressure sides. The refrigerant at high pressure undergoes a pressure reduction when it exits the condenser before

entering the nozzle which causes the low-pressure refrigerant from the evaporator to be entrained. After mixing in the mixing chamber the diffuser recovers energy from the mixed fluid that was produced [138]. Disawas and Wongwises [167] conducted research to assess how evaporator and condenser temperature variations affect ejector-based expansion refrigeration cycle efficiency. R-134a experienced decreased COP when the condenser temperature rose yet its discharge temperatures and pressure ratios remained below those of standard vapor compression cycles (VCCs). According to Li and Groll [168] in their 2005 study about CO_2 refrigeration cycles the researchers discovered the same outcome. The research demonstrated that using an ejector resulted in a more than 16% increase of the COP compared to traditional VCC systems. The authors discovered that the ejector cycle operated effectively based on the separator efficiency level.

A two-phase ejector system functions by dividing the refrigerant flow from the condenser into two streams that lead to different paths: one stream enters the ejector nozzle, and the other stream passes through an isenthalpic throttle before reaching the evaporator. The mixed output from the mixing chamber is then fed to a secondary evaporator [169]. Boumaraf et al. [170] performed numerical simulation to evaluate how the two-phase ejector system performed with R-134a and R-1234yf when compared to standard vapor compression cycles. The research established that COP improvements exceeding 17% became achievable when the condenser operated at 40°C for both refrigerants. The research showed that R-1234yf performed better at elevated temperatures but R-134a produced higher COP values throughout the entire range. Lawrence and Elbel [171] performed experimental work to evaluate this two-phase ejector setup when using R-1234yf and R-134a as refrigerants. The system delivered COP increases of 12% for R-1234yf and 8% for R-1234yf compared to systems using expansion valves. These findings demonstrate that properties of refrigerants directly impact the operational efficiency of ejector cycles. Hafner et al. [172] researched R-744-based supermarket refrigeration systems by implementing ejectors in their investigation. The research findings indicated that heating cases provided between 20-30% COP improvements while cooling cases achieved between 5-17% improvements. Zhang and Tian [173] proposed using ejectors instead of expansion valves to reduce throttling losses in CO_2 cycles. The research team created a thermodynamic model for transcritical CO_2 ejector expansion cycle (Figure 8a) which showed a maximum COP improvement of 45.1% and reduced exergy destruction by 43.0%.

Jeon et al. [174] studied how different ejector geometries impact R-600 compact refrigeration system performance at multiple operating points. The experimental study examined how compressor speed and entrainment ratio (ER) and nozzle position and mixing section diameter affected the system performance. Their research revealed that expansion losses decreased when they reduced the entrainment ratio and increased compressor speed. When the compressor operated at 45 Hz and the entrainment ratio was 0.3 the system achieved a 6.8% better COP compared to the base cycle through

optimal mixing section diameter selection. The authors specified proper mixing section diameters for different operating parameters.

2.5.3 Multi-stage Cycle

The difference between evaporation-condensation temperatures leads to lower system efficiency and reliability when operating under extreme ambient conditions. This results from the greater irreversibilities in compression and smaller refrigerant mass flow. Among various technological advancements for solving these disadvantages multi-stage cycles have emerged as a primary focus for recent years [139].

2.5.3.1 Two-stage Cycle

The various injection methods depend on refrigerant phase as they use liquid or vapor or two-phase injection. The research on liquid injection performance by Dutta et al. and Cho et al. involved experimental analysis of its effects on scroll compressors. The researchers demonstrated that higher injection ratios resulted in significant drops of discharge temperature [175], [176]. Winandy and Lebrun performed both experimental and simulation-based investigations on an R-22 heat pump system which incorporated liquid and vapor injection to demonstrate that liquid injection decreased compressor discharge temperature by approximately 1.2 °C with each increase in injection ratio. The two main configurations of vapor injection systems consist of flash tank and subcooler. A flash tank system enables phase separation to take place in the tank for vapor injection purposes. The system faces compressor flooding challenges at elevated operating speeds because of difficulties in precise injection volume control. The subcooler cycle produces its injected vapor by exploiting temperature differences across the high-pressure expansion valve during a heat exchange operation. The subcooler system provides better control stability for injection procedures but its thermal performance tends to be inferior to the flash tank cycle [177].

Heo et al. studied an R-410A flash tank system to demonstrate that the system achieved a 10% COP improvement and a 25% heating capacity increase at −15 °C ambient temperature without injection systems [178]. Wang et al. performed tests on flash tank and subcooler systems using R-410A refrigerant to demonstrate superior performance compared to systems with no injection. The maximum cooling conditions led to a 15% increase in cooling capacity and a 2% improvement in COP. At −17.8 °C the flash tank system reached its highest COP increase of 23% [179]. Heo et al. expanded their research to include two advanced vapor injection configurations: the Combined Flash Tank and Subcooler (FTSC) cycle and the Double Expansion Subcooler (DESC) cycle which appear in Figure 32. The DESC system transforms the subcooler by introducing an electronic expansion valve after the

condenser outlet for pressure management. The FTSC cycle links both flash tank and subcooler elements to enhance evaporator enthalpy difference through gas elimination and improve injection control accuracy.

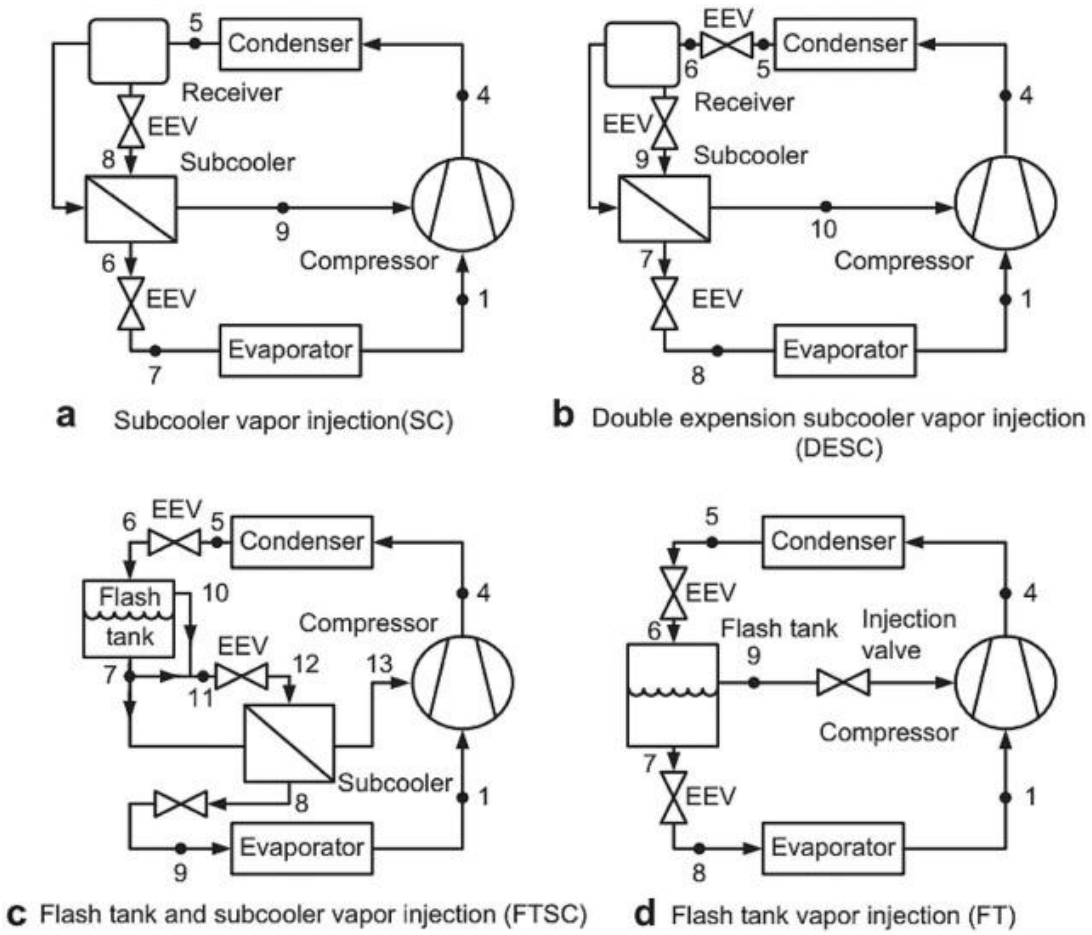

Figure 32 Schematic Diagram of the Vapor Injection Cycles [184]

The heating capacity values for the flash tank and FTSC and DESC cycles exceeded those of the subcooler cycle by 14.4%, 6.0% and 3.8% respectively. The flash tank cycle delivered superior heating capacity performance even though the different configurations maintained similar coefficients of performance (COPs). The FTSC system proved to be a more dependable choice for applications requiring stable and precise control because flash tanks become vulnerable to flooding at high speeds [180]. Xu et al. studied flash tank vapor injection systems while developing an innovative control methodology. The research demonstrated that a PID controller operating the electronic expansion valve (EEV) precisely controlled the superheat target through measurements of vapor superheat levels at the upper-stage expansion valve [181], [182], [183].

2.5.3.2 Saturation Cycle

The authors Lee et al. created saturation cycles for VCC improvement through reduced single-phase gas compression and isenthalpic expansion losses. The method combines saturation expansion with compression as well as traditional evaporation and condensation operations. The i-stage refrigerant injection systems depicted in Figure 33 can simulate ideal saturation cycles because they use near-saturation paths for compression and expansion operations.

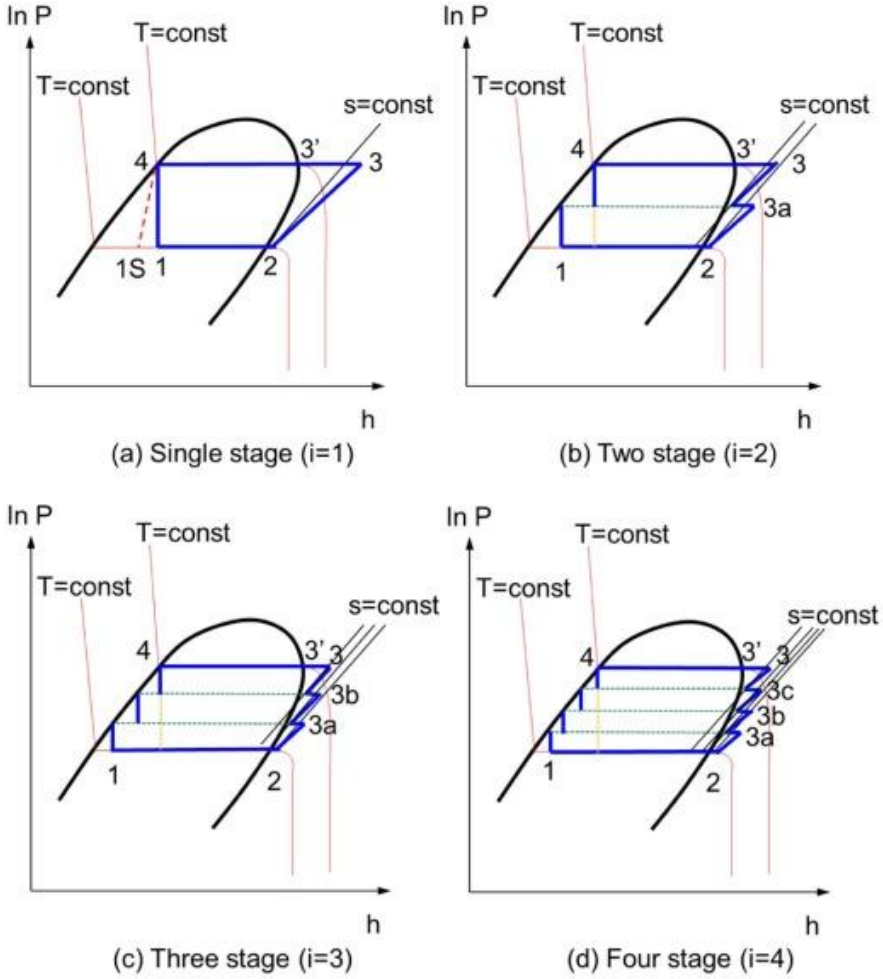

Single-Stage Configuration (a)
Three Variations of Multi-Stage Cycles (b–d) [188]

Figure 33 Illustration of the Saturation Cycle Concept

Multiple stages can be used as long as the compressor design supports this integration. The number of stages in the cycle results in saturation behavior as shown in Figure 34. The partially expanded two-phase flow can be separated through a phase separator or the main flow from the condenser can be used to heat a branch stream. The compressor receives cold vapor along with a liquid portion from the injection, but the remaining low-enthalpy liquid moves to following stages for expansion.

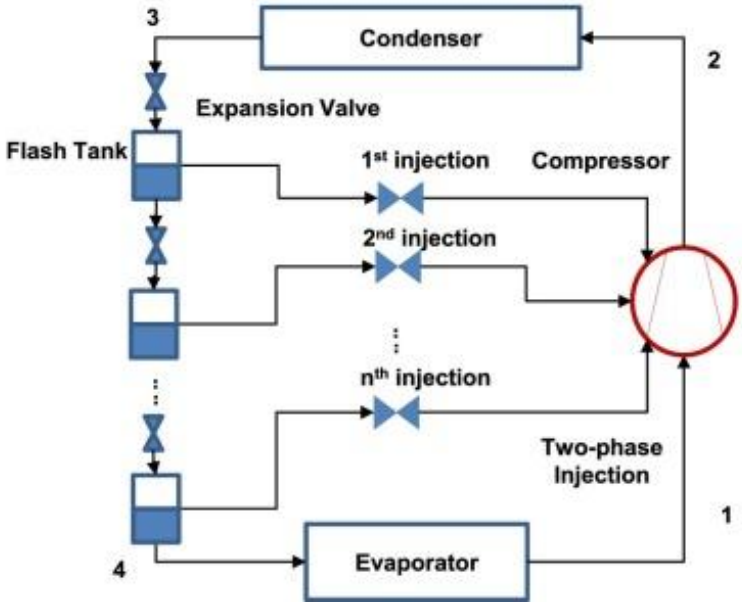

Figure 34 Configuration Overview of a Multi-Stage Vapor Compression Cycle Utilizing Two-Phase Injection [189]

The configured cycle shows better performance in terms of both capacity and COP. Real-time control of refrigerant state after injection becomes possible through two-phase injection when equipped with pressure-temperature sensors [184]. Lee et al. performed additional studies by simulating COP values for two refrigerants under five operating conditions. The simulations demonstrate that COP values increase with an increase in stage number. The heating COP of a four-stage cycle outperformed its single-stage counterparts by 42.4% for R-410A and by 38.2% for propane [185].

Chapter 3

Experimental Setup and Methodology

3. Experimental Setup and Methodology

3.1 Description of Experimental Freezing System

3.1.1 Refrigeration Circuit: Components and Layout

The experimental setup used to gather data on a scroll compressor with vapor–liquid injection consists of three main circuits: the refrigeration circuit, the water circuit for the condenser, and the air circuit for the walk-in freezer, as shown in Figure 35. In this configuration, the refrigeration system uses 4kgs R448A refrigerant to generate low temperatures needed for food preservation. The walk-in freezer allows precise control of air temperature within a set range (-23 °C to -33 °C), while the water circuit regulates condensation pressure. The freezer's temperature control system and the electronic expansion valve work together to adjust the evaporating temperature and superheat. A brazed plate heat exchanger; commonly known as an economizer; is also an essential part of the refrigeration system.

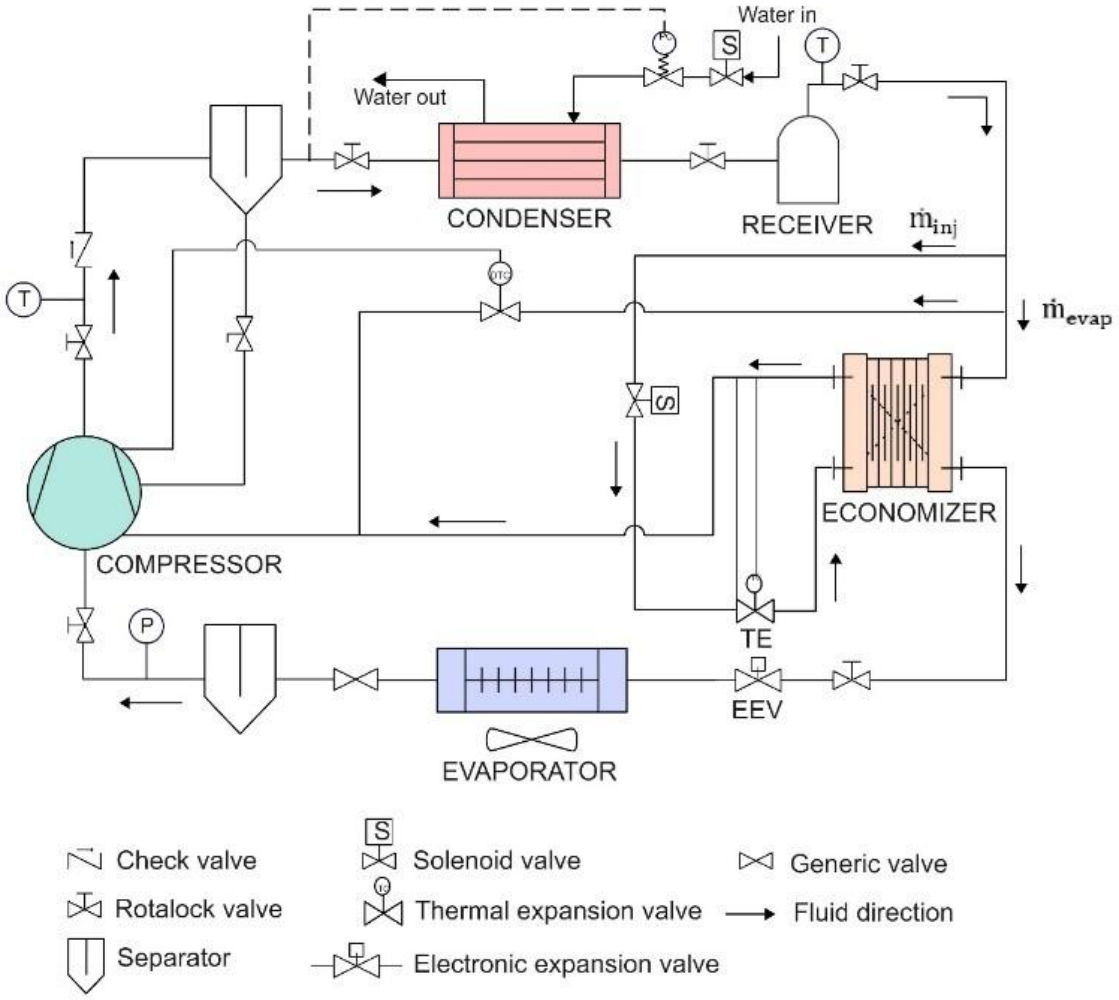

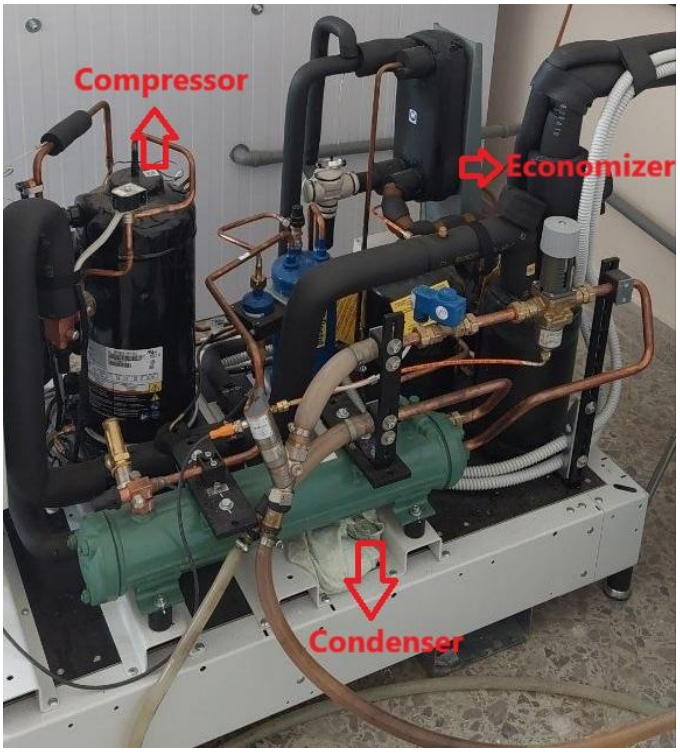

Figure 35 Test Rig

Figure 35 also represents how heat is transmitted into the economizer between the refrigerant used for injection and the refrigerant flowing through the evaporator line. The secondary expansion valve, referred to as the thermal expansion valve in Figure 35, mainly regulates the intermediate superheat. For a given compressor, once the intermediate superheat is achieved, the intermediate pressure is determined by the heat transfer between the evaporator mass flow rate ($\dot{m}_{evp}$) and the injection mass flow rate ($\dot{m}_{inj}$) in the economizer. Therefore, for a specific compressor, pressure ratio, and economizer size, the intermediate pressure remains relatively constant.

3.1.1.1 Condenser Heat Exchanger

It is beyond doubt that many types of heat exchangers exist, categorized based on heat transfer methods, functionality, fluid flow direction, surface compactness, and structural design. In this experimental setup, a water-cooled shell-and-tube heat exchanger (model K073H-4P) is used.

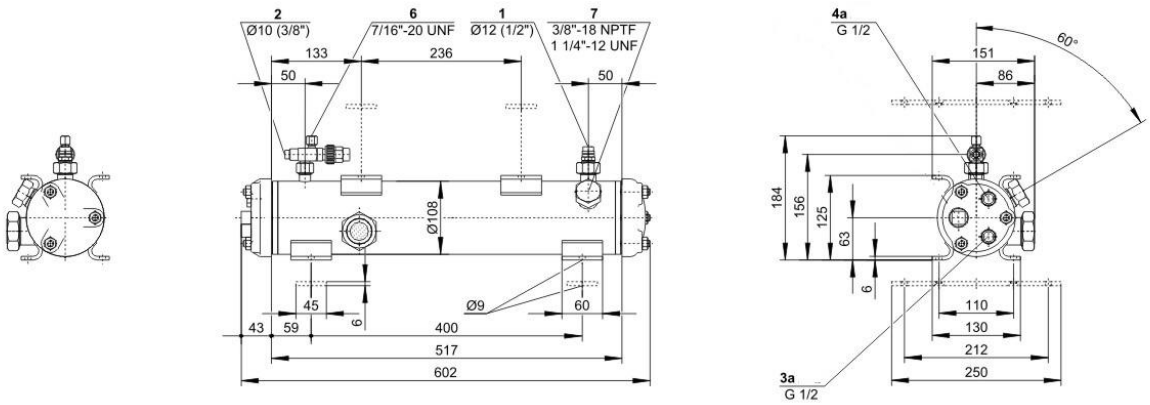

1	Refrigerant Inlet	5	Coolant Drain	9	Oil Drain
2	Refrigerant Outlet	6	Connection for Pressure Gauge	10	Vent Plug
3	Coolant Inlet	7	Connection for pressure relief valve Internal thread 3/8-18 NPTF, external thread 1 1/4-12 UNF	11	Fixing Rail, bottom
3a	4 Pass	8	Sight Glass	12	Fixing Rail, top
4a	Coolant Outlet				

Figure 36 Dimension of Water-Cooled Shell-and-Tube Heat Exchanger

This type of heat exchanger is compatible with several refrigerants, including R134a, R22, R290, R1270, R1234yf, R1234ze(E), R404A, R507A, R407C, R448A, R449A, R450A, and R513A. The connections and dimensions are shown in Figure 36, 37, and the specifications are provided in Table 3.

Figure 37 Water-Cooled Shell-and-Tube Heat Exchanger in Experimental Setup

Description	Vessel Zone	Piping Zone
Weight	11 kg	
Allowable Fluids	EN378: Safety Group A1	Water
Maximum Pressure	33 bar	10 bar
Minimum Pressure	-10 bar	0 bar
Maximum Temperature	120 ℃	95 ℃
Minimum Temperature	-10 ℃	4 ℃

Table 3 General Specification of Condenser

3.1.1.2 Evaporator Heat Exchanger

The R448A refrigerant flows into the cold room and, after going through the expansion valve, enters the finned-tube heat exchanger of Figure 38.

As the refrigerant flows through the tubes of the exchanger, there is an exchange of heat with the air within the cold room. By means of the intermittent operation of the system, the set temperature is reached. The heat exchanger has an air circulation fan, which promotes forced circulation and speeds up the energy exchange between the two fluids. The cold room specifications are given in Section 3.1.2 Cold Room Specifications. This item also has certain characteristics, which are enumerated in Table 4.

Parameters	Dimension	Value
Design Temperature, T_{min}	℃	-50
Design Temperature, T_{max}	℃	110
Design Pressure, P_{min}	bar	-1
Design Pressure, P_{max}	bar	30
Test Pressure, P	bar	43
Volume	L	12.78
Fluid Type	HFC	

Table 4 Finned-Tube Heat Exchanger (Evaporator)

Figure 38 Finned-Tube Heat Exchanger (Evaporator)

3.1.1.3 Economizer

The economizer is a key component to improve the performance of vapor injection systems. The main task of the economizer is to supply further subcooling of the liquid refrigerant exiting the condenser. A part of the refrigerant flow is bypassed, expanded through the injection expansion valve, and evaporated within the economizer by absorbing heat from the main liquid stream. This reduces the enthalpy of the liquid refrigerant entering the main expansion valve, and hence, the evaporation capacity increases. The vaporized refrigerant from the economizer is injected into the compressor through the injection port. The injected vapor not only cools the compression process and lowers the discharge temperature but also elevates the overall mass flow rate through the compressor, resulting in better volumetric efficiency. Thus, the economizer improves system stability and reliability by avoiding excessive discharge temperature that can damage the compressor or cause decomposition of the refrigerant and

lubricant. The existence of the economizer creates an intermediate pressure in the system, at which an optimum trade-off can be established between the elevated evaporation capacity and the increasing compression work. At this optimum intermediate pressure, the system COP is at its highest value. Further details will be discussed in the thermodynamics chapter. The economizer adopted in this experimental setup is embedded in the cycle, as depicted in Figure 39, and its technical characteristics are outlined in Table 5.

(a)

(b)

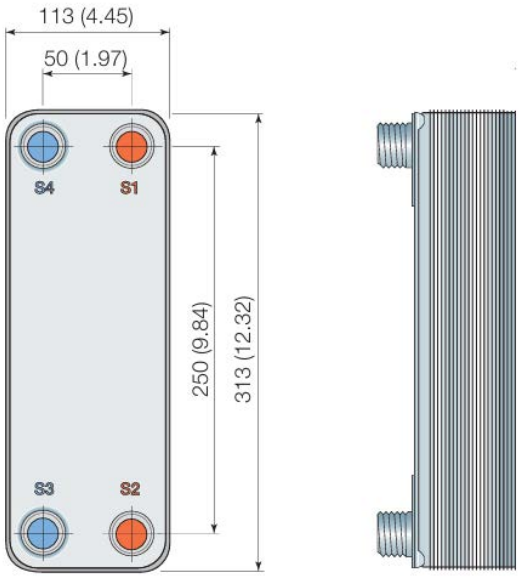

(c)

Plate Heat Exchanger Employed in the Setup (a)
Commercial Type of a Plate Heat Exchanger (b)
Geometrical specifications of the plate heat exchanger (c)

Figure 39 Plate Heat Exchanger (a), Commercial Type Heat Exchanger (b), Geometrical Plate Heat Exchanger (c)

Standard Material		**Standard Data**	
Cover Plates	Stainless Steel	Volume per Channel, Litres	0.054
Connections	Stainless Steel	Max. particle size, mm	1
Plates	Stainless Steel	Max. flowrate1 m^3/h	14
Brazing Filler	Copper	Flow Direction	Parallel
Weight		1.2 kg	

Table 5 Specification of Economizer

3.1.1.4 Oil Separator

Oil management is one of the most important areas in compressor design. The goal is to keep oil inside the compressor and minimize its flow through the rest of the system. Inside the compressor, oil plays crucial functions such as lubrication, sealing, and cooling of internal components. However, in other parts of the system, excessive oil flow can have undesirable consequences, such as, reduced heat transfer performance and additional pressure losses. Oil separators are widely used in HVACR systems to remedy this issue. They are usually placed between the compressor discharge port and the condenser inlet. They work by stripping oil mist from the vaporized refrigerant. The separated oil collects at the bottom of the separator under the influence of gravitational force and is then returned to the compressor crankcase when a certain level is reached. In smaller systems, some methods of oil separation are integrally built into the extended volume of the compressor. Figure 40 illustrates the oil separator incorporated into the system.

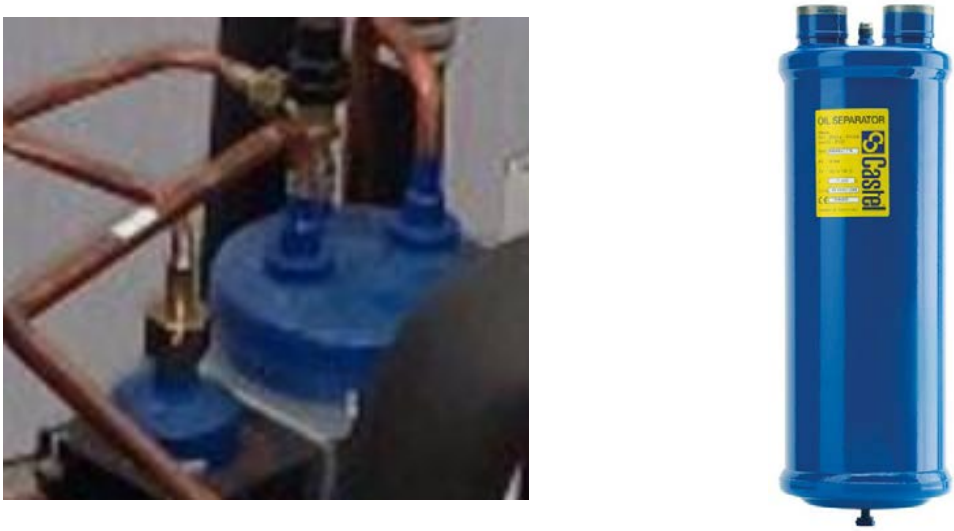

(a) (b)

Figure 40 Oil Separator Employed in the Setup (a), Commercial Type of an Oil Separator (b)

The design of an oil separator requires efficiency, size, and pressure drop to be recognized. The major aim from a practical point of view is to achieve effective separation in a smaller volume while keeping the pressure losses within acceptable levels. For this purpose, it is necessary to investigate the fundamental principles of mist elimination with a focus on the interactions of oil droplets, films, and solid surfaces. In common with other equipment, this separator possesses technical specifications, which are reported in Table 6.

Pressure (bar)	Minimum Temperature (°C)	Maximum Temperature (°C)
32	+130	-10

Table 6 Oil Separator Details

3.1.1.5 Receiver

The liquid receiver indicates a key element of vapor compression refrigeration systems and is located after the condenser. Its essential function is to collect and store the condensed refrigerant in liquid state while guaranteeing a steady and continuous supply throughout the cycle. Acting as a buffer, it balances variations in thermal load and operating conditions, thus avoiding the presence of vapor bubbles at the expansion valve inlet. Such stability is vital, since the reliable operation of the system requires the expansion device to receive only pure liquid refrigerant; otherwise, vapor entrainment would cause performance degradation and unstable behavior (Figure 41).

Figure 41 Liquid Receiver

Beyond its operational purpose, the receiver also facilitates servicing and maintenance by serving as a reservoir for surplus refrigerant during charging, discharging, or system adjustments. This role becomes even more critical in advanced cycles such as vapor injection systems equipped with an economizer. The receiver ensures a consistent liquid flow toward both the main and injection expansion valves, a prerequisite for maintaining intermediate pressure stability and enhancing overall system efficiency. Therefore, the liquid receiver not only contributes to the secure and steady functioning of the cycle but also reinforces efficiency improvements in complex refrigeration configurations.

3.1.1.6 Compressor

The compressor plays a main role in the vapor-injection refrigeration cycle, as it governs both the circulation of the refrigerant and the overall system energy consumption. In this configuration, a scroll compressor with vapor injection is applied, equipped with three ports: suction, discharge, and an additional injection port. Through this design, the refrigerant vapor from both the evaporator and the economizer can be simultaneously introduced into the compression volume.

This twin inflow modifies the compression process in two significant ways. Firstly, the injected refrigerant provides an intercooling effect that reduces the discharge temperature, thereby preventing thermal degradation of the lubricant and minimizing mechanical stress on the compressor components. Second, the additional vapor stream increases the total mass flow rate through the compressor, which enhances the system's cooling capacity. Figure 42 presents the schematic and dimensions of the scroll compressor used in the experimental setup. The inlet and outlet ports are clearly indicated.

From a performance standpoint, the compressor's task is to compress the low-pressure vapor drawn from the evaporator together with the injection vapor supplied at intermediate pressure. As the intermediate pressure increases, the bypass mass flow rate also rises, resulting in higher volumetric flow through the compressor. Consequently, compression work increases with intermediate pressure, but this trade-off is offset by the improvement in evaporator capacity and system COP when the intermediate pressure is close to its optimum value.

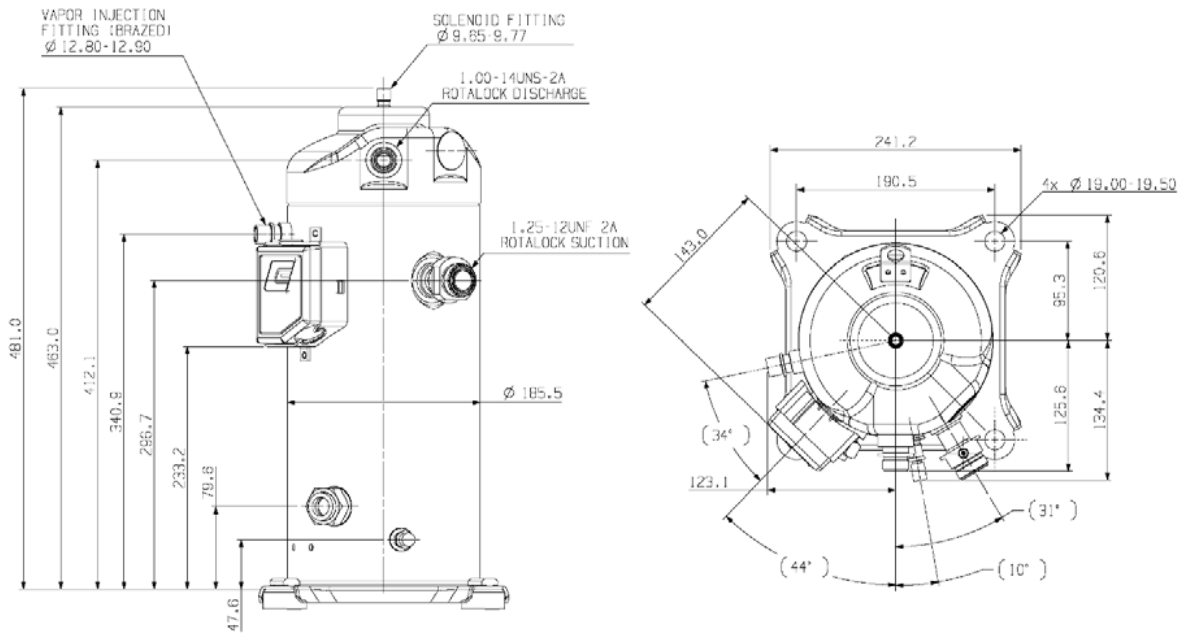

(a)

(b)

Figure 42 Dimensions of Vapor Injection Scroll Compressor (a), Copeland Compressor Unit (ZFD13KVE-TFD551)

Overall, the compressor not only offers the mechanical work necessary for refrigerant circulation but also acts as a regulating component in determining the system's efficiency. Its ability to balance the additional cooling effect of vapor injection with the corresponding increase in power demand is critical for achieving optimal system performance. The details of the compressor used in the setup are listed in Table 7.

Mechanical Data	
Displacement at 50 Hz, m^3/h	11.7
Net Weight	38.6
Rotalock Suction, inch	1 1/4
Rotalock Discharge, inch	1
Oil Quantity, L	1.89
Oil Type (Original Type)	POE RL32-3MAF
High Side Pressure Gauge, bar	32
Low Side Pressure Gauge, bar	21
Refrigerant Classification	A1
Electrical Data of Compressor	
Maximum Operating Current, A	9
Locked Rotor Current, A	64

Table 7 Technical Data of Scroll Compressor

3.1.1.7 Coolant Pump

In the vapor compression test rig, the coolant pump serves a role that is both very straightforward in nature and vitally significant to the overall operation of the system: it is tasked with ensuring a continuous and stable circulation of the secondary fluid as it flows through the whole loop. This uniform motion is important in that it allows for effective and efficient heat exchange between the refrigerant cycle and the load side, both of which are key elements of the refrigeration process. In case of any disruption or irregularity in the coolant flow, even a well-designed compressor or evaporator would fail to deliver the expected level of performance. This is because the process of thermal energy transfer would get chaotic and unevenly distributed to the detriment of the overall efficiency and functionality of the system.

The pump circulates the coolant, which is typically a blend that contains either a brine solution or a mix of water and glycol, between two major components: the evaporator and the receiver tank. In addition, by providing the assurance that there is a well-regulated flow rate sustained during the operation of the

pump, researchers can effectively and accurately control the load conditions imposed on the refrigeration system. This precise control is highly essential and has a very important part to play when it comes to measuring and determining the performance of the compressor during its operation under vapor injection conditions. Figure 43 illustrates the dimensions and the coolant pump used in the test rig.

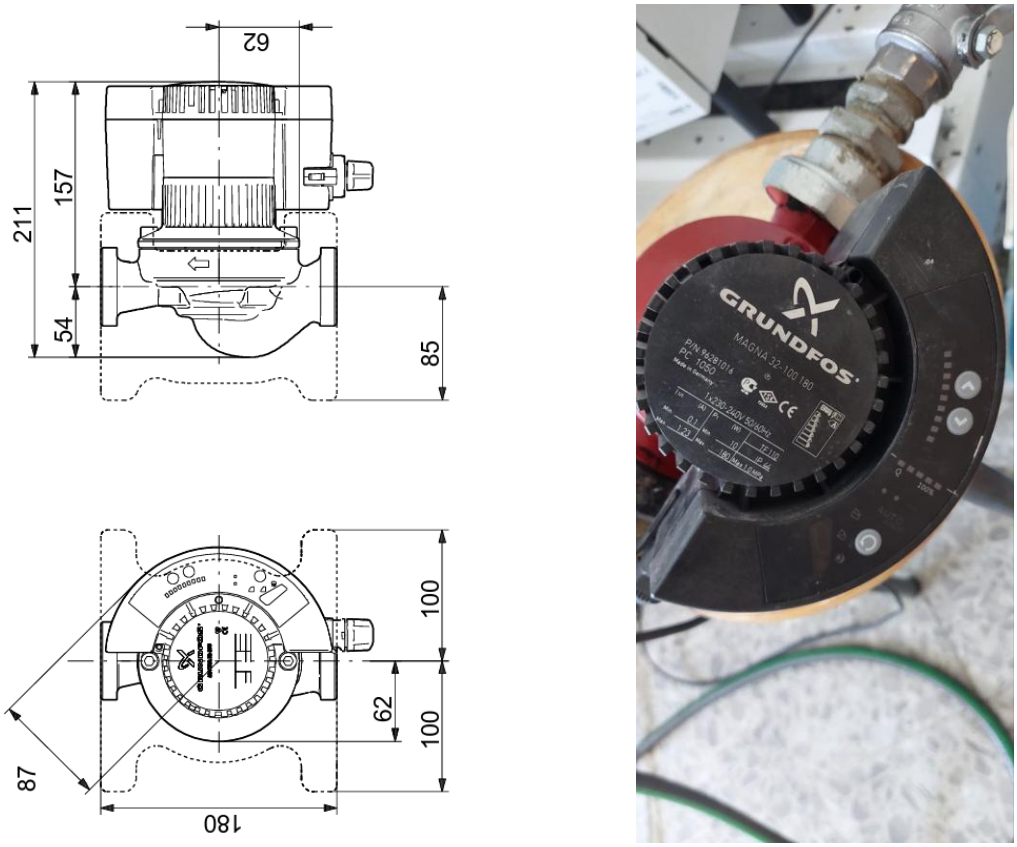

(a) (b)

Figure 43 Dimensions of Coolant Pump (a), Coolant Pump of Test Rig (b)

At the systems level, the coolant pump is more than just a passive fluid mover. It also acts as a stabilizer. It provides constant boundary conditions to the heat exchangers, prevents overheating or localized freezing, and ensures repeatability of experiments. That is, while the compressor imposes the thermodynamic cycle, the coolant pump unobtrusively ensures that the cycle can be effectively tested under controlled and measurable conditions. The specifications of the coolant pump utilized in the setup are presented in Table 8.

Liquid:	
Pumped Liquid	Water
Liquid Temperature Range	2 to 95 ℃
Materials:	
Pump Housing	Cast Iron, EN-JL1040, ASTM 35B-40B
Installation:	
Range of Ambient Temperature	0 to 40 ℃
Maximum Operating Pressure	10 bar
Electrical Data	10 to 180 W
Maximum Current Consumption	0.1 to 1.23 A
Others:	
Net Weight	4.4 kg
Gross Weight	5.58 kg

Table 8 Coolant Pump Specifications

3.1.1.8 Valves and Other Connections

In refrigeration test rigs, valves and auxiliary fittings are not merely add-on components; they play a crucial role in ensuring the safety, controllability, and reliability of the entire system. Each valve operates with a defined purpose—whether it is safeguarding the equipment, regulating refrigerant flow, or enabling accurate monitoring of system performance under varying operating conditions. Without these elements, conducting experiments in a safe and consistent manner would be practically impossible.

In the mentioned test rig, a range of components including the direct-loaded safety valve, check valve, vibration absorber, sight glass, shut-off ball valve, pressure-operated water valve, solenoid valve, pipes, and others have been employed, which are described in the following section.

(i) Direct Loaded Safety

Within vapor compression refrigeration systems, the safety valve provides an important protection function, avoiding over-pressurization on the high-pressure side of the cycle. In case of fault conditions—such as condenser failure, restricted refrigerant flow, or elevated ambient temperatures—the pressure of the system can rise above tolerable levels. To prevent such a threat, the valve is set to operate independently when pressure goes beyond its preset level, thus releasing a volume of refrigerant and returning the system to a safe level of pressure (Figure 44).

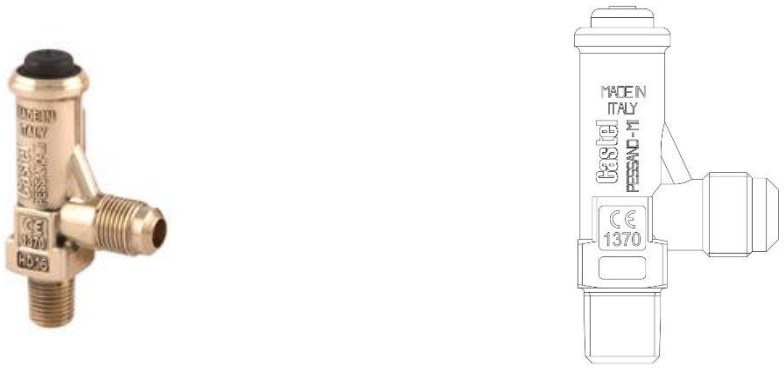

Figure 44 Direct-Loaded Safety Valve in Test Rig

In addition, protecting the structural integrity of key components such as the compressor, condenser, and piping system, the safety valve also acts as the first line of defense for people and the environment. By keeping system pressure within acceptable ranges, it reduces the likelihood of equipment failure, refrigerant leakage, or catastrophic failure. As such, the safety valve is not just an accessory; it is a vital safety device that ensures the system operates reliably and securely. Additional details of this component are presented in Table 9.

Description	Detail
Set pressure range, bar	9-50
Pressure, bar	55
Minimum Temperature, ℃	-50
Maximum Temperature, ℃	+120

Table 9 Specifications of Direct-Loaded Safety Valve

(ii) Sight Glass

The sight glass, though a relatively small component, serves an important role in vapor-compression refrigeration systems and is typically installed along the liquid line. Its primary function is to provide a direct visual check of the refrigerant flow. By monitoring this device, operators can identify the presence of bubbles, which signal either an undercharged system or incomplete condensation. Maintaining a bubble-free liquid stream is pivotal, since the expansion valve requires fully condensed refrigerant to operate efficiently and stably.

In many cases, sight glasses also include a moisture indicator that changes color when excess moisture is detected in the refrigerant. In summary, the sight glass functions as a “window” into the refrigeration cycle, allowing verification of refrigerant quality while supporting the safe and reliable operation of the system (Figure 45).

(iii) Shut-Off Ball Valve

The shut-off ball valve is utilized in vapor compression systems for isolating specific parts of the cycle. Its ball-and-seat construction enables the flow of refrigerant to be either wide open or completely closed by a quarter turn, making it a reliable and convenient device. This is especially useful for maintenance and repair operations since it permits servicing or replacement of individual components—like the compressor, condenser, or evaporator—without requiring that the entire refrigerant discharge the system.

Apart from maintenance purposes, the shut-off ball valve also plays an important role in ensuring operational safety (Figure 46).

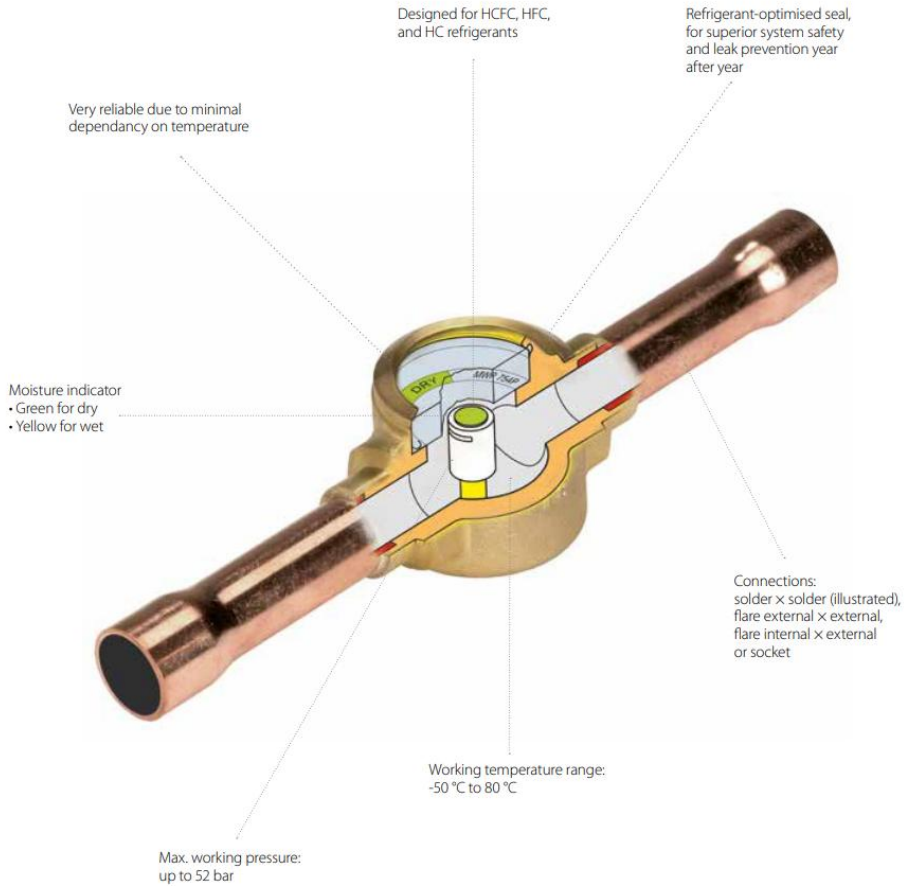

Figure 45 Details of Sight Glass

During emergency conditions, it allows for the instant interruption of refrigerant flow, thus minimizing the risk of leaks, equipment failure, or possible hazards to people and the environment. In short, the valve exists not just as a device for controlling flow but also as an important tool that adds to both the safety and serviceability of the refrigeration system. Table 10 summarizes supplementary information regarding this valve.

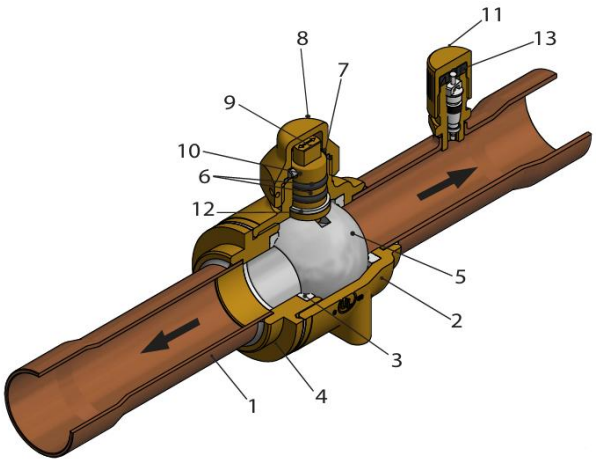

1	Connection Tube
2	Valve Body
3	Ball Seat
4	Valve Tail
5	Ball
6	Double O-Ring Seal in Spindle
7	Cap Seal
8	Seal Cap
9	Spindle
10	Pin
11	Access Port Cap
12	Guide Ring
13	Schrader Valve

(a)

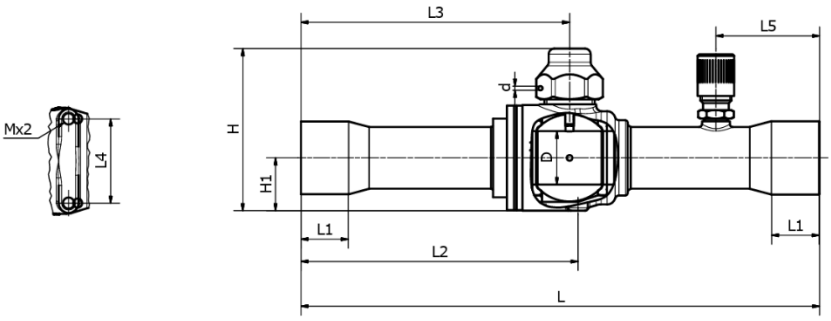

H	43 mm
H1	12 mm
L	139 mm
L1	9 mm
L2	73 mm
L3	73 mm
L4	17 mm
L5	31 mm
D	11.1 mm
d	1.5 mm
M	M3×0.5

(b)

Figure 46 Different parts of Shut-Off Ball Valve (a), Dimensions (b)

Details	**Value**
Maximum Working Pressure, bar	45
Media Temperature Range, ℃	-40 ~ +100
Environmental Transport/Storage Temperature and Humidity, ℃ and %	-40 ~ +65/ Air Humidity ≤ 95
Flow Direction	Bi Flow

Table 10 Technical Data of Shut-Off Ball Valve

(iv) Pressure Operated Water Valve

The pressure-operated water valve is a control device widely used in vapor compression systems with water-cooled condensers. The major function is to automatically regulate the flow of cooling water according to the condensing pressure of the refrigerant. As the discharge pressure exceeds the predefined value, the valve opens incrementally, permitting a larger flow of water to enter the condenser to reject the surplus heat. When the condensing pressure lowers, the valve throttles the water flow, thus preventing wastage of water as a coolant.

By regulating the water flow in this manner, the valve keeps the condenser pressure at a set range to provide stable operating conditions for the overall refrigeration system. Not only does this control improve energy efficiency and conserve water, but it also protects major components like the compressor from unnecessarily high pressure. In Figure 47, a clearer visual understanding of this component can be obtained.

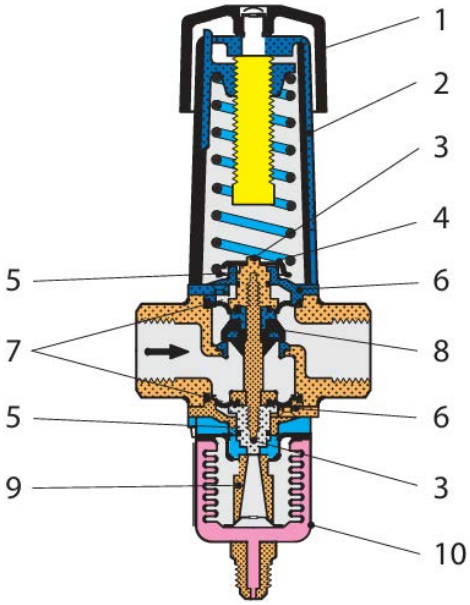

(a)

1	Handwheel
2	Spring Housing
3	Spindle Guide
4	Spring Retainer
5	O-ring
6	Guide Bush
7	Diaphragm
8	Valve Cone
9	Thrust Pad
10	Bellows Element

H1	91 mm
H2	133 mm
L	72 mm

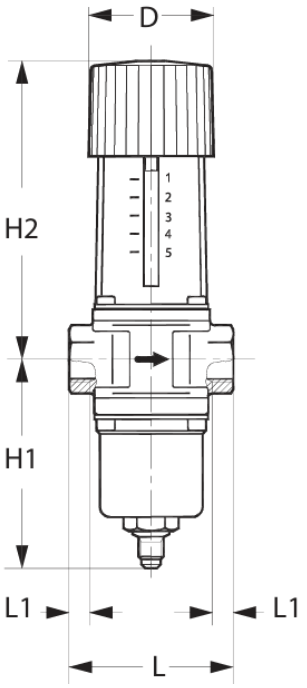

L1	11 mm
L2	73 mm
D	55 mm

(b)

Figure 47 Different parts of Pressure Operated Water Valve (a), Dimensions (b)

Fundamentally, the pressure-operated water valve is an automatic balancing device that serves both the reliability and sustainability of system performance (Table 11).

Condenser Side	
Refrigerant	R448A
Control Pressure Adjustable Opening Pressure, bar	3.5 – 16
Maximum Working Pressure, bar	26.4
Maximum Test Pressure, bar	29.0
Liquid Side	
Media	Fresh Water, Sea Water
Maximum Working Pressure, bar	16
Maximum Test Pressure, bar	24
K_v, Value, m^3/h^*	1.4
Weight, kg	1

*The K_v value is the flow of water in m^3/h at a pressure drop across valve of 1 bar, ρ = 1000 kg/m^3.

Table 11 Technical Data of Pressure Operated Water Valve

(v) Solenoid Valve

The solenoid valve is an electromechanical device that is commonly utilized in refrigeration systems for automatic control of refrigerant flow. Driven by an electromagnetic coil, the valve closes or opens when subjected to electrical signals, which are normally issued by a thermostat or control module.

The ability of rapid switching enables for accurate control of refrigerant circulation, especially in the liquid line supplying the expansion device. As shown in Figure 48, the dimensions and appearance of the component are presented, and furthermore, its technical specifications are listed in Table 12.

One of its key functions is to prevent liquid refrigerant migration to the compressor during shutdown periods. By closing the liquid line when the system stops, the solenoid valve helps avoid liquid slugging, which might critically impair the compressor components. Moreover, it improves energy efficiency by allowing refrigerant flow only, when necessary, thereby optimizing the overall performance of the system. Apart from these functional benefits, the solenoid valve also increases operational safety and provides flexibility in test rigs, where automatic switching between different operating conditions is often required.

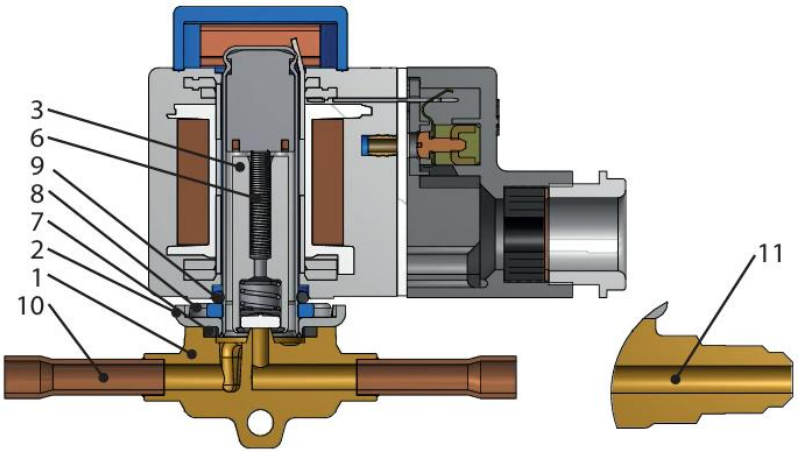

(a)

1	Valve Housing Assembly
2	Cover
3	Armature Assembly
4	Diaphragm Assembly
5	Support Washer
6	Armature Spring
7	Seal
8	Screws
9	O-ring
10	Solder Connection
11	Flare Connection

H1	14 mm
H2	73 mm

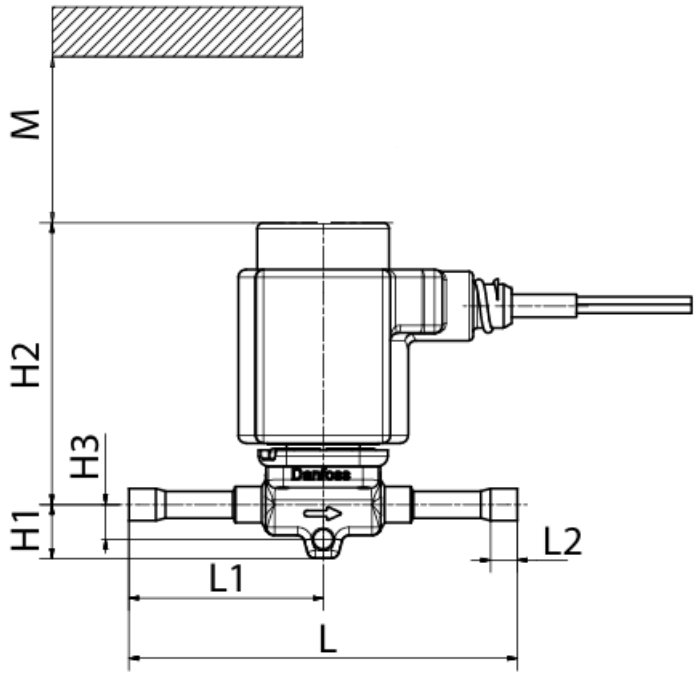

H3	9 mm
M	65 mm (Min)
L	101 mm
L1	50.5 mm
L2	7 mm
W	34

(b)

Figure 48 Different parts of Solenoid Valve (a), Component Dimensions (b)

Description	Value
Net Weight	0.176 kg
Ambient Temperature, ℃	-40 ~ 80
Direction	Straightway
Fluid Group	A1, A2
K_v, Value, m^3/h	0.27
Maximum Working Pressure, bar	45.2
Medium Temperature Range (Max), ℃	+105
Medium Temperature Range (Min), ℃	-40
Valve Operation	Direct

Table 12 Technical Data of Solenoid Valve

(vi) Check Valve

The check valve is a straightforward but essential device in refrigeration systems. The main purpose is to let refrigerant flow in one direction but not the other. Its one-way control is especially crucial during compressor shutdown, when pressure gradients would otherwise allow refrigerant to flow in reverse toward the compressor. By preventing reverse flow, the check valve saves the compressor from damage in the form of liquid hammer or reverse rotation. The check valve applied in the test rig, along with its technical details, is listed in Table 13.

Description	Value
Environmental Transport/Storage Temperature and Humidity, ℃, %	-40 ~ 65/ Air Humidity: RH ≤ 95
Flow direction	Single Flow
Serviceable	No

Table 13 Technical Data of Check Valve

In addition to safeguarding the compressor, check valves serve an important function in systems that have parallel circuits, for instance, those with multiple evaporators or compressors. They provide proper distribution of flow and eliminate crossflow between the branches, thus improving the steadiness and trustworthiness of the system cycle. Finally, while simple mechanically, the check valve is an important safety and control component that ensures the proper direction of refrigerant flow and helps provide long-term life to the refrigeration system (Figure 49).

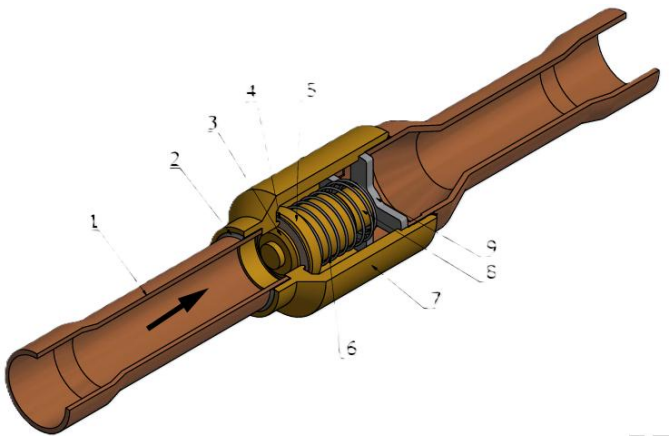

1	Connection tube
2	Solder ring
3	Washer
4	Disk
5	Piston
6	Spring
7	Valve Body
8	Guide
9	Stop Face

(a)

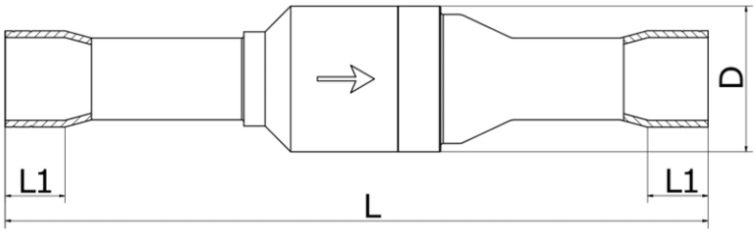

L	109 mm
L1	9 mm
D	18 mm

(b)

Figure 49 Different parts of Check Valve (a), Dimensions of Check Valve (b)

3.1.2 Cold Room Specifications

A temperature-controlled cold room (see Figure 50) was developed to allow performance testing of the refrigeration system in conditions closely resembling real-world operation. The chamber was

constructed using insulated panels to reduce heat ingress, helping to maintain a stable internal temperature throughout the test cycles. To ensure both thermal isolation and ease of use, reinforced seals and robust hinges were integrated into the design, allowing straightforward access for loading and unloading samples.

Figure 50 Walk-in Freezer

This controlled setup makes it possible to gather consistent performance data, including cooling capacity, energy usage, and temperature distribution. Maintaining thermal consistency within the chamber improves the repeatability of each test and contributes to more dependable comparisons across datasets, as outlined in Table 14.

Description	Value
Dimensions:	1800mm × 1800 mm × 2200 mm
Thickness:	150 mm
Material:	Polyurethane and Aluminum

Table 14 Technical Data of Walk-in Freezer

3.2 Instrumentation and Data Acquisition System

To assess the performance of the refrigeration system, several calibrated instruments were employed, including thermocouples for temperature monitoring, pressure transducers, and flowmeters. These tools

enabled accurate tracking of the system's key operating parameters under controlled laboratory conditions. Sensor outputs were collected through a data acquisition system (DAQ), which digitized the readings and transmitted them to a computer for storage and follow-up analysis. This setup allowed for reliable data collection, minimized the possibility of operator mistakes, and supported real-time observation of system behavior.

In this study, three different data acquisition platforms were utilized to gain a comprehensive understanding of the system's operation:

i. Pego Electrical Board (Refrigeration Plant): Responsible for recording data related to the evaporator and expansion valve functions.
ii. CAREL Electronic Control Unit: Used to monitor compressor and condenser performance parameters.
iii. Yokogawa Data Logger: Deployed to capture detailed temperature readings at several critical locations across the system.

The integration of data from these platforms offered a complete overview of system functionality, supporting the evaluation of its performance with good measurement fidelity. Additional details on each device are presented in the subsequent sections.

3.2.1 Data Logger

This section explains the role and specifications of the three data loggers utilized.

3.2.1.1 Pego Electrical Board

This instrumentation for data logging consists of three main components: the VISION TOUCH AB electronic panel, the 100N Master3 driver, and the NEXUSP20 electronic regulator for controlling. Together, these units form an integrated package that enables robust monitoring and governance of the system.

In the following sections, the VISION TOUCH AB electronic panel and the 100N Master3 driver will be detailed in conjunction, while the NEXUSP20 electronic regulator for controlling will be explained in detail separately.

- **NEXUSP20 regulator**

  The NEXUSP20 is an electronic regulator for controlling the ON/OFF electronic expansion valve equipped with a coil designed to operate at standard supply voltages of 230 V, 110 V, or 24 V AC, as well as 24 V DC. This regulator manages the most common ON/OFF electronic expansion valves

and integrates evaporator superheat management. Dimensions and technical data are listed in Figure 51 and Table 17.

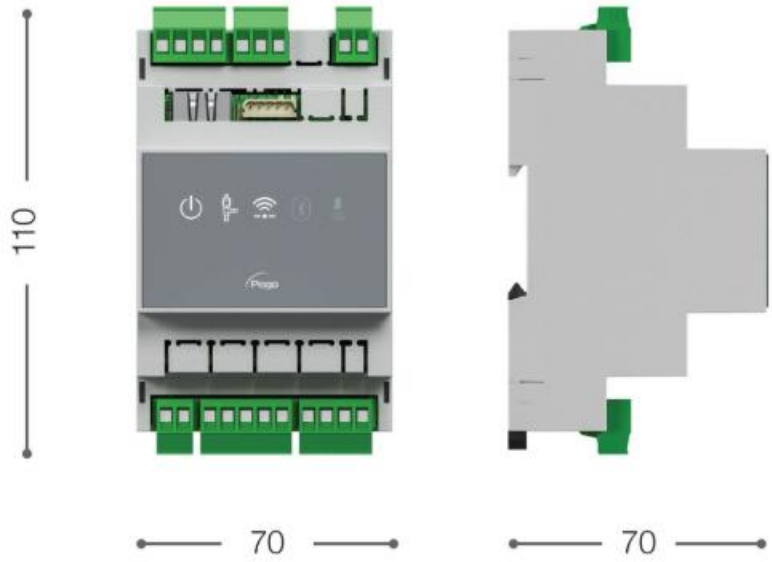

Figure 51 NEXUSP20 Electronic Regulator

Feature	Details
Main Voltage	24 V ~ ±10 % 50 – 60 Hz
Maximum Power Consumption (Electronic Control Only)	~ 7 VA
Operating Temperature	-5 – 50 ℃, RH ≤ 90%, non-condensing
Storage Temperature	-10 – 70 ℃, RH ≤ 90%, non-condensing
Compatible Types of Temperature Sensor	Temperature Sensors: NTC 10K 1% / PTC / PT1000
Resolution of Temperature Sensors	0.1 ℃
Precision of Temperature Sensor Detection	± 0.5 ℃
Range of Temperature Sensor Detection	-45 – 99 ℃
Compatible Type of Pressure Sensor	Pressure Sensor: 4/20 mA

Table 15 Technical Feature of NEXUSP20 Electronic Regulator

- **VISION TOUCH AB Electronic Panel**

The VISION TOUCH AB electronic interface is designed to manage the primary operational components of a refrigeration unit. Through this panel, users are able to regulate essential functions such as evaporator fan operation, defrost heater cycles, and illumination within the cold room environment. Rapid refrigeration of products is achieved through programmed control, which can be terminated either by a predefined time setting or the detection of target temperature via a piercing probe. The control system is composed of the 100N MASTER3 unit—serving as the central hub for all electrical connections—and the VISION TOUCH AB console, which provides the interactive control interface. For additional technical specifications and system details, refer to Figure 52 and Table 16.

Figure 52 VISION TOUCH AB Electronic Panel

Feature	Details
Main Voltage	110 - 230 V ~ ±10 % 50 – 60 Hz
Maximum Power Consumption (Electronic Controller Only)	~ 15 VA
Operating Temperature	-5 – 50 ℃, RH ≤ 90%, non-condensing
Storage Temperature	-10 – 70 ℃, RH ≤ 90%, non-condensing
Type of Connectable Probes (Temperature)	NTC 10K 1%
Resolution (Ambient Temperature)	0.1 ℃
Precision of Probe Detection (Ambient Temperature)	±0.5 ℃
Reading Range	-45 – 99 ℃

Table 16 Technical Feature of VISION TOUCH AB Electronic Panel

3.2.1.2 CAREL Electronic Control Unit

The µRack controller, developed by CAREL, has been designed for the regulation of small compressor racks commonly employed in refrigeration systems. Engineered as a compact unit, it integrates both control and monitoring functionalities to support the efficient operation of compressors and associated auxiliary components. Its modular design facilitates precise sequencing and capacity management of compressors, contributing to energy efficiency and reliable performance across varying load conditions.

In addition to compressor regulation, the µRack incorporates alarm handling, data logging, and protective mechanisms. These features not only safeguard system integrity but also support performance analysis and fault diagnostics. A range of accessories is available for this controller, including

- Connector kit with wired connectors,
- Temperature sensors,
- Pressure sensors,

Due to its adaptable architecture and scalability, the µRack has proven suitable for both laboratory testing and commercial refrigeration, offering stable and accurate control over the refrigeration cycle. For further information regarding technical details and system specifications, refer to Figure 53 and Table 19 in section 3.2.2.

(a)

(b)

(c)

(d)

Figure 53 CAREL Controller (a), Connector Kit with Wired Connectors (b), Temperature Sensors (c), Pressure Sensors

3.2.1.3 Yokogawa Data Logger

The Yokogawa DC100 Data Logger is a compact, multi-channel instrument designed for recording, monitoring, and analyzing a wide range of process variables. It provides flexibility by supporting different input types such as thermocouples, RTDs, DC voltage, and current signals, making it highly suitable for laboratory experiments and industrial test setups. Equipped with a large color TFT LCD display, it allows real-time visualization of data.

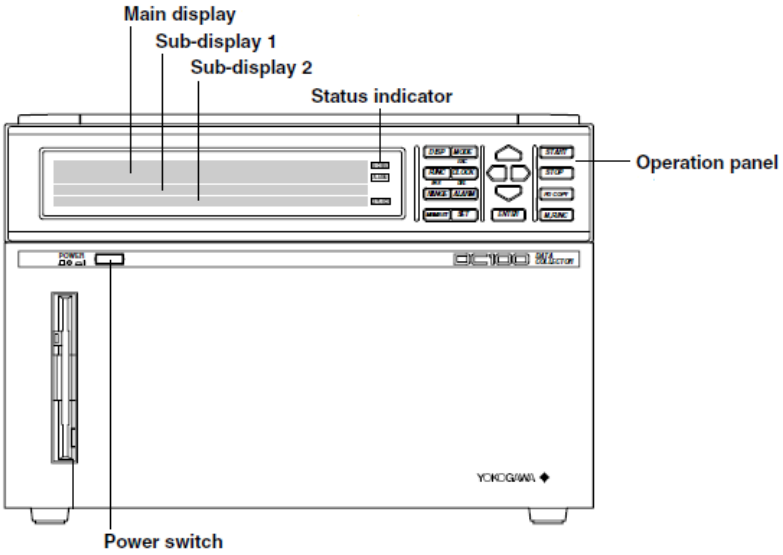

(a)

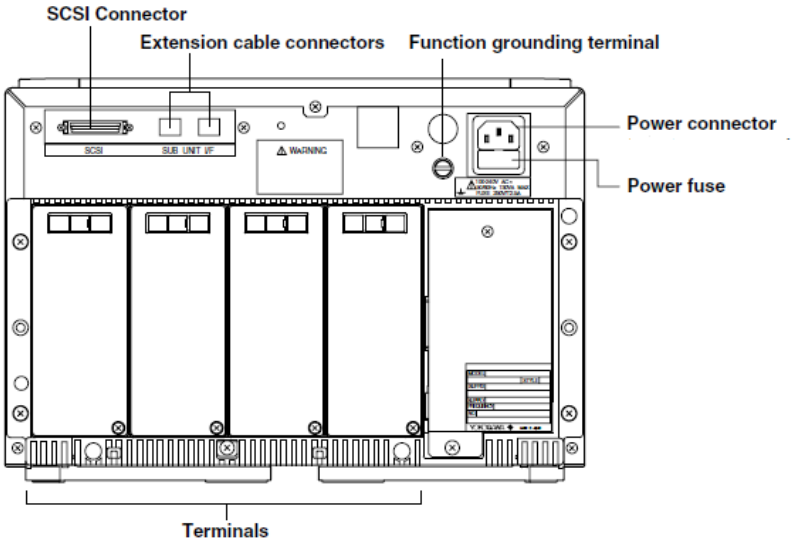

(b)

(c)

Figure 54 Front view of the DC100 data logger (a), Back panel of the DC100 data logger (b), Test Rig DC100 Data Logger (c)

This logger provides high measurement accuracy and flexible sampling intervals and precise monitoring of system dynamics across different timescales. Data can be stored internally or exported via external memory devices. This 20-channel data logger is connected to a PC via cable, through which the measured data are transferred and stored for further analysis. Alarm functions further ensure that abnormal events can be quickly detected and documented (Technical data in Table 17).

Overall, as shown in Figure 54, the DC100 combines measurement reliability, versatile input capability, and user-friendly operation, making it a practical choice for advanced data acquisition tasks.

3.2.2 Measurement Equipment for Independent variables

As established in fundamental thermodynamic principles, pressure and temperature are considered independent properties. In this study, both parameters were recorded with dedicated sensors, which are further described in the following sections.

Parameter	Specification
Number of Channels	20
Input Types	Thermocouples, RTDs, DC Voltage, DC Current
Measurement Accuracy	± (0.1% of reading + 1 digit) for V/I; ±1.0 °C for TC
Sampling Interval	3 s ~ 3600 s
Communication Interface	SCSI (Small Computer System Interface) Cable
Power Supply	100 to 240 V AC
Power Consumption	About 90 VA Max

Table 17 General Specifications of DC100 Data Logger

3.2.2.1 Temperature Sensors

Temperature measurements were acquired using two independent data loggers connected to separate sets of sensors. Type-T thermocouples, utilized in conjunction with the DC100 data logger, are defined by the specifications provided in Table 18. The characteristics of the sensors connected to the CAREL data logger are also included in the same table.

Description	Parameters	
T-Type Thermocouple		
Material	Copper (+)	Constantan: Cu & Cu-Ni Alloy (-)
Thermocouple Grade Wire	-270 ℃ to +370 ℃	
Accuracy	Standard	± 1.0 ℃ or ± 0.75 %
	Special Limits of Error	± 0.5 ℃ Cor 4 %
CAREL Sensor		
Operating Range	-50 ℃ to +105 ℃ in Air, -50 ℃ to +50 ℃ in Fluid	
Connections	Stripped Ends, Dimensions:5 ± 1 mm	
Sensor	NTC 10 kΩ ± 1 % a 25 ℃ Beta 3435	
Dissipation Factor (in air)	3 mW/℃	

Thermal Constant Over Time (in Air)	Approx. 25 s	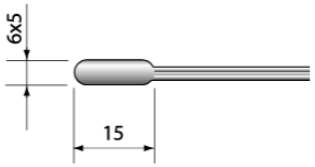
Operating Range	-50 ℃ to +105 ℃	
Connections	Stripped Ends, Dimensions:6 ± 1 mm	
Sensor	R (25 ℃) = 10 kΩ ± 1 %; Beta 3435	
Dissipation Factor (in air)	3mW	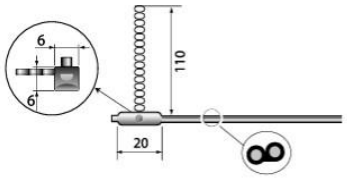
Thermal Constant Over Time (in Air)	Approx. 50 s	
Sensor	50 kΩ ± 1% @ 25 ℃, IP67	
Operating Range	-30 to +100 ℃ 95% RH in Air (150 ℃ in a Dry Environment)	

Table 18 Specifications of Temperature Instrument

3.2.2.2 Pressure Sensors

A pressure sensor is employed to measure the pressure of a fluid—whether in liquid or gaseous form—and to convert this physical quantity into an electrical signal suitable for acquisition and analysis. Within vapor compression systems, such transducers are vital for monitoring the operating conditions of major components, including the compressor, condenser, and evaporator. By continuously recording pressure variations, these sensors provide critical input for performance evaluation, system control, and safety assurance.

The operating principle typically involves a pressure-sensitive element, such as a diaphragm, which deforms in response to the applied pressure. This deformation is transformed into a standardized electrical output, most commonly a 4–20 mA signal, ensuring compatibility with data acquisition devices and control systems. Accurate pressure measurement plays a key role not only in thermodynamic assessment but also in the early detection of faults such as over-pressurization or underperforming condition.

Specification	Value
Pressure Range	-0.5 ~ 7 bar
Current Range	4 ~ 20 mA
Pressure Over Range	15 bar
Pressure Brust	530 bar
Material	316L Stainless Steel
Operating Conditions	-40 ℃ ~ 135 ℃
Storage Conditions	-40 ℃ ~ 135 ℃
Total Precision	Typical ± 1 % FS, Max ± 2 % FS (0 ~ 50 ℃), Max ± 4 % FS (-20 ~ 80 ℃)

Table 19 Technical Data of Pressure Transducer

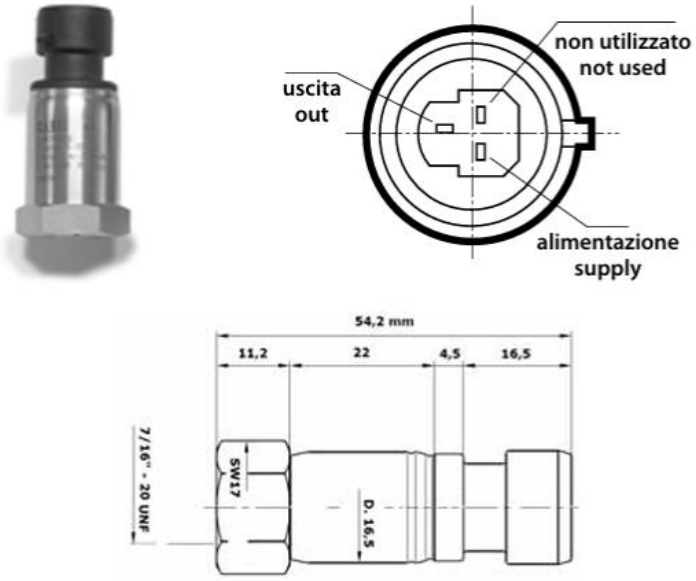

Figure 55 Dimensions and Different Parts of Pressure Probe

In the present experimental setup, the transducer model SPKT0021C0 was selected. Its technical specifications are summarized in Table 19 and visually represented in Figure 55.

3.2.2.3 Volume Flowmeter

The SU-01 is designed to work both as an ultrasonic flowmeter and as a monitoring device, operating on the time-of-flight difference principle. In simple terms, two ultrasonic transducers take turns sending and receiving signals. As the fluid moves, the sound waves travel faster in one direction and slower in the other, creating a small but measurable time difference. This difference reveals the average flow

velocity, and with the tube's internal diameter known, the device's microprocessor calculates the volumetric flow rate automatically.

The results are shown clearly on a 7-segment LED display, with flexible unit options such as liters per minute (l/min), cubic meters per hour (m³/h), gallons per minute (gpm), or gallons per hour (gph). The SU-01 also includes two programmable transistor outputs, which can be set as normally open or normally closed and adjusted for switching point, hysteresis, or mode. A window function is available, along with start-up delay (0–99.9 s) and on/off delay (0–9.9 s) settings. In models with analog output, the measured range can also be mapped to a standard 4–20 mA signal.

Beyond measurement, the SU-01 is built for reliability. It features a keypad lock, strong resistance to vibration and shock, long-term stability, and a display unit that can be rotated in 90° steps for easy viewing. Thanks to its low pressure drop and simple installation, it provides dependable flow monitoring with minimal hassle. More details on its specifications and settings can be found in Figure 56 and Table 20.

Description	Details
Measuring Ranges	10 l/min, 25 l/min, 40 l/min, 100 l/min, 170 l/min
Process connections	G 3/4", G 1", G 1 1/4", G 2"
Measuring Medium	Water and water-like liquids
Maximum Pressure	25 bar
Medium Temperature	+4 ℃ to +130 ℃ (with Separated Mounting)
Electronics Temperature	-10 ℃ to +70 ℃
Storage Temperature	-30 ℃ to +80 ℃
Linearity Error	± 2.5 % of Measured Value (at 25 °C)
Power Consumption	Approx. 50 mA without load
Digital Display	4-digit 7-segment LED, red, digit height 12 mm

Table 20 Specifications of Volume Flowmeter

(a)

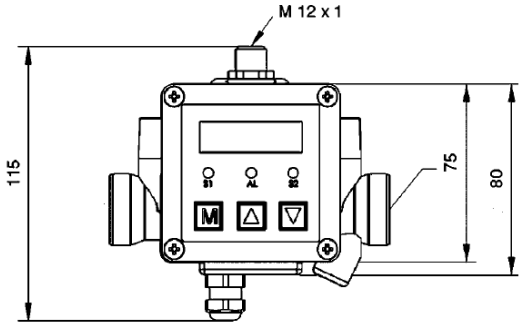

(b)

Figure 56 Volume Flowmeter in Test rig (a), Dimensions of Flowmeter (b)

3.2.3 Measurement Equipment for Dependent Variables

In vapor compression refrigeration and energy systems, things like energy use, power demand, and efficiency do not come as fixed values; they shift depending on how the system is running. To measure these outcomes accurately, precise instruments are needed. Tools such as power quality analyzers, flowmeters, and data loggers are used to keep track of both the electrical and thermal performance. With this kind of monitoring, it becomes possible to clearly understand how the system behaves under real operating conditions.

3.2.3.1 Power Quality Analyzer

To monitor the electrical performance of the vapor compression system, a Fluke 434 Series II Power Quality Analyzer was employed. This instrument is specifically designed for comprehensive power diagnostics, enabling the measurement of parameters such as voltage, current, active and reactive power, apparent power, harmonic distortion, and cumulative energy consumption over extended periods.

The device's high-resolution sampling capacity allows it to capture transient and steady-state conditions, providing a detailed understanding of system behavior across varying load profiles. With its multi-channel capability, it can simultaneously record three-phase power inputs, offering a holistic evaluation of the refrigeration system's operational efficiency. The technical specifications and visual representation of the Fluke 434 Power Quality Analyzer are provided in Figure 57 and Table 21, respectively.

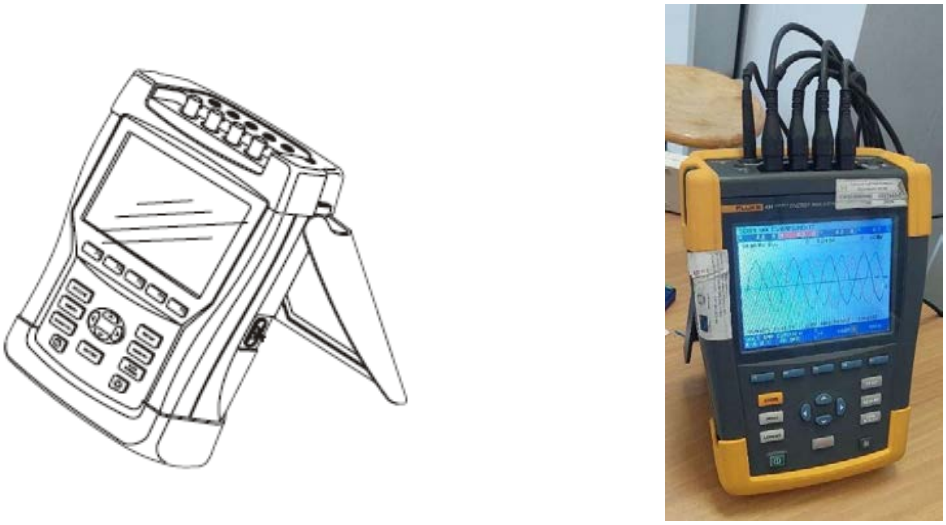

Figure 57 Power Quality Analyzer

Surpassing baseline measurements, the analyzer serves a crucial role in identifying power quality anomalies—such as voltage dips, surges, harmonic interference, or momentary outages—that could negatively impact system performance or component longevity. This dual functionality makes it not only a measurement tool but also a diagnostic asset, applicable in both experimental setups and industrial field conditions.

Specifications	**Features**		
Scope	Vrms, Arms, Vcursor, Acursor, Vfund, Afund, Hz, V phase angles, A phase angles		
Power and Energy	Watts, VA, VAR, Power factor, Cos φ / DPF, Arms, Vrms, kWh, kVAh, KVARh, peak demand interval using trend, KYZ revenue meter verification via optional input.		
	Measurement Range	**Resolution**	**Accuracy**
Watt (VA, VAR)	1.0 ~ 20.00 MW	0.1 ~ 1 kW	± 1.5 % ± 10 counts
kWh (kVA, kVAR)	00.00 kWhr ~ 200.0 GWhr	0.01 Whr ~ 100 Whr1	± 1.5 % ± 10 counts
Cos φ / DPF	0 ~ 1	0.01	± 0.03
Power Factor	0 ~ 1	0.01	± 0.03

Table 21 Specifications of Power Analyzer (Power and Energy Section)

3.3 Measurement Uncertainty and Calibration

3.3.1 Data Logger Yokogawa (DC100)

To ensure accuracy and dependability in the measurement process, the Yokogawa DC100 data logger used in this study was calibrated with the EN ISO/IEC 17025:2017 standard [186]. This internationally

acceptable standard emphasizes traceability of measurements and compliance to quality assurance protocols. During calibration, the data logger's output was benchmarked against certified reference instruments, thereby minimizing uncertainty and confirming the instrument's suitability for both research applications. This step not only enhances the credibility of the experimental outcomes but also aligns the research methodology with globally accepted standards in metrology and testing practices.

3.3.2 Energy Meter Fluke 434

Confirming the validity of power quality measurements entails frequent calibration of the Fluke 434 Power Quality Analyzer. Due to the complexity of its internal architecture and the sensitivity of its measurements, the device cannot be calibrated by the end user. Calibration is rather required to be undertaken using qualified Fluke service centers or accredited calibrating laboratories with special reference instruments. Calibration usually requires choosing an authorized calibrating facility using Fluke or its authorized distributors, booking the service by defining the procedure, cost, and turnaround time, and properly shipping the instrument using the service center's instructions. At the conclusion of the procedure, the analyzer is returned with the official calibration certificate, which confirms conformance with international requirements and ensures the measurement provenance. The need for professional calibration is justified on three grounds.

First, high-precision test equipment such as reference voltage and current sources and sophisticated oscilloscopes are not available to ordinary end-users.

Second, the internal calibration processes are technically complex and require knowledge of specifications and measurement principles of the device.

Third, professional calibration ensures traceability to international metrology standards, and this is essential to the reliability and validity of power quality data.

For these reasons, it is only feasible that the credibility of measurements both in research and industrial practice can be maintained using calibration services of approved centers [187].

3.3.3 K-Type Thermocouple

Calibration of K-type thermocouples is very essential for accuracy of measurement, especially where dependable thermal information is needed in experimental work. This procedure typically consists of placing the thermocouple within a sequence of steady-state, pre-specified temperatures within its range of operation using equipment like precision thermal baths or furnaces and a calibrated reference standard. Pre-calibration preparation involves proper connection using high-grade extension wires

supplemented by verification of electrical continuity and attainment of a steady cold junction, which is usually kept at 0 °C via an ice bath. During the measurement of their calibrations, both the test thermocouple and the reference sensor are placed within the controlled thermal atmosphere and adequate time (about 10 to 15 minutes) is given before the system is allowed to come into thermal equilibrium. After stability is attained, the output voltage of the thermocouple is simultaneously recorded with the reference instrument-issued corresponding temperature.

This measurement is repeated at several points of the temperature to span the applicable measurement range. These obtained data are then referenced against the standard reference tables of type K thermocouples defining the relation of the temperature with the thermoelectric voltage. Differences between outputs measured and standard values are computed and used to quantify error at each of the calibration points. These findings are then summarized into a calibration certificate showing the performance of the thermocouple and its characteristics and containing correction factors where applicable and hence traceable and reliable measurement of temperature is obtained subsequently [188], [189].

3.3.4 Negative Temperature Coefficient (NTC) Thermistors

Precise use of Negative Temperature Coefficient (NTC) thermistors requires calibration, since even small variations in manufacturing can affect the resistance and temperature curve of each sensor. The procedure is based on measuring the thermistor's resistance at several fixed, well-controlled temperatures. Typically, the sensor is placed in a temperature-controlled environment such as a stirred bath, freezer, or furnace, together with a precision reference device. To minimize errors, the thermistor is mounted in a simple circuit with a known high-accuracy resistor, usually as part of a voltage divider, and powered by a stable voltage source. A drop of thermal paste is often applied to improve contact with the medium, and the system is left to stabilize before any readings are taken. Resistance values are recorded at several points that span the sensor's expected operating range, for instance, 0 °C, 25 °C, and 50 °C are common choices. Once collected, these data can be used in two ways: either by building a lookup table that directly links resistance to temperature or by recalculating the coefficients in equations such as the Steinhart–Hart relation or the simpler Beta parameter model. Tailoring these coefficients to the actual device improves the accuracy of temperature conversion significantly. In applications where high precision is essential, it is good practice to compare the thermistor's behavior against a calibrated reference sensor with traceable certification. Care should also be taken to avoid external influences like sunlight or unstable ambient conditions during calibration, as these can distort results. The outcome is usually a correction table or a set of updated coefficients that allow the thermistor to provide reliable and consistent temperature measurements in real operating conditions [190].

3.3.5 Pressure Sensor

The calibration of pressure sensors, such as SPKT0021C0 model used in this study, is a critical step to ensure the precision and repeatability of pressure measurements in both laboratory and industrial settings. The calibration procedure begins by supplying the sensor with the recommended excitation voltage and linking it to a high-accuracy multimeter or a calibrated data acquisition system to capture its electrical output.

Prior to the application of pressure, a zero-load reference is obtained through recording the sensor's response under ambient, no-load conditions. This zero point serves as a baseline for all subsequent readings. The sensor is then sequentially exposed to known pressure values, applied using a traceable and certified reference pressure source. The chosen calibration points are intended to capture the whole measurement range of the sensor. At each step, the output signal from the sensor is compared against the corresponding reference pressure. Any discrepancies are noted, indicating possible sensor drift, offset, or non-linearity. All calibration activities were conducted in certified laboratories equipped to meet international standards [261], [191].

3.4 Operating Conditions and Data Acquisition

There are several technical issues that are linked with experimental studies of refrigeration systems. At the first stage of the experiment, there were various operational challenges and equipment malfunctions when the experimental set up was being started. After performing a lot of troubleshooting and application of remedial actions the system was brought to a stable state of operation thus making the planned performance tests to be implemented. Several experimental situations were developed to have a better understanding of the behavior of the system.

Since the freezer under consideration is supposed to be used mainly in the fisheries industry, it was necessary to consider the environmental factors, namely, the temperature of seawater which serves as the cooling agent of the condenser.

The Mediterranean Sea is a semi-enclosed and warm basin, and its sea-surface temperature (SST) varies by about 10 °C per annum. It is generally warmer in its eastern parts as compared to the western parts. The SST is relatively cool in winter, with a range of 14-19 °C in southern regions during the period between December and March but reaches 24-30 °C in summer (June-September), especially in the eastern basin. The lowest month is usually in February (around 10 °C in the coldest areas), and July is the hottest (around 32 °C in the hottest ones). The average SST of the Mediterranean per year is approximately 21 °C [192].

The climate is moderate on the Black Sea with temperatures moderately cold during the winter and warm in summer days. In winter (December- February), SSTs range between approximately 7 °C in the northwest area and 13 °C in the sheltered southeast. Though the black sea hardly ever freezes (except in insular bays), there can be local freezes of up to 0 °C in February. During the summer (June–August), the surface temperatures vary between 21 °C and 27 °C, and the hottest (approximately 27-28 °C) along Turkish, Bulgarian, and Romanian coasts. The hottest month is usually July (maximum of about 31 °C), and the coldest is usually February (minimum of about 0 °C). The SST of the black sea is approximately 14 °C annually [193].

The North Sea is a shallow, temperate sea between Great Britain and Scandinavia, which has cold winters and mild summers. During winter (December-February), SSTs vary between near freezing 2 °C in the northeast (Skagerrak) and approximately 7 °C in the northwest, depending on the Atlantic current. The lowest temperatures are normally experienced during January-February when the SST may reach -1 °C in some regions along the coastline. In summer (June to August), the temperatures are 13-18 °C (with the highest temperature of approximately 18 °C in August) in the southern portion and lower in the north (12-14 °C). The warmest month is July (approximately 23 °C in shallow southern bays), and the mean SST of the North Sea is approximately 10 °C /year [194].

Taking these temperature characteristics into account, three experimental condenser-inlet water temperatures (10 °C, 15 °C, and 20 °C) were chosen to represent the situation of North Sea (approximately 10 °C annual mean) in Northern Europe, the Black Sea (approximately 15 °C) in Eastern Europe and the Mediterranean Sea (approximately 20 °C) in Southern Europe.

Moreover, the expansion valves had been driven at four opening ratios, i.e. 60, 70, 80, and 90 percent, to determine their effect on the stability and performance of the system.

There were also three target set-temperatures of the freezer compartment as per the international standards and reference values used in fisheries and food industries: -23 °C, -28 °C and -33 °C. Table 22 shows the entire matrix of the constructed experiments.

$T_{cw,in}$ (Sea Water Temperature)	Maximum Opening EEV	T_{set} (Set Temperature of Chamber)
°C	%	°C
20.00	60.00	-23.00
20.00	60.00	-28.00
20.00	60.00	-33.00
20.00	70.00	-23.00
20.00	70.00	-28.00
20.00	70.00	-33.00

15.00	70.00	-23.00
15.00	70.00	-28.00
15.00	70.00	-33.00
15.00	80.00	-23.00
15.00	80.00	-28.00
15.00	80.00	-33.00
15.00	90.00	-23.00
15.00	90.00	-28.00
15.00	90.00	-33.00
10.00	70.00	-23.00
10.00	70.00	-28.00
10.00	70.00	-33.00
10.00	80.00	-23.00
10.00	80.00	-28.00
10.00	80.00	-33.00
10.00	90.00	-23.00
10.00	90.00	-28.00
10.00	90.00	-33.00
20.00	60.00	-33.00
15.00	90.00	-33.00
10.00	80.00	-33.00

Table 22 Test Configuration

The experiments in this study are separated into four major groups, and a total of 27 separate tests are completed. The initial one is performed at a condenser temperature ($T_{cw,in}$) of 20 °C, the second one at 15 °C, and the third one at 10 °C. These preliminary tests are conducted without freezing a product (fish and other samples) to ascertain what operating conditions result in reduced energy usage.

Three further experiments are chosen after determining the most energy-efficient settings, i.e., with T_{CND} values of 10, 15, and 20 °C, the expansion valves are adjusted to their maximum opening values, and various target temperatures are selected. During such tests, the fish samples are put in the freezing chamber, and the respective analyses are conducted.

In the experimental part 1 ($T_{cw,in} = 20$ °C), the expansion valve maximum opening is set to 60 and 70 percent, and three target temperatures, -23, -28 and -33 °C are set in each case. It should be mentioned that Figure 58 shows that the refrigeration system and the storage chamber were arranged as follows during the tests.

The largest openings of the valves will be established at 70, 80 and 90 percent in the second group ($T_{CND} = 15\,°C$), and the three target temperatures will be -23, -28, and -33 °C. Likewise, in the third set ($T_{CND} = 10\,°C$), the valve apertures are adjusted to 70, 80 and 90 percent, and the target temperatures are the same as those in the two preceding sets.

The fourth category consists of the most appropriate operating conditions that have been found at each temperature of the condenser (in terms of energy consumption). During these tests, fish are put in the freezing chamber, and the thermal behavior of the product is examined. The specific findings and arguments that pertain to these analyses are explained in the subsequent chapters.

To conclude, the obtained data are gathered by the equipment that was described in the previous sections, and the following subsections convey a detailed description of the obtained results.

3.5 Data Processing and Key Performance Indicator

In this system, sensor instrumentation measures temperature and pressure which are taken to be independent variables at different points in the refrigeration cycle. The main thermodynamic parameters, the coefficient of performance (COP), the heat-transfer rate in the evaporator (Q_{evp}), mechanical work (W) and the variables are measured as to each experiment cycle. The first step is the definition of twenty-four different operating conditions of the system, from which the most efficient ones are selected based on energy consumption. Such cases (three experiments) are then tested and assessed against marine products like fish. The next chapter contains a description of the thermodynamic side of it and the experimental methods.

3.6 Uncertainty Evaluation

The experimental uncertainties of the calculated parameters (COP, cooling capacity) were determined according to the standard propagation of error methodology (Kline and McClintock / ISO GUM framework). The expanded uncertainty of the final calculated variables was obtained using the root-sum-square (RSS) method, combining the independent instrumental uncertainties of thermocouples, pressure transducers, and flow meters reported in Tables 18–21, and 24.

- **Relative Uncertainty of Suction Mass Flow Rate**

  The suction mass flow rate $\dot{m}_{suc}$ is an amount calculated based on the governing equations of the thermodynamic cycle (Section 3.7.2). It was never truly measured, so its experimental variability was statistically assessed throughout the identified steady-state window.

  The relative standard uncertainty is calculated as:

$$u_{rel}(\dot{m}_{suc}) = \frac{s(\dot{m}_{suc})}{\overline{\dot{m}_{suc}}} \times 100 \qquad \text{Eq. 1}$$

where:

- $\overline{\dot{m}_{suc}}$ is the mean value over the steady-state interval,
- $s(\dot{m}_{suc})$ is the experimental standard deviation.

This represents a Type-A statistical uncertainty and reflects short-term variability due to measurement noise and control modulation.

- **Uncertainty of Evaporator Enthalpy Difference (Δh_{evp}):**

The evaporator specific enthalpy difference is defined as:

$$\Delta h_{evp} = \frac{Q_{evp}.3600}{\dot{m}_{suc}} \qquad (kJ/kg) \qquad \text{Eq. 2}$$

The standard uncertainty was evaluated statistically as:

$$u(\Delta h_{evp}) = s\left(\frac{Q_{evp}.3600}{\dot{m}_{suc}}\right) \qquad \text{Eq. 3}$$

This uncertainty accounts for the combined variability of cooling capacity and suction mass flow rate within the steady-state window.

- **Uncertainty of Equivalent Specific Work (w_{eq})**

The equivalent specific compressor work was defined as:

$$w_{eq} = \frac{W.3600}{\dot{m}_{suc}} \qquad (kJ/kg) \qquad \text{Eq. 4}$$

The standard uncertainty was computed as:

$$u(w_{eq}) = s\left(\frac{W.3600}{\dot{m}_{suc}}\right) \qquad \text{Eq. 5}$$

As with Δh_{evp}, this represents Type-A statistical variability and reflects fluctuations in both electrical input power and calculated mass flow rate.

- **Type-B (instrument) uncertainty and combination with Type-A**

In addition to Type-A uncertainties estimated from fluctuations within the steady-state window, Type-B uncertainties associated with instrument accuracy were considered based on manufacturers'

specifications (Tables 17–21). For each measured variable x, the combined standard uncertainty was evaluated as:

$$u_c(x) = \sqrt{u_A(x)^2 + u_B(x)^2} \quad \text{Eq. 6}$$

The resulting combined uncertainties were then propagated to Q_{evp}, W, and COP using the ISO GUM law of propagation of uncertainty.

- **Propagation of Uncertainty to Q_{evp} and W**

According to the ISO GUM law of propagation of uncertainty:

$$u_c(y) = \sqrt{\sum \left(\frac{\partial y}{\partial x_i} u(x_i) \right)^2} \quad \text{Eq. 7}$$

Cooling capacity

$$Q_{evp} = \frac{\dot{m}_{suc} . \Delta h_{evp}}{3600} \quad \text{Eq. 8}$$

The propagated uncertainty becomes:

$$u(Q_{evp}) = \sqrt{\left(\frac{\Delta h_{evp}}{3600} u(\dot{m}_{suc}) \right)^2 + \left(\frac{\dot{m}_{suc}}{3600} u(\Delta h_{evp}) \right)^2} \quad \text{Eq. 9}$$

Compressor work:

$$W = \frac{\dot{m}_{suc} . w_{eq}}{3600} \quad \text{Eq. 10}$$

$$u(W) = \sqrt{\left(\frac{w_{eq}}{3600} u(\dot{m}_{suc}) \right)^2 + \left(\frac{\dot{m}_{suc}}{3600} u(w_{eq}) \right)^2} \quad \text{Eq. 11}$$

- **Uncertainty of COP**

The coefficient of performance is defined as:

$$COP = \frac{Q_{evp}}{W} \quad \text{Eq. 12}$$

$$u(COP) = COP.\sqrt{\left(\frac{u(Q_{evp})}{Q_{evp}}\right)^2 + \left(\frac{u(W)}{W}\right)^2} \quad \text{Eq. 13}$$

$$\frac{u(COP)}{COP} = \sqrt{\left(\frac{u(Q_{evp})}{Q_{evp}}\right)^2 + \left(\frac{u(W)}{W}\right)^2} \quad \text{Eq. 14}$$

Each performance indicator is reported as:

$$X = \overline{X} \pm u(X) \qquad k = 1 \quad \text{Eq. 15}$$

If expanded uncertainty is required at 95% confidence:

$$U = k.\,u(X) \qquad k = 2 \quad \text{Eq. 16}$$

The uncertainty analysis was applied to the three experimental cases using the ISO GUM law of propagation of uncertainty [195,196]. For each test, the steady-state window was identified; Type-A standard uncertainties were calculated from the experimental fluctuations, and Type-B contributions were assigned from the instruments' specifications summary (Tables 24). The combined uncertainties were then propagated to Q_{evp}, W, and COP (Table 23).

The data acquisition system recorded the main variables with a sampling interval of 3 s (Table 17). For KPI evaluation, the raw signals were additionally averaged over 30-s bins to reduce noise and to provide consistent statistics. The overall uncertainty of COP was primarily influenced by uncertainties in pressure measurement and refrigerant property calculation, while cooling capacity uncertainty was mainly affected by mass flow rate and temperature measurement errors.

There is variation in the steady-state window period of all three experimental situations (21 min, 16 min, and 74 min) because of variation in stabilization behavior in each operating condition. Each test is initiated by a brief pull-down period in the system as the temperature of the chamber is stabilized at the desired temperature of -33 °C. Currently there are observable changes in COP, compressor power, pressures, and mass flow rate, and hence this does not qualify as a steady-state process. Moreover, at low temperatures (-33 °C) shortly after the chamber is initially brought to that temperature, there can be intermittent on-off cycling of the compressor because of controller hysteresis; this is not representative of steady-state operation. This is why steady-state conditions are considered only when the chamber is stabilized at a temperature of -33 °C initially and the fish sample is added, when the thermodynamic variables have reached a narrow and stable range of values.

$T_{cw,in} = 10$ °C, Max Opening Expansion Valve = 80%, $T_{cell} = -33$ °C		$T_{cw,in} = 15$ °C, Max Opening Expansion Valve = 90%, $T_{cell} = -33$ °C		$T_{cw,in} = 20$ °C, Max Opening Expansion Valve = 60%, $T_{cell} = -33$ °C	
Steady-state window	42 points	Steady-state window	32 points	Steady-state window	148 points
Time	21 mins	Time	16 mins	Time	74 mins
COP_{mean}	1.20	COP_{mean}	1.17	COP_{mean}	1.14
u(COP)	0.107	u(COP)	0.114	u(COP)	0.111
Relative uncertainty of COP [%]	8.89	Relative uncertainty of COP [%]	9.80	Relative uncertainty of COP [%]	9.73
$COP = 1.20 \pm 0.11$		$COP = 1.17 \pm 0.11$		$COP = 1.14 \pm 0.11$	
W_{mean}	2.73	W_{mean}	3.37	W_{mean}	3.24
u(W)	0.212	u(W)	0.262	u(W)	0.231
Relative uncertainty of W [%]	7.78	Relative uncertainty of W [%]	7.79	Relative uncertainty of W [%]	7.15
$W = 2.73 \pm 0.21$		$W = 3.37 \pm 0.26$		$W = 3.24 \pm 0.23$	
$Q_{evp,mean}$	3.27	$Q_{evp,mean}$	3.93	$Q_{evp,mean}$	3.71
u (Q_{evp})	0.231	u (Q_{evp})	0.347	u (Q_{evp})	0.320
Relative uncertainty of Q_{evp} [%]	7.07	Relative uncertainty of Q_{evp} [%]	8.83	Relative uncertainty of Q_{evp} [%]	8.63
$Q_{evp} = 3.27 \pm 0.23$		$Q_{evp} = 3.93 \pm 0.35$		$Q_{evp} = 3.71 \pm 0.32$	

Table 23 Uncertainty Analysis Result for Three Experiments with Fish

This longer steady-state window of $T_{cw,in} = 20$ °C is also related to the more demanding operating condition since the condensing temperature is higher and the compressor loading is higher, so the compressor operates close to its maximum permissible operating conditions. Conversely, cases with 10 °C and 15 °C condenser inlet water temperatures are linked to milder operating conditions and higher stabilization rates, thus shorter but statistically significant steady-state periods.

Measured Variable	Sensor Type/ Model	Measurement Range	Instrumental Uncertainty
Temperature	T-type Thermocouple	-270 ℃ to $+$ 370 ℃	$\pm$1.0 ℃ or $\pm$ 0.75%
	NTC	-50 ℃ to $+$ 105 ℃ in Air	$\pm$1.0%
Pressure	Pressure Transducer	-0.5 to 7.0 bar	$\pm$1.0% FS
Volumetric Flow rate (Water)	Magnetic Flow meter	Up to 170 LPM	$\pm$2.5% m. v.
Electrical Power	Power Analyzer	1.0 to 20.0 MW	$\pm$1.5% $\pm$ 10 counts

Table 24 Instruments' Specifications Summary

3.7 Thermodynamic Calculations

3.7.1 Determination of Thermodynamic Points

Figure 63 is a simplistic diagram of the studied refrigeration cycle. The refrigerant used in the system is a zeotropic mixture of refrigerant R32 (26 %), R125 (26 %), R134a (21 %), and the hydrofluoroolefin compounds R1234yf (20 %) and R1234ze(E) (7 %) which is the refrigerant 448A colloquially referred to as N-40. R448A is also nonflammable, and its global warming potential is 1390 which makes it one of the popular low GW transitional alternatives to R404A (GWP 3922) [197].

Although more refrigerants with even lower GWP values are available, their implementation is limited by high costs and the need to make large-scale system alterations. Nowadays, many installations use R404A and this contributes to a significant amount of environmental concern due to its high GWP. Due to the thermophysical similarity of the refrigerants R448A and R404A, the former has an extremely low GWP and is thus considered technically and economically feasible as a replacement, specifically during the phase of changing to ultra-low-GWP refrigerants. Its wide availability, cost-effectiveness, and adaptability to retrofit applications further demonstrate its practical applicability.

In the analyzed cycle, the refrigerant passes through the compressor in state point (1) and exits it in a pressure and temperature state (2) that is higher. Then the heat is discharged to coolant (water) passing through the condenser. Points (3) and (4) are in inlet and outlet of condenser. After condensing, the flow of refrigerant is divided into two streams before entering the economizer, which is an equipment that aims at enhancing the efficacy of the cycle. One of the streams flows to the economizer at point (7), and the other flows through injection expansion valve at point (9). In the economizer, the two streams replace heat, with the former flowing to the main expansion valve at point (8) and the latter flowing after gaining heat, back into the compressor in form of vapor at point (10).

This pressure and temperature drop of the refrigerant going through the main expansion valve before it enters the evaporator at state point (5) and absorbs heat in the freezing chamber containing marine products at state point (6).

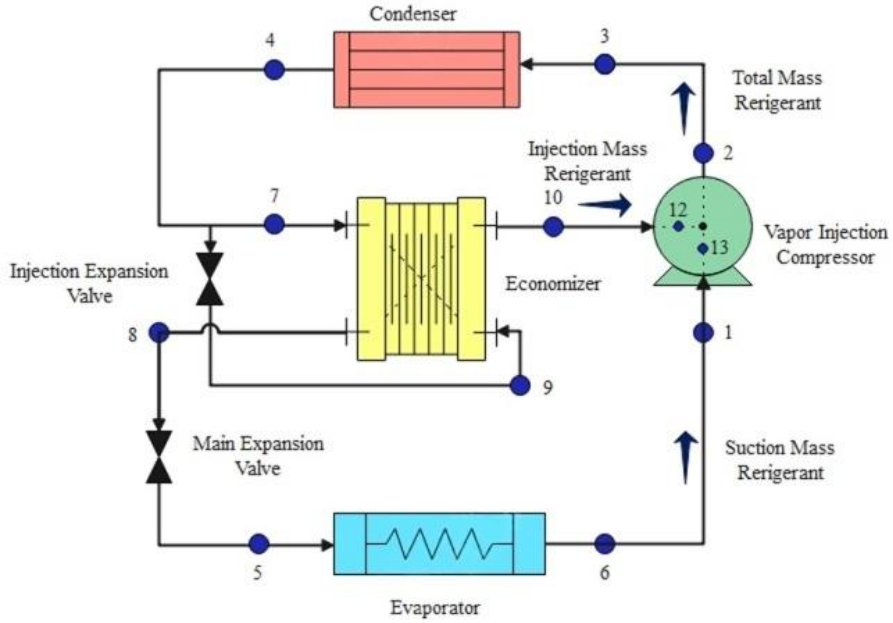

Figure 58 Simplified Schematic Diagram of the Vapor Injection Refrigeration System with Economizer

Considering that the compressor is operated in a vapor-injection regime, the additional state points (12) and (13) are added to determine the thermodynamic influence of the injected vapor. Besides, as the compression process is not ideal isentropic, the actual enthalpy along point (13) should be determined based on the isentropic efficiency of the compressor.

3.7.2 Governing Equations of the Thermodynamic Cycle

Equations (1-25) are the thermodynamic equations of the economizer as shown in Figure 59. A balance of energy on the economizer results in the mass-flow ratio ($\frac{\dot{m}_{inj}}{\dot{m}_{suc}}$) expressed in the enthalpies at the different state points. Based on this, COP and W are determined using the measured temperature and pressure measurements in the cycle (Equations 17-15).

$$Q_{main} = \dot{m}_{suc}(h_7 - h_8) \quad \text{Eq. 17} \qquad Q_{inj} = \dot{m}_{inj}(h_9 - h_{10}) \quad \text{Eq. 18}$$

$$\dot{m}_{suc}(h_7 - h_8) + \dot{m}_{inj}(h_9 - h_{10}) = 0 \quad \text{Eq. 19}$$

$$\frac{\dot{m}_{inj}}{\dot{m}_{suc}} = \frac{h_7 - h_8}{h_{10} - h_9} = \frac{h_7 - h_8}{h_{10} - h_4} \quad \text{Eq. 20}$$

$$\frac{\dot{m}_{inj}}{\dot{m}_{tot}} = \frac{h_7 - h_8}{h_7 - h_8 + h_{10} - h_4} \quad \text{Eq. 21}$$

$$\frac{\dot{m}_{suc}}{\dot{m}_{tot}} = \frac{h_{10} - h_4}{h_7 - h_8 + h_{10} - h_4} \quad \text{Eq. 22}$$

$$Q_{evp} = \dot{m}_{suc}(h_6 - h_5) \quad \text{Eq. 23} \qquad W = L_1 + L_2 \quad \text{Eq. 24}$$

$$L_1 = \dot{m}_{suc}(h_{13} - h_1) \quad \text{Eq. 25} \qquad L_2 = (\dot{m}_{suc} + \dot{m}_{inj})(h_2 - h_{12}) \quad \text{Eq. 26}$$

$$W = \dot{m}_{suc}(h_{13} - h_1 + h_2 - h_{12}) + \dot{m}_{inj}(h_2 - h_{12}) \quad \text{Eq. 27}$$

$$\dot{m}_{inj}h_9 + \dot{m}_{suc}h_{13} = \dot{m}_{tot}h_{12} \quad \text{Eq. 28}$$

$$h_{12} = \frac{(h_7 - h_8)h_9 + (h_{10} - h_4)h_{13}}{h_7 - h_8 + h_{10} - h_4} \quad \text{Eq. 29}$$

$$COP = \frac{Q_{evp}}{W} \quad \text{Eq. 30}$$

$$COP = \frac{h_6 - h_5}{(h_{13} - h_1 + h_2 - h_{12}) + \left(\frac{h_7 - h_8}{h_{10} - h_4}\right)\left(h_2 - \frac{(h_7 - h_8)h_9 + (h_{10} - h_4)h_{13}}{h_7 - h_8 + h_{10} - h_4}\right)} \quad \text{Eq. 31}$$

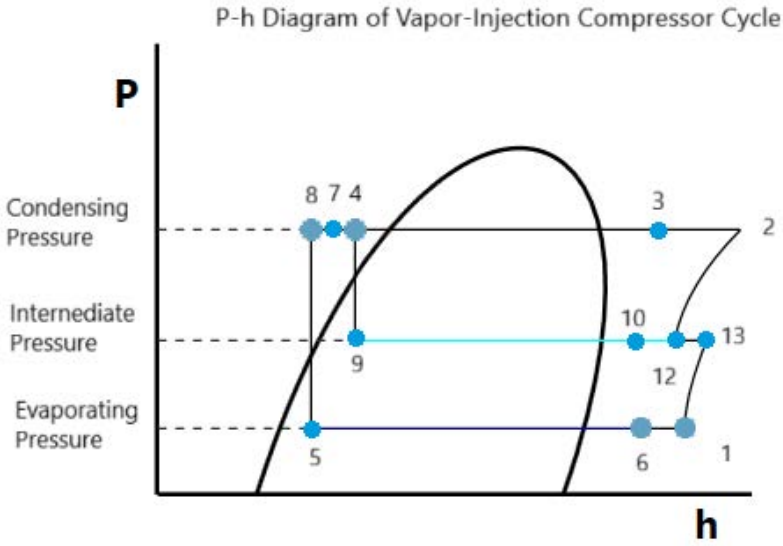

Figure 59 P–h Diagram of the Vapor Injection Refrigeration Cycle

It is necessary to mention that the enthalpies of point 8 and point 5 are not equal. Point 5 is in the two-phase with one of the most important variables being the quality of the vapor (x). If x = 1 at the evaporating pressure gives the temperature of the vapor at this pressure, and x = 0 at the same pressure gives the temperature of the saturated liquid. Based on this, h_5 can be obtained using the two-phase mixture thermodynamic relations (Equations 32-38).

Two Phase Mixture: $m_5 = m_{5,l} + m_{5,v}$ Eq. 32

Total Enthalpy of Mixture: $H_5 = m_{5,l}h_{5,l} + m_{5,v}h_{5,v}$ Eq. 33

$$X = \frac{m_{5,v}}{m_{5,v} + m_{5,l}}$$ Eq. 34

$$m_{5,v} = X(m_{5,v} + m_{5,l})$$ Eq. 35

$$m_{5,l} = (1 - X)(m_{5,v} + m_{5,l})$$ Eq. 36

$$h_5 = \frac{H_5}{m_5}$$ Eq. 37

$$h_5 = h_{5,l} + X(h_{5,v} - h_{5,l})$$ Eq. 38

Mechanical, thermal and entropy losses need to be taken into consideration in the compressor section, and therefore, the isentropic efficiency (η_{is}) is presented to indicate the same.

$$\eta_{is} = \frac{\text{Isentropic Work}}{\text{Real Work}}$$ Eq. 39

$$\eta_{is} = \frac{h_{13} - h_1}{h_{13,real} - h_1}$$ Eq. 40

$$h_{13,real} = h_1 + \frac{h_{13} - h_1}{\eta_{is}}$$ Eq. 41

Refrigerant R448A thermodynamic calculations were performed by Engineering Equation Solver (EES) software, version V10.561-3D. The isentropic efficiency of ZFD13KVE-TFD EVI compressor was calculated by examining various conditions of evaporating and condensing temperatures with help of Select 8 version 8.38.2.5260. Correlation analysis was complemented using Python 3.11.7 with the following results:

Linear Equation:

$$\eta_{is} = 106.947619 - 0.620333\ T_4 + 0.871714\ T_5$$ Eq. 42

Polynomial Equation:

$$\eta_{is} = 61.033333 + 0.851167\ T_4 - 0.442714\ T_5 - 0.011650\ T^2{}_4 - 0.009286\ T^2{}_5 + 0.020600\ T_4\ T_5$$ Eq. 43

Equations (42-43) results, which are summarized in Table 25, show that the highest R^2 is noted when the polynomial is used. This equation is taken up in thermodynamic computations and system performance analysis.

	R^2	RMSE (Root Mean Square Error)	MAE (Mean Absolute Error)
Linear	0.986024	0.628522	0.541481
Polynomial	0.999633	0.101897	0.074032

Table 25 Linear and Polynomial Equations for Isentropic Efficiency

Both linear and polynomial regressions were examined to describe the compressor isentropic efficiency based on the measured operating conditions. The polynomial relationship showed a slightly lower RMSE and a higher R^2 within the experimental range; therefore, it was selected as an empirical fit for the current dataset. It should be noted that this relationship is not proposed as a universal predictive model and must not be applied outside the experimental bounds considered in this work.

Chapter 4

Simulation and Modeling

4. Simulation and Modeling

4.1 Analysis of Thermal Fields in Bodies Using the FEM (Finite Element Method)

As described in previous chapters, among in methods of fish preservation and concludes that the best preservation process over several months up to a few years can be done using the freezing process in the industry. This requires accurate calculation of the temperature inside the frozen material because there are substantial heat transfer rates in this process. The use of finite element methods in freezing calculations has been highlighted in this section because such methods are quite versatile when modeling different shapes or scenarios in freezing.

4.1.1 Governing Equations Conduction Heat Transfer

The second law of thermodynamics demonstrates that heat will naturally move from hotter areas to cooler areas. The freezing process of fish products follows this principle because heat moves between the fish at its initial high temperature and the cold refrigerated environment which needs to be at lower temperatures for proper product preservation. The product core loses heat to its surface which experiences the fastest cooling because it touches the air stream from the air evaporator. The cooling process advances from the outside to the inside of the product while heat transfer moves in the opposite direction. The heat transfer process continues until the product reaches thermal equilibrium at temperatures that support long-term microbiological stability and preservation. The heat equation for thermal conduction in fish bodies requires a negative thermal gradient to model this phenomenon.

The freezing process is driven by temperature gradients that control the conductive heat transfer process in the first stage of freezing. The temperature (T) in a solid material with homogeneous and isotropic properties depends on the three-dimensional coordinates and the time variable and is described by the following equation.

$$T = T(x, y, z, t) \qquad \text{Eq. 44}$$

The body remains in steady state when the surfaces are fixed in shape and position. Transient-state conditions exist in the body when temperature differences cause surfaces' shape and position change. This has been explained with the help of the figure 60.

The system involves an isothermal surface with point P where the temperature in that region is denoted by t_1 with the area element dS passing via point P. The temperature in the other isothermal surface is t_2, denoting t_1 by a negligible amount. The distance dn in the normal direction from both surfaces always exists in point P. The rate of the transfer of dQ -amount of 'heat' through dS in $d\tau$-time τ defines the function (Eq. 45).

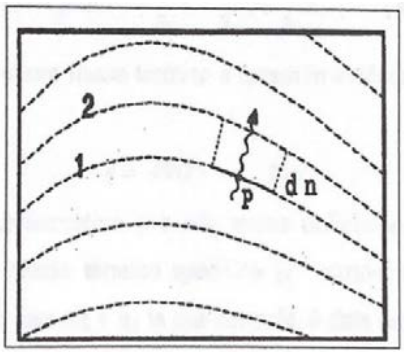

Figure 60 Conduction Through an Isothermal Surface Element in a Body

$$dQ = -\lambda\left(\frac{\partial t}{\partial n}\right) dS\, d\tau \qquad \text{Eq. 45}$$

This relation matches the Fourier equation, based upon experimental evidence. The λ in this equation symbolizes the thermal conductivity; this is a material-dependent quantity. The negative sign in this equation ensures that the rate of flow of heat across the infinitesimal surface area dS in the direction of the unit vector dn is positive if there's a decrease in temperature in that direction. The process of heat transfer is a vector quantity with direction perpendicular to the isothermal surfaces and from regions of higher temperature towards regions of lower temperature based upon the second law of thermodynamics. The heat flux can be defined by the following vector quantity, which being in the form of power is measured in units of watts (W):

$$dQ' = -\lambda\left(\frac{\partial t}{\partial n}\right) dS \qquad \text{Eq. 46}$$

$$dQ'' = -\lambda\left(\frac{\partial t}{\partial n}\right) \qquad \text{Specific Heat Flux } (^{W}/_{m^2}) \qquad \text{Eq. 47}$$

$$Q'' = -\lambda\vec{\nabla}T\vec{n} \qquad \text{Eq. 48}$$

The temperature gradient, represented by the vector $\vec{\nabla}T$, defines how temperature varies in the material across which the heat flow takes place. This vector is always normal to the isothermal surface that passes through the point in consideration and always pointed in the direction of increasing temperature. The temperature gradient can be obtained with the Operator (∇) acting on the temperature function T in the following way:

$$\nabla T = \text{grad}(T) = \left(\frac{\partial T}{\partial x}\right)\vec{\imath} + \left(\frac{\partial T}{\partial y}\right)\vec{\jmath} + \left(\frac{\partial T}{\partial z}\right)\vec{k} \qquad \text{Eq. 49}$$

The heat flux vector is highlighted by the equation 34:

$$\vec{q} = -\lambda\vec{\nabla}T \qquad \text{Eq. 50}$$

$$\vec{q} = -\lambda\text{grad}(T) = -\lambda \times \left(\left(\frac{\partial T}{\partial x}\right)\vec{\imath} + \left(\frac{\partial T}{\partial y}\right)\vec{\jmath} + \left(\frac{\partial T}{\partial z}\right)\vec{k}\right) \qquad \text{Eq. 51}$$

The heat flux vector defines a conservative vector field with temperature T being the potential function. The procedure here would be to consider an infinitely small cuboid piece of size dx, dy, dz, aligned with the Cartesian unit vector i, j, k. An analysis of the heat current through each of the faces with normals in the x-direction would start the process of formation of the equations of conduction (Equations 52-56).

$$d\phi_x = -k\frac{\partial T}{\partial x}.dy.dz \quad \text{Eq. 52}$$

$$d\phi_{(x+dx)} = -[\left(-k\frac{\partial T}{\partial x}\right) + \frac{\partial}{\partial x}\left(-k\frac{\partial T}{\partial x}\right).dx].dy.dz \quad \text{Eq. 53}$$

$$d\phi_x + d\phi_{(x+dx)} = \frac{\partial}{\partial x}\left(k\frac{\partial T}{\partial x}\right).dx.dy.dz \quad \text{Eq. 54}$$

And:

$$d\phi_y + d\phi_{(y+dy)} = \frac{\partial}{\partial y}\left(k\frac{\partial T}{\partial y}\right).dx.dy.dz \quad \text{Eq. 55}$$

$$d\phi_z + d\phi_{(z+dz)} = \frac{\partial}{\partial z}\left(k\frac{\partial T}{\partial z}\right).dx.dy.dz \quad \text{Eq. 56}$$

The first law of thermodynamics shows that dq' represents the rate at which internal energy changes.

$$d\phi = dq' = c\,\rho\,dv\left(\frac{\partial T}{\partial t}\right) \quad \text{Eq. 57}$$

where c denotes the specific heat and ρ the density. With suitable simplifications, this expression can be reduced to the standard heat-conduction equation in Cartesian coordinates:

$$\left[\frac{\partial}{\partial x}\left(k\frac{\partial T}{\partial x}\right) + \frac{\partial}{\partial y}\left(k\frac{\partial T}{\partial y}\right) + \frac{\partial}{\partial z}\left(k\frac{\partial T}{\partial z}\right)\right] = c\,\rho\left(\frac{\partial T}{\partial t}\right) \quad \text{Eq. 58}$$

In cylindrical coordinate system:

$$\left[\frac{k}{r}\frac{\partial T}{\partial r} + \frac{\partial}{\partial r}\left(k\frac{\partial T}{\partial r}\right)\right] + \left[\frac{1}{r^2}\frac{\partial T}{\partial \theta}\left(k\frac{\partial T}{\partial \theta}\right)\right] + \left[\frac{\partial}{\partial z}\left(k\frac{\partial T}{\partial z}\right)\right] = c\,\rho\left(\frac{\partial T}{\partial t}\right) \quad \text{Eq. 59}$$

And in spherical coordinate system:

$$\left[\frac{1}{r^2}\frac{\partial}{\partial r}\left(r^2\frac{\partial T}{\partial r}\right)\right] + \left[\frac{1}{r^2\sin(\theta)}\frac{\partial T}{\partial \theta}\left(\sin(\theta)\frac{\partial T}{\partial \theta}\right)\right] + \left[\frac{1}{r^2\sin(\theta)}\left(\frac{\partial^2 T}{\partial \psi^2}\right)\right] = c\,\frac{\rho}{k}\left(\frac{\partial T}{\partial t}\right) \quad \text{Eq. 60}$$

These differential equations provide the core framework for numerical methods that model how heat moves inside solid bodies [198].

4.1.2 The Finite Element Method (FEM)

Finite Element Method (FEM) relies on the process of subdividing an intricate system into many simpler elements. This process involves the use of algebraic equations that are derived from mathematical formulations and experiments. FEM provides the capability to analyze complex behaviors that are difficult to analyze by subdividing difficult problems into manageable subsystems and, if necessary, into smaller units. Then, the response of the entire system is calculated based on the responses of the individual elements. The widespread use of FEM as a tool for solving various problems has been mainly promoted by achievements in computation, as FEM involves considerable numerical calculations. After the definition of the geometry and material characteristics, FEM can pursue the whole analysis and, automatically, deal with the nonlinearity by means of iterative computation. In short, FEM offers an efficient tool for the numerical simulation of heat transfer and various other physical processes for domains of any shape and complexity.

In FEM, the continuous body is idealized as having a finite number of small sub volumes, called finite elements, intersecting at certain boundary points called nodes. In the case where the total volume V of the body is divided into sub volumes, there are three important characteristics satisfied by each sub volume

1. The physical properties such as temperature, conductivity, density, and heat capacity, and others, are assumed to satisfy the values prescribed for the representative point P inside the sub volume.

2. Its boundaries either lie on the outer boundary of the body (labeled as A_i) or it is common to the adjacent component (labeled as A_{ij}).

3. In the case of two adjacent elements, the line joining the representative points P_i and P_j must be perpendicular to the common surface, A_{ij}.

At last, the heat flux (Q'') through the oriented surface element dA, whose normal vector is n_A, can be expressed as the projection of the heat flux vector $\vec{q}$ onto the vector $\vec{n}_A$.

$$d\phi = dq' = -\lambda\left(\frac{\partial T}{\partial n_A}\right) dA \qquad \text{Eq. 61}$$

$$d\phi = Q'' dS = Q' \qquad \text{Eq. 62}$$

For the above equation, the following discussion will show the heat flow $d\phi$ through surfaces of varying orientation as the system has been divided into elements. In the body C, there is an internal finite element volume V, which gets enclosed by the surface area A. The heat flux equation becomes integrable using the oriented surface elements, which are directed inside the element (Equation 47).

$$q' = -\oint_A \lambda\left(\frac{\partial T}{\partial n_A}\right) dA \qquad \text{Eq. 63}$$

The internal energy of the element varies with time, expressed as the equation above.

$$\left(\frac{dU}{dt}\right) = \oint_V C\left(\frac{\partial T}{\partial t}\right) dV \qquad \text{Eq. 64}$$

If $C = c\,\rho$ then:

$$-\oint_A \lambda\left(\frac{\partial T}{\partial n_A}\right) dA = \oint_V c\,\rho\left(\frac{\partial T}{\partial t}\right) dV \qquad \text{Eq. 65}$$

The resulting equation can be applied to a body that has been divided into a finite number of elements. However, it is also necessary to account for how thermal conductivity behaves. Because conductivity depends on temperature, we usually assume it varies linearly between two points, P_i and P_j, moving along the direction n_{ij}.

$$k_{ij} = \frac{k\left[t_i\left(n_{ij} - m_{ij}\right) + t_j m_{ij}\right]}{n_{ij}} \qquad \forall_j \in F_i \qquad \text{Eq. 66}$$

Based on the last assumption, the above relationship can now be written for an internal element V_i of the body as follows:

$$-\sum_{j \in F_i} k_{ij} \frac{T_i - T_j}{n_{ij}} A_{ij} = C_i V_i \frac{dT_i}{dt} \qquad \text{Eq. 67}$$

$$K_{ij} = k_{ij} \frac{A_{ij}}{n_{ij}} \qquad \text{Eq. 68}$$

$$T_i\left(-\sum_{j \in F_i} K_{ij}\right) + \left(\sum_{j \in F_i} K_{ij} T_j\right) = C_i V_i \frac{dT_i}{dt} \qquad \text{Eq. 69}$$

Focusing the equation on the internal elements only ($A_i = 0$) and introducing the following definitions:

$$K_{ii} = -\sum_{j \in F_i} K_{ij} \quad \text{Eq. 70}$$

$$W_i = C_i V_i \quad \text{Eq. 71}$$

V_i in matrix form:

$$[K]\left[\vec{T}\right] = [W]\left[\vec{T}\right] \quad \text{Eq. 72}$$

In this formulation, $[K]$ represents the thermal conductivity matrix, $\left[\vec{T}\right]$ is the vector of the time derivatives of the degrees of freedom; which, in a thermal analysis, corresponds to temperatures; and $[W]$ is the thermal mass matrix. This last aspect deserves particular attention because it is essential for understanding the approach described so far.

$$C = c\,\rho \quad \text{Eq. 73}$$

where r represents the density of the i-th sub volume, expressed in kg/m^3, while c indicates the specific heat, expressed in $J/kg.K$. The product of these two terms represents the volumetric heat capacity in $J/m^3.K$. In thermal analysis based on the finite element method, it is assumed that this thermal capacity is concentrated at the nodes rather than distributed throughout the domain. This assumption leads to the formulation of a diagonal thermal mass matrix, which has important computational advantages: on the one hand, it simplifies numerical calculations; on the other, it results in greater stability of the resulting linear system, with obvious benefits in terms of simulation efficiency and robustness [199].

4.1.3 Boundary Conditions

Boundary conditions for every volumetric mesh point outside the domain must be specified. The possible conditions for the boundaries may be convection conditions, specification of the heat flux, thermally insulated boundaries, or temperature specifications at certain points. Below comes the analysis of the mentioned conditions:

Convection: This represents a process of transferring heat through a fluid. This process is governed by Newton's law of convection. According to Newton's law of convection, the rate of convective transfer of heat is proportional to the temperature difference between the solid surface and the fluid. This can be written mathematically:

$$q' = hA(T_S - T_\infty) \quad \text{Eq. 74}$$

Which is: h is heat transfer coefficient, W/m^2K; A heat exchange surface between the fluid and the wall, m^2; T_S temperature of the solid surface, K; and T_∞ temperature of the undisturbed fluid, K. For a general boundary element:

$$q_i' = h_i A_i (T_{si} - T_{\infty i}) \quad \text{Eq. 75}$$

Applying the first law of thermodynamics to the differential volume element V_i and the heat transfer over its surface:

$$h_i A_i (T_{si} - T_{\infty i}) + T_i \left(-\sum_{j \epsilon F_i} K_{ij} \right) + \left(\sum_{j \epsilon F_i} K_{ij} T_j \right) = C_i V_i \frac{dT_i}{dt} \quad \text{Eq. 76}$$

setting $H_i = -h_i A_i$ and $B_i = h_i A_i T_{\infty i}$, respectively the proportional contribution to the amount of heat entering or leaving the i-th node and the external thermal contribution associated with the i-th node, the above equation can be rewritten in the following form:

$$T_i (K_{ii} + H_i) + \left(\sum_{j \epsilon F_i} K_{ij} T_j \right) + B_i = C_i V_i \dot{T}_i \quad \text{Eq. 77}$$

Specific Heat Flux: The energy equation needs to be modified when heat flux appears as a boundary condition. This calls for a modification of the energy equation to account for the true surface involved in heat transfer. To this end, the boundary parameter needs to be included in the modified energy equation because this parameter signifies the boundary surface Ai between the globe volume and the environment. This parameter allows for heat transfer due to environmental fluid convection as well as extra heat sources. In FEM methods, this adjustment leads to a stiffness matrix augmentation represented by a new matrix denoted as H. This H matrix describes the effect of convective forces on boundary nodes. The effect of convection for each boundary node is considered uniquely. Therefore, this adjustment leads to a stiffness matrix expressed as a diagonal denoted as H. The heat-transfer matrix is thus generated with a combination of conduction and convection heat transfer coefficients, along with a boundary load vector.

Boundary heat-flux condition:

$$B_i = A_i (T_i T_{\infty i} + q_i'') \quad \text{Eq. 78}$$

Finite-Element Equation Including Convection:

$$(K + H)\vec{T} + \vec{B} = W\vec{T} \quad \text{Eq. 79}$$

Diagonal form of convective matrix:

$$H_{ij} = H_i\delta_{ij} \quad \text{Eq. 80}$$

Kronecker delta definition:

$$\delta_{ij} = \begin{cases} 0 & i \neq j \\ 1 & i = j \end{cases} \quad \text{Eq. 81}$$

Thermally Insulated Boundary: A thermally insulated boundary does not allow heat flow through its surface. The calculation of heat flux on the boundary surface gives a result of zero for a typical heat flux to the boundary. For a finite-element solution to a convection problem, when the boundary heat transfer coefficient tends to zero, the effects of convection are removed from the solution. The boundary heat transfer coefficient has no effect on the resulting global equation because its components are zero. This means that the problem becomes more amenable to analysis because convection and other heat sources are no longer affecting this boundary.

Zero-flux condition:

$$q_i'' = 0 \quad \text{Eq. 82}$$

Resulting boundary coefficients:

$$H_i = B_i = 0 \quad \text{Eq. 83}$$

Reduced matrix equation:

$$K\vec{T} = W\vec{T} \quad \text{Eq. 84}$$

In the thermal simulation process, some nodes are required to keep a constant temperature a priori. Nodes in group G_G maintain a specified temperature T_{jG}. The equations require the explicit inclusion of such specified temperatures represented by nodes with fixed values. Accordingly, for a free node i, two types of terms are introduced based on neighbouring nodes with fixed temperatures and temperatures with unknown values. A vector D_{iG} represents additional components that are later added to a vector of loads. The substitution process redescribes the problem system in a single variable form represented by a matrix equation that merges conduction and convection effects with boundary conditions (Equations 85-89).

T_{jG}: imposed temperature at node $j \in G_G$

K_{ij}: conductive stiffness coefficient

H_i: convective contribution at node i

B_i: boundary heat-load term

D_{iG}: additional known contribution from prescribed-temperature neighbors

C_iV_i: heat capacity of control volume i

W: matrix associated with transient terms

$$T_j = T_{jG} = \text{Constant} \quad \text{Eq. 85}$$

$$T_i(K_{ii} + H_i) + \left(\sum_{j\epsilon F_i} K_{ij}T_j\right) + B_i = C_iV_i\dot{T}_i \quad \text{Eq. 86}$$

$$T_i(K_{ii} + H_i) + \left(\sum_{j\epsilon F_i - F_{iG}} K_{ij}T_j\right) + \left(\sum_{j\epsilon F_{iG}} K_{ij}T_{jG}\right) + B_i = C_iV_i\dot{T}_i \quad \text{Eq. 87}$$

$$D_{iG} = \left(\sum_{j\epsilon F_{iG}} K_{ij}T_{jG}\right) \quad \text{Eq. 88}$$

$$\vec{D}_G = D_{iG(i\epsilon 1 - G_G)} \quad \text{Eq. 89}$$

Obtain the following matrix form:

$$(K + H)\vec{T} + \vec{B} + \overrightarrow{D_G} = W\vec{T} \quad \text{Eq. 90}$$

$$X\vec{T} + \vec{E} = W\vec{T} \qquad X = (K + H) \text{ and } \vec{E} = \vec{B} + \overrightarrow{D_G} \quad \text{Eq. 91}$$

The first principle takes a compact form achieved through Dirichlet boundary conditions. In this scenario, quantities such as $\vec{T}$ and the matrices X and W vary with time and temperature. This physical system has elements with temperatures dependent on specific heat and density parameters aside from a column vector of $\vec{E}$. This physical system exhibits first-order equations expressing unknown variables such as $T_1(t)$, $T_1(t)$, and $T_p(t)$. Owing to their complex nature, solving such equations becomes extremely cumbersome. As such, researchers pick specific values for time variables along with temperatures for ease of calculation. In this current model, discretization of time variables occurs.

The time ΔT allows formation of a temperature vector $T^{[i]}$, which comprises all temperatures recorded at time instant $i\Delta T$. A matrix form emerges based on the explanation, where the use of T' as a substitute for values of the ratio with increments results in a governing equation expressed as:

$$X^{[i]}\overline{T}^{[i]} + \overline{E}^{[i]} = W^{[i]}\left(\frac{\overline{T}^{[i+1]} - \overline{T}^{[i]}}{\Delta T}\right) \quad \text{Eq. 92}$$

Solving the equation for $\overline{T}^{[i+1]}$,

$$\overline{T}^{[i+1]} = \overline{T}^{[i]} + W^{-1}\left(X\overline{T}^{[i]} + \overline{E}\right)\Delta T \qquad \text{Eq. 93}$$

This equation may be solved once a specification of initial temperatures has been made, this being a condition naturally satisfied as a beginning state of a constant temperature has been assumed for the body. As the initial form of the W matrix has been assumed to be invertible with a diagonal form for its inverse, one of the equations for p may be specified:

$$T_s^{[i+1]} = T_s^{[i]} + \Delta T\left[\left[\sum_{j=1}^{p}\left[\sum_{r=1}^{p} W_{rs}^{-1}X_{rj}\right]T_j^{[i]}\right] + \left[\sum_{j=1}^{p} W_{rs}^{-1}E_j\right]\right] \qquad \text{Eq. 94}$$

But $W_{sj}^{-1} = 0$ for $i = j$, and since the matrix W^{-1} is diagonal:

$$T_s^{[i+1]} = T_s^{[i]} + \Delta T\left[\left[\sum_{j=1}^{p}(W_{ss}^{-1}X_{sj})\,T_j^{[i]}\right] + W_{ss}^{-1}E_s\right] \qquad \text{Eq. 95}$$

$$T_s^{[i+1]} = T_s^{[i]}(1 + \Delta T W_{ss}^{-1}X_{ss}) + \Delta T\left[\left[\sum_{j=1,2,3,\ldots,s-1,s+1}^{p}(W_{ss}^{-1}X_{sj})T_j^{[i]}\right] + W_{ss}^{-1}E_s\right] \qquad \text{Eq. 96}$$

It is also necessary to enforce a condition that makes sure the process does not violate the second law of thermodynamics.

$$0 \leq (1 + \Delta T W_{ss}^{-1}X_{ss}) < 1 \qquad \text{Eq. 97}$$

In other words, the coefficient of $T_s^{[i]}$ must never take on negative values.

4.2 Calculating the Physical Properties of Food

4.2.1 Preliminary Considerations

Before the FEM simulation of the freezing process is performed, it is necessary to know the thermophysical properties of the fish. This is a crucial step because the process of freezing is a transient process that depends upon the temperature and the flow of time. The needed thermophysical properties include density, specific heat capacity, and thermal conductivity, and they are taken from the empirical

and semiempirical equations of ASHRAE. The composition of the fish and the temperature where ice starts to form are needed in the equations, and for this work, the values for the Atlantic mackerel fish are used [200], [201].

The composition according to ASHRAE is fixed at the following levels: 63.55% water, 18.6% protein, 13.89% fat, 0% carbohydrates, 0% fiber, 1.35.

The simulations will be conducted using ANSYS 2025 R2, a reliable platform for detailed thermal analyses. The application of ANSYS will facilitate the determination of the temperature distributions of the product at any instant in the freezing process. Another factor to consider is the proportion of water that has frozen at a certain temperature. To calculate this, the study employs the following relation put forward by Tchigeov (1979), a commonly referenced form by the ASHRAE organization:

$$x_{ice} = \frac{1.105 x_{wo}}{1 + \frac{0.7138}{\ln(t_f - t + 1)}} \quad \text{Eq. 98}$$

Where x_{wo} is the proportion of unfrozen water, t_f is the initial freezing point, and t is the fish temperature. The equation for unfrozen water is given by:

$$x_w = x_{wo} - x_{ice} \quad \text{Eq. 99}$$

4.2.2 Density

In calculating the density of the Atlantic mackerel, equations 100 through 103 are combined with the known composition values: water, protein, fat, and ash content.

$$\rho_w = 9.9718 \times 10^2 + 3.1439 \times 10^{-3} t - 3.7574 \times 10^{-3} t^2 \quad \text{Eq. 100}$$

$$\rho_p = 1.3299 \times 10^3 - 5.1840 \times 10^{-1} t \quad \text{Eq. 101}$$

$$\rho_f = 9.2559 \times 10^2 - 4.1757 \times 10^{-1} t \quad \text{Eq. 102}$$

$$\rho_a = 2.4238 \times 10^3 - 2.8063 \times 10^{-1} t \quad \text{Eq. 103}$$

At a temperature where values are less than −2.2 °C, a point where freezing begins to occur, it becomes necessary to calculate the following additional values:

bound water fraction (Eq. 104),

$$x_b = 0.4 x_p \quad \text{Eq. 104}$$

the amount of freezable water (Eq. 105),

$$x_{w,freezable} = x_{wo} - x_b \quad \text{Eq. 105}$$

the fraction of solids (Eq. 106),

$$x_s = 1 - x_{wo} \quad \text{Eq. 106}$$

relative molecular mass of the soluble solids (Eq. 107),

$$M_s = \frac{x_s R T_0^2}{-(x_{wo} - x_b) L_0 t_f} \quad \text{Eq. 107}$$

the fraction of ice formed (Eq. 108),

$$x_{ice} = \frac{x_s R T_0^2 (t_f - t)}{M_s L_0 t_f t} \quad \text{Eq. 108}$$

the amount of remaining liquid water (Eq. 109),

$$x_{w,liq} = x_{wo} - x_{ice} \quad \text{Eq. 109}$$

and the ice density (Eq. 110).

$$\rho_{ice} = 9.1689 \times 10^2 - 1.3071 \times 10^{-1} t \quad \text{Eq. 110}$$

R as universal gas constant is 8.314 $kJ/kg.mol.K$, t_f as Mackerel fish initial freezing point is -2.2 °C, T_0 as freezing point of water is 273.2 K, and L_0 as latent heat of fusion of water at 273.2 K is 333.6 kJ/kg.

Using the above parameters, the density of the fish species has been computed to be within the temperatures of −2.2 to −30 °C. The values have been shown below and then input into ANSYS 2025R2 to produce figure 61.

T (°C)	Density (kg/m^3)	T (°C)	Density (kg/m^3)	T (°C)	Density (kg/m^3)	T (°C)	Density (kg/m^3)
-30	981.42	-15	982.38	0	1026.5	15	1018.9
-29	981.36	-14	982.73	1	1026	16	1018.4
-28	981.31	-13	983.17	2	1025.5	17	1017.9
-27	981.27	-12	983.72	3	1025	18	1017.4
-26	981.25	-11	984.4	4	1024.5	19	1016.9
-25	981.24	-10	985.26	5	1024	20	1016.4
-24	981.24	-9	986.36	6	1023.5	21	1015.9
-23	981.25	-8	987.79	7	1022.9	22	1015.4
-22	981.29	-7	989.68	8	1022.4	23	1014.9
-21	981.35	-6	992.29	9	1021.9	24	1014.3
-20	981.43	-5	996.05	10	1021.4	25	1013.8
-19	981.54	-4	1001.8	11	1020.9		

-18	981.68	-3	1011.8	12	1020.4
-17	981.86	-2	1026.5	13	1019.9
-16	982.09	-1	1026.5	14	1019.4

Table 26 Fish Density in (-30 ≤ T ≤ 25 °C)

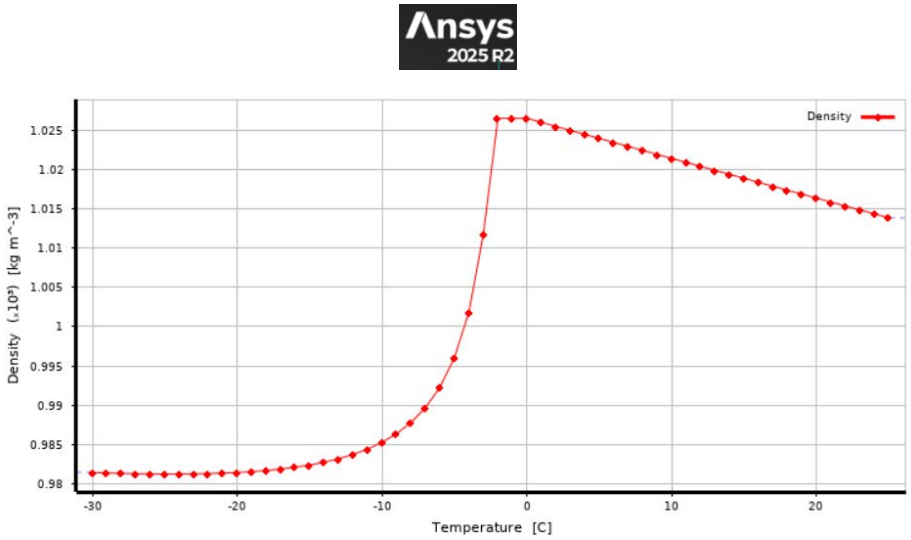

Figure 61 Density–Temperature Relationship in Mackerel Fish

4.2.3 Specific Heat

The specific heat capacity measures the amount of energy needed to increase the temperature of a food product by a degree in Celsius. For this reason, it is an important factor in calculating the heat load that a refrigeration system must handle in the process of cooling or freezing the food product. Several ASHRAE guidelines and several empirical and semi-empirical formulas ranging from -30 to +25 °C provide a basis for the determination of the factor in question.

The Mackarel fish involved in the current investigation consists of water, proteins, fat, ash, and, at sufficiently low temperatures, ice. The heat capacity function of water from 0 to -40 °C is determined through equation 111, while for temperatures ranging from 0 to 150 °C, the function is derived through equation 112.

$$c_w = 4.1289 - 5.3062 \times 10^{-3}t + 9.9516 \times 10^{-4}t^2 \quad \text{Eq. 111}$$

$$c_w = 4.1289 - 9.0864 \times 10^{-5}t + 5.4731 \times 10^{-6}t^2 \quad \text{Eq. 112}$$

Below -2.2 °C, the process of freezing starts, and a certain amount of water turns to ice, requiring the use of equation 113. For temperatures above -2.2 °C, the fish components are derived through equations 113-116.

$$c_{ice} = 2.0623 + 6.0769 \times 10^{-3}t \quad \text{Eq. 113}$$

$$c_p = 2.0082 + 1.2089 \times 10^{-3}t - 1.3129 \times 10^{-6}t^2 \quad \text{Eq. 114}$$

$$c_f = 1.9842 + 1.4733 \times 10^{-3}t - 4.8008 \times 10^{-6}t^2 \quad \text{Eq. 115}$$

$$c_a = 1.0926 + 1.8896 \times 10^{-3}t - 3.6817 \times 10^{-6}t^2 \quad \text{Eq. 116}$$

Further, for temperatures lower than freezing, the following expressions involving equation 117 can be used to determine the value of effective heat capacity:

$$c_a = c_f + (x_{wo} - x_b)\left[\frac{L_0(T_0 - t_f)}{(T_0 - t)^2}\right] \quad -2.2 \leq t \leq -30 \quad \text{Eq. 117}$$

The results obtained are presented in Table 25. In addition, these data were supplied as Engineering Data in Ansys 2025R2, producing the output shown in Figure 62.

T (°C)	Specific Heat (J/kg. °C)	T (°C)	Specific Heat (kJ/kg. °C)	T (°C)	Specific Heat (kJ/kg. °C)	T (°C)	Specific Heat (kJ/kg. °C)
-30	2738.2	-15	4262.9	0	3444.8	15	3453.9
-29	2773.9	-14	4563.7	1	3448.1	16	3454.3
-28	2813.4	-13	4936.6	2	3448.5	17	3454.8
-27	2857.4	-12	5406.4	3	3448.9	18	3455.3
-26	2906.6	-11	6010.2	4	3449.3	19	3455.7
-25	2961.9	-10	6804.1	5	3449.7	20	3456.2
-24	3024.1	-9	7877	6	3450.1	21	3456.7
-23	3094.7	-8	9377	7	3450.5	22	3457.2
-22	3175.1	-7	11565	8	3450.9	23	3457.7
-21	3267.2	-6	14936	9	3451.3	24	3458.2
-20	3373.5	-5	20526	10	3451.7	25	3458.7
-19	3497.1	-4	30818	11	3452.1		
-18	3641.8	-3	53053	12	3452.6		
-17	3812.7	-2	3451.2	13	3453		
-16	4016.7	-1	3447.3	14	3453.4		

Table 27 Fish Specific Heat in (-30 ≤ T ≤ 25 °C)

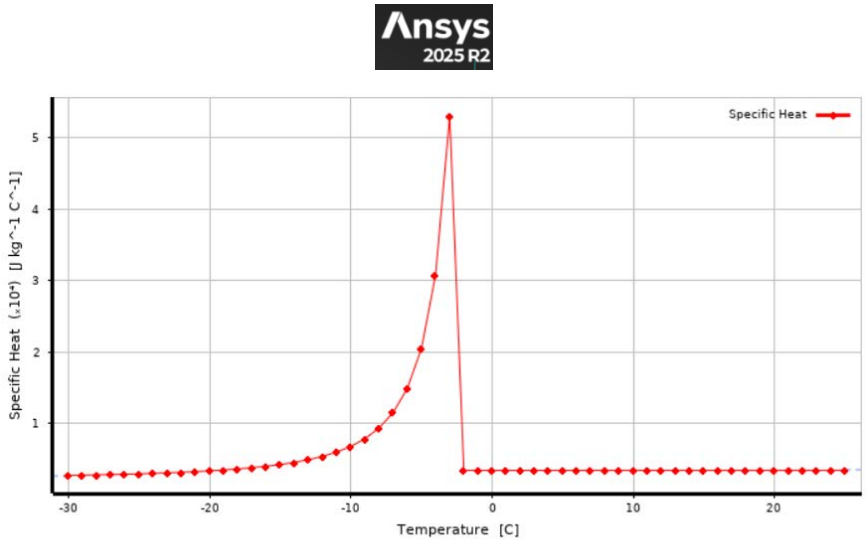

Figure 62 Specific Heat–Temperature Relationship in Mackerel Fish

4.2.4 Thermal Conductivity

Since fish tissue comprises various components that differ in their thermal response, each constituent requires individual consideration in the analysis. Since the thermal behavior of fish tissue depends on its complex structure and on the phase, changes occurring within its constituents, the model must account for all components present in the tissue. The first components include water, protein, fat, ash, and ice, whose proportions need to be established. At temperatures above -2.2 °C, the proportions are estimated by Equations 118-122, while at temperatures below -2.2°C, the unfrozen water and ice fraction are estimated by Equations 109 and 123.

$$x_w = \frac{\frac{x_w}{\rho_w}}{\left(\frac{x_w}{\rho_w}\right) + \left(\frac{x_p}{\rho_p}\right) + \left(\frac{x_f}{\rho_f}\right) + \left(\frac{x_a}{\rho_a}\right)} \quad \text{Eq. 118}$$

$$x_p = \frac{\frac{x_p}{\rho_p}}{\left(\frac{x_w}{\rho_w}\right) + \left(\frac{x_p}{\rho_p}\right) + \left(\frac{x_f}{\rho_f}\right) + \left(\frac{x_a}{\rho_a}\right)} \quad \text{Eq. 119}$$

$$x_f = \frac{\frac{x_f}{\rho_f}}{\left(\frac{x_w}{\rho_w}\right) + \left(\frac{x_p}{\rho_p}\right) + \left(\frac{x_f}{\rho_f}\right) + \left(\frac{x_a}{\rho_a}\right)} \quad \text{Eq. 120}$$

$$x_a = \frac{\frac{x_a}{\rho_a}}{\left(\frac{x_w}{\rho_w}\right) + \left(\frac{x_p}{\rho_p}\right) + \left(\frac{x_f}{\rho_f}\right) + \left(\frac{x_a}{\rho_a}\right)} \quad \text{Eq. 121}$$

$$x_{ice} = (x_{wo} - 0.4x_p)\left(1 - \frac{t_f}{t}\right) \quad \text{Eq. 122}$$

Based on the ASHRAE guideline and Equations 123 through 127, the values of thermal conductivity for each component (water, protein, fat, ash, and ice) will be determined. At the same time, equations from 100-103 and 110 give the density of each component in terms of temperature, and the total density is given by equation 128.

$$k_w = 5.7109 \times 10^{-1} + 1.7625 \times 10^{-3}t - 6.7036 \times 10^{-6}t^2 \quad \text{Eq. 123}$$

$$k_{ice} = 2.2196 - 6.2489 \times 10^{-3}t + 1.0154 \times 10^{-4}t^2 \quad \text{Eq. 124}$$

$$k_p = 1.7881 \times 10^{-1} + 1.1958 \times 10^{-3}t - 2.7178 \times 10^{-6}t^2 \quad \text{Eq. 125}$$

$$k_f = 1.8071 \times 10^{-1} - 2.7604 \times 10^{-4}t - 1.7749 \times 10^{-7}t^2 \quad \text{Eq. 126}$$

$$k_a = 3.2962 \times 10^{-1} + 1.4011 \times 10^{-3}t - 2.9069 \times 10^{-6}t^2 \quad \text{Eq. 127}$$

$$\rho = \frac{1 - \varepsilon}{\sum \frac{x_i}{\rho_i}} \quad \text{Eq. 128}$$

Several investigators have suggested using parallel and perpendicular (series) models to estimate the effective thermal conductivity of food materials, drawing on their analogy to electrical resistance networks (Murakami & Okos, 1989). The parallel model calculation involves adding the respective conductivity values of the components based on their volume fractions:

$$k_{\parallel} = \sum x_i^{\upsilon} k_i \quad \text{Eq. 129}$$

where x_i^{υ} is the volume fraction of component i, given by the following equation:

$$x_i^{\upsilon} = \frac{\frac{x_i}{\rho_i}}{\sum \frac{x_i}{\rho_i}} \quad \text{Eq. 130}$$

The perpendicular model is based upon the reciprocal of the sum, over all components, of each volume fraction divided by its corresponding thermal conductivity:

$$k_{\perp} = \frac{1}{\sum x_i^{\upsilon} k_i} \quad \text{Eq. 131}$$

Owing to the directional dependence of the heat conduction process in fish, the orthotropic properties are assigned to the material in ANSYS while defining the thermal properties of the fish. Based on this,

the value of the effective conductivity along the X-direction is assigned the parallel value ($k_x = k_\parallel$), and the values of the Y-direction and Z-direction are assigned the perpendicular value ($k_y = k_z = k_\perp$).

T	$k_\parallel$	$k_\perp$	T	$k_\parallel$	$k_\perp$	T	$k_\parallel$	$k_\perp$	T	$k_\parallel$	$k_\perp$
-30	1.6392	0.61005	-15	1.4592	0.68532	0	0.45543	2.1957	15	0.47379	2.1106
-29	1.6288	0.61397	-14	1.4423	0.69333	1	0.45672	2.1895	16	0.47494	2.1055
-28	1.6183	0.61795	-13	1.4239	0.70231	2	0.4580	2.1834	17	0.47607	2.1005
-27	1.6077	0.62202	-12	1.4034	0.71254	3	0.45928	2.1773	18	0.4772	2.0956
-26	1.5970	0.62618	-11	1.3804	0.72445	4	0.46054	2.1714	19	0.47832	2.0907
-25	1.5862	0.63045	-10	1.3539	0.73862	5	0.46179	2.1655	20	0.47942	2.0858
-24	1.5752	0.63484	-9	1.3227	0.75601	6	0.46304	2.1597	21	0.48052	2.0811
-23	1.5640	0.63938	-8	1.2851	0.77813	7	0.46427	2.1539	22	0.48161	2.0764
-22	1.5526	0.64408	-7	1.2382	0.80763	8	0.46549	2.1483	23	0.48269	2.0717
-21	1.5409	0.64899	-6	1.1771	0.84956	9	0.46671	2.1427	24	0.48376	2.0671
-20	1.5288	0.65413	-5	1.0930	0.91489	10	0.46791	2.1372	25	0.48482	2.0626
-19	1.5162	0.65954	-4	0.96818	1.0329	11	0.46911	2.1317			
-18	1.5031	0.66529	-3	0.75996	1.3159	12	0.47029	2.1261			
-17	1.4893	0.67144	-2	0.45281	2.2084	13	0.47147	2.1210			
-16	1.4748	0.67808	-1	0.45413	2.2020	14	0.47263	2.1158			

Table 28 Fish Thermal Conductivity in ($-30 \leq T \leq 25$ °C)

4.2.5 Thermal Diffusivity

During transient heat transfer analyses, the main thermophysical property involved is the thermal diffusivity, α, which appears in the Fourier heat conduction equation given by Equation 132.

$$\frac{\partial T}{\partial \theta} = \alpha \left[\frac{\partial^2 T}{\partial x^2} + \frac{\partial^2 T}{\partial y^2} + \frac{\partial^2 T}{\partial z^2} \right] \quad \text{Eq. 132}$$

In the equation, x, y, and z are the Cartesian coordinates, T is the temperature, and θ is the time. The equation for thermal diffusivity is given by Equation 133, where α is the diffusivity, k is the thermal conductivity, ρ is the density, and c is the specific heat.

$$\alpha = \frac{k}{\rho c} \quad \text{Eq. 133}$$

Experimental data on the thermal diffusivity of food substances are not readily attainable. However, α can be determined using Equation 116 if the conductivity, specific heat, and density are appropriately known. In ANSYS 2025 R2, the thermal diffusivity need not be explicitly defined. This software can

calculate thermal diffusivity using the defined material properties, which include conductivity, specific heat, and density.

4.3 FEM Applied to Fish Products: Introductory Considerations and Geometric Discretization

This section explains the numerical formulation of the mathematical model developed above, relating to the frost formation process of fish products. A finite element model (FEM) was developed using ANSYS software to model the temperature evolution process of the products during the rapid cooling stage. Numerical modeling provides a useful tool for exploring the development of the thermal field, hence playing a central role between the model formulation and experimental validation. In the current study, the numerical model provides an intermediate stage for evaluating the reliability and robustness of the proposed model.

One of the important steps involved in the development of FEM analysis is the discretization of the geometry, because the geometry representation used exerts a direct influence on the balance between the accuracy of numerical results and the complexity of the calculation. To reach this balance, specifically within the limitations of the student version of ANSYS, there was a need to use a simplified, meaningful geometry. The biological geometry of the fish was approximated using a three-dimensional body, characterized by typical parameters of about **35 cm** length, **8 cm** width at the widest part, and **5 cm** thickness. These parameters satisfy the minimum size standards for the Mediterranean fish species, according to the Regulation (EC) No. 1967/2006, regarding the mackerel fish considered within the current study. The three-dimensional geometry was developed using the software provided by the University of Palermo, named Fusion 360. This geometry was exported in .step format for the import process into the ANSYS environment.

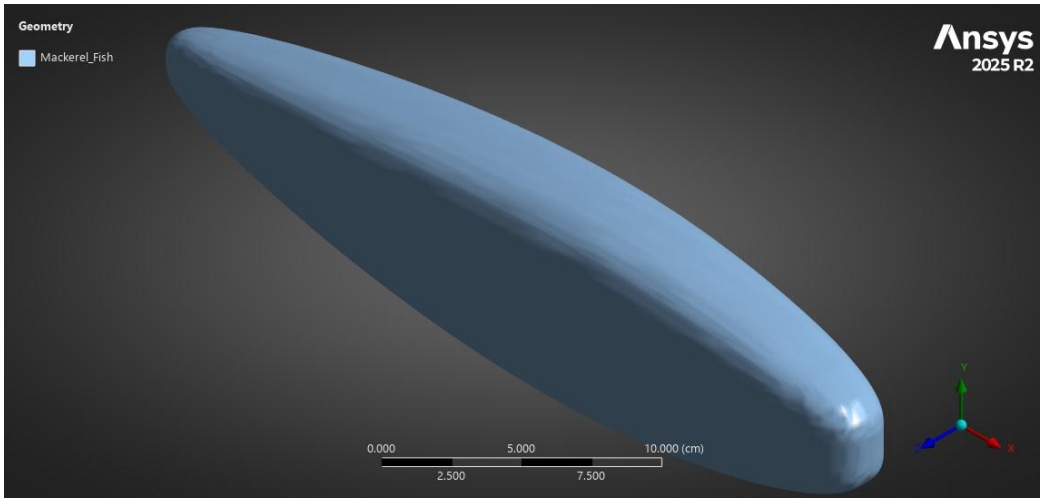

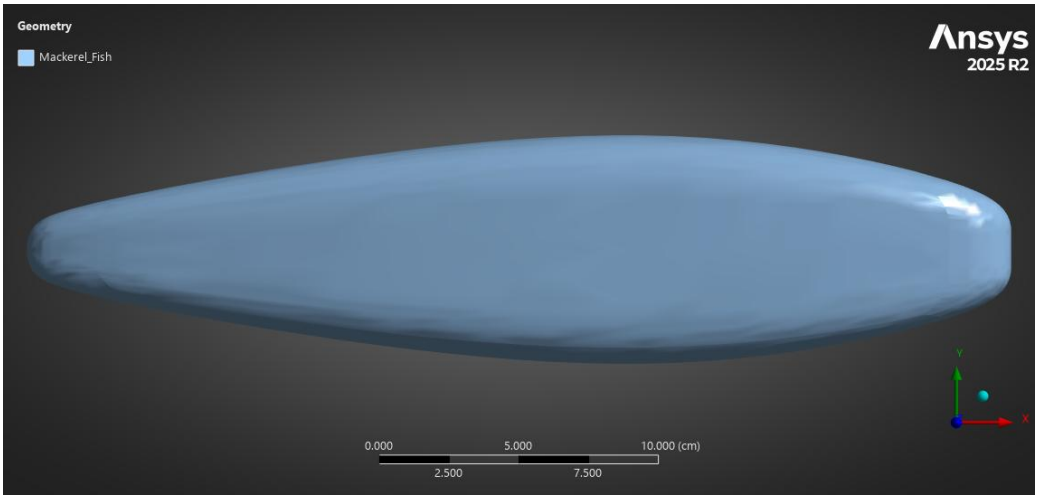

Figure 63 3D Rendering of the Model's Geometric Configuration

In the numerical formulation, the material is modeled as homogeneous and isotropic, with a temperature-dependent thermal behavior, but without any spatial variation of properties. After the definition of the material density and geometric properties, the software can automatically calculate the corresponding volume and weight of the model, which will be discussed below.

Volume: 927 cm^3

Mass: 941 g

4.3.1 Mesh Generation

For the finite element analysis of the three-dimensional fish model, it is necessary that the continuous geometry of the model be discretized, that is, transformed into a computational domain. This discretization of the model is accomplished by meshing, whereby the model is divided into many finite elements, the nodes of which can be used for the calculation of the temperature and other variables.

The mesh developed for the fish model produces a dense and organized mesh that follows the body shapes. For the meshing parameters used, the mesh will consist of:

290,281 Nodes and **1,578,560** Elements

Such a level of sophistication provides the necessary spatial resolution for the representation of the temperature fields, which is very essential for transient analyses, for example, the process of freezing. The dimension of the elements is set at 1.0×10^{-3} m (Figure 64).

4.3.2 Main Meshing Features

- **Element sizing strategy:**

An adaptive sizing strategy was used for controlling the sizes of the elements, which allowed for the automatic refinement of complex areas with the retention of the larger elements in the remaining areas. The Fast transition mode and Coarse span angle helped for the smooth transition of the element sizes.

Geometric parameters extracted from the mesh are:

- Bounding Box Diagonal: 36.583 cm

- Average Surface Area: 110.33 cm^2

- Minimum edge length: 0.98661 cm

These results verify that the element distribution matches the model geometry and that the mesh follows the fish without major distortions.

- **Mesh Quality Assessment:**

Being the effect of the reliability of finite element solutions, mesh quality was measured using the Aggressive Mechanical. This rendered the following results:

- Minimum Quality: 0.30032

- Maximum Quality: 0.99994

- Average Quality: 0.82028

- Standard Deviation: 0.098274.

This suggests that the geometry is very stable, with the preponderance of the points lying in ranges that are suitable for curved shapes.

- **Automatic meshing methods:**

The meshing process involved:

- Sheet body method: Prime Quad Dominant

- Sweepable body method: MultiZone

These approaches, together, helped create an efficient multi-zone mesh that suited the elongated, tapered shape of the fish. The verification of the mesh, carried out at the end, helped ensure that the mesh and the mesh quality are sufficient for the analyses of the thermal gradients performed during the freezing process.

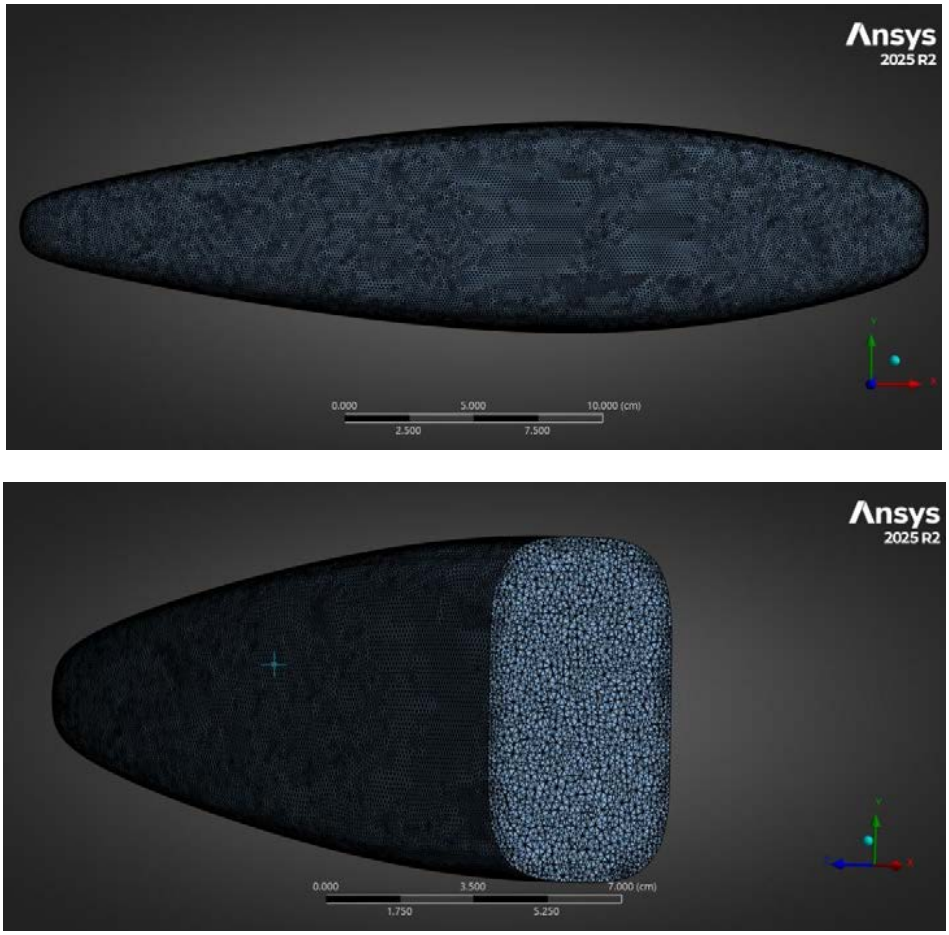

Figure 64 3D Rendering of the Mesh Generation

4.4 Transient thermal analysis

The thermal analysis performed using ANSYS software was developed to model rapid freezing, also known as super-freezing, of a fishery product, with the aim of investigating how the temperature distribution in a fish body changes when it undergoes forced cooling. This, as already explained, involves the finite element method, where a three-dimensional representation of a fish body is approximated by a mesh consisting of a set of interconnected finite elements, which are terminated by nodes. The Fourier heat conduction equation is employed in each element, using thermophysical properties that are a function of fish tissue characteristics, including thermal conductivity, specific heat, thermal diffusivity, and density, which depend upon fish body temperature as well as a physical state of matter described as a liquid or solid.

Boundary conditions are imposed that are characteristic of a cryogenics setup, with a constant air temperature in the cabinet below 0 °C, and forced convection over the outer surface of the fish. A transient analysis simulation follows, which reveals information on how quickly a freeze front will develop in the product, as well as how quickly it will cool. With ANSYS, a complete set of temperature data and heat flow patterns are obtained, from which critical areas, requiring a longer period to reach

microbiological safety, as ensured in regulatory requirements, are determined. This simulation becomes a critical tool in the optimization of the rapid freezing process, analyzing thermocycling performance, speeding up processing, and hence playing a role in increasing product shelf life.

4.4.1 Initial Thermal State of the Product

The definition of the initial temperature distribution is a necessary step in setting up a thermal problem. In this simulation, a 23 °C initial temperature for rapid freezing was used, which represents the fish's surface. Upon being introduced into the freezing compartment, it was considered that the surface in contact with cold air was of constant temperature. This model has been adopted since, in practical situations, the warming of the cooling medium takes place from the surface, which in turn becomes the earliest area around which a marked diminution in temperature takes place. Thus, a homogeneous initial distribution of temperature for the entire geometry with no initial variation between the core and surface of fish has been introduced. This model takes into consideration the realistic operation of the simulation, allowing for a proper evaluation of the progression of the freezing front and the corresponding time needed for the fish core to reach the safety limit.

4.4.2 Time Parameters Selection

Another important element of transient thermal analysis involves specifying various parameters in relation to time that are necessary for performing the analysis over this domain. Here, a total simulation time of 7240 seconds with 121-time steps was considered. The size of a particular time step greatly influences numerical stability in this simulation, where small sizes result in a longer simulation period, even when used in a relatively small total number of steps. A manual setting of the values for "Current Step Number" and "Step and Time" was done in ANSYS. "Step" as used in engineering simulation represents a certain stage either in time or in a logical progression where certain boundaries are taken into consideration. The setting of the total simulation time to 7300 seconds means that ANSYS should simulate until then. The Auto Time Stepping function was turned on, allowing ANSYS to vary the value of the step size to counteract numerical instabilities.

4.4.3 Modeling Heat

In the modeled result, convection was considered as the major mechanism of heat flow between the fish product and the surrounding air. This takes place when a fluid with a different temperature from a solid surface pass over it, resulting in a certain amount of energy flow, which depends on the magnitude of the temperature difference. To model this in ANSYS, Newton's equation of cooling was used for heat

flow calculations on all external surfaces of the fish. Two variables were used here, which are necessary for this calculation: the convective heat transfer coefficient and air temperature. A constant value of 34 $W/m^2.℃$ was used.

4.4.3.1 Determination of the Convective Heat Transfer Coefficient

Correct calculation of the convective heat transfer coefficient is one of the key problems of the study of freezing processes because the given parameter is the direct determinant of the determination of freezing times and, by extension, the quality of the products and food safety. This is why specific attention was paid to its definition in the numerical model in ANSYS.

A rough convective heat transfer coefficient of 30 $W/m^2.℃$ was taken at the initial step to initialise three-dimensional model and to set up major thermal boundary conditions. As much as this value is an initial assumption that was made, it was found sufficient to initially calibrate the model and enable the physical and temporal behaviour of the system to be modeled in a consistent and stable way. Based on the results of experimental observations during the test campaign, additional simulations were then conducted to check the appropriateness of this assumption and to explore how the thermal response depends on changes in the convective coefficient. The numerical analysis has considered the convective heat transfer coefficients lower and higher than the original estimation. Specifically, when simulated at smaller values, within the range of 25-30 $W/m^2.℃$, the product core temperature never fell below -18 °C, which is the threshold needed in the chapters to meet the food safety requirements. By contrast, simulations employing higher convective heat transfer coefficients (above 30 $W/m^2.℃$) showed that the initial value of 30 $W/m^2.℃$ does not accurately represent the heat transfer process, whereas a coefficient of approximately 34 $W/m^2.℃$ allows the product core temperature to reach −18 °C.

Meanwhile, an organized process was considered when estimating air velocity. In the first place, the operating conditions were determined based on the characterization of air temperature in the inner chamber, the temperature of surfaces of the fish sample and the typical length of the product, known by its longitudinal dimension, necessary to assess the dimensionless numbers. The temperature of the film was then estimated as a mean temperature between the air temperature and the surface temperature, of the thermophysical properties of the fluid could be assessed at an average condition in the thermal boundary layer, which is generally suggested to be used when forced-convection correlations are to be determined. The volumetric flow rate and the effective flow cross-section were used to estimate the air velocity using the technical data of the air evaporator. The following value (around 3.5 m/s) is within the acceptable range that has been reported as freezing tunnels using forced air. This method allowed a

more accurate solution of the air properties, i.e. viscosity, thermal conductivity, density, Prandtling number, hence restricting uncertainties in the solution of the Reynolds and Nusselt numbers.

Thermophysical data of the film temperature was acquired with the help of the Engineering Equation Solver (EES) which provides consistency and reliability of the data that will be used later in calculation. When the classical Dittus Boelter correlation was used, however, in its original form, the convective heat transfer coefficient was found to vary not entirely with the value necessary to obtain the numerical result. This is the reason why the modified version of the correlation was presented having offered a more closely related convective coefficient to the behaviour in the simulations. This modification brought about consistency between the theoretical development and the numerical results.

Dittus–Boelter in its original form:

$$\mathrm{Nu} = 0.023\mathrm{Re}^{0.8}\mathrm{Pr}^{0.3} \qquad \text{Eq. 134}$$

Dittus–Boelter in its modified form:

$$\mathrm{Nu} = 0.055\mathrm{Re}^{0.8}\mathrm{Pr}^{0.3} \qquad \text{Eq. 135}$$

Lastly, it is necessary to say, that even more precise assessment of air velocity might have been done by direct experimental measurements with the use of an anemometer, which was placed near the product surface within the cold chamber. This would take into consideration the real flow situation in which the sample is exposed and would give a more realistic value compared to an abstract estimate.

4.4.4 Insights Derived from the Analysis

The simulation provided a comprehensive model of how the surface temperature changed over the course of rapid freezing. These simulation results reveal a steady fall in temperature with spatial temperature variations. The initial surface and core temperatures were 20 °C and 23 °C, respectively.

Figure below illustrates how fish core temperature ($T_{core,fish}$) and fish surface temperature ($T_{surf,fish}$) changed during the freezing period.

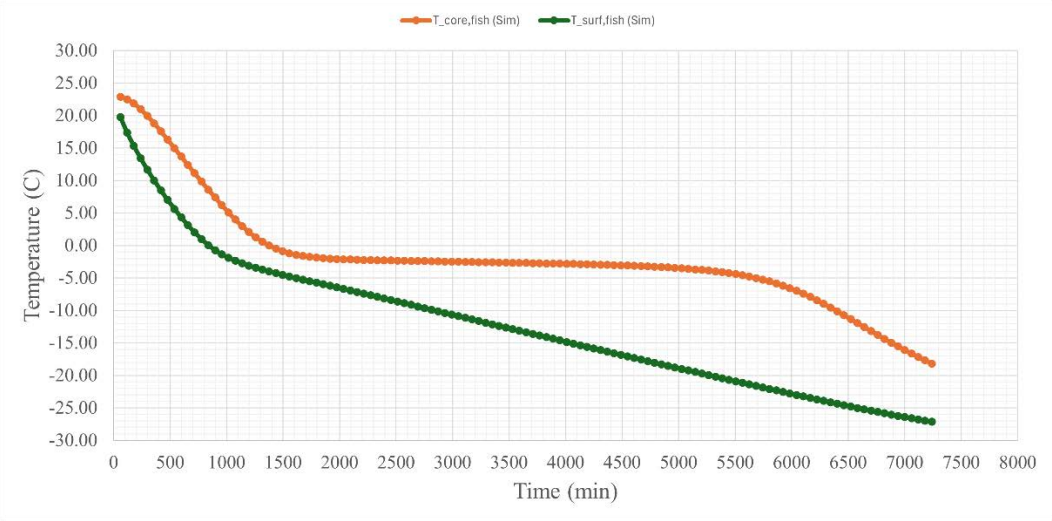

Figure 65 Fish Temperature vs. Time During Freezing

This aligns with expectations where the surface temperature dropped quickly in the initial stages due to being in direct contact with low-temperature air, while the core temperature takes a relatively longer period with a noticeable delay. This crystallization period, as shown in figure 65, lasted for about 4000 seconds.

After this period, the gap between the surface and core temperatures reduces, and both lines continue to move towards further subzero temperatures. The core reached a temperature of -18 °C, which is the limit for frozen fish, around 7240 seconds, that is, around 121 minutes. Meanwhile, the rate of cooling of the surface temperature was much faster, dropping beyond -18 °C. Such observations are characteristic of forced-air freezing, where convective cooling brings about a rapid decrease in surface temperature, but removal of heat from the core takes longer until total freezing occurs.

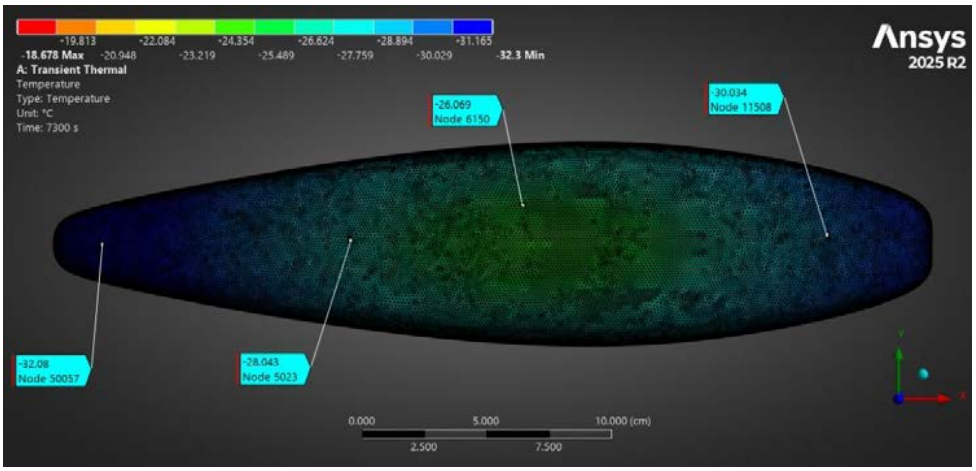

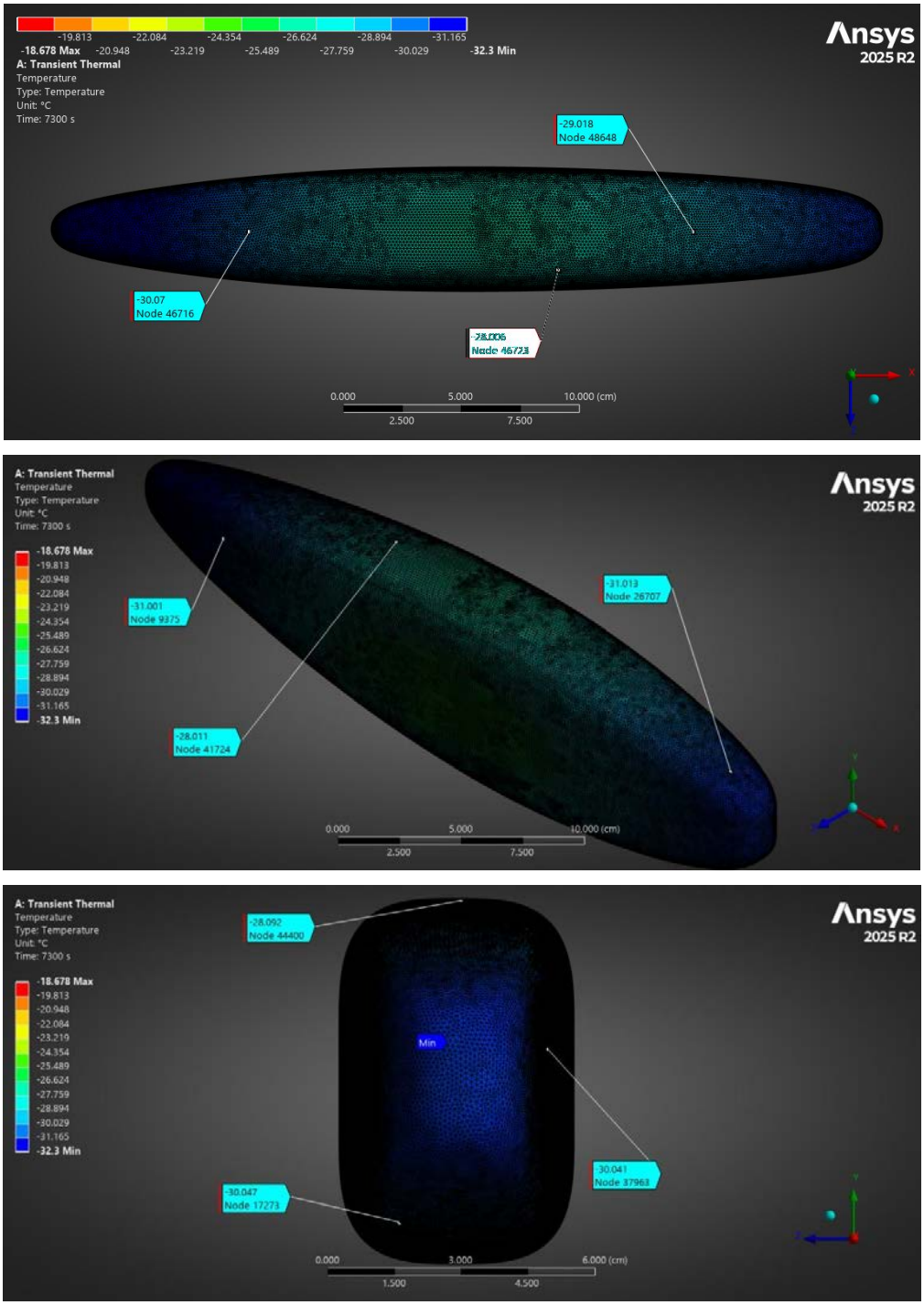

Figure 66 Temperature Distribution of the Fish Geometry in Top-, Side-, Iso-, and Front-View Representations

Figure 66 above show the ANSYS temperature gradations in various viewpoints: top, side, isometric, and front.

Note that, as shown, the fish body approaches a temperature close to that of the -33 °C environment. Also, in areas reaching a higher density, it approaches a higher temperature but keeps to the -18 °C limit. The cross-sectional views in Figure 67 below highlight where in the body it reaches that -18 °C.

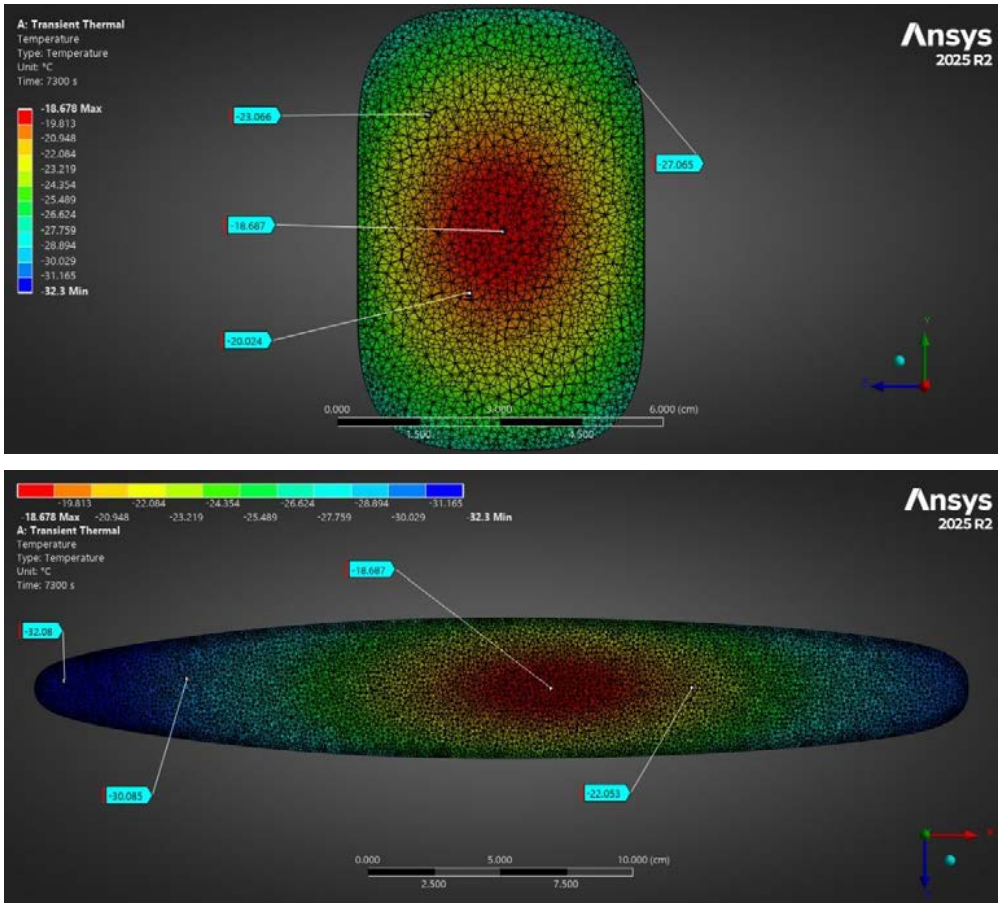

Figure 67 Temperature Distribution in the Longitudinal and Transverse Cross-Sections of the Fish Model

After discretizing the system, it becomes necessary to implement the equations of Chapter 4.2 to all internal nodes. A general expression for nodal temperature, as evident from equations of a particular step i, reveals that the value of temperature in step (i+1) for a certain node has a dependency on the values of that node for step i and those around it. With a computational tool, this process allowed the determination of temperature variation over time (Equation 136).

$$T_s^{[i+1]} = T_s^{[i]}(1 + \Delta T W_{ss}^{-1} X_{ss}) + \Delta T \left[\left[\sum_{j=1,2,\ldots s-1,s+1}^{p} (W_{ss}^{-1} X_{sj}) T_j^{[i]} \right] + W_{ss}^{-1} E_s \right] \quad \text{Eq. 136}$$

It should be emphasized that the numerical and regression-based results presented in this section describe the observed behavior within the investigated experimental range. The developed correlations and polynomial regressions are data-driven representations derived from the available dataset and should not be interpreted as validated predictive tools beyond the studied operating conditions.

Chapter 5

Experimental Findings and Discussion

5 Experimental Findings and Discussion

This chapter describes a detailed analysis as well as discussion of test results obtained from experiments. The working conditions are analyzed for a condenser water inlet temperature of 20 °C ($T_{cw,in} = 20$ ℃), then further tests are carried out for 15 ℃ and 10 ℃. The role of important variables such as the chamber temperature of T_{cell}, coefficient of performance, compressor work, and other related variables for working conditions are analyzed. The graphs were generated using Python 3.10.0

5.1 $T_{cw,in} = 20$ ℃, Maximum Opening Expansion Valve = 60% and 70%, $T_{cell} = -23$ ℃, -28 ℃, -33 ℃ (6 Tests)

The COP at a chamber cell temperature of -23 °C at EV=60% and EV=70% starts with relatively high values, which keep decreasing with time as the experiment continues. This reduction is consistent with the natural growth in cooling load and the slow increase in the pressure difference across the cycle. Although 70% of opening shows growing oscillations in both instances, the oscillations are significantly larger, which means that the pressure behavior is less steady, and more pronounced fluctuations in the compressor load are observed. Even though the average COP of EV = 60 % is somewhat lower, it has a smooth temporal trend, and the rate of change is less steep. EV = 70 % on the other end provides a higher instantaneous COP at the expense of stronger ΔP variations, implying lower controllability of the refrigeration cycle. As such, EV = 70 % is more efficient in operation at 23 °C, but EV=60% has better stability of operation (Figure 68).

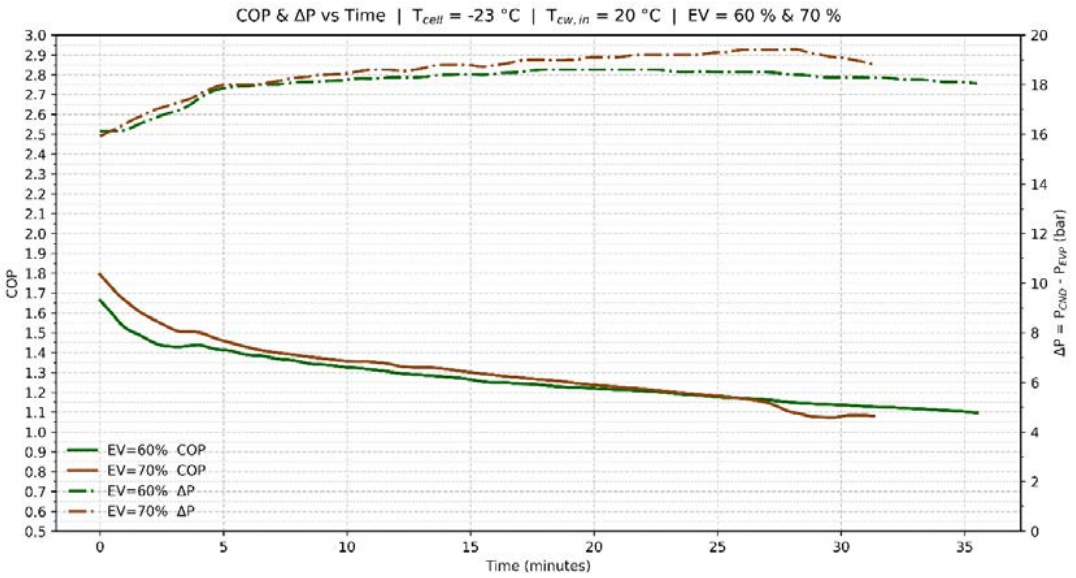

Figure 68 COP and ΔP VS Time ($T_{cw,in} = 20$ ℃/ $T_{cell} = -23$ °C)

As shown in Figure 69, the trend of behavior of COP at -28 °C is very different compared to the behavior of the coefficient of performance at -23 °C. The COP values of both expansion valve (EV) settings are

initially smaller, and this is quite consistent with the fact that the compressor needs higher work sources at lower evaporating temperatures. In addition, the COP profile of the 60% valve opening is more stable and smoother than the 70% opening of the valve. Changes in pressure (ΔP) are observed within a smaller band. Conversely, as the valve opening grows to 70, bigger COP oscillations can be seen, which means that the compressor is subjected to increased mechanical and thermal load. Hence, in both the stability of the system and the energy efficiency, the 60% valve opening state is the one that works better.

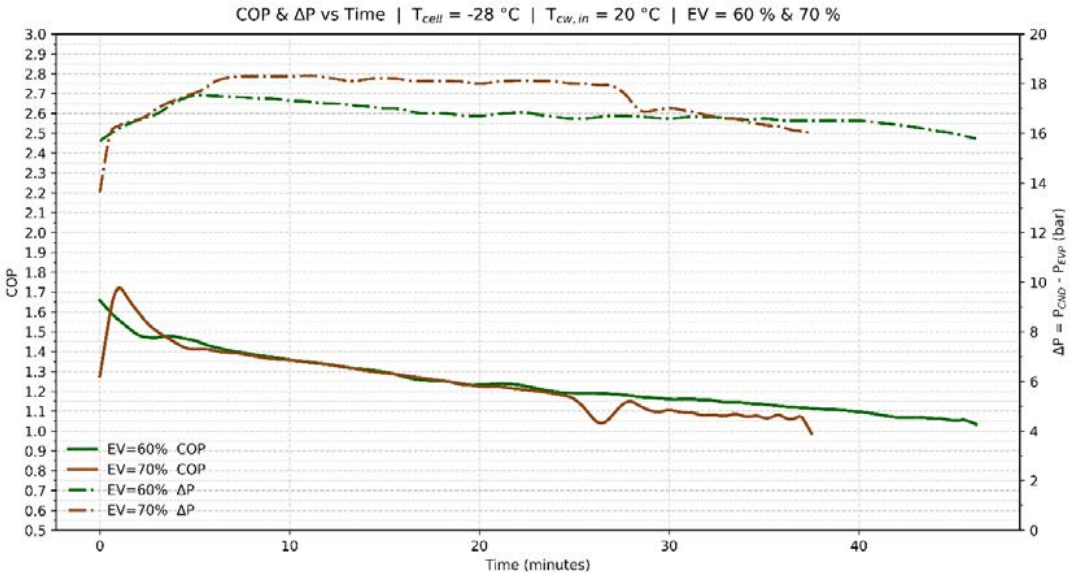

Figure 69 COP and ΔP VS Time ($T_{cw,in} = 20\ ℃/\ T_{cell} = -28\ °C$)

On the chamber set point of -33°C, which is the lowest temperature considered, it is observed that there are significant variations between the different expansion valve openings. Even though the total COP values are lower in comparison with the former two temperatures, the 60 percent valve opening also has stable and smooth operational behavior. Conversely, the opening of 70 percent depicts strong oscillations, which have a lot of changes, especially at the end of the test when the system is close to the desired temperature. The ΔP curves of the two instances are mostly similar, albeit that the 70% arrangement exhibits a little greater instability. In general, the influence of the 60% expansion valve opening is evident as the most stable in terms of operation at the temperature of -33°C. Although the 70% setting can occasionally result in larger instantaneous values of COP, it has the cost of serious pressure instability and lower system reliability (Figure 70).

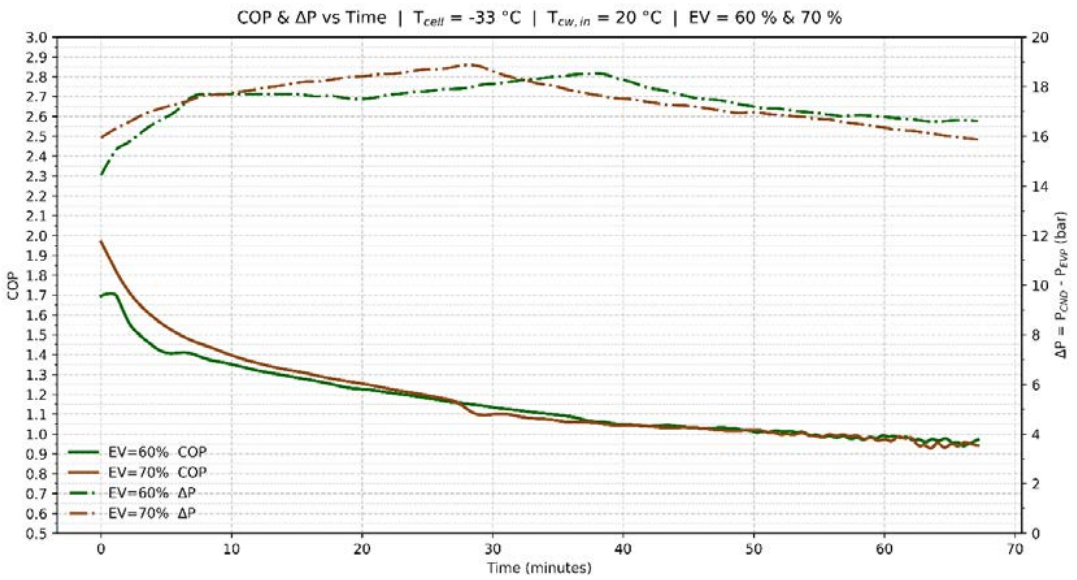

Figure 70 COP and ΔP VS Time ($T_{cw,in} = 20$ ℃/ $T_{cell} = -33$ °C)

Overall, the greater the lower the temperature of operation, the more advantageous is the 60 % opening of the expansion valve in ensuring stability in the system. Stability of the refrigeration cycle, accuracy of control, and the stability of pressure profiles are equally important in freezing processes, especially of sensitive products like fish, as much as maximum efficiency is attained. Therefore, the behavior at low temperature (-33 °C) is of special significance to such applications.

The COP of each of the two operating modes (EV = 60 % and EV = 70 %) at a chamber temperature of -23°C is initially high but continues to decline as the system approaches a more stable operating state. The distinction between the two cases does not represent a significant difference, but the 70-percent valve opening tends to give a higher COP value during most of the test period, which is mostly due to the higher mass flow rate of refrigerant and the augmentation of heat transfer as a result. The temperature of the chamber decreases smoothly in both configurations, but the decrease of the temperature is a bit higher in the 70 % opening. However, the stability of temperature control is greater in the case of 60 %, where smaller variations are recorded. At this level of temperature, the difference in performance is not critical, and both situations produce acceptable results, although the 60 percent opening is more controllable (Figure 71)

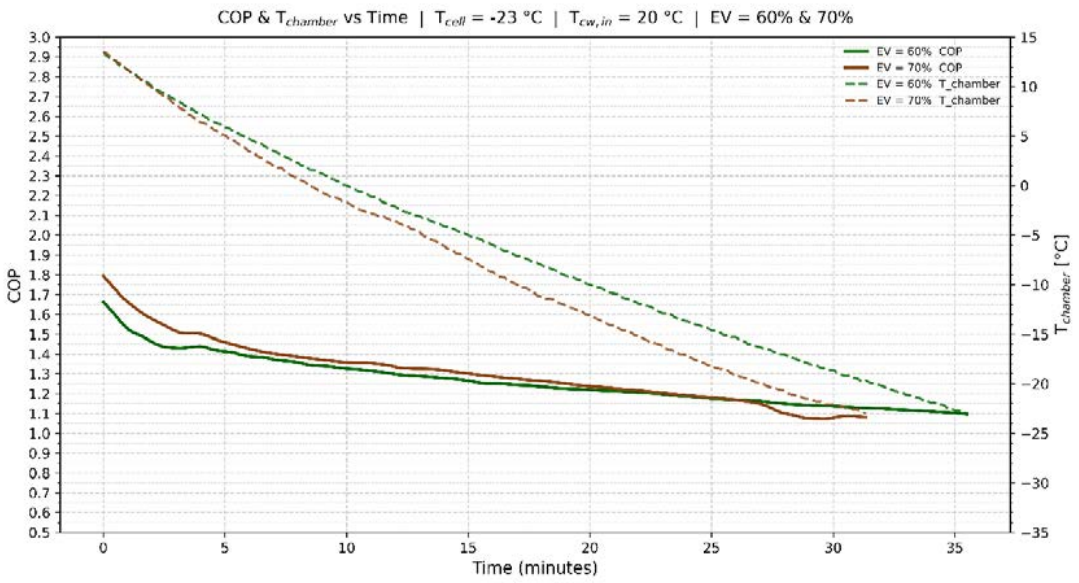

Figure 71 COP and $T_{chamber}$ VS Time ($T_{cw,in} = 20$ ℃/ $T_{cell} = -23\ °C$)

As shown in Figure 72, at -28 °C, the difference between the two operating modes becomes more evident than at -23 °C. The COP trend in the EV = 60 % case shows a steady and uniform pattern, but the EV = 70 % condition produces small and ongoing variations. These variations are mainly attributed to oscillations in the refrigerant mass flow rate occurring under the 70 % valve opening. The chamber temperature behavior shows a clear difference in its behavior. The 60 % configuration maintains a continuous temperature drop in the chamber space at a consistent rate without any sudden variations. In contrast, at 70 % opening, although the initial cooling rate is higher, the temperature profile of the storage chamber exhibits visible ripples, indicating a non-uniform cooling rate. Such fluctuations may lead to temperature non-uniformity within the food samples, which is undesirable, particularly when the objective is to achieve rapid yet uniform freezing. The 60 % valve opening provides superior performance in temperature stability and COP uniformity compared to the 70 % configuration, which provides minimal additional cooling power but causes greater temperature variations and less stable operation.

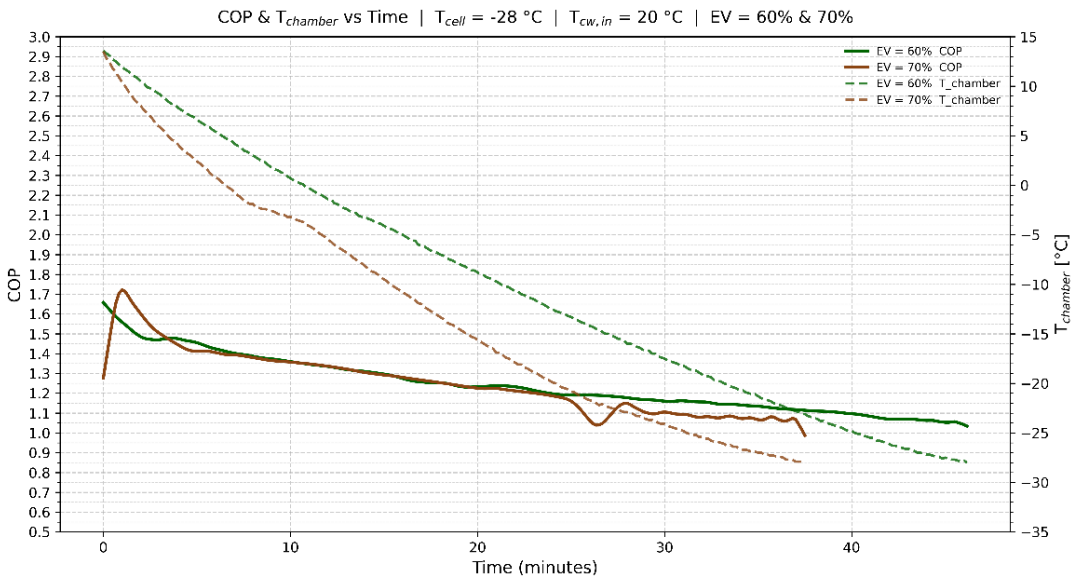

Figure 72 COP and $T_{chamber}$ VS Time ($T_{cw,in} = 20$ ℃/ $T_{cell} = -28\,°C$)

The COP values at -33 °C show a significant decrease when compared to warmer temperatures because the pressure difference rises substantially while the evaporating pressure drops. The two operating modes show different behavior because the COP maintains a stable and smooth value at EV = 60% but becomes unstable with frequent small oscillations at EV = 70 %. This behavior is directly reflected in the chamber temperature ($T_{chamber}$) as well. The 60% opening of expansion valve in chamber results in a uniform temperature decrease which remains smooth and allows for precise control. The cooling curve shows irregular patterns at 70 % opening during the freezing process with small fluctuations throughout the entire freezing period.

Food freezing operations need exact temperature management between -30 and -35 °C to prevent ice crystal formation that damages food structure and decreases product quality. The operational results show that the 60 % opening of expansion valve at -33 °C represents the best condition because it produces a stable COP and controlled temperature drop and minimal variations in cooling performance, as shown in Figure 73.

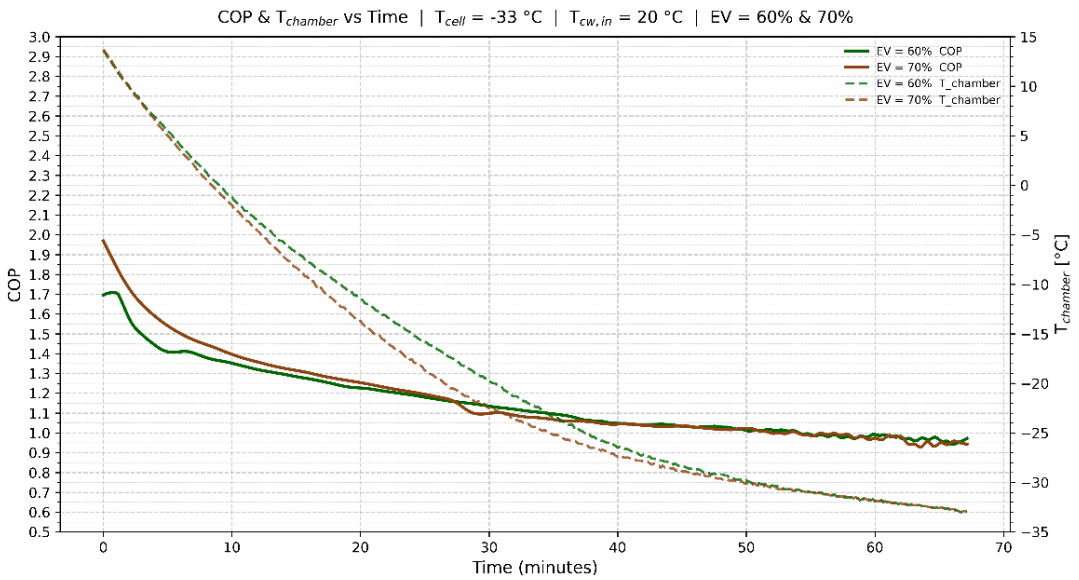

Figure 73 COP and $T_{chamber}$ VS Time ($T_{cw,in} = 20$ ℃/ $T_{cell} = -33\ °C$)

At $T_{cell} = -23$ ℃ the compressor power W, calculated from the enthalpy difference between the inlet and outlet states, exhibits a smooth and nearly uniform trend for both EV = 60 % and EV = 70 % conditions. The value of W starts at a lower point before it rises with increasing cooling load until the system reaches its steady-state condition. This behavior is fully consistent with the thermodynamic model of the vapor-compression cycle. The Active Power measured by the energy analyzer shows a higher value than W because it includes all mechanical, electrical, aerodynamic and thermal losses that occur in the compressor. The Active Power profile shows no significant change between the two cases, yet the EV = 70 % configuration produces higher Active Power readings because of its elevated refrigerant mass flow rate which results in greater real compressor work. The Active Power levels in the EV = 60 % case remain lower while the power fluctuations decrease which results in lower mechanical stress on the compressor. The difference between W and Active Power shows no significant change between the two operating conditions which indicates that the compressor maintains stable volumetric and electromechanical performance at -23 °C (Figure 74).

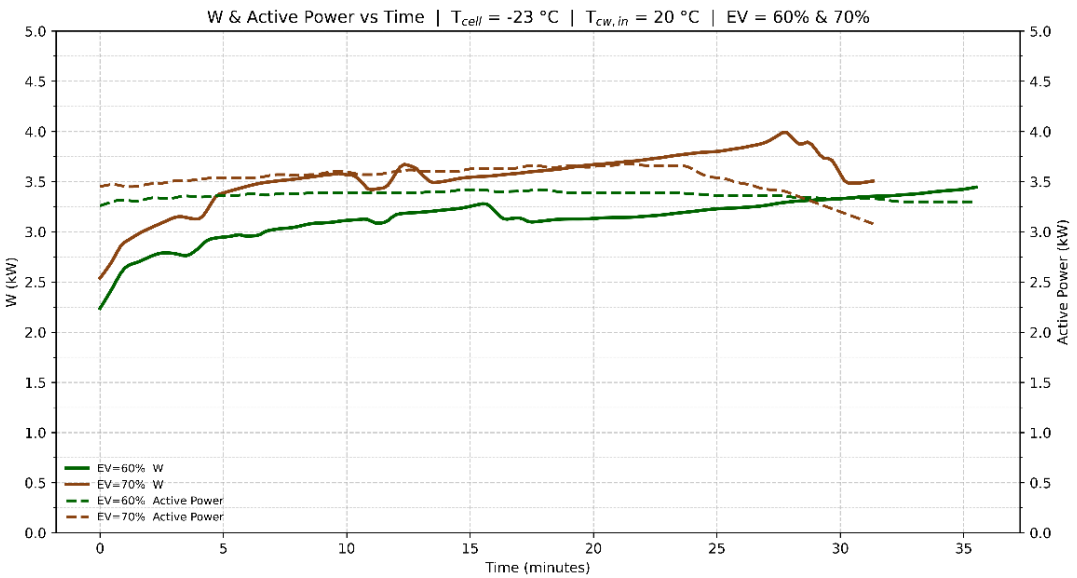

Figure 74 Active Power and W VS Time ($T_{cw,in} = 20$ ℃/ $T_{cell} = -23\ °C$)

At -28 °C, the compressor power W in both the EV = 60 % and EV = 70 % configurations increases compared with the values at -23 °C. This rise is a direct consequence of the lower evaporating pressure and the resulting increase in the compressor pressure ratio. The rate of increase in W over time remains smooth in both cases, though the magnitude is higher for EV = 70 % due to the greater refrigerant mass flow rate and the corresponding demand for higher compression work. The behavior of the Active Power follows a similar trend but with a larger amplitude. The difference between Active Power measurements and W calculations exceeds the -23 °C results because mechanical and electrical losses become more important when operating at higher loads. The system shows bigger Active Power variations when operating at EV = 70 % because this operating point leads to unstable system operation at elevated operating levels.

The EV = 60 % configuration provides superior performance because it keeps power output steady, while the EV = 70 % setting produces more power at the cost of increased losses and decreased system stability (Figure 75).

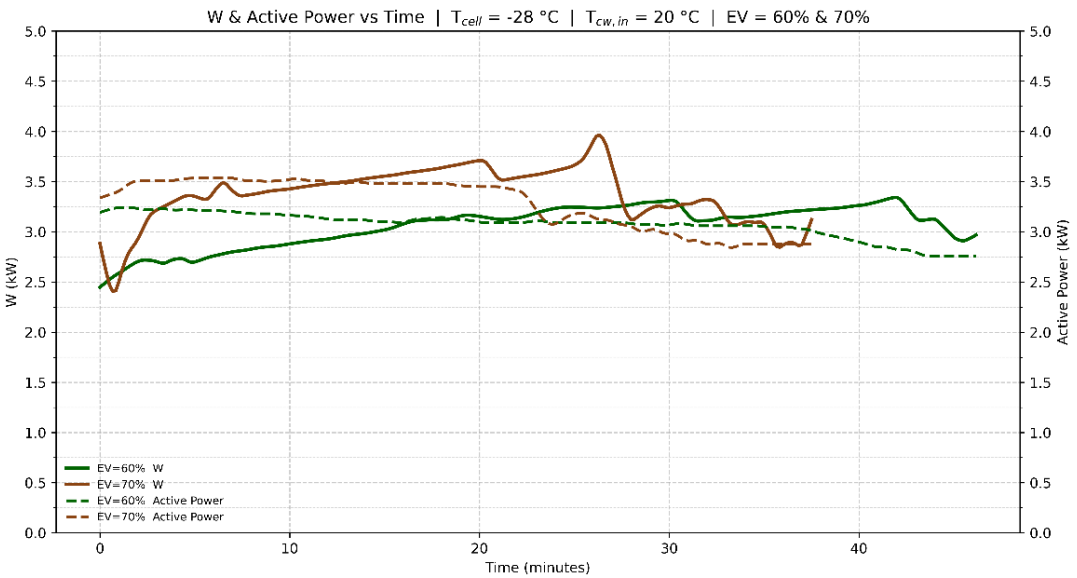

Figure 75 Active Power and W VS Time ($T_{cw,in} = 20$ ℃/ $T_{cell} = -28\,°C$)

As illustrated in Figure 76, the -33 °C operating condition serves as the most critical test point because it replicates real-world freezing conditions while generating the maximum compressor load. The magnitude of W at -33 °C is clearly higher than at -23 °C and -28 °C, indicating that more work is required per kilogram of refrigerant, a direct consequence of operating at a lower evaporating temperature.

Similarly, the Active Power in both expansion valve settings is higher than in the previous temperature cases. The system requires more power because compression work increases thermodynamically and the total losses from mechanical and electrical system components rise. The W and Active Power curves show more continuous behavior and remain closer together when under EV = 60 %. The comparison shows that Active Power and W values remain close to each other at 70% EV, but Active Power variations become more extreme, which causes higher compressor stress and unstable operation.

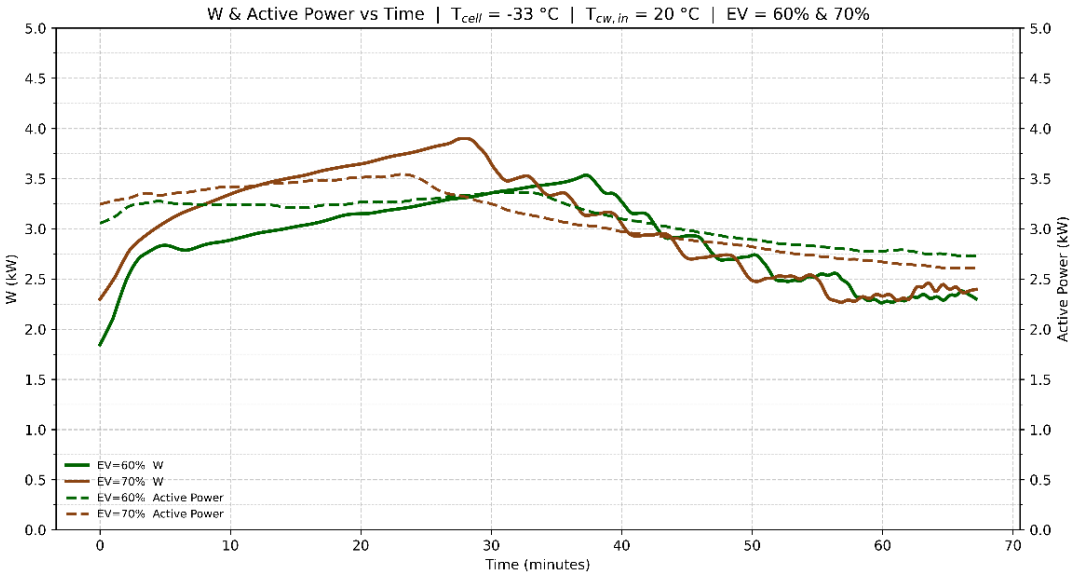

Figure 76 Active Power and W VS Time ($T_{cw,in} = 20$ ℃/ $T_{cell} = -33\ °C$)

The compressor power W and Active Power rise as the chamber temperature drops between -23 °C and -33 °C because of the increased pressure ratio and additional compression work needed at lower evaporating temperatures. At all temperature levels, the 70 % expansion valve opening results in higher values of W and Active Power compared with the 60 % case; however, the gap between the two curves and the amplitude of power fluctuations also become larger, particularly evident at −33 °C. The compressor operates at reduced efficiency because electromechanical losses become more significant when the system experiences higher loads.

The EV = 60 % configuration shows better temperature stability and more stable behavior at all tested temperatures with the best results at -33 °C and it also has a better ratio between thermodynamic work and electrical power consumption. From the standpoint of long-term operation and product freezing applications, this condition is clearly the more desirable one.

The Active Energy chart compares the three operating temperatures of -23 °C, -28 °C, and -33 °C for both expansion valve openings, EV = 60 % and EV = 70 %. The numerical values displayed above the columns indicate that at $T_{cell} = -23$ ℃, the Active Energy values for both valve openings are nearly identical, showing only a negligible difference. This means that, at the relatively higher temperature, the increased refrigerant mass flow rate in the 70% case does not significantly raise the compressor load, and both configurations perform almost equally in terms of energy consumption. As the chamber temperature reaches $T_{cell} = -28$ ℃, a clear distinction appears: the Active Energy in the EV = 70 % configuration is noticeably lower than that in the EV = 60 % case. In other words, at this intermediate temperature, the system with a 70 % valve opening achieves the required cooling with lower total energy consumption. This occurs because, at -28 °C, the pressure ratio is not yet excessively high, allowing the increased refrigerant flow to enhance the cooling rate and reduce the effective operating time of the

compressor. However, at $T_{cell} = -33$ °C, the trend reverses completely. The EV = 70 % column displays a greater value than EV = 60% which means the total energy usage is higher. The compressor faces its most severe compression requirements at this lowest operating temperature because the suction pressure becomes very low and the pressure ratio becomes extremely high. The 70% configuration experiences increased mechanical and electrical losses because of its higher mass flow which exceeds the optimal operating range of the compressor and leads to elevated total energy usage. The pattern follows the thermodynamic behavior of vapor-compression cycles because higher refrigerant flow rates improve system performance at moderate temperatures but lead to negative effects at very low temperatures where compressor load and associated energy losses become excessive (Figure 82).

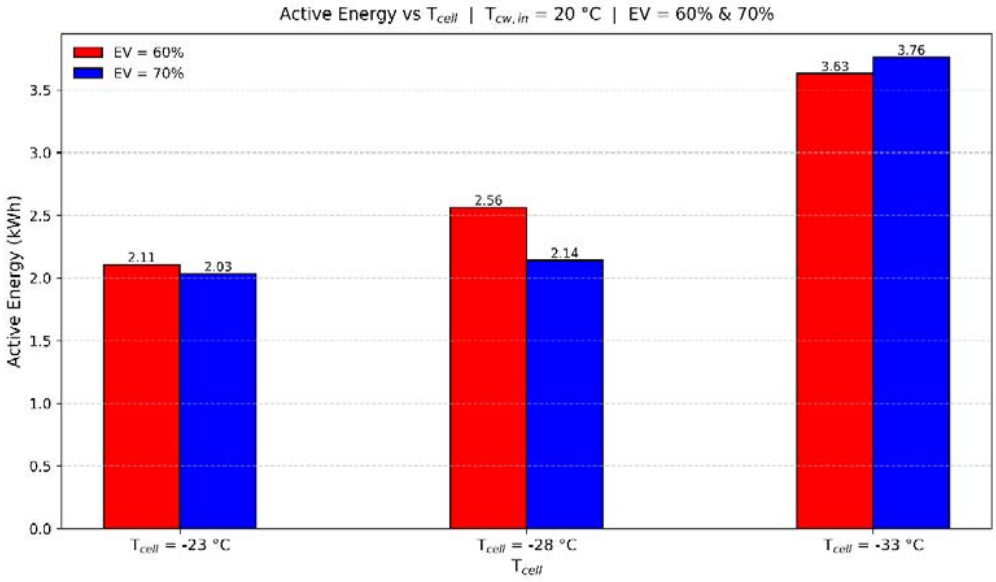

Figure 77 Active Energy VS T_{cell} ($T_{cw,in} = 20$ °C)

The COP values remain stable for both operating modes at -23 °C chamber temperature because the smoothed COP curves show minimal variation throughout the measurement period. The system operates at an efficient thermodynamic level because the evaporating pressure stays high and the compressor pressure ratio stays moderate (Figure 78).

The Q_{evp} values plotted on the secondary axis show that, for most of the test period, the cooling capacity in the EV = 70 % configuration is slightly higher than in the 60 % case, primarily due to the greater refrigerant mass flow rate.

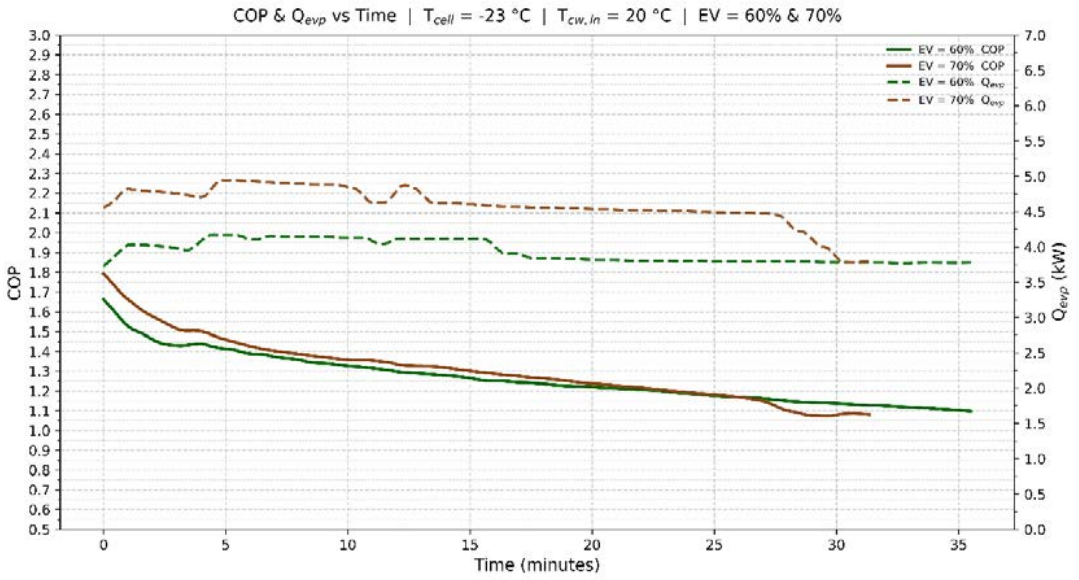

Figure 78 COP and Q_{evp} VS Time ($T_{cw,in} = 20$ ℃/ $T_{cell} = -23$ °C)

The two valve openings show identical performance at -23 °C because they achieve the same efficiency and cooling capacity with EV = 70 % which leads to better Q_{evp} results.

For -28 °C conditions, it is observed that the effect of low evaporating temperature in relation to the refrigeration cycle is more pronounced, making the differences between the COP values of both expansion valve positions (EV = 60 % vs. EV = 70 %) clearer.

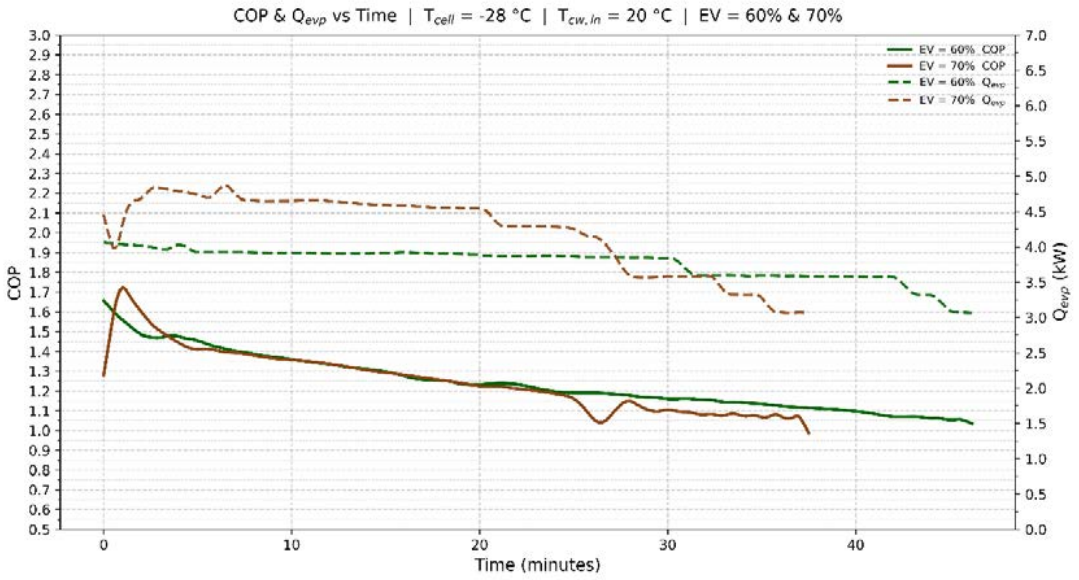

Figure 79 COP and Q_{evp} VS Time ($T_{cw,in} = 20$ ℃/ $T_{cell} = -28$ °C)

The COP values for the 60% case demonstrate higher values in a uniform manner, whereas for the other case (70% opening), smaller values of COP, having small regular variations, are observed. This specifies that even despite increased compression work due to higher mass flow of refrigerants in case of the 70 % opening, slightly decreased values of COP have started to appear. Nonetheless, from the

values of Q_{evp}, it is observed that for most of the time, in case of the evaporator in conditions of EV = 70 %, a slightly higher value of cooling capacity is observed than in conditions of EV = 60 % (Figure 79).

At -33 °C, it is clear from the results that the loading conditions for the system are much more significant. The COP graph for EV = 60 % is more stable and smoother, as well as having higher COP values, in contrast to those for EV = 70 %, for which the COP is lower, as well as more irregular in terms of variations in time. These variations occur due to the higher-pressure ratio as well as more significant compression loading because of higher mass flow of refrigerant for EV = 70 %.

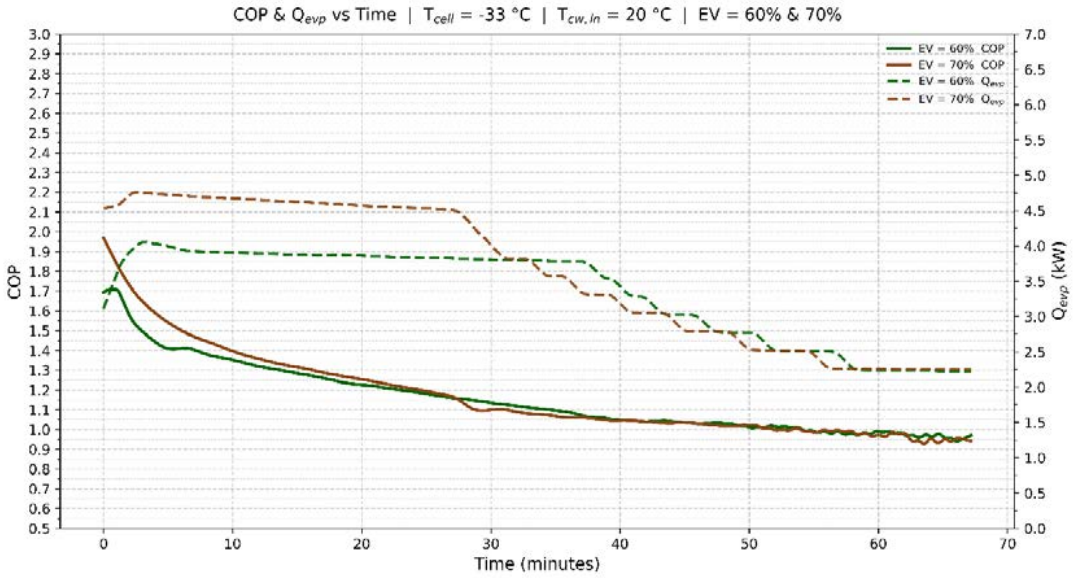

Figure 80 COP and Q_{evp} VS Time ($T_{cw,in} = 20$ ℃/ $T_{cell} = -33$ ℃)

As far as Q_{evp} is concerned, it is observed from the results that, in contrast to previous scenarios of -23°C and -28 °C, the graph of the cooling capacity for EV = 70 % does not have an edge over that for EV = 60 % in most ranges. This implies that at -33 °C, the secondary flow of refrigerants does not have an effective output in terms of useful cooling capacity but primarily affects compressor work in the form of losses. Under such conditions, at -33 °C, it is established that EV = 60% is more efficient in relation to stability, evaporation, as well as optimized functioning (Figure 80).

5.2 $T_{cw,in} = 15$ ℃, Maximum Opening Expansion Valve = 70%, 80%, and 90%, $T_{cell} = -23$ ℃, -28 ℃, -33 ℃ (6 Tests)

The system operates within a controlled compression ratio range at -23 °C because COP and ΔP show specific behavior. The cooling process maintains controlled ΔP increases because the system operates within a stable compression ratio range. The suction pressure decreases as $T_{chamber}$ approaches the set point while discharge pressure remains constant because $T_{cw,in}$ maintains a fixed value. The combined

effects of these trends lead to an increasing ΔP value. The compression ratio increases with higher ΔP values which results in lower COP values. The vapor-injection process operates within a pressure range that has not yet reached the point where its advantages start to decrease. The evaporator capacity increases when the EV opening reaches 90 % while the COP drop becomes less severe. The COP values between EV = 70 %, EV = 80%, and EV = 90 % show minimal differences at this temperature point. The operating zone benefits from vapor injection because it creates uniform temperature distribution and lowers discharge temperature which helps offset the increased energy costs from rising ΔP (Figure 81)

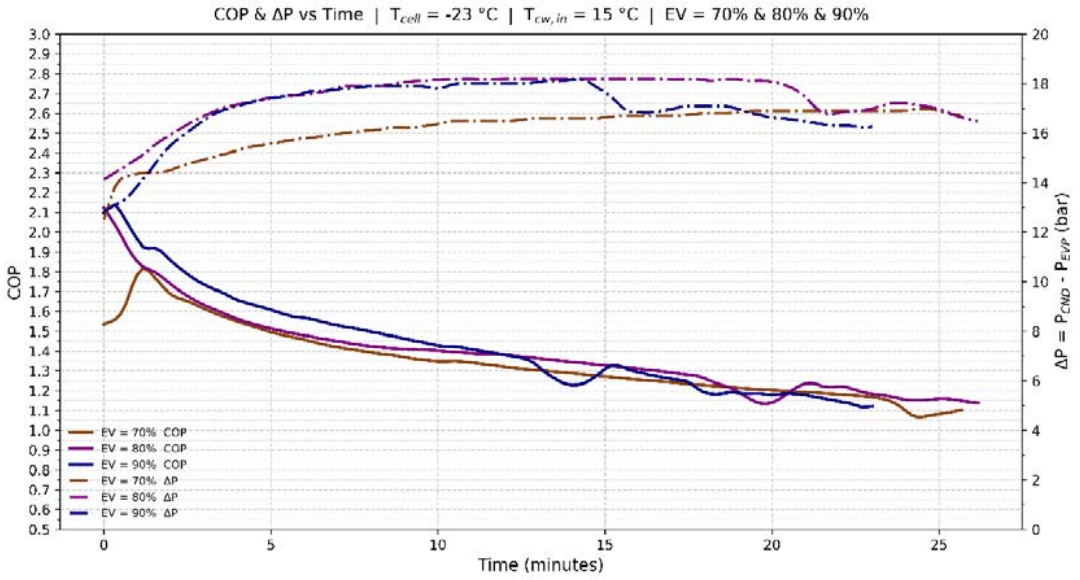

Figure 81 COP and ΔP VS Time ($T_{cw,in} = 15$ ℃/ $T_{cell} = -23$ °C)

According to figure 82, the system operates at -28 °C target temperature while the suction pressure decreases which causes the condenser–suction pressure difference (ΔP) to increase steadily. The increasing ΔP value indicates that the compressor pressure ratio rises which leads to a natural decrease in COP performance. The three EV settings at 70 %, 80 %, and 90 % maintain identical performance patterns throughout the measurement period without showing any sudden changes. The vapor-injection process operates within a stable zone at -28 °C because it does not create significant efficiency improvements or performance degradation through excessive compression work. The three EV configurations show identical performance patterns because ΔP increases with decreasing chamber temperature and decreasing suction pressure while COP decreases at a slow rate because of increasing compression ratio.

The three EV settings produce similar results which show no clear advantage from using the highest or lowest opening settings. The vapor-injection scroll compressor operates as expected during mid-range cooling applications because the injected vapor maintains cycle stability without reaching the point where injection mass flow affects overall performance.

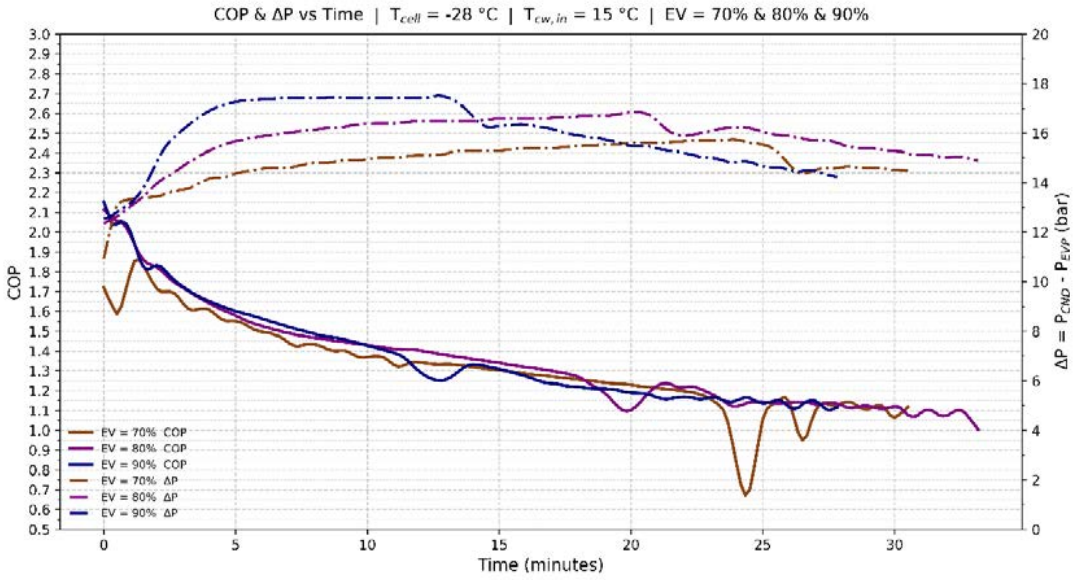

Figure 82 COP and ΔP VS Time ($T_{cw,in} = 15\ ℃/\ T_{cell} = -28\ °C$)

As illustrated in figure 83, the system operates at its peak when the target temperature reaches -33 °C because suction pressure reaches its lowest point while ΔP maintains high values throughout the process. The compressor pressure ratio reaches its highest point during this condition which results in the lowest COP values compared to other temperature points. The three EV settings at 70 %, 80 %, and 90 % operate identically under these conditions without showing any meaningful differences. The low evaporating temperatures make vapor injection function as a compressor stability maintenance tool instead of providing any benefit to compensate for the severe COP decrease from low suction pressure. The COP curves from all three EV openings show identical patterns while maintaining low values. The cooling load reaches such extreme levels at -33 °C that the expansion valve opening has no effect on COP performance. The compressor operates near its thermal boundaries at this point, so additional vapor injection helps control discharge temperature rise instead of enhancing system efficiency.

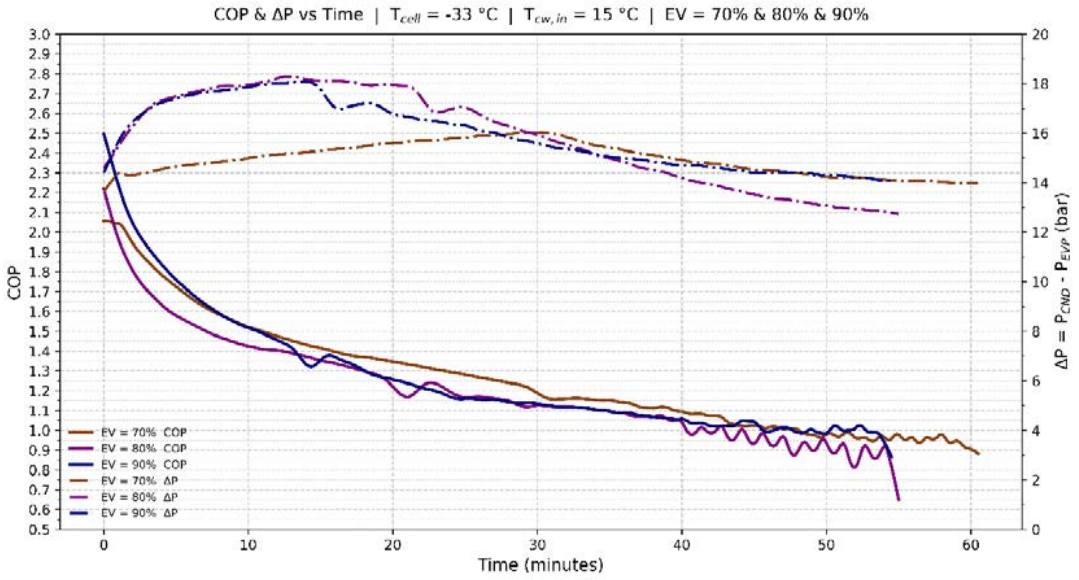

Figure 83 COP and ΔP VS Time ($T_{cw,in} = 15\ ℃/\ T_{cell} = -33\ °C$)

The suction pressure continues to decrease as T_{cell} drops from -23 °C to -33 °C which results in higher ΔP values that increase the compressor pressure ratio. The compressor operates under increasing pressure ratios because of the rising compression load which causes COP values to decrease until they reach their lowest points at -33 °C. The performance variations between the 70 %, 80 %, and 90 % EV settings become less noticeable when operating at temperatures below -33 °C because the system requires vapor injections to maintain compressor stability rather than achieve efficiency gains.

As shown in figure 84, the chamber temperature follows an exponential cooling pattern while decreasing from +13 °C to -23 °C at the target temperature of -23 °C. The COP curves indicate that the system starts with a COP of 2.0–2.1 during the initial cooling phase before it decreases to 1.1–1.2 as the chamber temperature reaches its target. The suction pressure decrease leads to increased compression ratio which results in higher compressor work W_{cmp}. The navy-blue line representing EV = 90 % delivers the highest performance throughout most of the operating period. The 90 % EV setting enables faster chamber cooling to reach -23 °C sooner while achieving better COP performance than the 70% and 80% configurations. The scroll compressor benefits from vapor injection because it enhances mass flow rates and improves compression efficiency during moderate cooling operations before injection work becomes significant enough to reduce COP.

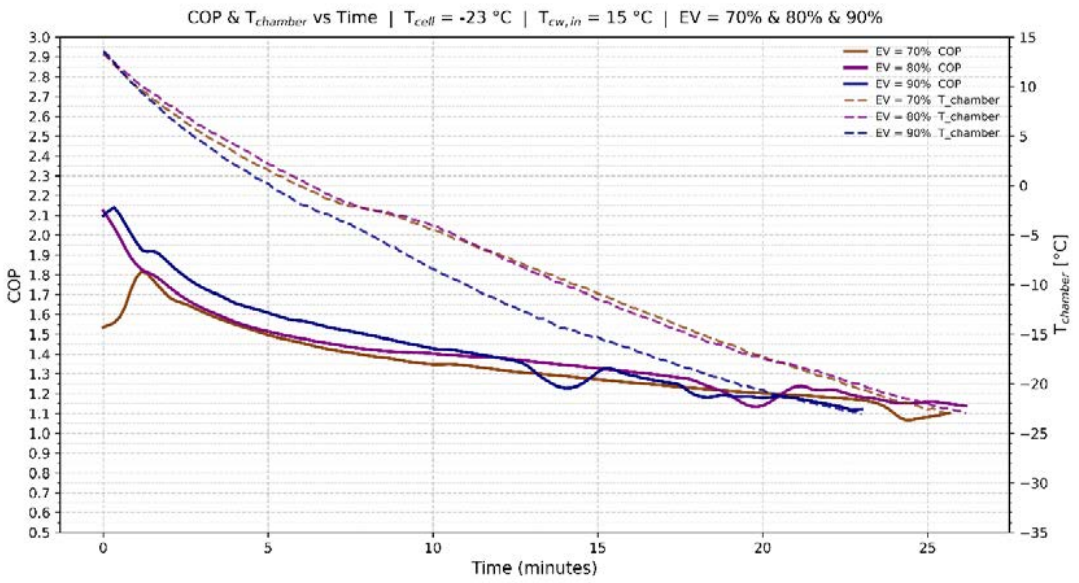

Figure 84 COP and $T_{chamber}$ VS Time ($T_{cw,in} = 15$ ℃/ $T_{cell} = -23\ °C$)

The system requires an extended period of demanding pull-down operations when operating at -28 °C. The chamber temperature begins at +13 °C before it reaches -28 °C during this test. The EV = 90 % curve shows the fastest temperature decrease from start to finish while maintaining lower $T_{chamber}$ values than the other two settings throughout the process. The EV = 80 % setting shows the slowest cooling rate while the EV = 90 % setting shows the fastest cooling rate throughout the entire cooling process.

The COP profiles show efficiency starting at 2.0–2.1 before it decreases to 1.0–1.1 throughout the process. The operating window shows EV = 90 % achieving the highest COP while EV = 70 % produces the lowest COP and EV = 80 % falls between them. A brief COP decrease occurs for EV = 70 % between minutes 24 and 25 because of a short-term control or operational issue but it does not affect the general pattern. The cooling process at -28 °C temperature achieves better thermodynamic performance through EV = 90 % vapor-injection because it provides faster chamber cooling and superior COP values compared to EV = 70 % and EV = 80 % (Figure 85).

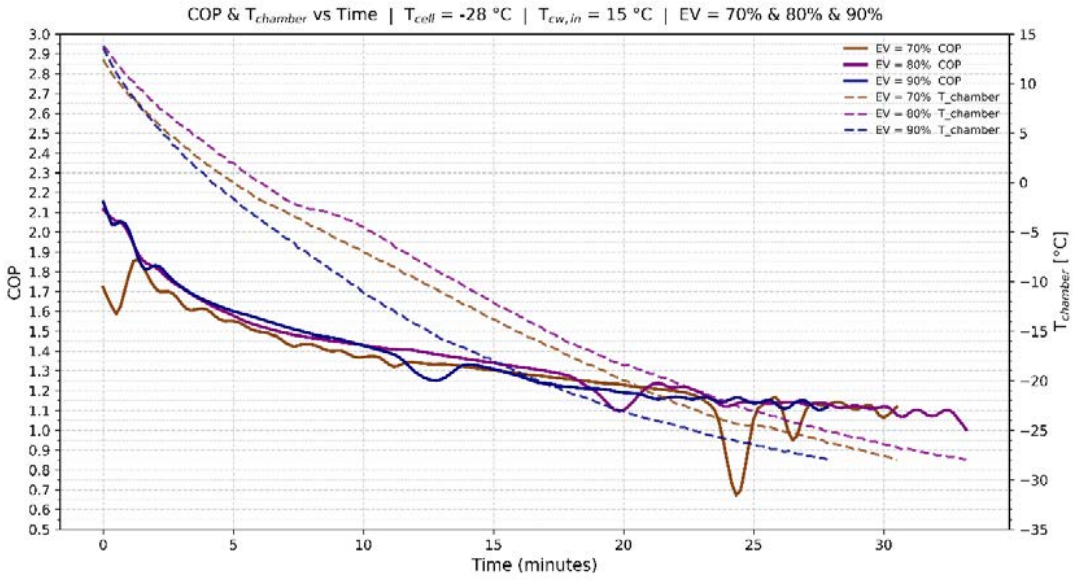

Figure 85 COP and $T_{chamber}$ VS Time ($T_{cw,in} = 15$ ℃/ $T_{cell} = -28\,°C$)

The system reaches its lowest operating temperature at -33 °C while the pull-down cycle extends its duration. below -30 °C before the other two settings do while EV = 70 % maintains the highest the three $T_{chamber}$ curves demonstrate that EV = 90 % produces the fastest cooling rate which reaches temperature and needs extended time to achieve the target temperature.

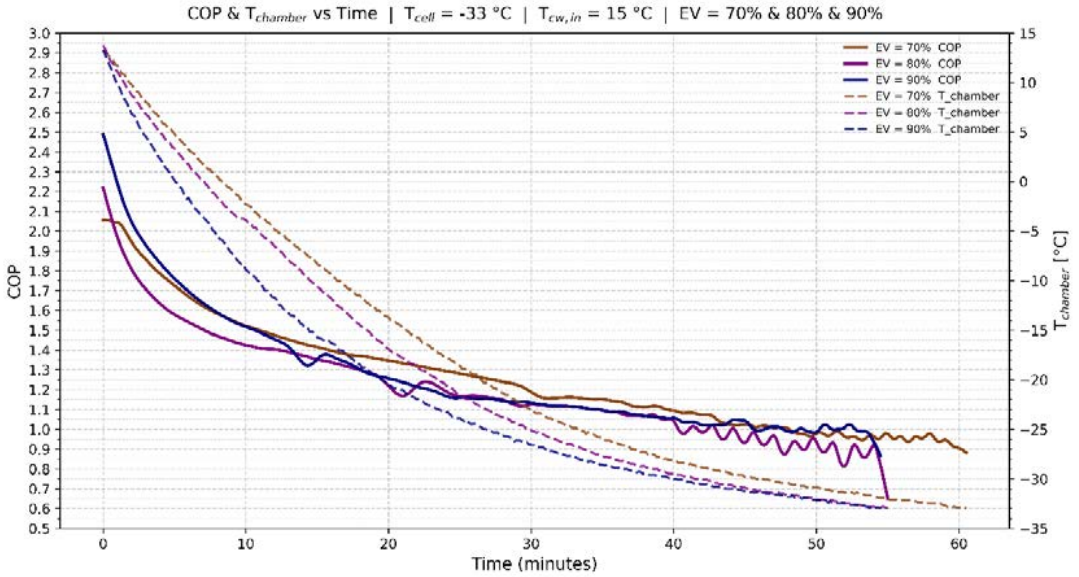

Figure 86 COP and $T_{chamber}$ VS Time ($T_{cw,in} = 15$ ℃/ $T_{cell} = -33\,°C$)

The initial COP values for EV = 90 % reach 2.3–2.4, but all three curves merge into a 0.9–1.1 range when $T_{chamber}$ approaches -33 °C. The suction pressure reaches extremely low levels when evaporating temperatures reach very low points, which causes the compressor pressure ratio to increase dramatically thus eliminating vapor injection efficiency advantages. As shown in figure 86, The high EV opening provides benefits for discharge temperature management and compressor stability, but it does not compensate for the efficiency losses caused by the large ΔP.

The chamber set point reduction from -23 °C to -33 °C causes the cooling process to decelerate while the system operates at successively lower evaporating temperatures. The system experiences decreasing suction pressure while the compressor pressure ratio increases because of this process. The COP values for all three EV settings decrease steadily until they approach 1 when the system operates at its lowest temperature. The system achieves better performance at -23 °C and -28 °C through EV = 90 % vapor injection because it enables faster chamber cooling and maintains higher COP values than EV = 70 % and EV = 80 %. The efficiency advantage of vapor injection becomes negligible when the target temperature reaches -33 °C. The system operates at deep-evaporation conditions where vapor injection functions as a stabilizing factor that controls discharge temperatures and protects compressor reliability instead of enhancing COP performance.

As shown in figure 87, the pull-down curve from the $T_{cell} = -23$ ℃ test shows the system moves from its initial warm state to a temperature range where the evaporator-chamber temperature difference becomes smaller. The initial process phase produces high instantaneous compression work W because the product/chamber air temperature difference with the evaporator surface remains large which results in maximum heat transfer into the evaporator. The Active Power reaches its highest value during the initial stages because the compressor needs to handle increased refrigerant mass flow and high-pressure ratios which create additional mechanical stress. The decreasing chamber temperature causes $T_{chamber}$ to reach -23 °C which results in reduced heat absorption by the evaporator until W reaches stable lower values. The Active Power shows identical behavior by moving toward a stable operating range when the system reaches thermal balance. The system operates in a temperature-holding phase after the pull-down phase because the pressure ratio remains acceptable and the electrical input power matches the compression work W at this point.

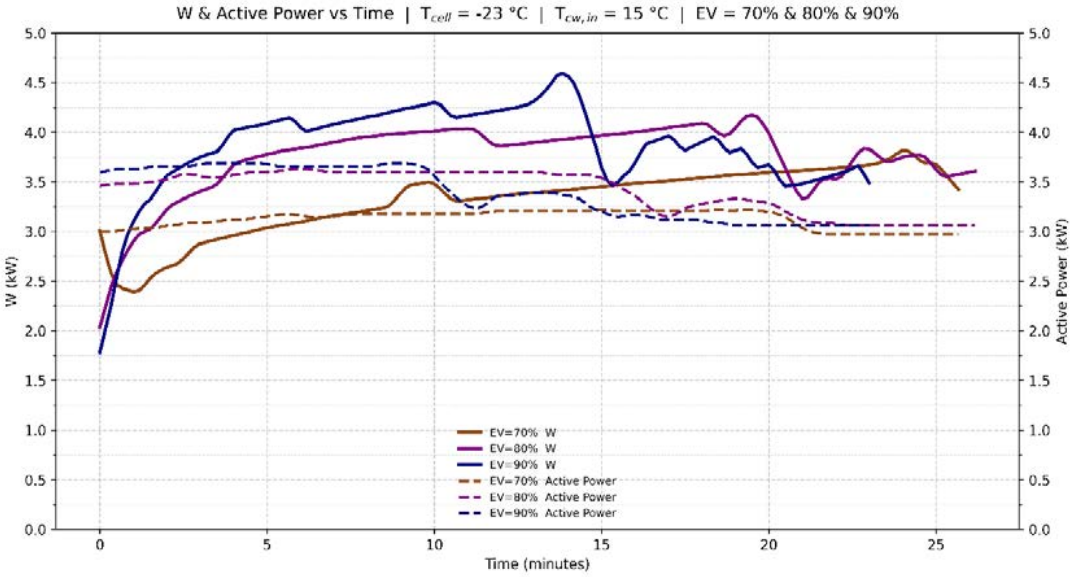

Figure 87 W and Active Power VS Time ($T_{cw,in} = 15$ ℃/ $T_{cell} = -23\ °C$)

The test with $T_{cell} = -28$ ℃ follows the same cooling process as before but requires the chamber to achieve a lower final temperature. The system needs to operate at lower suction pressure while handling a bigger temperature difference between the product and evaporator which results in an extended initial phase. The graph shows an extended initial phase because the system operates at high compression work W due to its large heat load.

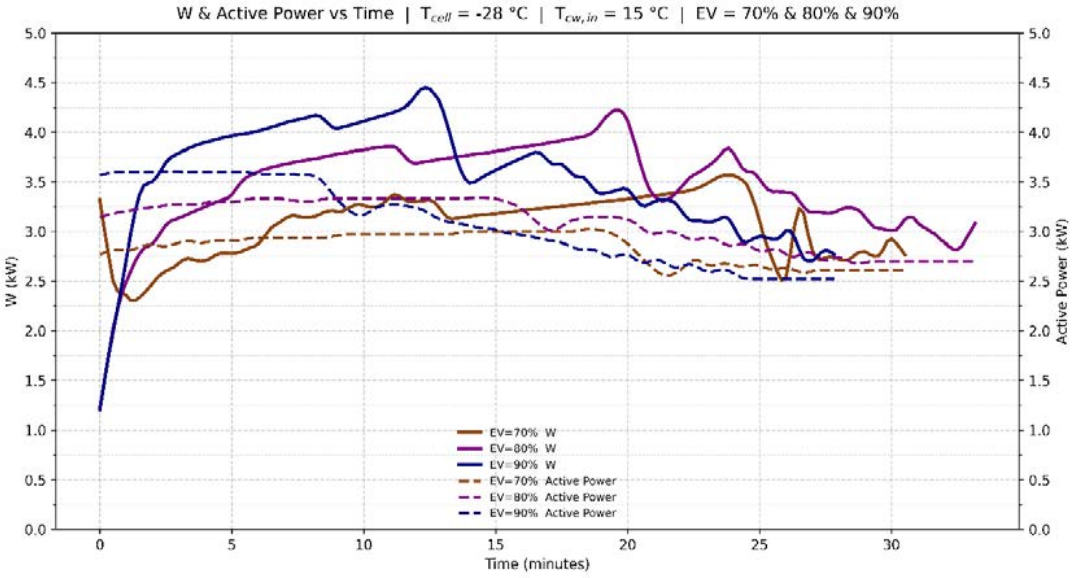

Figure 88 W and Active Power VS Time ($T_{cw,in} = 15$ ℃/ $T_{cell} = -28\,°C$)

Active Power maintains its high level because the system operates at both high ΔP and high refrigerant mass flow rates which increase compressor mechanical and electrical requirements (Figure 92). The thermal load decreases as $T_{chamber}$ approaches -28 °C which causes W to decrease but at a slower rate than in the -23 °C test. The system operates at high-load conditions for an extended period. The system operates at high load and high energy to achieve deep chamber cooling temperatures.

The system operates at its most challenging point during the $T_{cell} = -33$ ℃ test. The chamber needs to cool from its initial high temperature down to deep freezing temperatures which creates a long period where suction pressure stays low while condensing pressure stays stable. The system operates at high values for both ΔP and compressor pressure ratio during this time. The Active Power maintains high levels throughout this period because the compressor needs to fight against strong pressure differences while extracting substantial heat from the chamber to reach its target temperature. The compression work W maintains its high value throughout this period until the chamber temperature reaches -33 °C. The work value decreases slowly until it reaches a stable lower point. The system operates at a lower power level after reaching its final operating point, as shown in figure 89.

The system operates at a decreased electrical-to-cooling efficiency during deep freezing because it needs to maintain high power input while the evaporator load decreases with chamber temperature reduction.

Industrial freezing systems demonstrate this pattern because they require additional energy to achieve each degree of temperature decrease when operating at low temperatures.

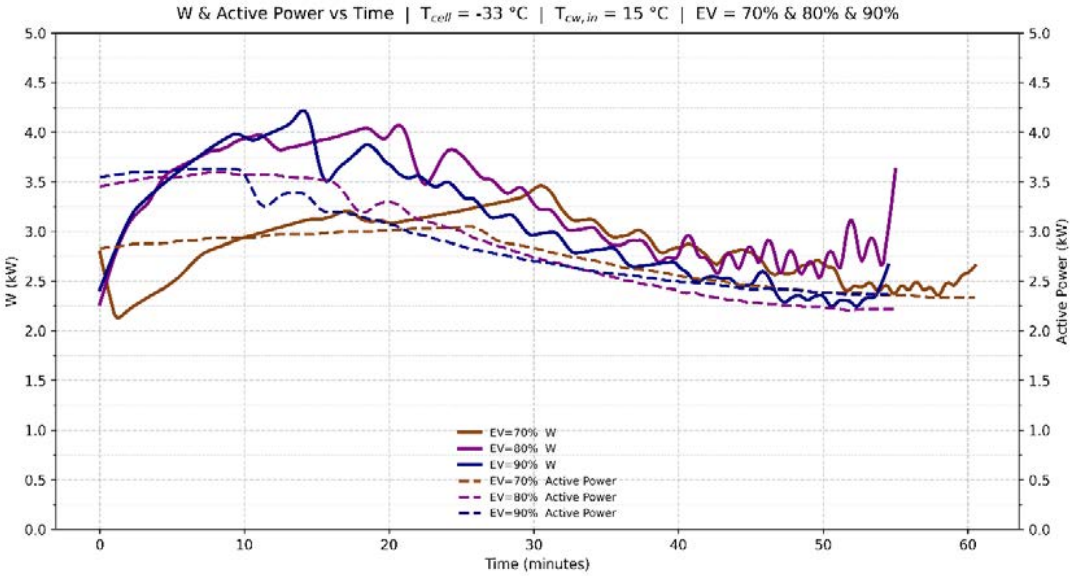

Figure 89 W and Active Power VS Time ($T_{cw,in} = 15$ ℃/ $T_{cell} = -33\,°C$)

The three plots demonstrate that the high-load phase duration extends when the chamber set point temperature decreases. The system maintains operation at high pressure ratios and substantial thermal loads for an increasing duration. The system needs to operate at higher pressure ratios and handle more thermal load during its extended high-load phase. The compressor needs more work input when T_{cell} decreases from -23 °C to -33 °C which results in lower efficiency for producing useful cooling units despite maintaining similar W and Active Power curve shapes.

Figure 90 demonstrates that the compressor electrical energy consumption grows continuously when the chamber set point decreases from -23 °C to -28 °C and then to -33 °C for all three EV operating modes. The process of temperature reduction at lower levels requires extended time under suboptimal operating conditions which results in higher total energy usage.

The EV = 80 % configuration consumes the most energy at -23 °C and -28 °C set points but the 70 % and 90 % settings demonstrate slightly better performance. The 80 % opening requires additional mass flow rate and higher power consumption which results in higher energy usage than any potential time savings during pull-down operations. The three EV settings demonstrate increased energy consumption at -33 °C but EV = 70 % shows the highest total energy usage while EV = 80 % and EV = 90 % settings achieve slightly better results. The shorter pull-down time of higher EV openings helps reduce their power consumption during deep-freezing operations although the process remains more energy-intensive than reaching the other two temperature levels.

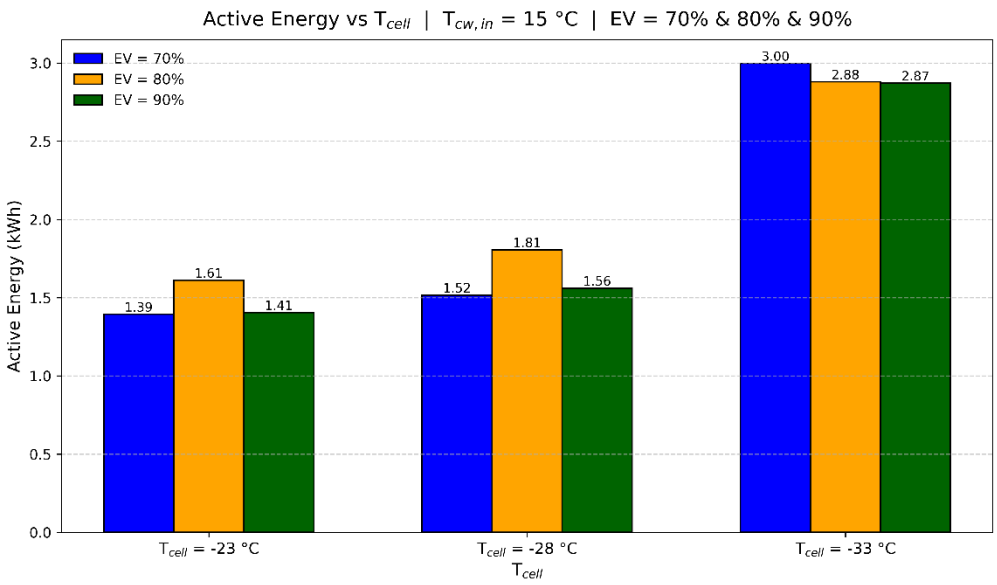

Figure 90 Active Energy VS T_{cell} ($T_{cw,in}$ = 15 ℃)

In figure 91, the T_{cell} plot shows three features that appear together at the beginning of the test: The evaporator cooling capacity Q_{evp} and COP reach their highest points at the start before they both decrease throughout the measurement period. The observed pattern matches what would happen during a typical moderate temperature reduction process. The system starts with high heat absorption from the evaporator because the chamber temperature remains warm and the refrigerant temperature difference with the internal air/product is at its maximum. The compressor operates at a reasonable efficiency during this initial period because the suction pressure remains high and the pressure ratio does not reach critical levels that would increase compressor energy consumption. The chamber temperature approaches its set point of -23 °C while the available heat load decreases, which causes Q_{evp} to decrease and the cycle efficiency decreases because of the continuing suction pressure reduction. The COP reaches a lower value because of this process. The curves show that the system maintains a balanced relationship between cooling requirements and operational expenses at this temperature point, which results in efficient and well-behaved pull-down operations.

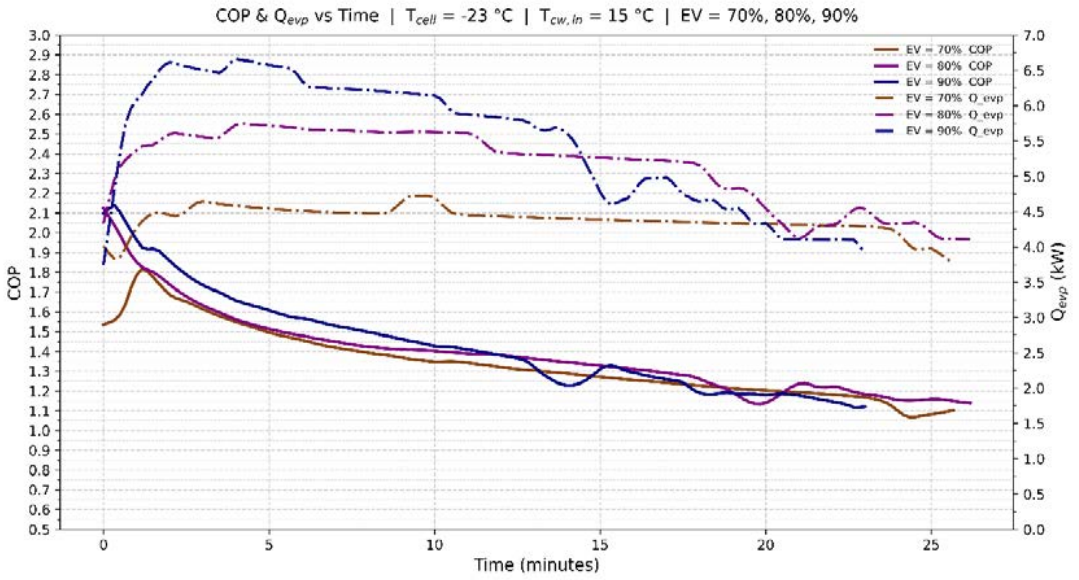

Figure 91 COP and Q_{evp} VS Time ($T_{cw,in} = 15$ ℃/ $T_{cell} = -23$ °C)

The system operates with the same thermodynamic principles as the -23 °C test but shows extended and heavier curves when the target temperature reaches -28 °C. The chamber needs to reach a lower temperature, so it stays in a warm refrigeration zone for an extended period. The system maintains high Q_{evp} values throughout an extended period before reaching the low-load region. The system needs to operate at a higher-pressure ratio because the suction pressure reaches levels below those of the -23 °C test. The graph demonstrates how lowering the set point temperature affects the system operation. The system needs to run at high cooling loads and heavy compression ratios when it operates at deeper target temperatures. The system maintains high cooling capacity throughout the cycle, but this results in decreased efficiency and increased energy expenses for refrigeration (Figure 92).

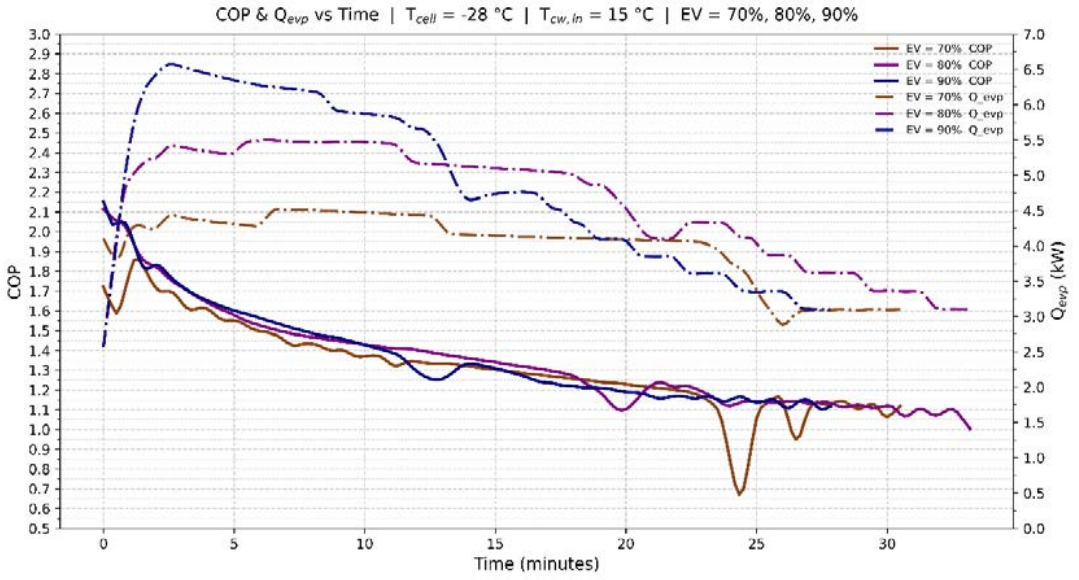

Figure 92 COP and Q_{evp} VS Time ($T_{cw,in} = 15$ ℃/ $T_{cell} = -28$ °C)

In figure 93, the system reaches its deepest cooling point at $T_{cell} = -33$ °C because the temperature plots demonstrate this condition. The Q_{evp} value remains high during the initial stage of the pull-down because the chamber maintains a large amount of stored heat. The Q_{evp} curve shows a steady decrease toward minimal values when the temperature reaches -33 °C. The system shifts from heat removal to temperature preservation because the thermal demand becomes minimal.

The COP values throughout this section show their lowest points before they merge into a flat band that represents the target temperature. The system experiences three main factors which cause this behavior: low suction pressure and high compression ratio and decreased cycle efficiency. The compressor needs to perform extensive mechanical operations to maintain refrigerant circulation because the evaporator operates at extremely low temperatures and has restricted heat removal capabilities.

The plot demonstrates that deep freezing requires a major thermodynamic cost because the cycle needs to use extra energy to achieve each unit of cooling at lower temperatures.

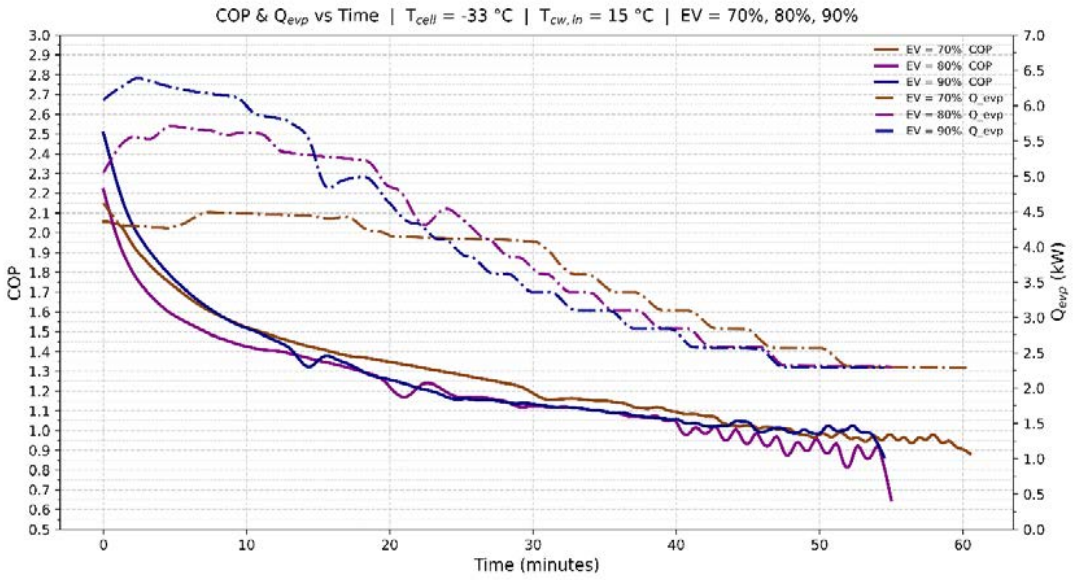

Figure 93 COP and Q_{evp} VS Time ($T_{cw,in} = 15$ ℃/ $T_{cell} = -28$ °C)

5.3 $T_{cw,in} = 10$ ℃, Maximum Opening Expansion Valve = 70%, 80%, and 90%, $T_{cell} = -23$ ℃, -28 ℃, -33 ℃ (6 Tests)

The system operates at -23 °C set point within a pressure range that maintains normal vapor-compression cycle conditions between the condenser and suction line. The time-dependent plot shows a moderate ΔP value which experiences minimal changes throughout the measurement period. The test results show high COP values which decrease slowly when the chamber temperature drops and the evaporating temperature decreases. The system operates at -23 °C within a temperature range where compressor work increases due to rising ΔP pressure difference but Q_{evp} decreases at a rate that

maintains acceptable energy efficiency. The three EV settings produce identical operational behavior at this condition because their curves show only minor vertical position changes without any fundamental changes in system operation (Figure 94).

As shown in figure 95, the -28 °C test requires the chamber to reach deeper temperatures which extends the compressor operation time under reduced suction pressure. The plot shows the ΔP curve maintaining elevated levels throughout an extended period of the pull-down process compared to the -23 °C test. The extended period of high-pressure difference between the system components leads to decreased COP values throughout the test. The cycle needs to stay in high work per kilogram operation for refrigerant during the -28 °C temperature achievement but the cooling load decreases when the chamber approaches the set point temperature. The figure 88 shows exactly what happens when the system operates under less favorable conditions because of the increased ΔP and decreased COP and extended operation time.

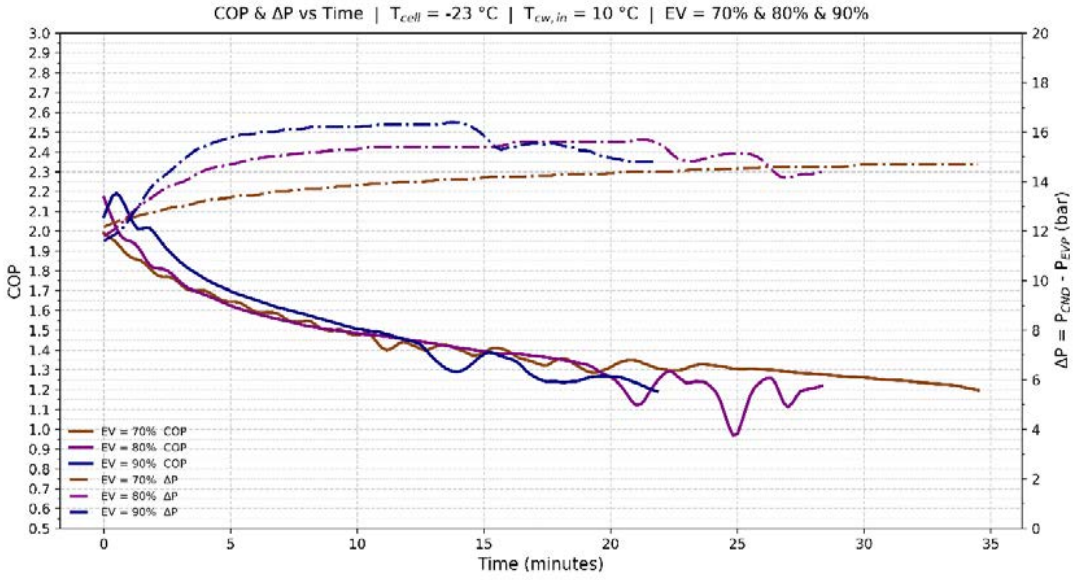

Figure 94 COP and ΔP VS Time ($T_{cw,in} = 10$ ℃/ $T_{cell} = -23\ °C$)

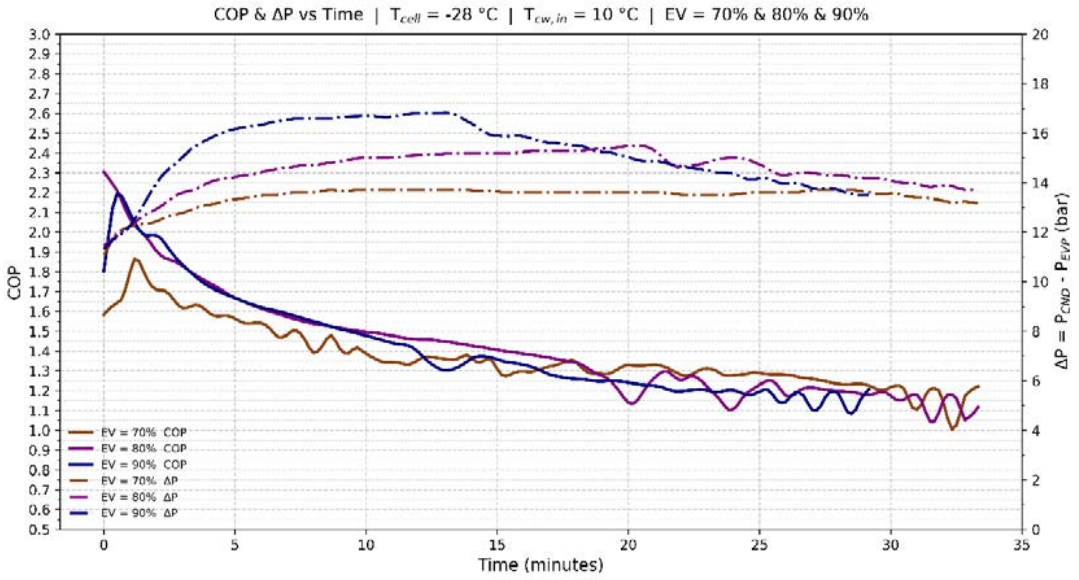

Figure 95 COP and ΔP VS Time ($T_{cw,in} = 10$ ℃/ $T_{cell} = -28$ °C)

The cycle operates at its most challenging point when the set point reaches -33 °C. The suction pressure reaches its lowest point during this test while the condenser–suction pressure difference stays at its peak throughout most of the pull-down process. The plot shows continuous high ΔP reading throughout most of the operating time.

Figure 100 provides a graphical representation of the trends.

The COP values reach their lowest points during the tests at all evaluated temperatures before the three EV settings approach identical low values during the final stages of the pull-down. The system's behavior shows that deep-freezing conditions make EV settings less important than the fundamental thermodynamic limitations which include low evaporation temperature and large compression ratio and high specific work needs despite small Q_{evp} values. The same fundamental conditions, which include low suction pressure and high ΔP values, dominate the system operation at −33 °C temperature regardless of the EV strategy used.

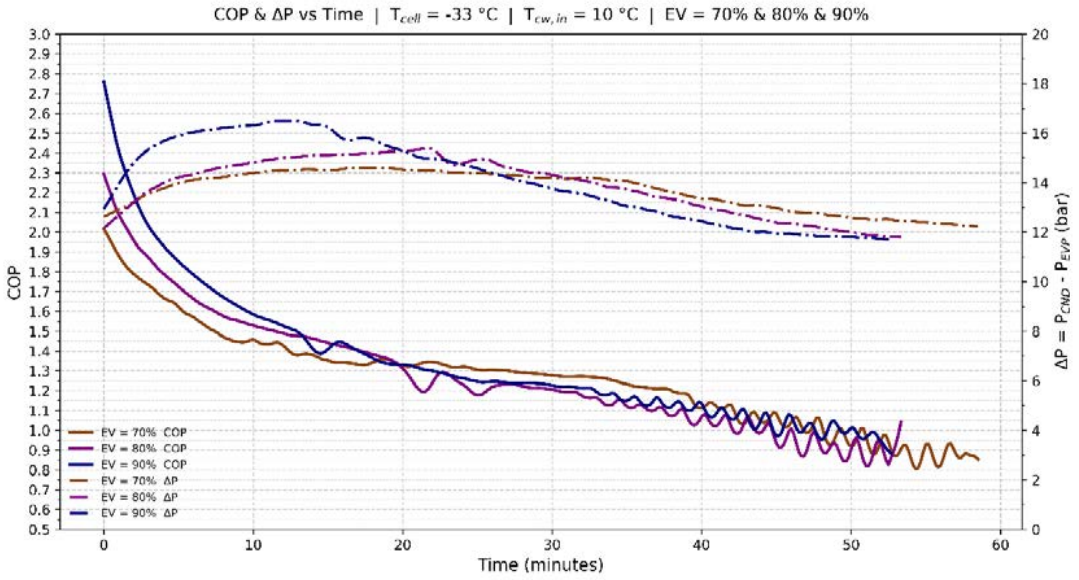

Figure 96 COP and ΔP VS Time ($T_{cw,in} = 10$ ℃/ $T_{cell} = -33$ °C)

The three plots demonstrate that T_{cell} operating point transitions from a balanced ΔP and acceptable COP region to a high ΔP and low COP region when the temperature decreases from -23 °C to -33 °C. The system maintains a suitable balance between cooling performance and compression work at -23 °C. The cycle spends more time under heavy compression at -28 °C which causes the COP to decrease substantially. The system operates in deep-evaporation conditions at -33 °C which creates massive pressure differences that dominate system performance while making EV settings less important.

As shown in figure 97, the T_{cell} plot shows $T_{chamber}$ temperature shifting from its initial warm state to its target value through a smooth and continuous process. The COP curves show that the system operates in a comfortable zone during the initial pull-down period because the chamber temperature remains high and suction pressure remains low, and the condenser to evaporator pressure difference stays moderate, thus preventing extreme compression ratios. The system starts with high COP values, which decrease slowly while the chamber temperature reaches its target.

The system experiences two simultaneous effects when $\mathrm{T_{chamber}}$ reaches -23 °C. The evaporator receives less thermal energy, which causes $\mathrm{Q_{evp}}$ to decrease while the suction pressure keeps dropping to increase compressor specific work. The figure 101 shows the exact pattern that emerges from these two opposing trends, which cause the COP curves to start at high values before reaching a stable lower region during the target temperature approach. The three different EV settings produce similar results at this temperature because they only affect small details in the curves without changing the basic operation of the cycle.

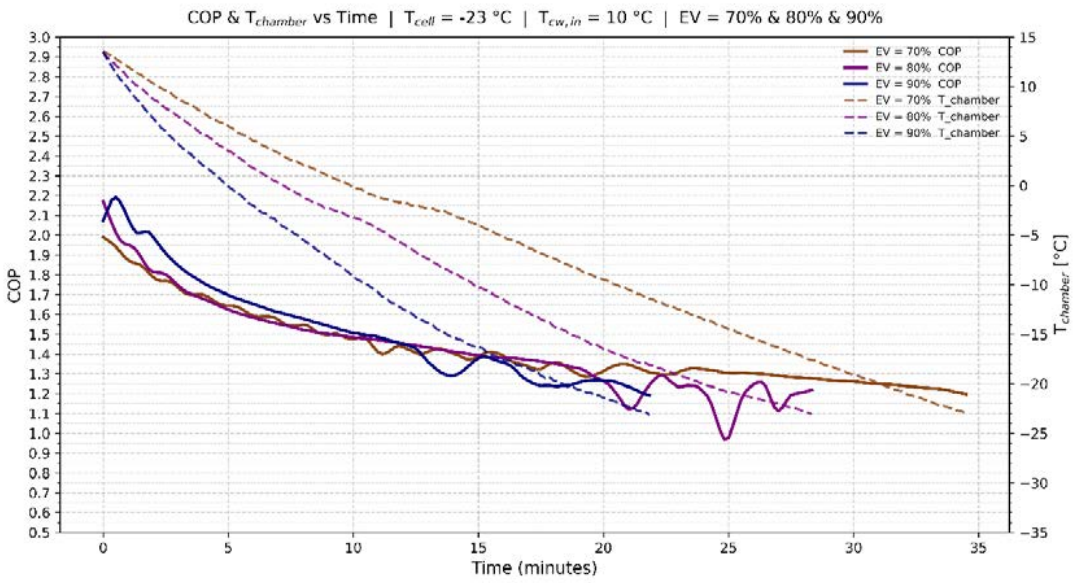

Figure 97 COP and $T_{chamber}$ VS Time ($T_{cw,in} = 10$ ℃/ $T_{cell} = -23\ °C$)

The $T_{chamber}$ curve of the plot at -28 ℃ shows that the chamber needs to reach a lower temperature for increased subzero condition time (Figure 98). The system operates with increased temperature differences between the evaporator and condenser during this extended period which results in lower suction pressure. The visual appearance of the COP curves shows this effect. The test starts with proper COP values which decrease at a faster rate than during the -23 ℃ test. The system enters a deep subzero zone when $T_{chamber}$ reaches zero temperature because it needs to cool the system at high rates. The system experiences increased stress during pull-down operations which leads to early entry into low-efficiency operating modes.

The three EV settings maintained equal performance during this temperature test without causing any system failures or performance enhancements. The system performance variations become more extreme at this temperature because the cycle undergoes additional thermodynamic testing.

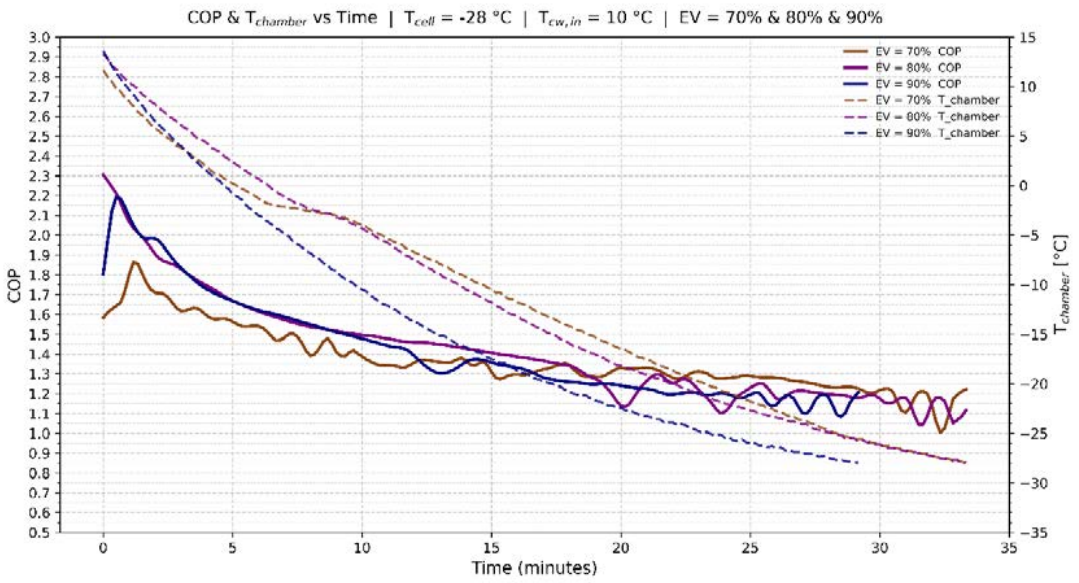

Figure 98 COP and $T_{chamber}$ VS Time ($T_{cw,in} = 10$ ℃/ $T_{cell} = -28\,°C$)

The $T_{chamber}$ curve in $T_{cell} = -33$ ℃ plot demonstrates that the chamber reached the lowest cooling range and stayed at extremely low temperatures over a long time. In terms of the cycle, this implies that the suction pressure remains at minimum over a large period, and the discharge suction pressure ratio is close to its most undesirable value.

In such circumstances the COP curves merely attest to this thermodynamic fact. They begin to fall below the tests of the -23 °C and -28 °C tests and, as the pull-down continues and the chamber reaches the temperature of -33 °C, the COP is confined to a very narrow and persistently low band. Towards the end of the test the three EV curves are concentrated around the same range, which means that the dominating effect of the deep-evaporation regime very low suction pressure in conjunction with a very high compression ratio overshadows the effect the EV setting introduces to a large degree.

Fluctuations in behavior are still possible at this point based on the EV configuration, however, past a certain point the cycle is merely being stretched to the point of demanding operation. Of course, the COP can be improved but very little, irrespective of fine adjustments to the injection or mass-flow setting (Figure 98).

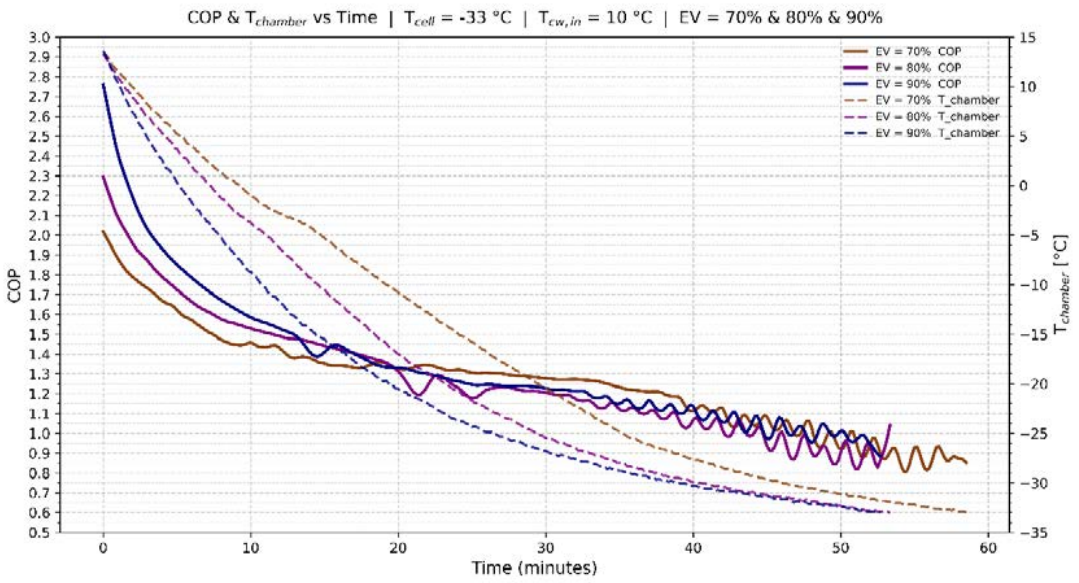

Figure 99 COP and $T_{chamber}$ VS Time ($T_{cw,in} = 10$ ℃/ $T_{cell} = -33\ °C$)

The system is still functioning in its comfortable performance range at the set point temperature of -23 °C. This first increase of W and Active Power is directly proportional to the thermal loading because, at this point, the chamber is still hot, but the suction pressure is not sufficiently low that the compressor is subjected to a hefty energetic penalty. In the central part of the plot, the balance between evaporator load and input power is reasonable as the compressor approaches a quasi-steady operating regime as the temperature in the chamber drops.

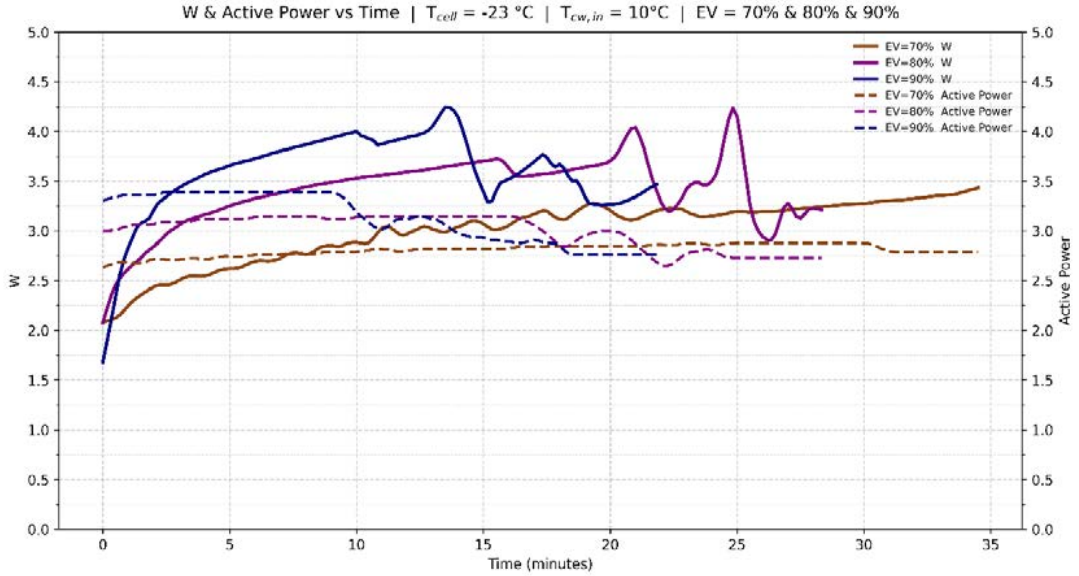

Figure 100 W and Active Power VS Time ($T_{cw,in} = 10$ ℃/ $T_{cell} = -23\ °C$)

The effect of the two curves is that as the pull-down progresses, the two curves begin to taper at the same time which shows that the system is moving in the direction of thermal equilibrium. In general,

the figure shows that a refrigeration cycle at -23 °C has a reasonable energy efficiency without subjecting the compressor to excessive mechanical or energetic demands (Figure 100).

As mentioned in figure 101, the -28 °C graph reveals that the less the chamber cools down and the lower the evaporation temperature, the more the characteristics of the W Active Power relationship will appear to be stretched. At the beginning of the test, the system acts like the one in that of -23 °C, and as the temperature drops, the suction pressure decreases to lesser values, and the compressor needs to do more work to circulate the same mass flow of refrigerant. This forms a long period where W is in a moderate level with Active Power being high. In practice, it means that the immediate load of the evaporator has reduced, but the energetic cost of compressor operation is also expensive.

The increasing discrepancy between the two variables represents a slow reduction in instantaneous efficiency: the cycle is still operating successfully but is increasingly finding itself in a more challenging operating regime. Towards the end of the test, both curves start to decrease but not with the same level of synchrony at the same time at 23 °C. Such behavior is completely anticipated at the temperature of -28 °C and demonstrates that it takes more specific compression work to move the system to lower cooling temperatures.

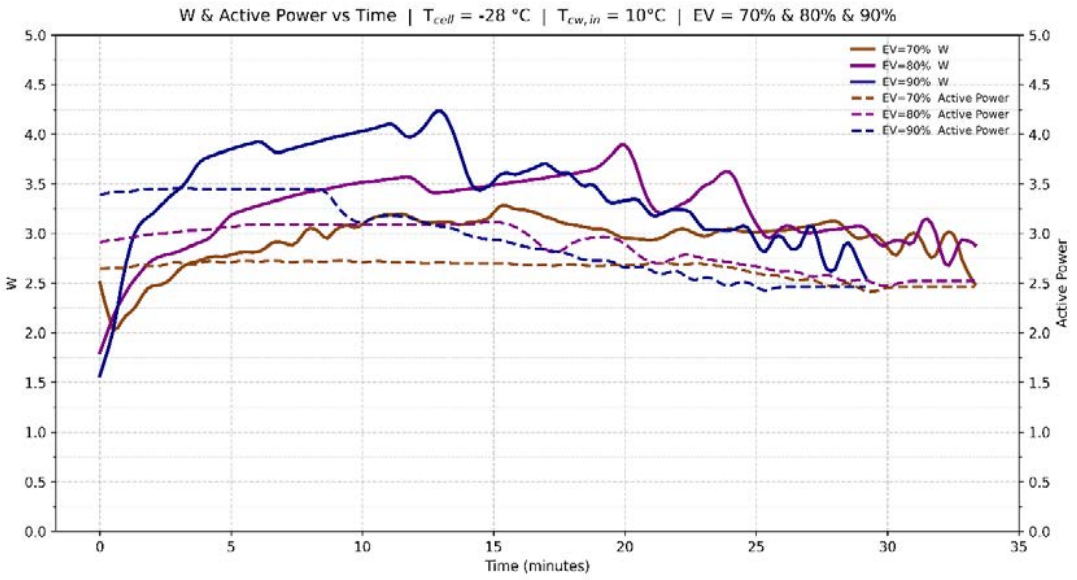

Figure 101 W and Active Power VS Time ($T_{cw,in} = 10$ °C/ $T_{cell} = -28\,°C$)

In the test, $T_{cell} = -33$ °C where the chamber is required to be drawn down to a deep-freezing target W and Active Power curves display that the system continues to show a definite bond among evaporator load and input power- however, now in a more exacting efficiency area than in the elevated temperature conditions. As the pull-down starts both variables increase correspondingly: the chamber remains warm, the thermal difference between the air and the surface of the evaporator is great, and the amount of removable heat (sensible and latent thermal content) is high. Consequently, W rapidly increases to relatively high values and the compressor in turn increases Active Power to obtain the necessary mass

flow and overcome the high-pressure difference. The connection between the two curves is quite natural in this initial phase, the system is working in a range where any improvement in the cooling capacity is instantly followed by increased power demand. During the process, once the chamber cools down, two contradictory trends begin to emerge. On the one hand, the thermal storage of the chamber is slowly exhausted and the amount of heat that gets to the evaporator reduces, and W is reduced. Conversely, evaporating temperature decreases to a very low value, the suction pressure is lowered further, and the compression ratio increases, and the inherent cycle efficiency declines. One of the main characteristics of such plot is that Active Power is also reduced in direct proportion to W. This is evidenced by the fact that the system reacts physically to the falling load of the evaporator, and the compressor stabilizes at lower operational power levels towards the conclusion of the test.

This is a behavior which points to the fact that, despite deep freezing, the system does not enter the bad regime of low cooling load and almost constant input power. Rather, evaporator load and electric power reduction follow each other closely. However, since this decrease occurs at very low evaporating temperatures and a very high compression ratio, the total COP is low, and the amount of energy it takes to complete one unit of useful cooling is far greater than in the high target temperatures (Figure 102).

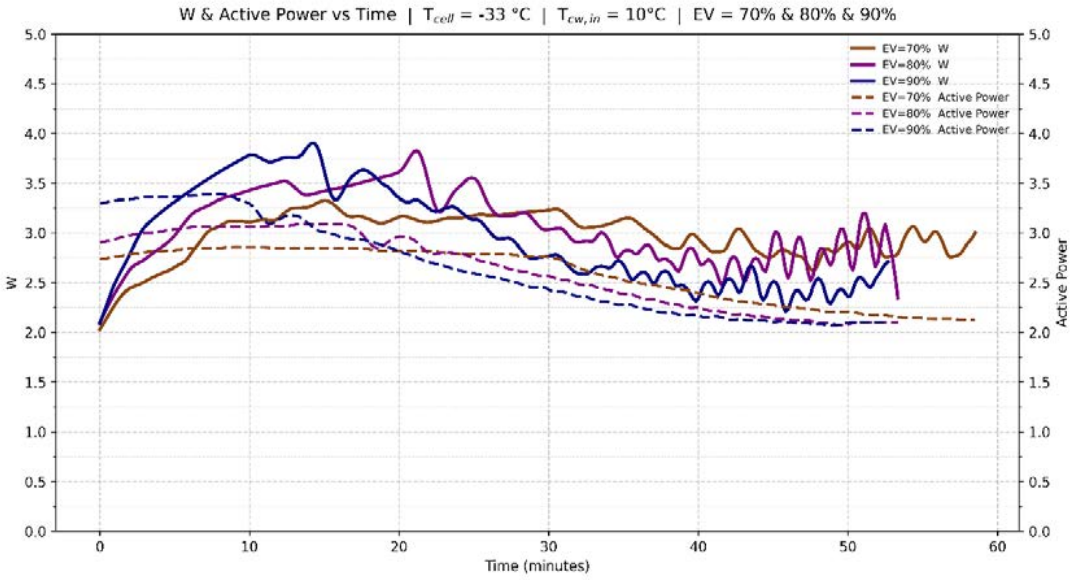

Figure 102 W and Active Power VS Time ($T_{cw,in} = 10$ °C/ $T_{cell} = -33$ °C)

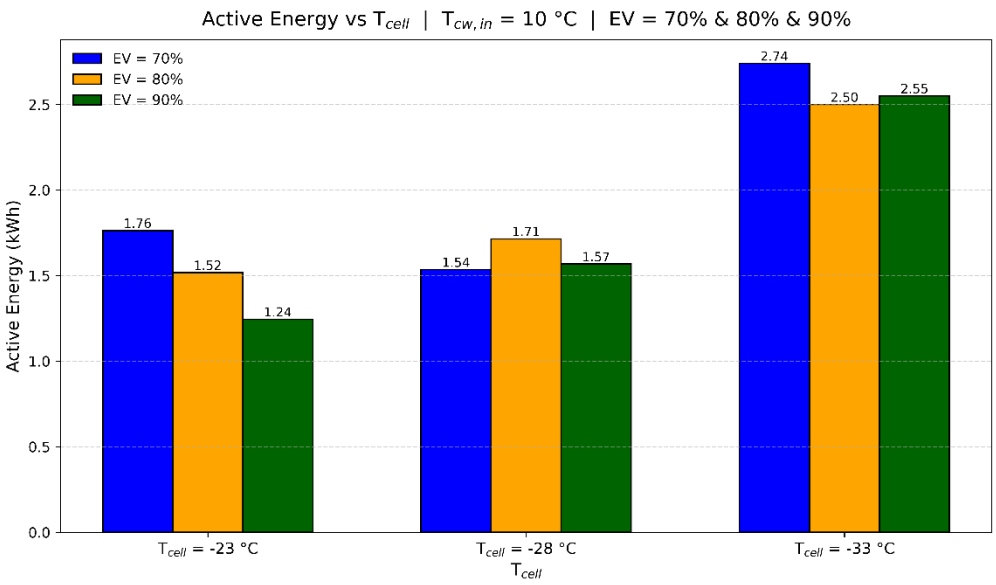

Figure 103 Active Energy VS T_{cell} ($T_{cw,in}$ = 10 ℃)

Figure 103 offers a concise and most useful perspective of real energy consumption it will take the refrigeration system to achieve the three desired temperatures of -23, -28 and -33 ℃. The figures depicted above every individual bar indicate the total electrical energy used by a compressor, i.e. the amount of power that the system needs to provide to bring the chamber down to the respective T_{cell}. An analysis of these bars will clearly show that there is a correlation where the lower the target temperature the more energy is required. It is quite simple, lower temperatures require the system to take more time to operate in areas with extremely low suction pressure, high compression ratio, and lower COP. Therefore, the cost of moving between any two temperatures of less than -28 ℃ and -33 ℃ is thermodynamically much more expensive than the cost of moving between two temperatures of less than -23 °C and less than -28 °C, and directly proportional to the numeric distance between the columns.

The three bars of EV of 70, 80 and 90 % at each temperature give further details. These differences demonstrate the impact of the EV on the trade-off between the pull-down time and instantaneous power demand. A higher bar out of a given EV signifies the presence of a longer pull-down period, higher average power rate of the compressor, or a combination of the two. In its turn, the shorter bar signifies how the system was able to pull down it faster or with a lower average power requirement.

Overall, the number shows that the target temperature itself is the powerful factor of energy consumption, and the setting of the EV is rather a behavioral-tuning factor than a major determinant of the cost of energy. The variations between EVs are on the comparatively fine scale, and those between -23, -28, and -33 ℃ are direct results of the thermodynamic nature of the vapor-compression cycle: the lower T_{cell}, the bigger the evaporating temperature lift, the lower the suction pressure, the more compression work, and therefore the more energy needed per unit of useful cooling.

As illustrated in figure 104, the system is still operating in a reliable zone at the -23 ℃ target condition with the evaporating temperature not yet dropping too low and the compressor functioning at a moderate compression ratio. With such operating conditions, the variations between the 70, 80, and 90 % EV settings is largely due to the changes in instantaneous capacity and not to inherent changes in the cycle behavior; the three curves differ in magnitude but almost have the same time variation. Simply, the cycle remains in its easy operating range at -23 °C, and a combination of a high COP and solid Q_{evp} profile point to a well-functioning, efficient system.

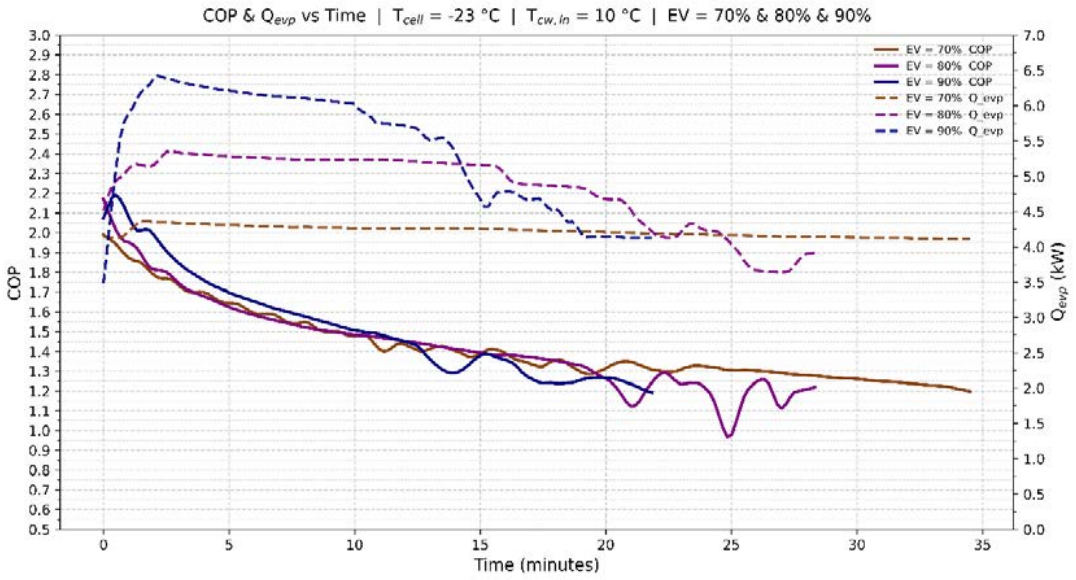

Figure 104 COP and Q_{evp} VS Time ($T_{CND} = 10$ ℃/ $T_{cell} = -23\ °C$)

The system operates in a more challenging temperature range when the target temperature reaches -28 °C. The system performance drops substantially because of the decreased suction pressure and elevated compression ratio and higher specific work per unit mass of refrigerant at this temperature. The average COP stays below 2.0 throughout the test period while operating between 1.2 and 1.8. The evaporator capacity remains high at the start of the pull-down process, but the duration of elevated capacity decreases and the capacity start to decrease sooner. The evaporator capacity (Q_{evp}) operates between 3.5 kW and 6.5 kW across different EV settings.

The system needs to perform additional compression work because its refrigeration capacity starts to decrease before the process reaches its end. The system performance becomes more dependent on EV settings when operating at these conditions because increased EV openings provide better initial capacity, but the system performance deteriorates faster than at -23 °C. The system performance deteriorates at −28 °C because the system operates outside its most efficient temperature range while dealing with both low suction pressure and substantial thermal loads (Figure 109).

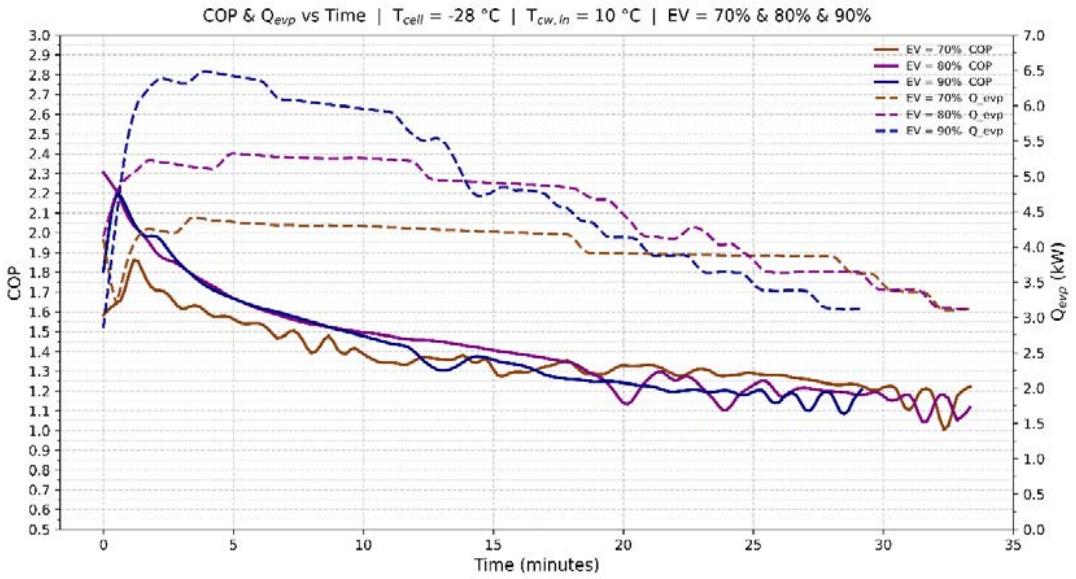

Figure 105 COP and Q_{evp} VS Time ($T_{CND} = 10$ ℃/ $T_{cell} = -28\,°C$)

The -33 °C plot shows how the system behaves under thermodynamic difficulties because it operates at this temperature. The suction pressure reaches extremely low levels because the evaporating temperature reaches such low points which results in increased compression ratio. The system operates at low efficiency throughout the test because the COP stays at the lowest point of the 0.5–3.0 scale. The system follows this specific pattern when operating under deep-freezing conditions because it loses cooling capacity while needing more energy to produce that capacity. The Q_{evp} curve supports this analysis. The evaporator capacity remains high during the initial stages of the pull-down because of the big temperature difference between the warm chamber and cold evaporator, but it rapidly decreases when the chamber temperature drops until it reaches stable lower levels before the other two cases. The system operates in a capacity-limited zone because the combination of decreased product heat load and reduced heat-transfer potential and low suction pressure limit the system's net cooling output.

The three EV settings produce minimal variations in this plot because the system behavior at -33 °C depends primarily on deep evaporation thermodynamic restrictions instead of mass-flow modulation or injection level. The EV settings produce minimal differences during the initial stages of the pull-down, but the system reaches a common suction-pressure restriction which leads to low-efficiency operation when the chamber temperature reaches certain levels. The system behavior follows established patterns which scientists have documented for vapor-injection scroll cycles when they operate at extremely low temperatures, as mentioned in figure 106.

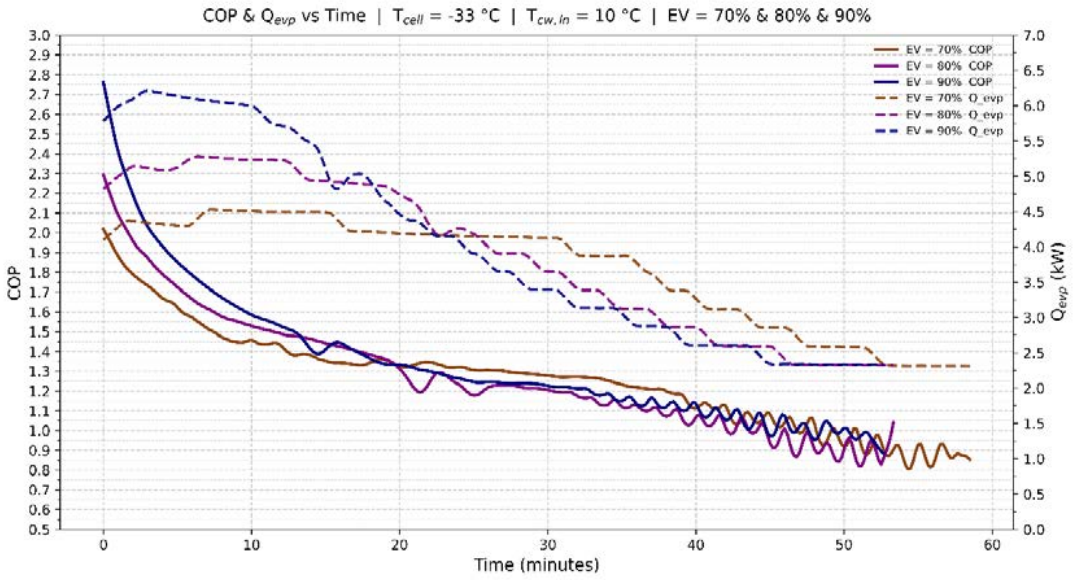

Figure 106 COP and and Q_{evp} VS Time ($T_{CND} = 10$ ℃/ $T_{cell} = -33$ ℃)

The principal international and European and North American food-safety standards establish -18 °C as the reference storage temperature for frozen seafood products. The storage of products at -18 °C temperature preserves their original texture and structural quality while safeguarding essential nutrients including vitamins and proteins and stopping water from moving through tissue. The combined effects of these processes lead to extended product shelf life which directly supports food safety for consumers [202–204].

The lowest target temperature of -18 °C was selected from the three options (-23 ℃, -28 ℃, -33 ℃) for all condenser-inlet conditions ($T_{cw,in} = 10, 15, 20$ ℃). The frozen fish surface temperature reached -27 °C to -28 °C under this condition which created a $6 \sim 7$ ℃ temperature difference between the chamber air and product surface. The surface temperature of the product would have reached -21 °C to -22 °C when the target temperature was set at -28 ℃. The system needs to run for an extended period to reach -18 °C internal product temperature because the surface temperature remains $3 \sim 4$ ℃ above this standard.

The product surface temperature at -23 °C would reach only $-16 \sim -17$ ℃ which falls short of the international standard requirement of -18 °C. The system needs to run for extended periods when operating at this temperature to reach core temperatures because short processing times are vital for maintaining food quality during freezing.

The Active Energy results from Figures 77, 90 and 103 support the selection of -18 °C as the best temperature for freezing actual fish products. The energy consumption patterns followed these patterns throughout the scenario:

- The Active Energy consumption between different EV settings remained similar at $T_{cw,in} = 10$ ℃ but EV = 80 % showed the lowest value.
- The lowest Active Energy value of 2.87 kWh occurred when $T_{cell} = -33$ ℃ and EV = 90% at $T_{cw,in} = 15$ ℃.
- The minimum Active Energy consumption of 3.63 kWh occurred when EV = 60 % during the −33 ℃ test at $T_{cw,in} = 20$ ℃.

Three test conditions were selected in which fish were placed inside the freezing chamber for evaluation (Table 29).

	T_{CND}	Maximum Opening Expansion Valve	T_{cell}
1	10 ℃	80 %	−33 ℃
2	15 ℃	90 %	−33 ℃
3	20 ℃	60 %	−33 ℃

Table 29 Test Conditions with Fish

5.4 $T_{cw,in} = 20$ ℃, Maximum Opening Expansion Valve = 60 %, $T_{cell} = -33$ ℃

The test condition requires condenser water entry at 20 °C while maintaining the chamber set point at −33 °C and expanding the expansion valve to its maximum position of 60 %. The system runs continuously until the chamber temperature reaches −33 °C after implementing these specific settings. The test reaches its endpoint at minute 64.2 when the chamber door opens to put the fish sample for placement on the shelf. The thermocouples are placed on the fish surface and inside its flesh, after which the door is closed immediately, as shown in Figure 107. The system starts operating again after door closure to achieve the desired product temperature of −18 °C.

The compressor operates in on-off mode throughout the experiment because it detects multiple occasions when the chamber temperature approaches −33 °C. The data-logging system, together with instrumentation described in earlier chapters, records all essential measurements including pressure readings and temperature data and electrical power consumption. The processed data undergoes thermodynamic calculations to generate additional parameters which become available for analysis. The experimental data serves as input to create the analytical graphs which follow in subsequent sections.

Figure 107 The Test Fish Along with its Temperature-Measuring Devices

The system enters a prolonged transient period after startup which causes the COP to decrease from its initial value of 1.86 to a stable range between 1.0 and 1.5 (Figure 108). The system follows this expected pattern because the chamber temperature approaches its set point while Q_{evp} decreases and the compressor needs to perform additional work to cool the system which results in a natural decrease of COP. The chamber door opens at 64.2 minutes and, after loading the fish at 69.8 minutes, the system continues its operation while the cycle experiences a thermal disturbance that causes the Active Power to increase, because the compressor must compensate for the higher thermal demand and the change in chamber conditions. After the door-opening event, the COP exhibits more pronounced fluctuations. These fluctuations occur due to the sudden change in thermal load and the thermodynamic effects of warm ambient air entering the cold chamber space. The system experiences a rapid increase in Q_{evp} which stabilizes at elevated operating levels because the product load requires additional cooling capacity. The system starts to reach a new operational equilibrium after the transient period, but the fish continues to lose heat, and its thermal requirements change so the system maintains oscillating operation at new average values.

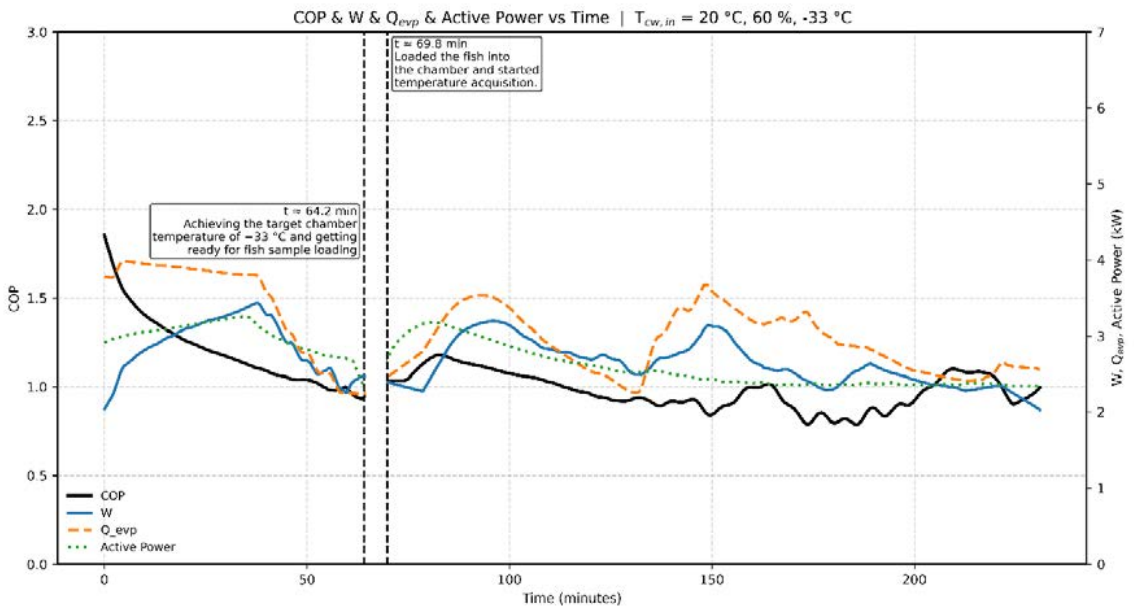

Figure 108 COP, W, Q_{evp}, and Active Power with Fish ($T_{cw,in}$=20 °C,60 %, -33 °C)

The product cooling process becomes evident through the data presented in Figure 109. The test starts with the chamber temperature decreasing from 13.7 °C ambient temperature to −33 °C at a steady rate which indicates the pre-cooling operation of the cabinet.

The fish enters the chamber at t ~ 69.8 min marks the beginning of the temperature decrease process. The fish surface and core temperatures remain above the chamber air temperature at this point which creates an intense temperature difference that leads to fast heat transfer between the product and its surroundings. The fish surface temperature rapidly decreases and reaches 0 °C within 19 minutes, then continues to cool until it reaches −27.50 °C at the end of the test. The core temperature of the fish requires a longer time and reaches 0 °C in 89 minutes. High-moisture food products show this specific behavior because their internal heat conduction rates determine how fast their central region can reach subzero temperatures after surface freezing.

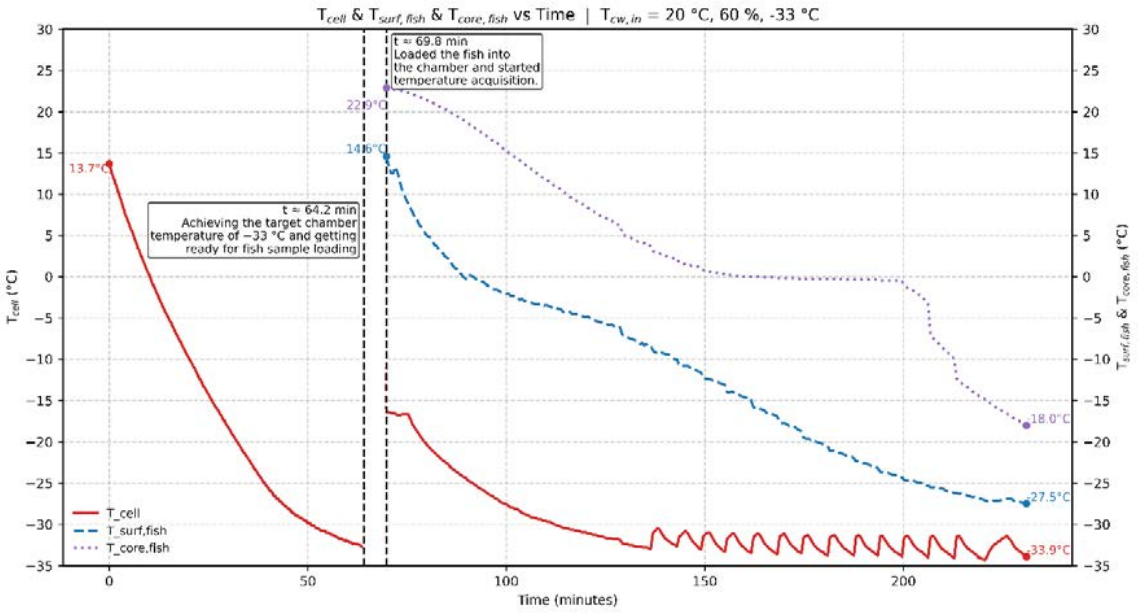

Figure 109 T_{cell}, $T_{surf,fish}$, $T_{core,fish}$ with Fish ($T_{cw,in}$ = 20 °C, 60 %, -33 °C)

Plot 110 shows how the COP and ΔP change over time to display both system transient behavior and product loading effects.

The system operates under pre-loading conditions from startup until t ~ 64.2 minutes. The system starts with high ΔP values because it operates at warm temperatures between suction and discharge pressures. The evaporator temperature decreases while condenser pressure stabilizes which causes ΔP to decrease until it reaches a stable range. The cooling capacity decreases while the chamber temperature approaches its target value which causes the COP to decrease at a steady rate. The system shows expected stable behavior for both COP and ΔP during this initial period.

The system experiences a sudden increase in cooling requirements when the fish enters the chamber at t ~ 69.8 minutes. The system needs to decrease suction pressure and increase its instant cooling capacity to maintain evaporating temperature stability. The system experiences a significant increase in ΔP because the suction pressure drops while the discharge pressure remains constant. The system experiences COP fluctuations during this time because it responds to the thermal impact of door opening and product addition. The system reaches a new stable ΔP value after the transient period while COP operates at a lower level to handle the increased cooling requirements from the product.

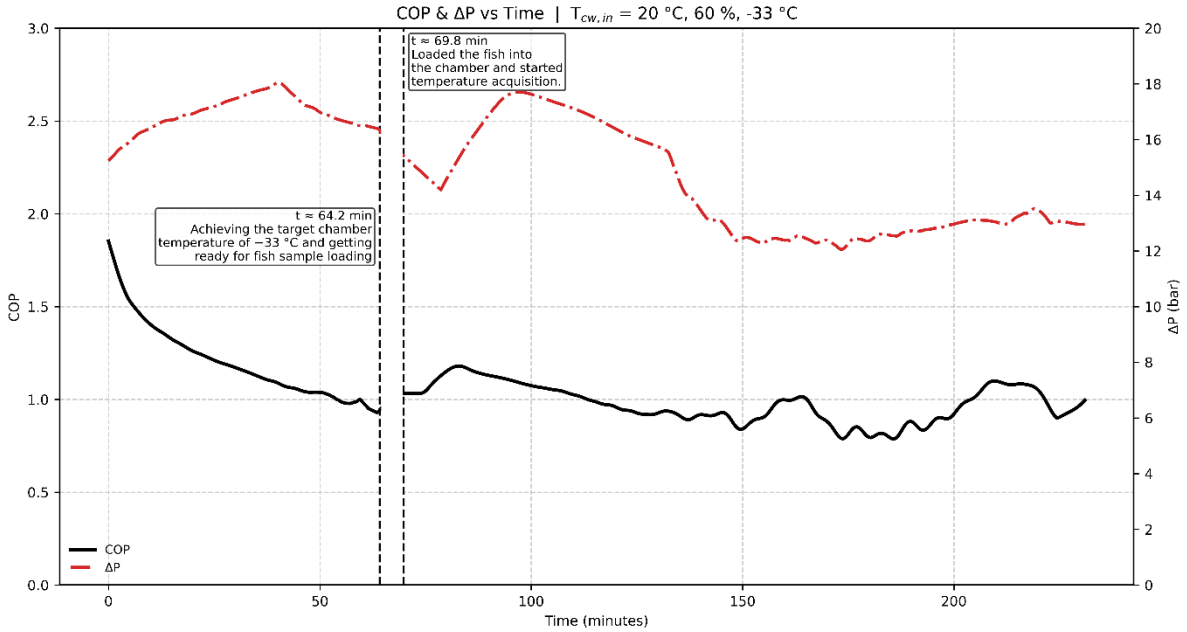

Figure 110 COP, ΔP with Fish ($T_{cw,in}$ = 20 °C, 60 %, -33 °C)

Figure 111 combines system energy patterns with product thermal reactions into one visual representation. The COP shows a continuous decrease while Q_{evp} stays constant because the chamber receives continuous ambient heat. The system requires more thermal capacity to handle rising demands which results in higher operational costs and decreased COP performance.

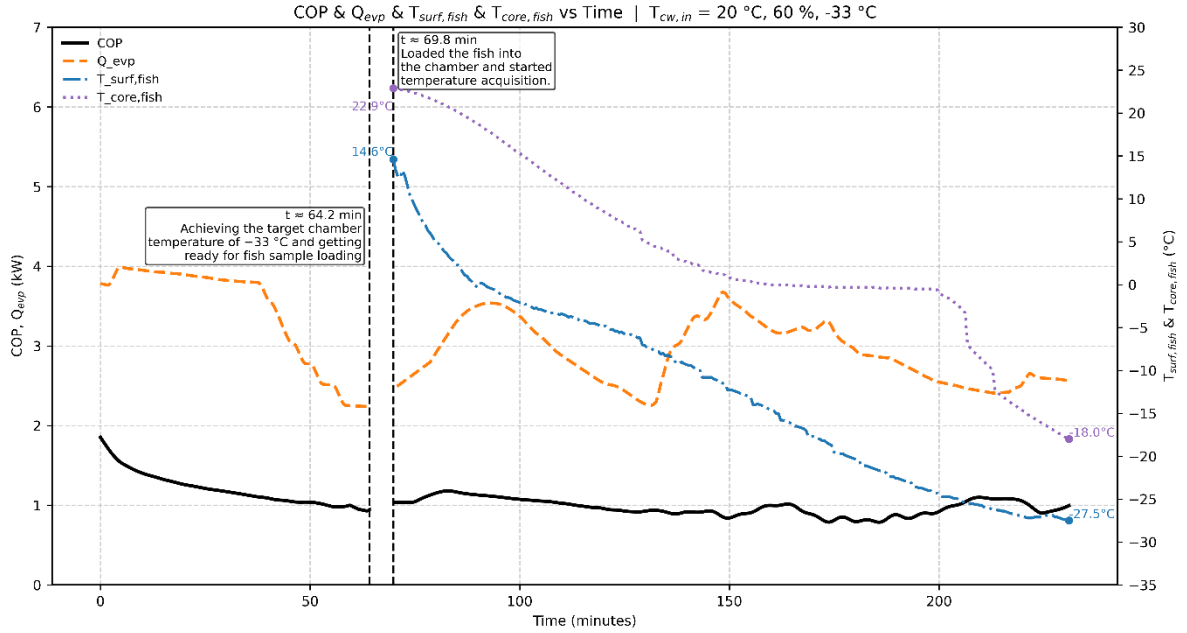

Figure 111 COP, Q_{evp}, $T_{surf,fish}$, $T_{core,fish}$ with Fish ($T_{cw,in}$ = 20 °C, 60 %, -33 °C)

After positioning fish in the chamber, the fish surface temperature approaches chamber temperature at a fast rate but the core temperature requires additional time to reach −18 °C because of product internal

thermal barriers and its higher thermal mass. The plot demonstrates how product cooling needs affect COP performance and how system energy response affects the duration needed for surface and core temperature equilibrium. The product temperature follows the increase in Q_{evp} values.

As condensing pressure and evaporation pressure both significantly influence the COP, as well as the refrigerant mass flow rate, it is necessary to point out their variability. As revealed by Table 27, the condensing pressure varies between 12.2 bar and 19.4 bar, while the evaporation pressure varies between 0.1 bar and 1.6 bar.

	P_{EVP}	P_{CND}	$\Delta P = P_{CND} - P_{EVP}$
Maximum	1.6	19.4	18.1
Minimum	0.1	12.2	10.7
Average	1.2	17.2	16.0

Table 29 Pressure variations in $T_{cw,in}$ = 20 ℃

As shown in Figure 112, the rate of heat transfer through the condenser, Q_{cnd}, is initially high, as expected with the existing high heat load and temperature difference existing at the beginning of the refrigeration cycle. As the system reduces the temperature in the chamber closer to the desired temperature of -33 °C, Q_{cnd} decreases. There is a definite point in the Q_{cnd} curve where the slope clearly changes around the first event, which is related to the temperature of the target chamber being reached and entering the quasi-steady state condition. Following the second event, with the loading of the product into the chamber, the Q_{cnd} tends to a new steady state with small fluctuations superposed upon it.

5.5 $T_{cw,in} = 15$ ℃, Maximum Opening Expansion Valve = 90%, $T_{cell} = -33$ ℃

Referring to Figure 113, it can also be noticed that the refrigeration cycle starts its cycle from a warm condition, during which its COP gradually started at 2.5 for some initial minutes before gradually decreasing to ca 1.05 to 1.10 around 50 minutes as the unit approaches its desired temperature setting. This kind of smooth reduction is very much correlated to another decreasing function: Q_{evp}, or the load of the evaporator, which starts around 6.0 kW and peaks at 6.5 kW for several initial minutes to 10 before gradually decreasing to around 1.0 to 1.56 kW as it approaches its desired temperature setting.

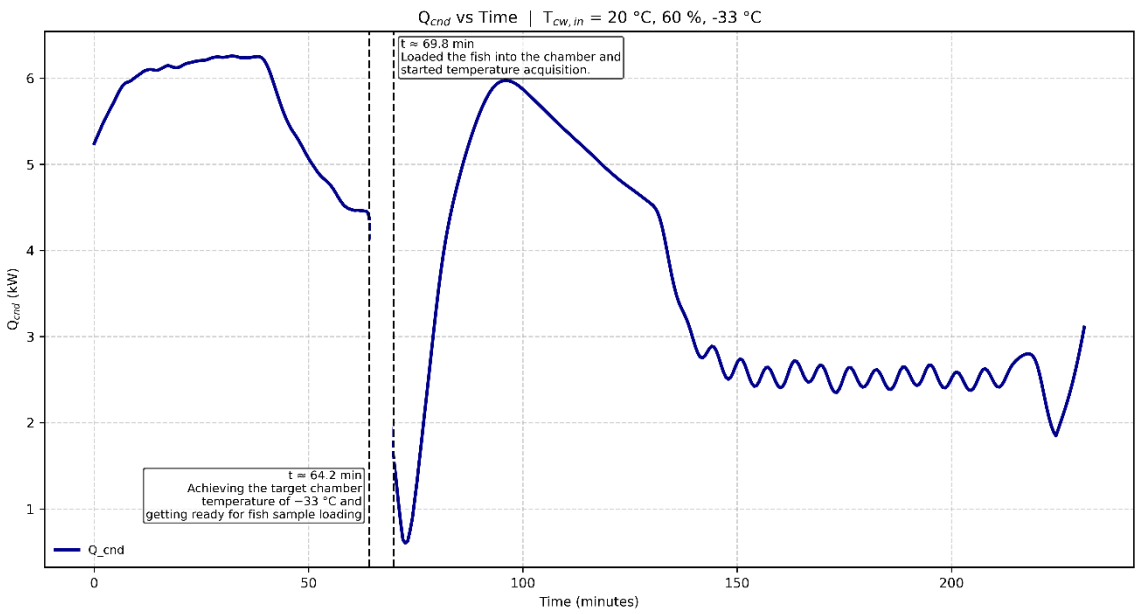

Figure 112 Q_{cnd} with Fish ($T_{cw,in}$ = 20 °C, 60 %, -33 °C)

Compressor power shows two-phase performance. Initially, W is no more than 2.40 kW, but W quickly settles between 3.5-4.0 kW for at least 20-30 minutes because of its increasing pressure ratio and additional cooling requirements for cabin temperature reduction. Eventually, as heat load reduces, power also reduces to stabilize around 2.60-3.0 kW as the aircraft cabin approaches its desired temperature setting. Active Power also behaves similarly to begin at 3.65 kW to reduce to around 2.40 kW as the cycle nears its steady state condition because of good correlation between actual electrical power input and calculated power values.

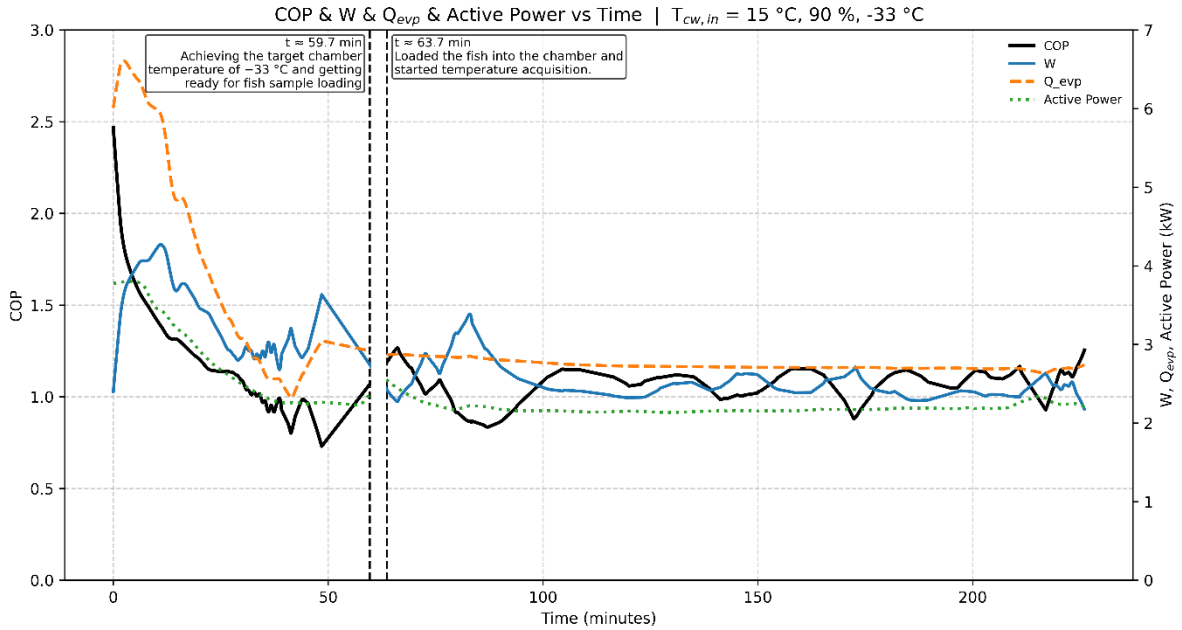

Figure 113 COP, W, Q_{evp}, and Active Power with Fish ($T_{cw,in}$=15 °C,90 %, -33 °C)

At t ~ 63.7 min, where the fish is introduced inside the chamber, the system clearly faces a heat disturbance. This triggers a brief increase in COP to 1.25 before falling back to values between 1.0 and 1.10 as the compressor attempts to cope with the new load condition. Correspondingly, values peak at 2.70-2.80 kW, while the power consumption of the compressor also goes high to around 3.0-3.40 kW. The Active Power momentarily drops to 2.0 kW but soon starts to recover. A new steady-state condition is thus achieved after experiencing the transient because of product introduction, during which the COP stabilizes between 1.0 and 1.20, and the power values for both the compressor and evaporator load remain between 2.50-3.00 kW and 2.60-2.70 kW, respectively.

The 114 plot shows the thermal response of the system. The initial temperature inside the cabin is 13.4 °C and drops very quickly: it reaches around −15 °C at around the middle of the pull-down and gets closer to −30 °C at t ~ 40-45 min. At t ~ 63.7 min, as soon as the fish is put inside the chamber, one can see a remarkable jump in T_{cell}: the air temperature goes from −30 °C to around −22 °C and, after 25-30 minutes, gets closer to −32 °C and stays around −32.2 °C with small fluctuations around this value. At the time of loading, the surface temperature of the fish is approximately 16.1 °C, and its central temperature is around 24.0 °C. When the fish is packed inside the freezing chamber, its surface temperature declines quickly to around 0 °C in 25-30 minutes, followed by a brief plateau at 0 to −2 °C, also confirming that it is entering the phase change period near its surface region. After this region, its temperature continues to decline steadily until it reaches −28 °C at the end of the test period.

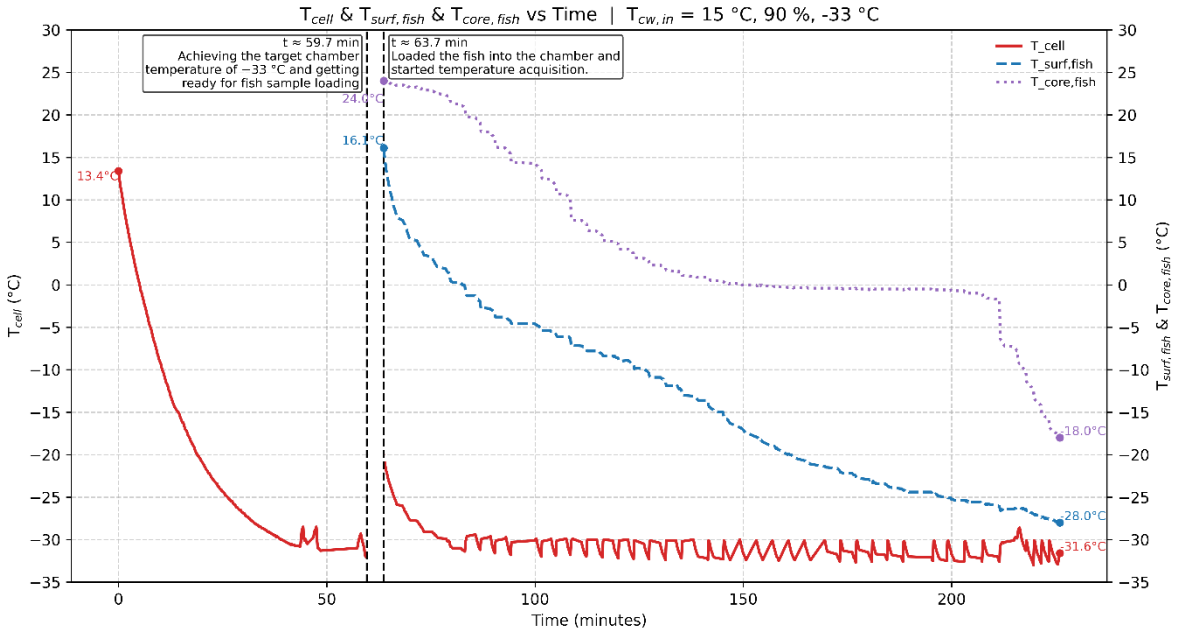

Figure 114 T_{cell}, $T_{surf,fish}$, $T_{core,fish}$ with Fish ($T_{cw,in}$ = 15 °C, 90 %, -33 °C)

The central temperature takes much longer to change. It starts off at 24.0 °C and reduces to around 10°C, then to 4–5 °C and subsequently settles around 0-1 °C for an extended amount of time—the

typical latent heat release associated with core freezing. At the end of the experiment, the central temperature is measured at -18.0 °C.

In Figure 115, COP is depicted on the axis to the left (scaling from 0 to 3 units) and ΔP for the compressor is shown on the axis to the right (ranging between 0 and 20 bar). In the initial precooling period, values of COP remain between 2.2 and 2.5 units, whereas values for ΔP (red curve) are between 16-18 bar. When cooling takes place inside the chamber, values of COP go on to reduce to 1.0 to 1.1 units at 50 minutes, while values for ΔP go down from 17 bar to 12.5 bar at around 50 minutes. This reduction in values for COP and for ΔP is because of reductions that take place inside the evaporator load as well as its consequent suction and discharge pressures for higher refrigeration flows. At this point, where the fish is loaded into the chamber (t ~ 63.7 min), both curves demonstrate a strong transient response. This is apparent as ΔP reduces abruptly to around 14 bar values, while COP shows a temporary increase to 1.2-1.3 but momentarily drops before stabilizing. Subsequently, after having completed this transient region, ΔP stabilizes around 12-13 bars and shows signs of increasing, while COP fluctuates between 1.00 and 1.20 values. Consequently, before the introduction of products into the system, both COP and ΔP demonstrate a monotonic "COP-ΔP co-decline" cycle, but after fish is added to the system, its latent heat components cause this cycle to become significantly nonlinear.

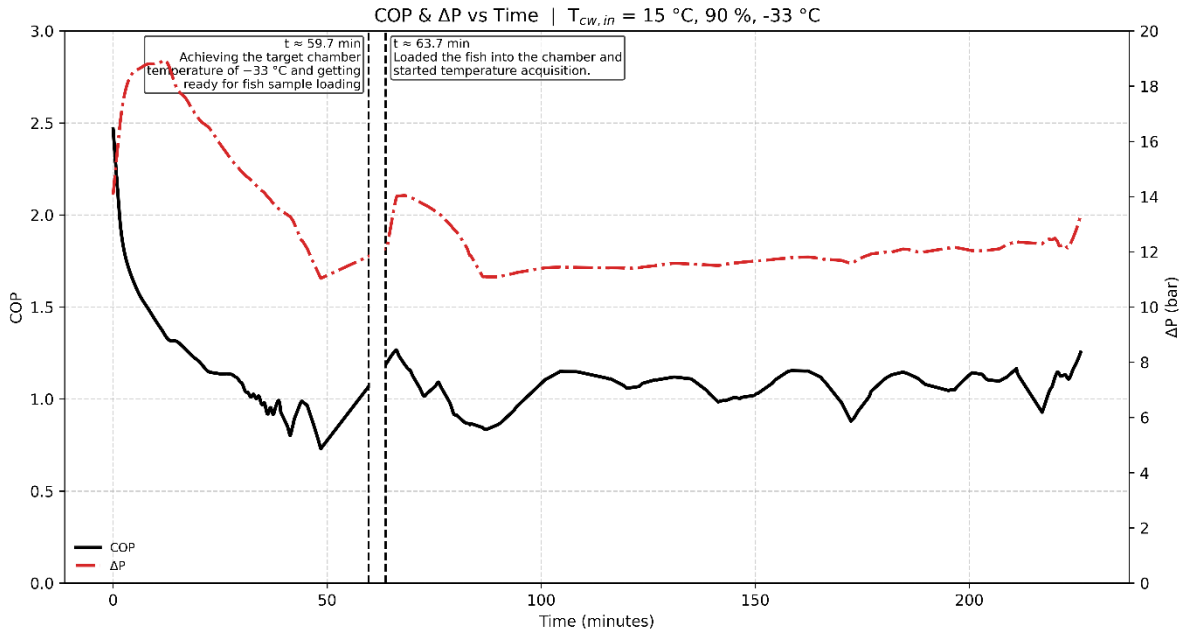

Figure 115 COP, ΔP with Fish ($T_{cw,in}$ = 15 °C, 90 %, -33 °C)

Figure 116 shows how cycle energy performance (COP and Q_{evp}) is interrelated product thermal performance (surface and core temperatures). At the beginning of testing, values for COP range between 2.4 and 2.5, while values for Q_{evp} range between 6.0 and 6.1 kW. When the empty chamber cools down, values for COP drop to around 1.1 at t = 50 min while values for Q_{evp} decrease from its initial value of

6.5 kW to 2.5–2.6 kW. This is expected because of the lowering rate of heat transfer and energy efficiency as it nears its final set temperature. At this point, when the chamber reaches the set point and the fish is introduced, Q_{evp} shows approximately 3.0 kW. This is indicative of the point at which a warmed-up product helps to bring back the load on the evaporator to values like those measured before minute 50. At this point, the COP values also fluctuated highly to stabilize between 1.0 to 1.20, displaying values suggestive of its need to generate higher cooling outputs at low Q_{evp}/W ratios.

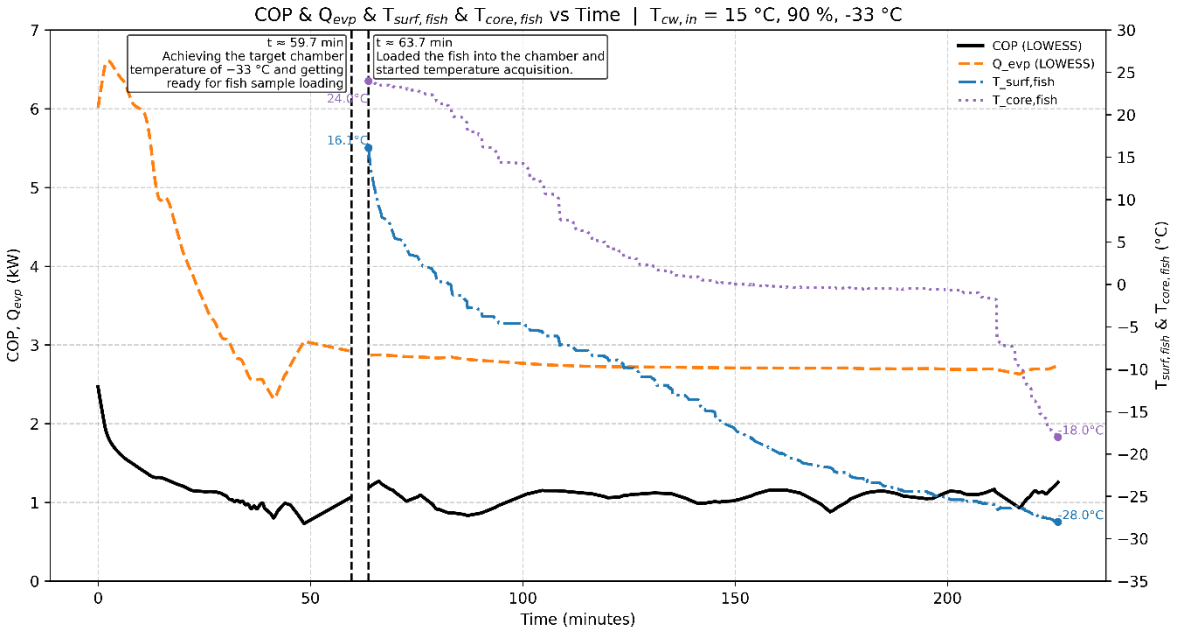

Figure 116 COP, Q_{evp}, $T_{surf,fish}$, $T_{core,fish}$ with Fish ($T_{cw,in}$ = 15 °C, 90 %, -33 °C)

At the same time, the temperatures of the fish's surface and core change physically correctly. The fish's surface temperature declines quickly from 16.0 °C to near 0 °C and then passes through a short plateau related to the freezing of water at its surface and drops to −28.0 °C at the end of testing. In comparison to this fast decline, the core's temperature takes much longer to drop from 24.0 °C to near −18 °C at the end of testing after passing through a plateau around 0–1 °C related to the latent heat release. A comparison between these values and those of Q_{evp} shows that there is a direct link between them: while the fish core is within the region around the freezing point, Q_{evp} stabilizes at around 2.7 to 2.9 kW, signifying that this is where a rather large amount of its power is being expended for latent heat removal. When the core temperature passes below zero and passes through the region where the phase change occurs, Q_{evp} reduces to around 2.6 to 2.7 kW while maintaining its COP at 1.1. This is further indicative of its being the most energy-intensive part of this entire procedure where careful consideration is required while designing such systems.

As condensing pressure and evaporation pressure both significantly influence the COP, as well as the refrigerant mass flow rate, it is necessary to point out their variability. As revealed by Table 28, the

condensing pressure varies between 10.9 bar and 21.4 bar, while the evaporating pressure varies between 0.8 bar and 2.5 bar.

	P_{EVP}	P_{CND}	$\Delta P = P_{CND} - P_{EVP}$
Maximum	2.5	21.4	19.1
Minimum	0.8	10.9	9.8
Average	1.3	15.4	14.0

Table 30 Pressure variations in $T_{cw,in}$=15 °C

To start with, the rate of heat transfer (Q_{cnd}) in the condenser is approximately 6.25 kW that rapidly increases to reach a peak of about 8.51 kW at t = 8.5 minutes; an indicator that the rates in the initial transient operation in the system are high thermal loads. After this, with time, Q_{cnd} starts to decrease gradually with time, finally reaching about 4.27 kW at the end of the first event at 64.2 minutes, a sign that the required temperature in the chamber has been reached. A small spike in the value of Q_{cnd} then occurs at the second occasion at t = 69.8 minutes and the rate of heat rejection spikes to about 5.23 kW due to the other thermal loads induced in the system. After this burst, Q_{cnd} then starts to decline again until it settles at a low value of about 2.05 kW at the same time at about t 108 minutes. At last, to ascertain the end performance of the system, Q_{cnd} becomes relatively constant with minor deviations between 2.05 kW and 2.53 kW with a mean of approximately 2.37 kW and relative error of less than 4.0, so then it would be an indication that the system is in a quasi-steady state. It is also relevant to mention that the rate of condenser heat rejection at the extreme values is significantly decreased by approximately 72 % to the ultimate values of the system in a steady state location which is evidence that the thermal loads in the system are significantly cut back during the entire stages of freezing (Figure 117).

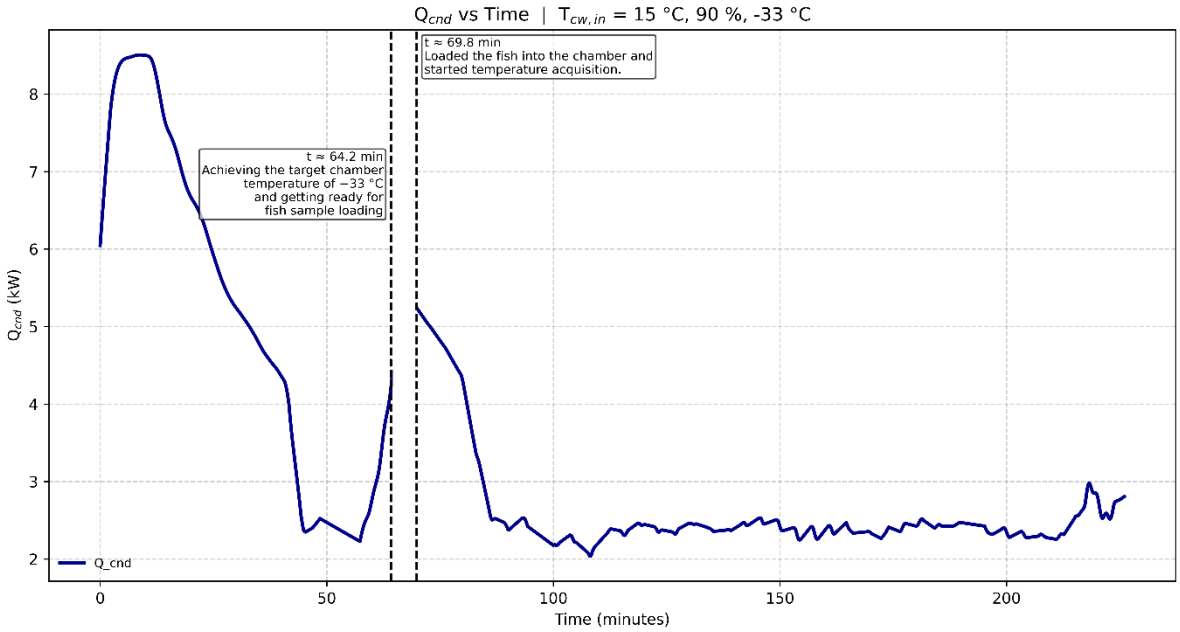

Figure 117 Q_{cnd} with Fish ($T_{cw,in}$ = 15 °C, 90 %, -33 °C)

5.6 $T_{cw,in}$ = 10 °C, Maximum Opening Expansion Valve = 80%, T_{cell} = −33 °C

Figure 118: The COP on the y-axis to the left (0–3) and W, Q_{evp}, and Active Power on the y-axis to the right (0–7 kW). At the beginning of the experiment, COP is around 2.4-2.5 units. At this point in time, Q_{evp} is seen to range around 4.9 to 5.0 kW on the right y-axis while W is around 2.0 to 2.10 kW. Likewise, Active Power is around 2.90-3.0 kW at this point of time, which is at the beginning of the initial pull down period during which evaporator load is at its peak and at which the temperature difference between the inside air and liquid is at its largest.

As time passes by and as the empty cabin gets cooler, its COP (black curve) continues to reduce steadily: to 1.4-1.5 at around 25 minutes and further to 1.15-1.20 at 50 minutes. Consequently, Q_{evp} also reduces during this time: from 4.7-4.8 kW at 50 minutes to 2.80-3.0 kW at 100 minutes. At the same time, W reduces gradually from 3.0-3.5 kW at 20-25 minutes to 2.20-2.40 kW at 50 minutes. It may also be noted that Active Power reduces at the same pace: from 3.0 kW to 2.10-2.30 kW. The simultaneous reduction of COP, Q_{evp}, W, and Active Power is indicative of the continuously decreasing thermal load of the chamber walls and air as it becomes closer to entering its quasi-steady state.

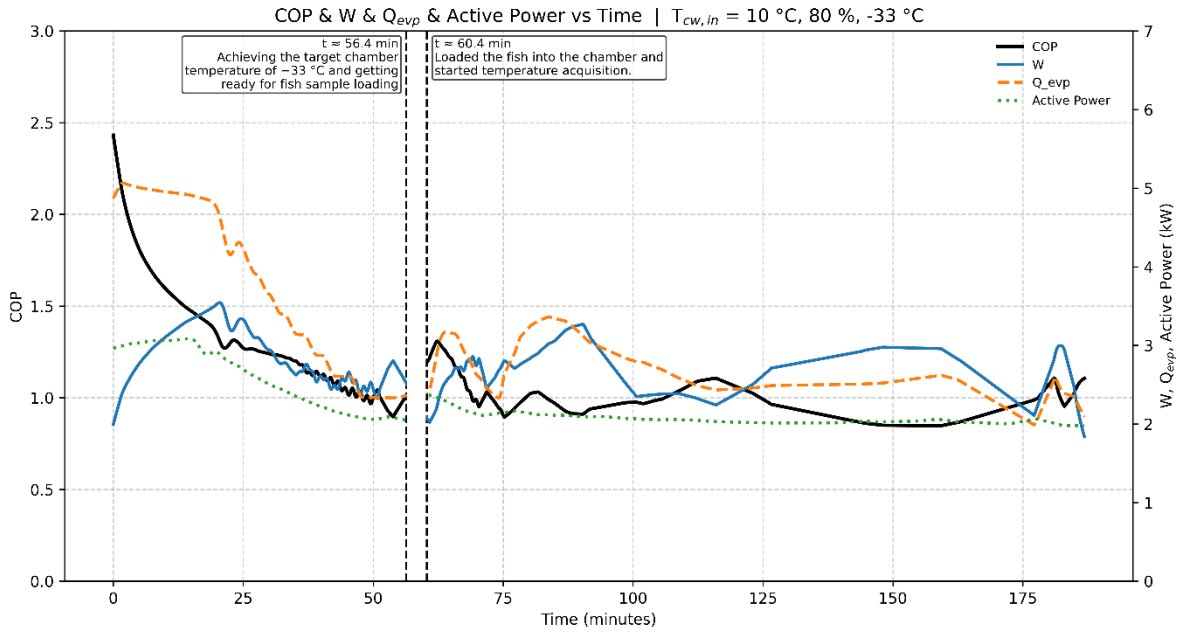

Figure 118 COP, W, Q_{evp}, and Active Power with Fish ($T_{cw,in}$=10 °C, 80 %, -33 °C)

At t ~ 56.4 min, the cooling chamber reaches its desired temperature of −33°C, and the door is opened for loading fish into the chamber. Just after loading product into the chamber (at 60.4 min), COP momentarily peaks to 1.3 while stabilizing around values between 0.95 and 1.10 after few moments. At this point, Q_{evp} is seen to have increased to between 2.9-3.1 kW from its initial reading of 2.5-2.6 kW before opening the door to load products. With this increase, Compressor Power also increases to 2.8-3.0 kW from 2.3-2.4 kW while Active Power stays around 2.1-2.2 kW.

From here until the end of the experiment (about 190 minutes), all three energy-related values: W, Q_{evp}, and Active Power, maintain themselves at or around 2.3-3.2 kW, while COP settles at 1.0 to 1.15. This is indicative of the obvious fact that by bringing in the warmed-up product, the load on the evaporator gets substantially higher and thus brings about a shift to another zone of operation at higher COP values.

In figure 119, while the axis on the left represents the temperature inside the cabin or T_{cell} (+30 to -35 °C), on the right axis, the fish temperatures are displayed (surface and core temperatures: +30 to -35 °C). The initial temperature inside the chamber is 16.4 °C, and it cools down at a constant speed to reach −33 °C, its desired target temperature in around 56.4 minutes. At the point at which the door opens for loading product (at t = 60.4 minutes), this slight increase happens to reach −23 °C, but afterwards, for around 15 minutes, it drops back down to around −32°C and continues to alternate between −31°C and −33 °C for the rest of the period.

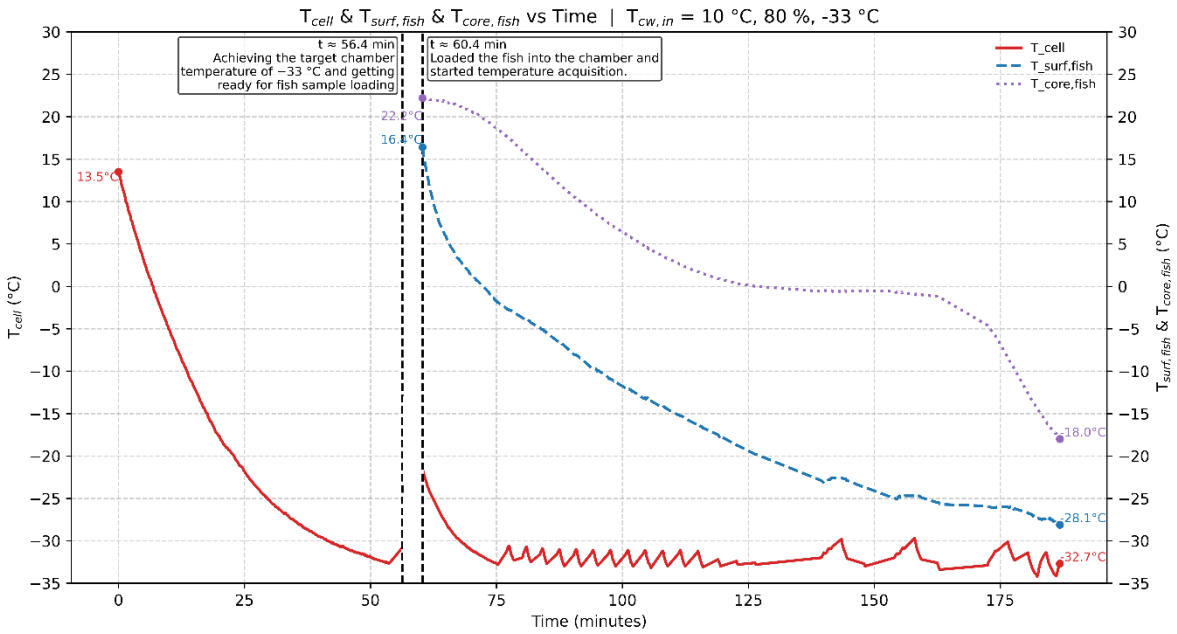

Figure 119 T_{cell}, $T_{surf,fish}$, $T_{core,fish}$ with Fish ($T_{cw,in}$ = 10 °C, 80 %, -33 °C)

The initial temperature of the fish's surface is 16.4 °C at the point of loading and quickly declines to around 0 °C within 15 minutes before entering the freezing point region and continuously decreasing at a constant rate to reach values of −28.1 °C at the end of the experiment.

The basic temperature $T_{core,fish}$ varies comparatively slowly. From 22.2°C, it reduces to 14-15 °C in 20 minutes and to 3-5 °C in around 30 minutes. It stabilizes at around 0 to 2°C for an extended period, the time interval appears to match perfectly to the latent heat period of the freezing process of water. At the end of the test period, its value is only at around −33°C because of slower heat transfer processes at this point inside the product itself.

Based on figure 120, while the values on the left scale denote COP (0–3), those on the right scale denote PD values for ΔP (0–20 bar). At the start of the experiment, while COP is between 2.4 and 2.5, ΔP values are around 14-16 bar. While the system is cooled and suction pressure reduces, values for ΔP reduce to around 12-12.5 bar just before the fish is introduced into the testing setup. Correspondingly, values for COP reduce from 2.5 to 1.0-1.1 at around 50 minutes. At the point of product introduction (t ~ 60.4 min), there is a drastic drop in ΔP to 10–11 bar values but later recovers to 12–13 bar values after the initial thermal effects. The COP also follows a similar transient response: It momentarily peaks at 1.2-1.3 but later stabilizes to 0.95-1.15 values.

Clearly, from the plot, before loading products into the refrigerator, COP and ΔP display a reliable and strongly correlated relationship. However, as soon as fish is put inside, this correlation does not exist anymore, and instead, instantaneous thermal load.

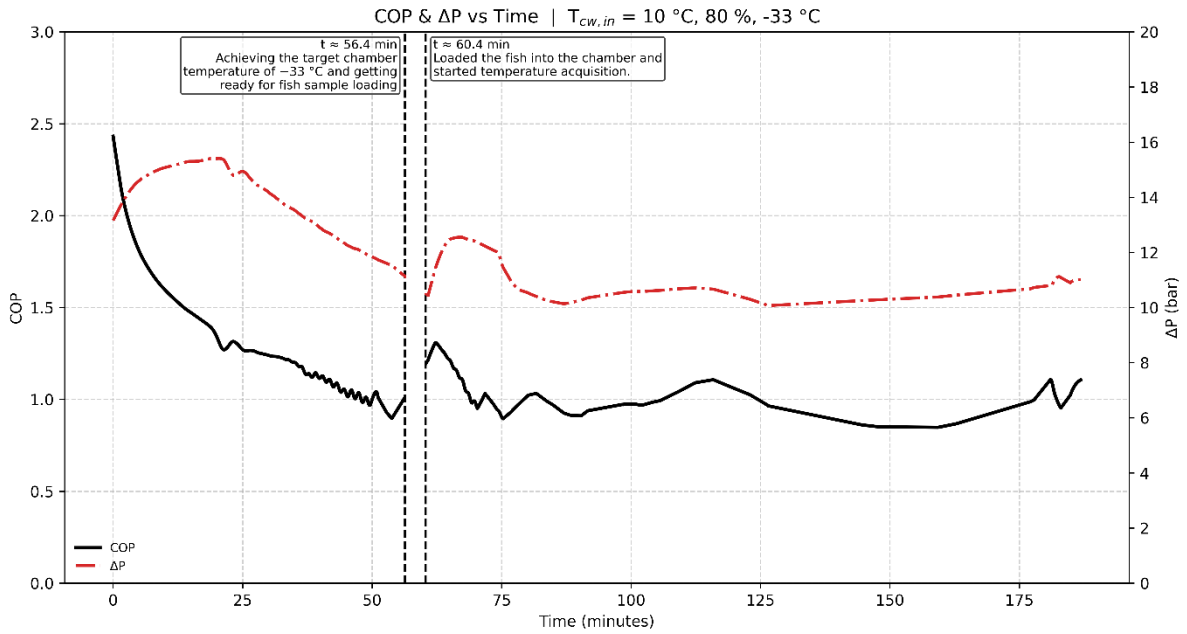

Figure 120 COP, ΔP with Fish ($T_{cw,in}$ = 15 °C, 90 %, -33 °C)

Figure 121: Energy performance of refrigeration cycle and thermal performance of product. One of the most detailed representations of how refrigeration cycle performance affects the actual freezer cycle is provided by Figure 121, which plots refrigeration cycle energy performance and product performance simultaneously. At the initial stage of the experiment, COP lies between 2.4 and 2.5, while the value of evaporation capacity Q_{evp} is around 5.0-5.1 kW. This corresponds to a cycle point at which the temperature differential between the ambient inside the cabin and the actual evaporation temperature is not too large yet. This implies that suction pressure is higher at this point. At this point, refrigerant entering the evaporation unit is massive, thus offering high refrigerating capacities too. From a refrigeration cycle point of view, this region is marked by moderate pressure ratio and high isentropic efficiency values. Hence, high values of COP are ensured.

As the temperature inside the cabin reduces, the suction temperature and pressure also reduce. The reduction in suction pressure causes the compression ratio to increase, which reduces the isentropic efficiency of the compressor and at the same time reduces the mass flow rate of refrigerants. This reduces Q_{evp} from 6.1 kW to 2.5-2.6 kW after around 50 minutes while at the same time decreasing the COP to 1.1 for the same amount of time. This is to be expected because as the evaporation temperature reduces and the distance between the evaporator and condenser increases, the compression work also increases while at the same time decreasing the COP.

At t ~ 60.4 min, the fish is put inside the chamber, causing a definite thermal shock to the system. This is because the warm product suddenly adds heat to the system. This produces instantaneous results: Q_{evp}, before this point, having leveled off at around 2.5 kW values, momentarily reduces because of disturbances and variations in air temperature and humidity but quickly kicks off again to higher values

of 2.8 to 3.0 kW. The quick jump or cut-off and final leveling off at Q_{evp} at this stage shows that the refrigeration system adjusts its refrigerant flow and evaporation rate to meet the required cooling rate for both sensible and latent heat transfer. The COP momentarily spiking to 1.2 to 1.3 but levelling off at 0.95 to 1.15 shows that while the load is high and generates higher demands for cooling, high compression ratio and low evaporation temperatures do not allow for any increase to happen in COP values. At this point, it is essential to take into consideration the combined cooling of the fish surface and its interior. While the initial temperature of 16.4 °C reduces to approximately 0 °C at a higher rate, it continues to reduce steadily to −28.1 °C at the end of the experiment period. Conversely, the interior freezes at a much slower rate: starting at 22.2 °C, it descends steadily until it reaches values near 0 to -2.2 °C, where it stays for an extended period. This stage corresponds to the latent-heat phase, during which the evaporator must remove the highest thermal load. Importantly, for all this period, Q_{evp} stays at approximately 2.7-2.9 kW, thereby highlighting that for all this period, heat is being removed at a constant rate to facilitate the freezing of the product inside. In terms of principles of thermal science, for all this period, the primary factor being responsible for controlling heat transfer is the interior thermal resistance offered by the product itself.

With the core temperature now below zero and moving away from the region of phase change, Q_{evp} slowly drops to 2.6-2.7 kW while maintaining a COP value of 1.1. This is because it is now apparent that while heat transfer is no longer dependent on evaporation or compression capabilities but rather on conductive heat transfer inside the core product itself. At this final stage of testing, core temperature is now at -18 °C, thus pointing to the inadequacy of testing time for deep-freeze core testing. These combined processes clearly indicate that the latent heat freezing of the product core is not only the most energy-demanding step but also sets the operating point for the refrigeration cycle. During this period, high cooling power is required for the evaporator, but at the same time, the COP is inherently bounded by low evaporation temperatures. In substance, Figure 108 points to one of the most substantial features of industrial scale freezing: efficient refrigeration cycle designs should recognize the special importance of the latent heat removal step in controlling energy consumption and final product quality during product freezing cycles.

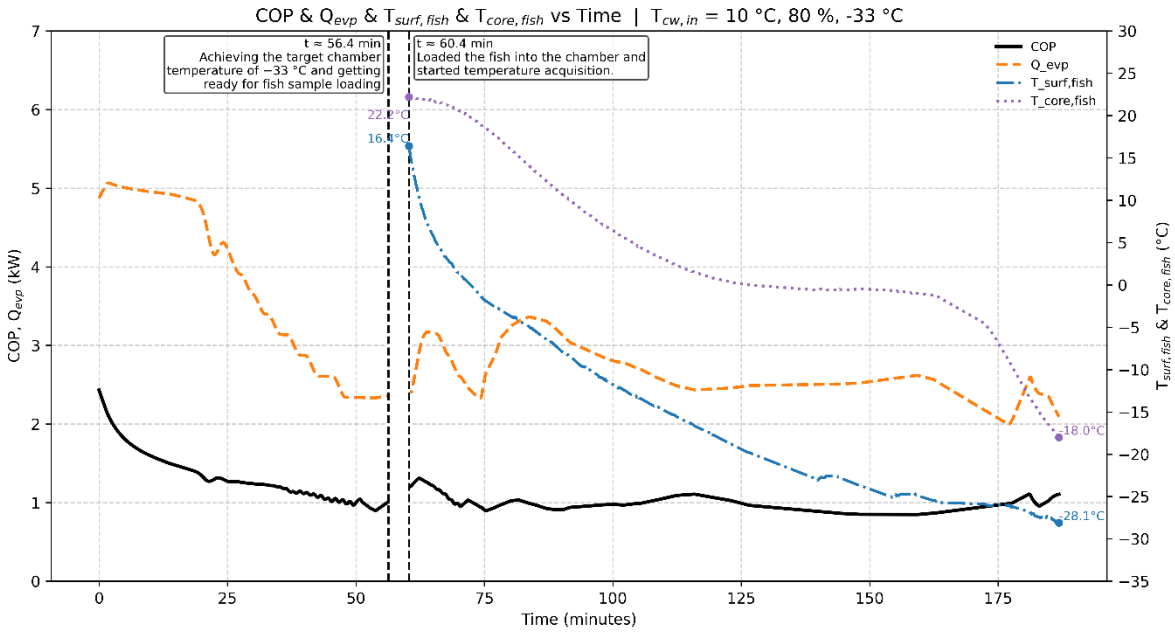

Figure 121 COP, Q_{evp}, $T_{surf,fish}$, $T_{core,fish}$ with Fish ($T_{cw,in}$ = 10 °C, 80 %, -33 °C)

As condensing pressure, and the evaporating pressure are the two parameters which have a major influence on COP, and the mass flow rate of the refrigerant, it is important to analyze the significance of both. As indicated in Table 29, it is possible to identify that the condensing pressure ranges from 10.1 bar to 17.2 bar, and the evaporating pressure ranges from 0.6 bar to 1.8 bar.

	P_{EVP}	P_{CND}	$\Delta P = P_{CND} - P_{EVP}$
Maximum	1.8	17.2	15.5
Minimum	0.6	10.1	8.5
Average	1.2	14.2	12.9

Table 31 Pressure variations in $T_{cw,in}$=10 °C

As illustrated in figure 122, the heat transfer rate (Q_{cnd}) at the beginning of the operation is around 6-7 kW with a maximum of 7.0-7.5 kW during the first minutes of the operation which demonstrates the high thermal load during the transient start-up period. The cooling process causes Q_{cnd} to decrease slowly and approach about 4-5 kW at t 40-50 min and indicating the slow decline in heat rejection as the system reaches its desired operating conditions. After this point, a pronounced negative gradient is found and at a point between 80 and 115 minutes the condenser heat transfer rate becomes constant in a smaller range of 2.0 to 2.5 kW indicating the beginning of a quasi-steady operating regime. After t = 120 mins extreme variability is largely connected with the fact that the cooling water temperature

difference under low-load conditions was smaller and therefore the calculated Q_{cnd} is very sensitive to minor temperature changes.

Generally, the condenser heat transfer rate reduces by over 65-70% of the original peak to the final operating level, which verifies a significant reduction in the thermal load to the system and the shift towards the low-load quasi-steady operation in the latter part of the freezing process.

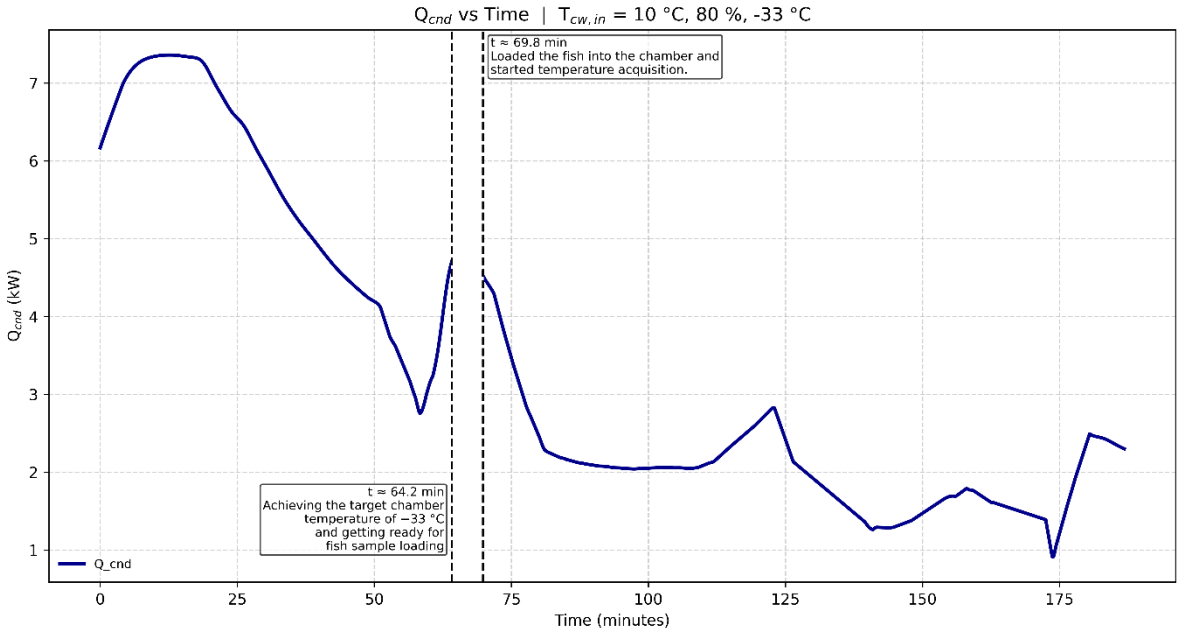

Figure 122 Q_{cnd} with Fis*h* *($T_{cw,in}$* = 10 °C, 80 %, -33 °C)

5.7 Impact of Condensing Temperature and Expansion Valve Opening at Fixed Chamber Temperature ($T_{cell} = -33$ °C)

It is always very significant to recognize and comprehend correlations among different parameters while pursuing any scientific or engineering task because these correlations usually demonstrate effective functioning of complex systems. On the same note, for effective interpretation of any refrigeration cycle system performance, correlations between different thermodynamic parameters within the refrigeration cycle also have significant importance. Among several effective techniques for correlation analysis, one is Pearson correlation technique.

In this analysis, the Pearson correlation coefficient was adopted to determine the most significant attributes among the features presented in the dataset. One of the most adopted techniques for evaluating correlation between two attributes is presented by the Pearson correlation coefficient. It is described as the ratio of covariance between attributes to their standard deviations' product. One may perceive correlation from covariance itself between normally distributed attributes, making comparison rather

easy for disparate attributes or measurements presented on different scales. The equation for correlation is provided by Eq. 138:

$$\text{Pearson Correlation } \rho_{X,Y} = \frac{\text{cov}(X,Y)}{\sigma_X \sigma_Y} \qquad \text{Eq. 138}$$

The Pearson correlation coefficient measures both the strength and direction of linear association between two variables, X and Y. This correlation coefficient is calculated using the covariance of the standardized (z-score transformed) values of both variables. This standardization of values makes it dimensionless and uninfluenced by any units of measurement for both variables. As shown in figure 123, The values of this correlation coefficient lie between −1 and +1; +1 shows perfect positive association, −1 shows perfect negative association, and 0 denotes no association at all between the two variables [205].

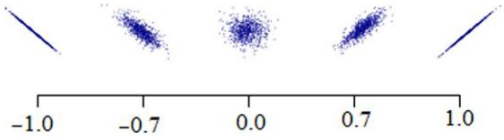

Figure 123 Correlations Between Two Variables in Pearson Correlation

In this heatmap (figure 124), COP is shown to have a strong positive correlation to all major variables except for mass flow rate of injection. The correlation between COP and the cabin temperature T_{cell} is 0.55, which shows that variations in COP are correlated to changes in T_{cell}, meaning that COP reacts to variations in T_{cell}. The correlation is 0.50 for evaporator load Q_{evp} and 0.48 for suction mass flow rate of refrigerant $\dot{m}_{suc}$. This shows that higher cooling and refrigerant mass flow rate positively correlate to higher COP but are less significant than T_{cell}.

The pressure difference ΔP is also positively correlated to COP (~ 0.47), which implies that for these particular operating points, while increasing COP is accompanied by increasing pressure difference values, it also implies for this region of operation that the positive impacts of increased mass flow rate and cooling load overcome the negative impact of increased Specific Compression Work. It is interesting to note that one of the correlations is for $\dot{m}_{inj}$, which negatively correlates to COP at ~ −0.19. This correlation implies that for $T_{cw,in} = 10$ °C and 80 % valve opening positions, increased injection mass flow rate contributes to decreased COP values primarily because of additional injection-related impacts that shift the actual point of operation of the compressor away from its preferred region of operation. The internal product temperature $T_{core,fish}$ is weakly but positively correlated (~ 0.12) to COP and negatively correlated (~ −0.26) to ΔP. Generally higher correlations between the operating parameters themselves are apparent in the top half of the correlation matrix: there is near perfect correlation between Q_{evp} and $\dot{m}_{suc}$ at 0.99, while each is strongly correlated to T_{cell} at 0.87 and 0.80,

respectively. Similarly high correlations exist between ΔP and Q_{evp} and between ΔP and $\dot{m}_{suc}$ at 0.73 and 0.76, respectively.

In total, for $T_{cell} = -33$ °C, all basic parameters of the main cycle are strongly interrelated to form what may be called a "dynamic package" governing the COP simultaneously.

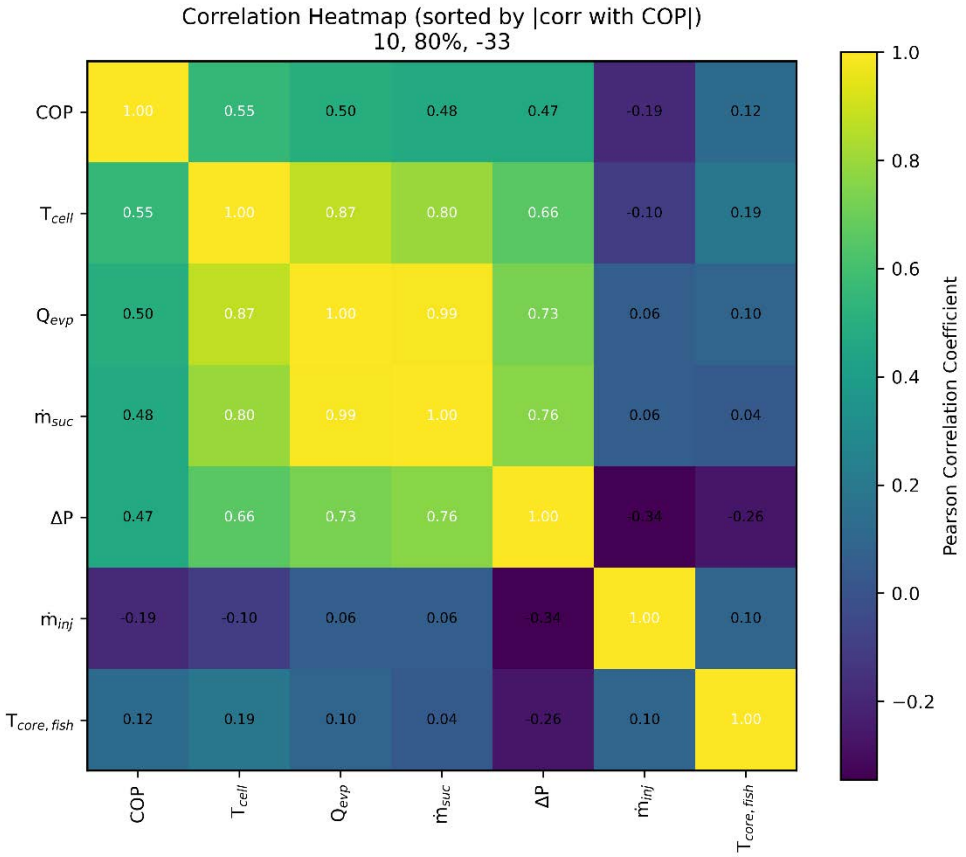

Figure 124 Correlation Heatmap (sorted by "correlation with COP"), $T_{cw,in}$ = 10 °C, 80 %, -33 °C

A rise in the condenser temperature to 15 °C and expansion valve opening to 90 % changes the correlation structure significantly (Figure 125). The correlation between COP and the cabin temperature T_{cell} reduces from 0.55 to around 0.51, suggesting that COP's dependence on the thermal condition of the chamber reduces to some extent. The correlation between COP and evaporation load Q_{evp} of 0.50 and between COP and suction mass flow rate $\dot{m}_{suc}$ of 0.47 is high but reduces slightly as compared to the 10 °C condition. However, the correlation between COP and pressure difference ΔP reduces to 0.39, suggesting that the importance of pressure differences to COP is gradually decreasing under this operating condition. One significant change appears in the correlation between COP and the injection mass flow rate, where the negative correlation becomes weaker from −0.19 to −0.11.

Again, the internal product temperature shows weak positive correlation with COP (around +0.12) but weak negative correlation for ΔP (around −0.29), meaning higher pressure differences are normally associated with lower product temperatures.

The correlation coefficient between T_{cell} and Q_{evp} improves to 0.94 and between T_{cell} and $\dot{m}_{suc}$ to 0.91. The correlation between Q_{evp} and $\dot{m}_{suc}$ also continues to remain very high (~ 0.99). At the same time, the correlation coefficients for ΔP with load and suction mass flow are now stronger (~ 0.79 and ~ 0.82, respectively) than before, which indicates that the pressure differential is now more coupled to mass flow and load dynamics at this condenser operating point. In general, from the heat map for $T_{cw,in} = 15$ ℃, cycle dynamics are increasingly dominated by a "pressure-flow-load core," while COP's behavior is getting closer to being a secondary result of this group. In this regard, vapor injection influence becomes even more disruptive to cycle efficiency.

As shown in figure 126, When run at the tougher operating condition of $T_{cw,in} = -20$ ℃ with expansion valve opening area limited to 60 %, the correlation subscripts differ markedly. At this operating condition, it is found that for COP while correlation coefficient is 0.48 for cabin temperature. This implies that even at tougher condensation conditions, variations of COP tend to follow roughly similarly to T_{cell} prevailing at each point of time. Conversely, correlation coefficients for COP vs. evaporation load Q_{evp} (0.37) and suction mass flow rate $\dot{m}_{suc}$ (0.29) reduce or are weaker than before.

One of the most significant shifts is the stronger negative correlation between COP and the mass flow rate of injection, which reaches –0.26.

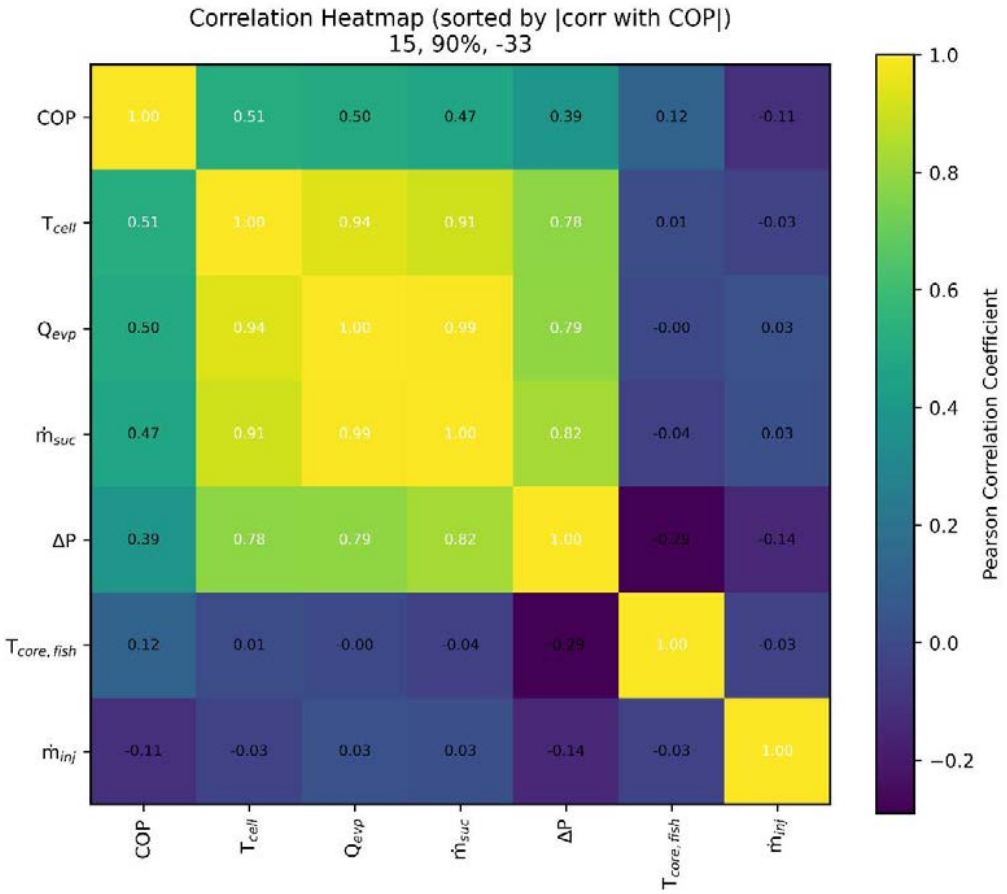

Figure 125 Correlation Heatmap (sorted by "correlation with COP"), $T_{cw,in}$ = 15 °C, 90 %, -33 °C

Based on these operating points, any increase in $\dot{m}_{inj}$ is expected to result in a notable reduction in COP values, thus stabilizing vapor injection as one of the limiting factors of cycle efficiency performance. The correlation between the pressure difference and COP is weak at 0.35. Additionally, for the core product temperature $T_{core,fish}$, it is positively correlated at 0.07 with COP but negatively correlated at −0.29 for pressures differences. This implies "light" operation points; the pressure differences; coinciding with higher temperatures and slight improvements in COP values.

The inter-relationships between the remaining parameters also offer another interesting insight. The correlation between Q_{evp} and $\dot{m}_{suc}$ is still very high (0.97), which implies that the basic load flow relationship is still driving the overall energy processes for this cycle. Both remain positively correlated to the cabin temperature (0.66 and 0.47). At the same time, ΔP is most negatively correlated to injection mass flow rate (–0.52), while having a moderate correlation to the internal temperature (–0.29). This implies that for this range of operation, higher vapor injection pressures reduce ΔP while making way for the reduction in COP performance. Overall, at $T_{CND} = -20$ °C, while the sensitivity of COP to vapor injection and cabin temperature becomes more apparent, the direct effect of Q_{evp} and ΔP on COP

becomes weaker. This is because the overall performance of the system is dominated by the effect of interaction between cabin temperature and vapor injection efficiency limitation factors.

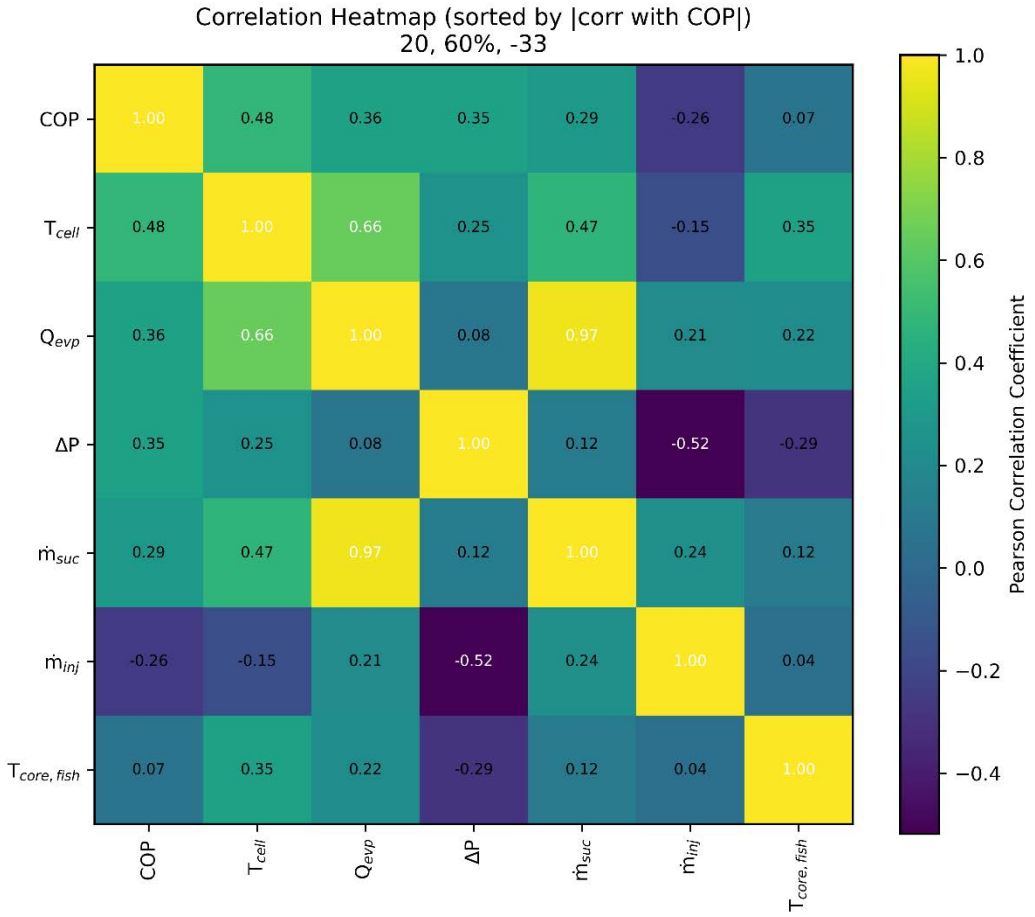

Figure 126 Correlation Heatmap (sorted by "correlation with COP"), $T_{cw,in}$ = 20 °C, 60 %, -33 °C

In plot 127, COP and Q_{evp} for all three coolant water temperatures: $T_{cw,in} = 10\ °C, 15\ °C,\ 20\ °C$, are shown on the left axis, while the product surface and core temperatures are shown on the right axis. There are three vertical dash lines representing for each $T_{cw,in}$ condition: When the target temperature of $-33\ °C$ is attained inside the cabin and when fish is introduced into the chamber.

A comparison at the beginning of testing shows very similar COP curves for $T_{cw,in} = 10\ °C$ and $T_{cw,in} = 15\ °C$ at around 2.4-2.5, while for $T_{cw,in} = 20\ °C$, the COP values are sensibly lower, at around 1.8-1.9.

Correspondingly, different initial values for Q_{evp} also exist around 5.0 kW for 10 °C, 6.0-6.2 kW for 15 °C, but no more than 3.8-4.0 kW for 20 °C. This means that, in terms of evaporation performance, the highest evaporation capability is achieved at a condensing temperature of 15 °C, whereas at 20 °C the performance is limited due to the 60 % valve opening constraint and the higher condensation pressure. In the precooling period of the empty chamber, COP continues to reduce for all three cases.

After approximately 50 minutes, COP reaches 1.1–1.2 for $T_{cw,in} = 10$ ℃ and 15 ℃, while for $T_{cw,in} =$ 20 ℃ it levels off at around 1.0–1.1. At the same time, Q_{evp} continues to reduce from 5.0 to 2.4-2.5 kW for 10 °C, from 6.0 to 3.0 kW for 15 °C, and from 3.9 to 2.8 for 20 °C.

This is because of the natural reduction of thermal load while approaching the desired temperature of the cabin.

The time taken for the interior to reach -33°C also shows large variabilities among tests: around 64.2 minutes for $T_{cw,in} = 20$ ℃, 59.7 minutes for 15 °C, and 56.4 minutes for 10 °C. At these points, the fish-core temperatures are 22.9 °C, 24.0 °C, and 22.2 °C for $T_{cw,in} = 20$ ℃, 15 ℃, and 10 ℃, respectively, while the corresponding surface temperatures are 14.6 °C, 16.1 °C, and 16.4 °C. When the fish is put inside the chamber, all three Q_{evp} curves demonstrate typical behavior: each pass through a transient region and stabilizes at 2.5 to 3.5 kW. This shows that for all operating points, the thermal load created by the fish takes roughly the same range of its capacity to evacuate heat. When COP is plotted for this region, it is found to swing between 0.95 and 1.15 values but to give clearly different values at each point: its bias is near higher values at 10 °C T_{CND}, around its center at 15 °C T_{CND}, and near its lower values at 20 °C T_{CND} points. Despite these differences in COP and Q_{evp}, the plots clearly show that all three operating modes eventually bring the product core temperature to approximately −18 °C. However, the time required to reach this temperature differs among the scenarios, reflecting variations in their effective cooling rates and thermal load distribution.

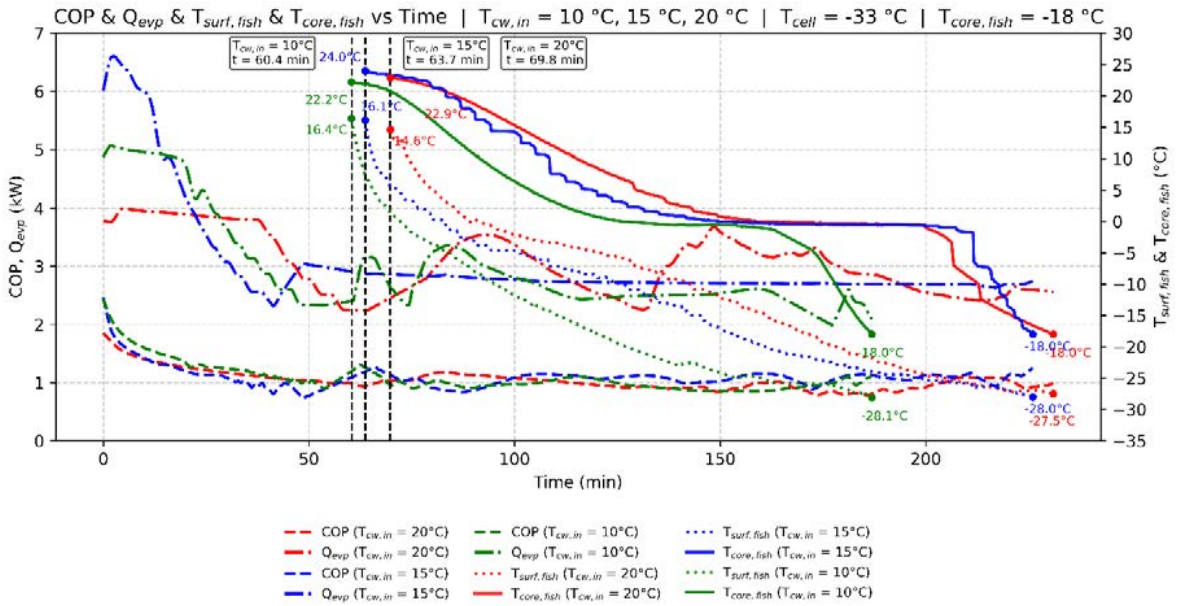

Figure 127 Comparative Analysis of Energy Performance and Freezing Dynamics Under Different Condensing Temperatures (10 °C, 15 °C, 20 °C)

Figure 131 shows the respective temperatures of the fish's surface and core for all three coolant water temperatures until setting is achieved for the core at around −18 °C. The three vertical Demarcating points indicate the respective loading points for each test: 69.8 for 20 °C, 63.7 for 15 °C, and 60.4 for 10 °C. At each point, the respective core temperatures are 22.9 °C, 24.0 °C, and 22.2 °C for 20 °C, 15 °C, and 10 °C tests, and their respective surface temperatures are 14.6 °C, 16.1 °C, and 16.4 °C.

After loading, the fish core cools at various rates based on $T_{cw,in}$ values. The reduction of core temperature is achieved at $T_{cw,in} = 20$ ℃, at which point the core cools to −18.0 °C at around 161 minutes while the surrounding surface is at −27.5 °C. When $T_{cw,in} = 10$ ℃, it takes approximately 127 minutes for the core temperature to reach −18.0 °C, at which point the surrounding temperature is about −28.1 °C. At $T_{cw,in} = 15$ ℃, the core reaches −18.0 °C at around 162 minutes while the surrounding temperature is about −28.0 °C. This indicates that the operating condition at 15 °C, with its associated condenser temperature and expansion valve setting, results in a comparatively slower freezing rate than the other two scenarios. A comparison of these three curves makes it clear: It is not necessarily true for all cases that higher values of $T_{cw,in}$ result in slower freeze times. Rather, each operating condition; defined by condenser temperature, valve opening limit, and cycle behavior; naturally leads to one of these three freezing times.

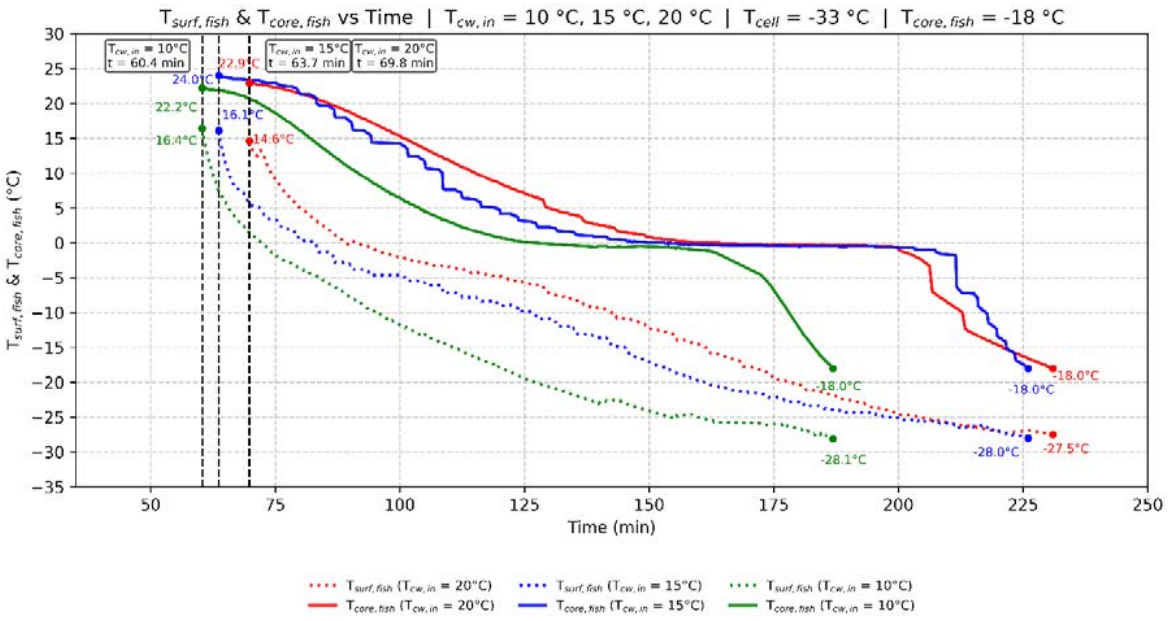

Figure 128 Comparison of Fish Surface and Core Temperature Profiles Under Different Condensing Temperatures (10 °C, 15 °C, 20 °C)

5.8 Experimental Results Analysis

The experimentation and analysis of the data were initially done in the Python programming environment to analytically define the development of temperature as a time-dependent variable. The time values recorded were changed to elapsed time in seconds since the start of each test, thus having the same numerical foundation for the regression analysis. Interpolating the experimental temperature profiles was then done using poly regression models.

Polynomial mathematical functions of higher degrees had been experimented with gradually to determine the most suitable analytical model of the observed thermal behavior. Specifically, first- to seventh-order polynomials were fit using a least-squares procedure to the data. Polynomial functions of increasing order were tested to provide a descriptive representation of the measured temperature data. The adequacy of each fit within the experimental dataset was evaluated using statistical criteria including RMSE, R^2, AIC, and BIC. The degree to which the experimental data agreed with the values that the regression model interpolated was measured by the coefficient of determination (R^2), and the root mean square error (RMSE) was a measure of the absolute error of fit. Moreover, the model selection criteria were proposed to restrict the chances of overfitting: the Akaike Information Criterion (AIC), which considers the trade-off between the goodness of fit and the complexity of a model, and the Bayesian Information Criterion (BIC), which is a stronger penalty imposed on the number of parameters in a model, were calculated at each degree of the polynomials. Even though higher-order polynomials tended to lead to an increase in R^2 values, the ultimate decision on the best regression model was strongly informed by the minimization of the BIC value where AIC was used as a secondary indicator. With this method, the identification of the polynomial models able to validate the experimental trend of temperatures with reasonable accuracy, maintaining numerical stability and physical interpretability, was possible. The analytical expressions obtained, along with their coefficients and other statistical measures, were then taken as reference models to do further analysis and comparison.

Polynomial fits are reported here to provide a smooth descriptive representation of the measured surface and core temperature trajectories during the tested freezing runs. The selected degree (based on AIC/BIC) is used to summarize trends within the observation interval and to facilitate comparison between operating conditions. These fits do not imply predictability of the process outside the measured time window and are not intended for extrapolation or general forecasting.

5.8.1 First Condition: $T_{cw,in}$ = 10 °C, 80 %, -33 °C

This condition involves two parts,

- Fish surface:

```
================================================================================
10,80,-33  |
================================================================================
 Degree       R2     RMSE          AIC          BIC
      1 0.906783 3.136201  2893.534834  2903.818908
      2 0.991477 0.948307  -128.177761  -112.751652
      3 0.994232 0.780153  -619.614569  -599.046422
      4 0.995086 0.720060  -820.248842  -794.538659
      5 0.997590 0.504283 -1718.712283 -1687.860064
      6 0.998363 0.415574 -2205.824063 -2169.829807
      7 0.998976 0.328727 -2796.470914 -2755.334622
```

Best polynomial equation by BIC:

Degree = 7, R^2 = 0.998976, RMSE = 0.328727

$$T(t) = -2.34194(10^{-24}.t^7) + 6.71168(10^{-20}t^6) - 7.82495(10^{-16}t^5) + 4.75068(10^{-12}t^4) - 1.59342(10^{-8}t^3) + 2.93958(10^{-5}t^2) - 0.0339308t + 16.6761 \quad \text{Eq. 139}$$

Degree = 7, R^2 = 0.998976, RMSE = 0.328727

$$T(t) = -2.34194(10^{-24}.t^7) + 6.71168(10^{-20}t^6) - 7.82495(10^{-16}t^5) + 4.75068(10^{-12}t^4) - 1.59342(10^{-8}t^3) + 2.93958(10^{-5}t^2) - 0.0339308t + 16.6761 \quad \text{Eq. 140}$$

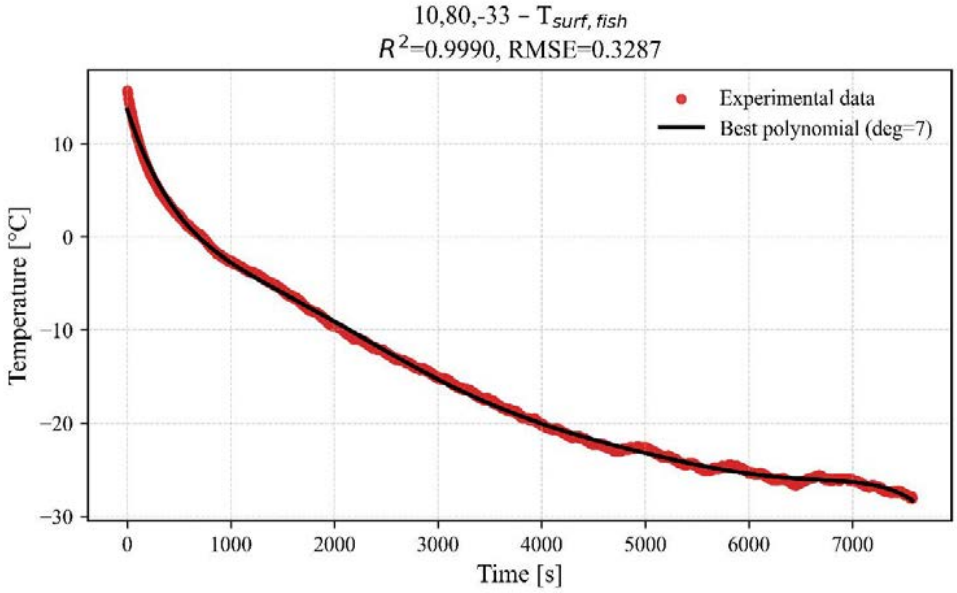

Figure 129 Surface Temperature Evolution of Fish During Freezing and 7th Order Polynomial Regression (Descriptive Fit within the Experimental Dataset) for $T_{cw,in}$ = 10 °C, 80 %, -33 °C

The polynomial regressions shown in Figures 129–134 provide a descriptive approximation of the measured temperature evolution. These higher-order fits are intended to illustrate trends within the collected dataset and do not imply extrapolative predictive capability.

- Fish core:

```
================================================================================================
10,80,-33  |
================================================================================================
 Degree       R2     RMSE          AIC          BIC
      1 0.888950 3.146560  2901.870972  2912.155045
      2 0.911381 2.810861  2618.665225  2634.091335
      3 0.962357 1.831977  1538.440597  1559.008743
      4 0.998636 0.348767 -2652.874487 -2627.164304
      5 0.998638 0.348478 -2652.969253 -2622.117034
      6 0.998765 0.331825 -2774.755833 -2738.761577
      7 0.999136 0.277592 -3223.890905 -3182.754612
```

Best polynomial equation by BIC:

Degree = 7, R^2 = 0.999136, RMSE = 0.277592

$$T(t) = 1.67461(10^{-24}.t^7) - 4.62792(10^{-20}t^6) + 5.0787(10^{-16}t^5) - 2.92135(10^{-12}t^4) + 9.63529(10^{-9}t^3) - 1.69696(10^{-5}t^2) + 0.00577234t + 21.4719$$ Eq. 141

Best polynomial equation by AIC:

Degree = 7, R^2 = 0.999136, RMSE = 0.277592

$$T(t) = 1.67461(10^{-24}.t^7) - 4.62792(10^{-20}t^6) + 5.0787(10^{-16}t^5) - 2.92135(10^{-12}t^4) + 9.63529(10^{-9}t^3) - 1.69696(10^{-5}t^2) + 0.00577234t + 21.4719$$ Eq. 142

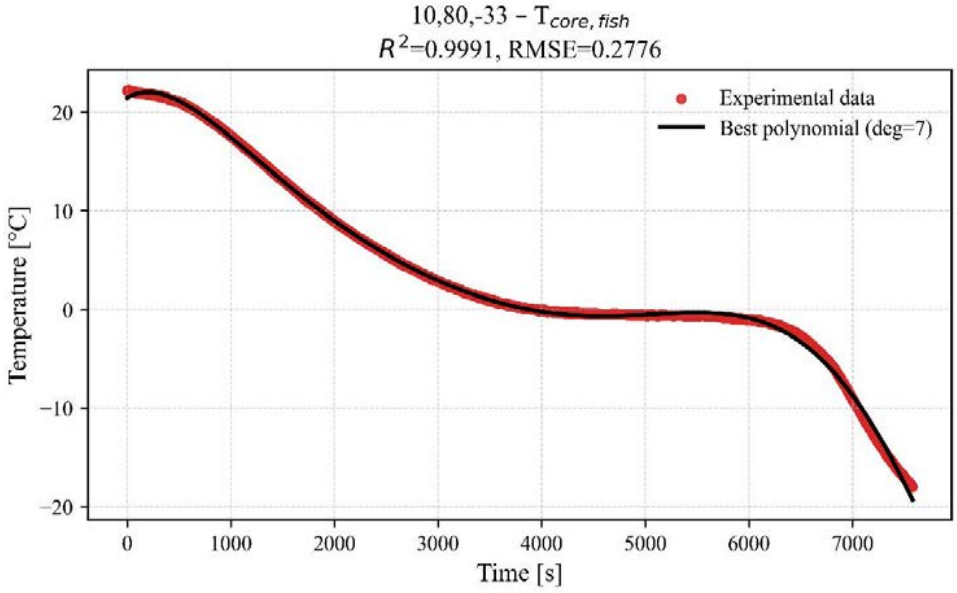

Figure 130 Core Temperature Evolution of Fish During Freezing and 7th Order Polynomial Regression (Descriptive Fit within the Experimental Dataset) for $T_{cw,in}$ = 10 °C, 80 %, -33 °C

5.8.2 Second Condition: $T_{cw,in}$ = 15 °C, 90 %, -33 °C

This condition can be divided into two parts,

- Fish surface:

```
================================================================================================
15,90,-33  |
================================================================================================
 Degree       R2     RMSE          AIC          BIC
      1 0.939537 2.507547  2964.162262  2974.930241
      2 0.983368 1.315156   888.136294   904.288262
      3 0.983377 1.314792   889.245628   910.781586
      4 0.987046 1.160660   489.745249   516.665197
      5 0.996704 0.585420 -1712.070925 -1679.766988
      6 0.999280 0.273555 -4159.928907 -4122.240980
      7 0.999368 0.256464 -4365.672545 -4322.600630
```

Best polynomial equation by BIC:

Degree = 7, R^2 = 0.999368, RMSE = 0.256464

$$T(t) = -1.61177(10^{-25}.t^7) - 7.56808(10^{-21}t^6) - 1.44207(10^{-16}t^5) + 1.41725(10^{-12}t^4) - 7.53315(10^{-9}t^3) + 2.0919(10^{-5}t^2) - 0.0308963t + 13.7935 \quad \text{Eq. 143}$$

Best polynomial equation by AIC:

Degree = 7, R^2 = 0.999368, RMSE = 0.256464

$$T(t) = -1.61177(10^{-25}.t^7) - 7.56808(10^{-21}t^6) - 1.44207(10^{-16}t^5) + 1.41725(10^{-12}t^4) - 7.53315(10^{-9}t^3) + 2.0919(10^{-5}t^2) - 0.0308963t + 13.7935 \quad \text{Eq. 144}$$

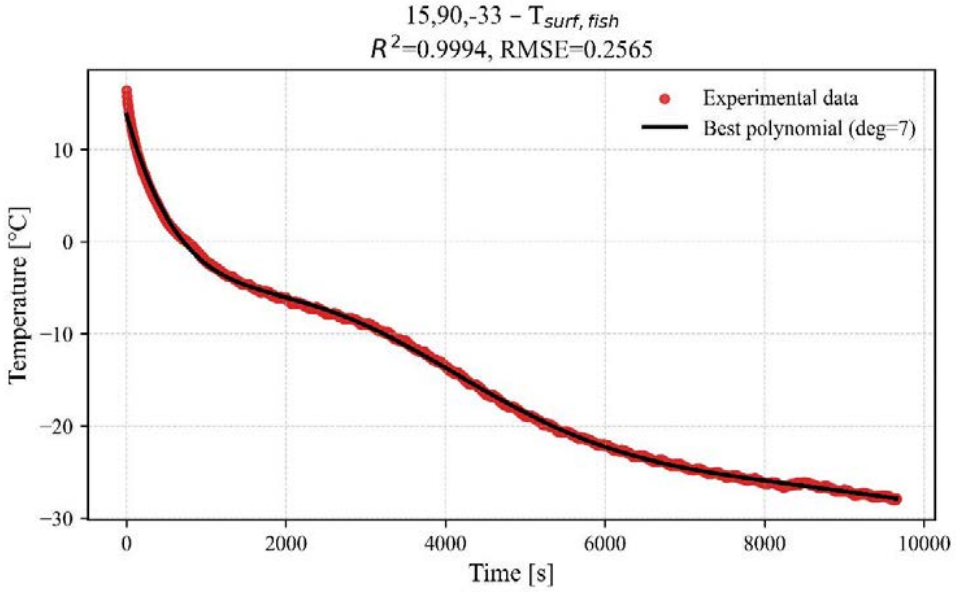

Figure 131 Surface Temperature Evolution of Fish During Freezing and 7th Order Polynomial Regression (Descriptive Fit within the Experimental Dataset) for $T_{cw,in}$ = 15 °C, 90 %, -33 °C

- Core Fish:

```
================================================================================================
15,90,-33  |
================================================================================================
 Degree       R2     RMSE          AIC          BIC
      1 0.865194 3.638584  4162.934844  4173.702823
      2 0.884060 3.374385  3922.205840  3938.357808
      3 0.977609 1.482907  1276.694979  1298.230937
      4 0.991928 0.890391  -363.822799  -336.902852
      5 0.995006 0.700339 -1134.935063 -1102.631127
      6 0.995370 0.674352 -1254.689346 -1217.001420
      7 0.998164 0.424684 -2741.641138 -2698.569222
```

Best polynomial equation by BIC:

Degree = 7, R^2 = 0.995245, RMSE = 0.770196

$$T(t) = 8.87059(10^{-25}.t^7) - 2.91979(10^{-20}t^6) + 3.83627(10^{-16}t^5) - 2.59929(10^{-12}t^4) + 9.65906(10^{-9}t^3) - 1.80436(10^{-5}t^2) + 0.00656078t + 22.9861 \quad \text{Eq. 145}$$

Degree = 7, R^2 = 0.995245, RMSE = 0.770196

$$T(t) = 8.87059(10^{-25}.t^7) - 2.91979(10^{-20}t^6) + 3.83627(10^{-16}t^5) - 2.59929(10^{-12}t^4) + 9.65906(10^{-9}t^3) - 1.80436(10^{-5}t^2) + 0.00656078t + 22.9861 \quad \text{Eq. 146}$$

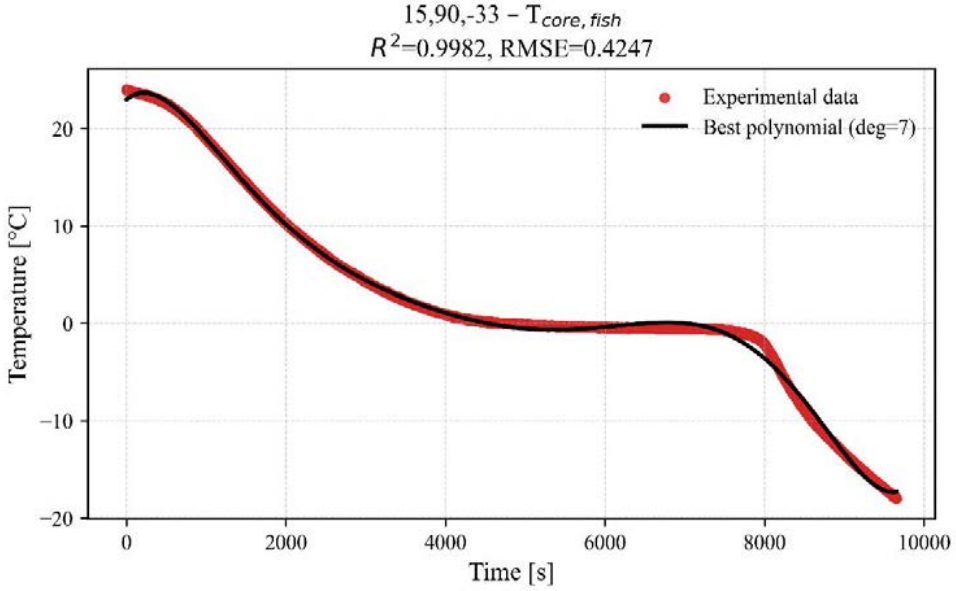

Figure 132 Core Temperature Evolution of Fish During Freezing and 7th Order Polynomial Regression (Descriptive Fit within the Experimental Dataset) for $T_{cw,in}$ = 15 °C, 90 %, -33 °C

5.8.3 Third Condition: $T_{cw,in}$ = 20 °C, 60 %, -33 °C

This condition also features two distinct parts,

- Fish surface

```
==========================================================================================
20,60,-33  |
==========================================================================================
 Degree       R2     RMSE          AIC          BIC
      1 0.956860 2.118041  1059.191151  1068.301865
      2 0.986615 1.179788   238.460842   252.126912
      3 0.987826 1.125141   173.778796   192.000224
      4 0.993442 0.825780  -259.146378  -236.369594
      5 0.997668 0.492413  -984.063857  -956.731715
      6 0.998878 0.341599 -1496.210252 -1464.322754
      7 0.999342 0.261501 -1869.891294 -1833.448438
```

Best polynomial equation by BIC:

Degree = 7, R^2 = 0.999342, RMSE = 0.223360

$$T(t) = -3.80126(10^{-25}.t^7) + 1.4276(10^{-20}t^6) - 2.19753(10^{-16}t^5) + 1.78317(10^{-12}t^4) - 8.11716(10^{-9}t^3) + 2.03229(10^{-5}t^2) - 0.0290666t + 14.5575 \quad \text{Eq. 147}$$

Best polynomial equation by AIC:

Degree = 7, R^2 = 0.999342, RMSE = 0.223360

$$T(t) = -3.80126(10^{-25}.t^7) + 1.4276(10^{-20}t^6) - 2.19753(10^{-16}t^5) + 1.78317(10^{-12}t^4) - 8.11716(10^{-9}t^3) + 2.03229(10^{-5}t^2) - 0.0290666t + 14.5575 \quad \text{Eq. 148}$$

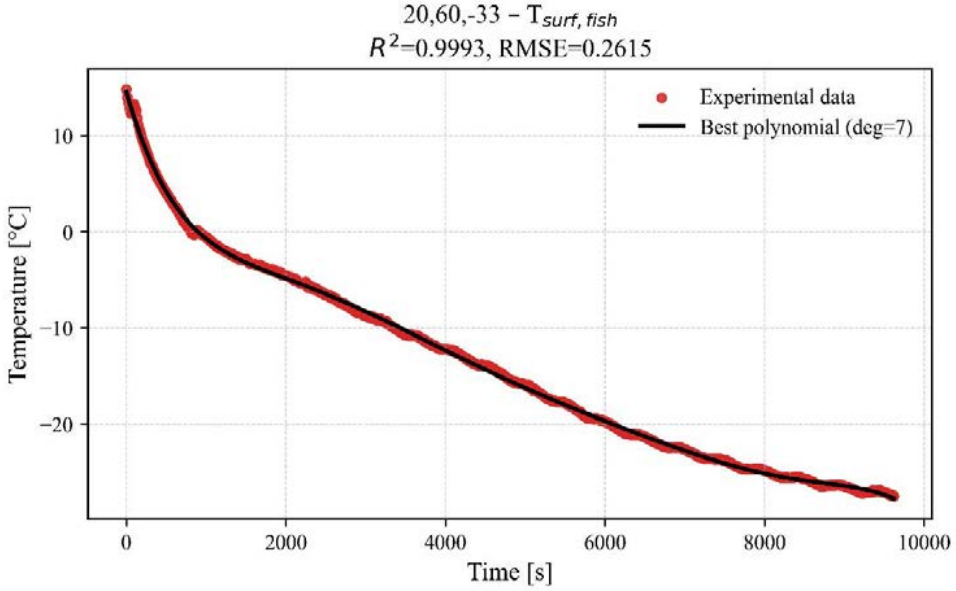

Figure 133 Surface Temperature Evolution of Fish During Freezing and 7th Order Polynomial Regression (Descriptive Fit within the Experimental Dataset) for $T_{cw,in}$ = 20 °C, 60 %, -33 °C

- Core Fish

```
================================================================================================
20,60,-33  |
================================================================================================
 Degree       R2     RMSE          AIC          BIC
      1 0.847858 3.642825  1821.619873  1830.730587
      2 0.863851 3.446037  1745.538179  1759.204249
      3 0.977256 1.408452   489.542830   507.764258
      4 0.992545 0.806388  -292.557216  -269.780432
      5 0.994541 0.690044  -509.625833  -482.293692
      6 0.994712 0.679158  -529.984029  -498.096531
      7 0.997709 0.447010 -1116.076630 -1079.633775
```

Best polynomial equation by BIC:

Degree = 7, R^2 = 0.997709, RMSE = 0.447010

$$T(t) = 8.84316(10^{-25}.t^7) - 2.92572(10^{-20}t^6) + 3.85797(10^{-16}t^5) - 2.61384(10^{-12}t^4) + 9.63602(10^{-9}t^3) - 1.75833(10^{-5}t^2) + 0.00575399t + 22.9194 \quad \text{Eq. 149}$$

Degree = 7, R^2 = 0.997709, RMSE = 0.447010

$$T(t) = 8.84316(10^{-25}.t^7) - 2.92572(10^{-20}t^6) + 3.85797(10^{-16}t^5) - 2.61384(10^{-12}t^4) + 9.63602(10^{-9}t^3) - 1.75833(10^{-5}t^2) + 0.00575399t + 22.9194 \quad \text{Eq. 150}$$

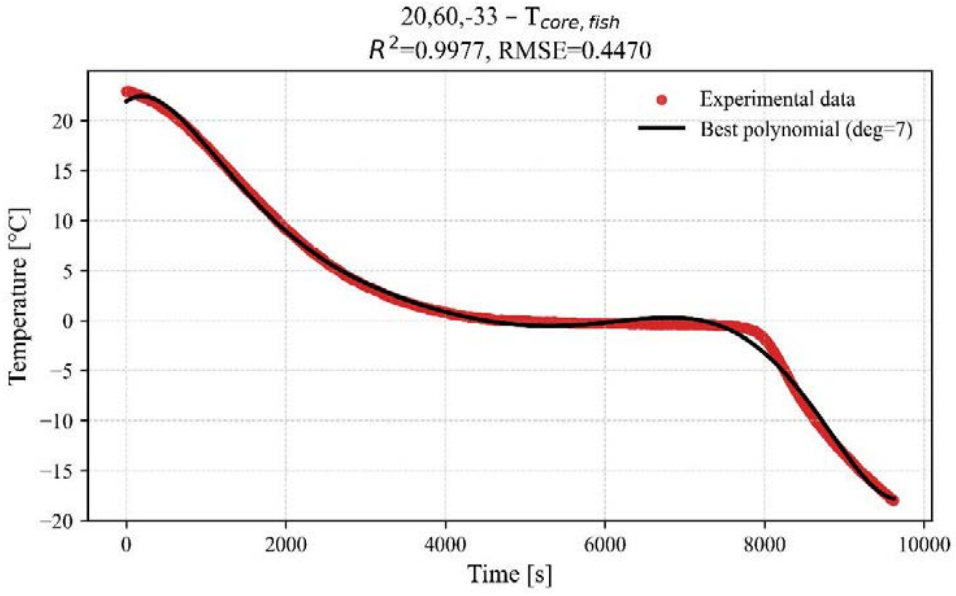

Figure 134 Core Temperature Evolution of Fish During Freezing and 7th Order Polynomial Regression (Descriptive Fit within the Experimental Dataset) for $T_{cw,in}$ = 20 °C, 60 %, -33 °C

Altogether, the given graphs show that the core and surface temperature changes are smooth and well represented during the whole freezing of the metal, the time lag between surface temperature stabilization and that of the core is also evident.

In addition, the sensitivity of the heat transfer rate and freezing rate to various operating conditions is also evident in the slope of the curves, which indicates the sensitivity of the process to the parameters of system control.

Overall, the fact that the core and surface temperature profiles are quite consistent indicates good stability of the freezing system work and a balanced heat distribution in the product, and these findings can be used to rely on in the future thermodynamic analysis, as well as energy optimization research.

5.8.4. Assessment of Numerical Model Results Compared with Experimental Measurements

The numerical model shows reasonable agreement with the experimental measurements within the measurement uncertainty band. The comparison demonstrates consistency within the investigated operating range; however, the model has not been validated using independent external datasets.

Figure 135 compares experimentally measured temperature profiles with numerically computed temperature profiles at the fish surface and core during the freezing process. The findings provide a similarity between simulation and experiment, which suggests that the numerical model can validate the key thermal behavior of the product within the operating conditions considered. The comparison of the fish surface temperature displays a very good level of agreement. It is validated by the fact that the coefficient of determination (R^2 = 0.97) is high, and the error values are small (RMSE = 3.46 °C and MAE = 3.03 °C). These findings reveal that the thermal conduction between the air and the product surface has been well modeled in the numerical model. Specifically, the prescribed convective boundary condition offers a clear description of the external heat transfer, and the simulated and experimental surface temperatures are found to be very close during the entire freezing process.

The fish core temperature has also been found to be very much in agreement. The outcome of the numerical results is R^2 = 0.80, which means that the overall cooling trend and internal thermal response of the product are represented by the model in a good way. Both the RMSE and MAE (7.68 °C and 6.64 °C, respectively) are realistic in transient freezing simulations using actual food products, where both the internal heterogeneity and phase-change effect are important. These findings affirm that the model can be used to describe leading heat transfer processes that control the temperature change at the product core (Table 30).

	R^2	RMSE	MAE
$T_{surf,fish}$ (SIM vs EXP)	0.9719	3.4637	3.0291
$T_{core,fish}$ (SIM vs EXP)	0.7965	7.6798	6.6379

Table 32 Comparison between Experimental and Numerical Temperature Profiles

The error of surface and core temperature estimation is a normal natural difference, and it has a physical meaning. The temperature of the surface is primarily regulated by external convection, whereas the temperature within the core is regulated by internal conduction and latent heat that comes with freezing. However, the reasonable consensus obtained in the case of the two sites indicates the strength of the numerical model and its applicability in modeling fish freezing.

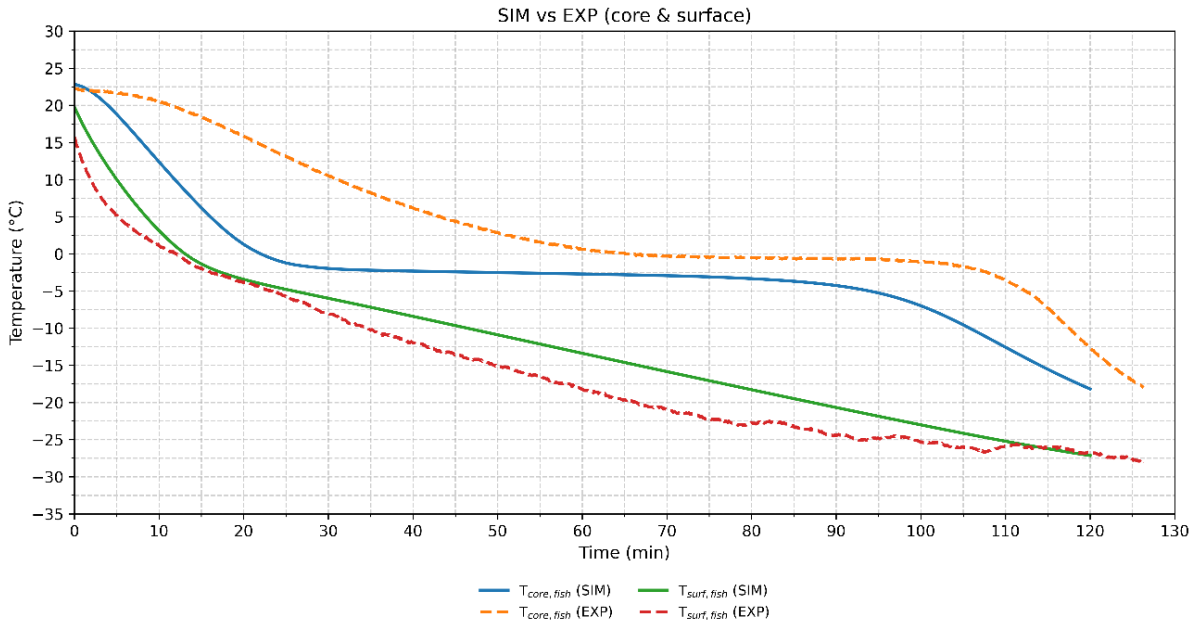

Figure 135 Comparison between Experimental and Numerical Temperature Profiles

Overall, the graphical comparison and statistical indicators demonstrate that the constructed numerical model adequately reproduces the observed surface and core temperature behavior under the investigated conditions. The findings achieved during this chapter substantiate the model as a qualified instrument for examining the freezing conduct, as well as serving as a guiding tool in additional research on the execution and effectiveness of industrial fish freezing units.

Chapter 6

Conclusions and Future Perspectives

6 Conclusions and Future Perspectives

6.1 Conclusions

This dissertation has provided an in-depth experimental, numerical, and analytical study of a low temperature seafood freezing system with a vapor injection scroll compressor and using low global warming potential refrigerant of R448A. The investigation was inspired by the growing necessity to find environmentally friendly and energy-efficient methods of freezing in the seafood sector where freezing contributes to the primary functions of the cold chain in the preservation of the products but at the same time is one of the most energy-consuming segments of the cold chain. The main goal of this paper was to evaluate the possibility of the combination of high-level compressor technology and the low-GWP refrigerant to meet the challenging operational needs of industrial seafood freezing and minimize the direct and indirect environmental effects. In this respect, the research sequentially studied the impacts of the condenser-side conditions, expansion valve regulation and vapor injection behavior on the performance of a system and applied it to the product level by means of finite element modeling of fish freezing dynamics.

At the system level, the experiment findings are clear indications on the usefulness of the vapor injection scroll compressor in counter-balancing the inherent constraints of traditional single-stage vapor compression systems that run at extremely low evaporating temperatures. Vapor injection also made operation of stable systems at high compression ratios possible, as it greatly reduced the discharge temperatures of the compressors and allowed thermal stress to be minimized on the critical components. The effect is especially applicable to industrial freezing plants, in which continuity of operation and long-term reliability are crucial.

The performance indicators of energy analysis showed that the efficiency of the system is highly dictated by operating conditions in the condenser-side. In experimental conditions, running at lower temperatures of the condenser cooling water inlet always led to the best performance. Specifically, conditions with $T_{cw,in}$ like $10\ ℃$ were the most favorable to the COP and the minimal power of the compressor in all the examined chamber temperatures. The systematic decrease in COP was noted with an increase in the condensing temperature to $15\ ℃$ and $20\ ℃$ with the corresponding increase in pressure ratios and work of compressors. These findings will be a quantitative measure of the fact that condenser-side optimization is among the most efficient methods of enhancing the energy efficiency of low-temperature seafood-freezing systems.

The variations between operating situations were especially striking at fixed deep-freezing conditions ($T_{cell} = 33\ ℃$), as is characteristic of industrial practice. Although, the vapor injection scroll compressor was able to continue operating steadily at all the conditions tested, the best balance between energy efficiency and operational stability was found in the instance where low condensing temperatures were coupled with moderate expansion valve openings. Valve openings that were surplus

raised the rate of refrigerant mass flow and cooling capacity, but did not give a corresponding increase in COP, since the corresponding increase in compressor power also increased the corresponding increase in cooling. A rule on expansion valve became a key parameter that determined the behavior of the system. In a variety of test cases, intermediate values of valve opening, usually between 70 and 80, gave the most favorable operating conditions.

The interaction of suction mass flow rate and vapor injection mass flow rate at these settings were found to be relatively balanced and the compressor was able to work well and there were no high discharge temperatures or pressure variations. By contrast, near-maximum openings of the valve strokes were inclined to drive the system towards higher loads with decreasing returns in energy efficiency, especially at high condensing temperatures. Vapor injection was not only a component of energy performance but also was a major source of operational robustness. In all the examined conditions, vapor injections proved to be useful in reducing the temperature of compressor discharge, which facilitated continuous and consistent operation even at extreme temperatures of low temperatures. The specified feature has a significant practical significance since it improves the durability of the systems and minimizes the chances of their performance deterioration over time. It was demonstrated that R448A is technically competent and environmentally beneficial as the working fluid in the studied system setup. Although having different thermodynamic properties than the legacy refrigerants like R404A was able to operate steadily in the entire variety of tested conditions.

Further, the improvements in COP were observed to be under favorable operating conditions, which suggests that the shift to R448A could lower not only indirect greenhouse gas emissions linked to the use of electricity but that the direct global warming potential of the latter is also significantly lower. In addition to the refrigeration cycle itself, this thesis embraced a product-based approach by liaising experimental measurements with the FEM model to determine the dynamics of temporary freezing of financial products. The numerical model has been able to validate the behavior of the temperature fields in the product such as the movement of the freezing boundary as well as the large temperature gradients across the surface and the core during the latent heat removal. Scenarios with reduced condensing temperature not only enhanced energy performance of the system, but it also resulted in reduced freezing times, especially at the critical phase-change period. Significantly, this accelerated freezing rate was made possible without bringing on too much thermal non-uniformity to the product meaning that energy saving operation of the systems is compatible with efficient and controlled product freezing. The combination of system-level performance analysis and product-level thermal modeling are one of the major contributions of this work. It shows that the operating scenarios, which are optimum, that is, when the condensing temperatures are low accompanied by moderate expansion valve openings and constant vapor injection operation, can also improve the energy efficiency coupled with the freezing effectiveness. This combined point of view is particularly effective with the seafood industry, in which energy consumption and the quality of products themselves have a direct impact on the sustainability

of the economy and the environment. Although the given research has a wide scope, some limitations are to be admitted. The operating conditions analyzed in the experiment were steady-state, and no transient process like start-up, changes in load or defrost cycles were taken into consideration.

Moreover, the results are determined in relation to a particular arrangement of compressor and refrigerant and its direct extrapolation to other systems needs to be confirmed by additional research. The product analysis focus was on thermal behavior, and it did not include microbiological or nutritional quality analysis.

Table 33 summarizes the main results obtained in this study. It is worth noting that all reported values were extracted within the steady state window, where the system performance was stable and reliable.

	1st Test with Fish	**2nd Test with Fish**	**3rd Test with Fish**
$T_{cw,in}$ (℃)	10	15	20
Max Opening EEV (%)	80	90	60
Chamber Temperature (℃)	-33	-33	-33
Fish Core Temperature (℃)	-18	-18	-18
COP_{min}	0.96	1.14	0.99
COP_{mean}	1.20	1.17	1.14
COP_{max}	1.24	1.22	1.25
W_{min} (kW)	2.56	3.12	2.85
W_{mean} (kW)	2.73	3.37	3.24
W_{max} (kW)	3.27	3.57	3.46
$Q_{evp,min}$ (kW)	3.12	3.58	3.03
$Q_{evp,mean}$ (kW)	3.27	3.93	3.71
$Q_{evp,max}$ (kW)	3.66	4.29	3.89
Relative Uncertainty of COP (%)	8.89	9.80	9.73
Relative Uncertainty of W (%)	7.78	7.79	7.15
Relative Uncertainty of Q_{evp} (%)	7.07	8.83	8.63
COP	1.20 ± 0.11	1.17 ± 0.11	1.14 ± 0.11
W (kW)	2.73 ± 0.21	3.37 ± 0.26	3.24 ± 0.23
Q_{evp} (kW)	3.27 ± 0.23	3.93 ± 0.35	3.71 ± 0.32

Table 33 Key Findings from Fish Freezing Experiments

A comparison between the FEM model of fish and the experimental measurements is presented in Table 34 for $T_{cw,in} = 10$ °C. Overall, the agreement between the numerical and experimental results is satisfactory. The difference in freezing time was around 4%, which can be considered acceptable for this type of modeling approach.

	R^2	Time (EXP), min	Time (SIM), min
$T_{surf,fish}$ (SIM vs EXP)	0.9719	125	120
$T_{core,fish}$ (SIM vs EXP)	0.7965	125	120

Table 34 Comparative Performance Indicators for Fish Freezing Test

In terms of the coefficient of determination (R^2), the values at the fish surface were closer to 1 than those at the core, as shown in the table. This behavior is mainly related to the heterogeneous structure and tissue composition of the fish. A detailed investigation of these biological aspects, however, is beyond the scope of the present work.

6.2 Future Perspectives

The findings of this work open several directions for future research, both at system and product levels. The following lines of investigation are proposed:

6.2.1 Alternative low-GWP and natural refrigerants

Future studies should test the vapor injection system with alternative low-GWP synthetic blends and natural refrigerants (such as CO_2 or hydrocarbons) under comparable operating conditions, to quantify differences in COP, capacity, discharge temperature and controllability relative to R448A. Experimental campaigns combined with thermodynamic modelling would support the identification of refrigerant–compressor combinations that maximize performance while complying with emerging regulatory constraints.

6.2.2 Extension to transient and real-duty operation

The present analysis could be generalized to fully transient operating modes, including start-up, product loading/unloading, door-opening events, load changes and defrost cycles. High-resolution experimental measurements and dynamic modelling would allow assessment of how vapor injection and control strategies perform under realistic duty cycles and how these transients impact cumulative energy use and component stress.

6.2.3 Data-driven performance prediction and control

Machine learning and advanced data-driven approaches could be employed to forecast COP, compressor power consumption, evaporator load and freezing time based on measured operating variables (e.g. pressures, temperatures, valve position, mass flow rates). Such models could be integrated into supervisory control schemes to implement predictive optimization of operating conditions and to support fault detection and diagnosis in industrial freezing plants.

6.2.4 Product quality and microstructural assessment

The product analysis should be expanded beyond thermal behavior to include quality indicators such as texture, drip loss, color, microstructure (ice crystal size and distribution) and sensory attributes after thawing. Coupling thermal models with experimental quality measurements would clarify the relationship between freezing rate, operating strategy and final product quality, and could lead to process criteria that jointly optimize energy use and quality preservation.

6.2.5 Life cycle and techno-economic assessment

Comprehensive life cycle assessment (LCA) should be carried out to quantify the overall environmental footprint of vapor injection seafood freezing systems using low-GWP refrigerants, considering both direct refrigerant emissions and indirect emissions from electricity use. In parallel, techno-economic analyses and scaling studies are needed to evaluate investment costs, operating expenses and payback times for the deployment of these technologies in full-scale industrial seafood freezing plants.

Developing these research directions would further consolidate the role of vapor injection scroll compressors and low-GWP refrigerants as viable solutions for sustainable, energy-efficient and product-quality-oriented seafood freezing systems.

References:

[1] The State of World Fisheries and Aquaculture 2024. FAO; 2024. https://doi.org/10.4060/cd0683en.

[2] Baha M., Hammami S., Dupont J-L. The Role of Refrigeration in the Global Economy 3rd edition, 60th IIR Technical Brief on Refrigeration Technologies. Paris: 2025.

[3] Dipper F. Human impacts 1: sea fisheries and aquaculture. Elements of Marine Ecology, Elsevier; 2022, p. 389–458. https://doi.org/10.1016/B978-0-08-102826-1.00006-5.

[4] Martindale W, Schiebel W. The impact of food preservation on food waste. British Food Journal 2017;119:2510–8. https://doi.org/10.1108/BFJ-02-2017-0114.

[5] REGULATION (EU) 2024/573 OF THE EUROPEAN PARLIAMENT AND OF THE COUNCIL. Brussels : 2024.

[6] Ludig S, Jörß W, Liste V. ETC CM Eionet Report 2022/3 – Climate change mitigation in Europe: policies, progress and effectiveness. Copenhagen: 2022.

[7] Liu G, Arthur M, Viglia S, Xue J, Meng F, Lombardi GV. Seafood-energy-water nexus: A study on resource use efficiency and the environmental impact of seafood consumption in China. J Clean Prod 2020;277:124088. https://doi.org/10.1016/j.jclepro.2020.124088.

[8] Sovacool BK, Bazilian M, Griffiths S, Kim J, Foley A, Rooney D. Decarbonizing the food and beverages industry: A critical and systematic review of developments, sociotechnical systems and policy options. Renewable and Sustainable Energy Reviews 2021;143:110856. https://doi.org/10.1016/j.rser.2021.110856.

[9] Heredia-Aricapa Y, Belman-Flores JM, Mota-Babiloni A, Serrano-Arellano J, García-Pabón JJ. Overview of low GWP mixtures for the replacement of HFC refrigerants: R134a, R404A and R410A. International Journal of Refrigeration 2020;111:113–23. https://doi.org/10.1016/j.ijrefrig.2019.11.012.

[10] Calm JM. The next generation of refrigerants – Historical review, considerations, and outlook. International Journal of Refrigeration 2008;31:1123–33. https://doi.org/10.1016/j.ijrefrig.2008.01.013.

[11] Ciconkov R. Refrigerants: There is still no vision for sustainable solutions. International Journal of Refrigeration 2018;86:441–8. https://doi.org/10.1016/j.ijrefrig.2017.12.006.

[12] Arora P, Seshadri G, Tyagi AK. Fourth-Generation Refrigerant:HFO 1234yf. Curr Sci 2018;115:1497. https://doi.org/10.18520/cs/v115/i8/1497-1503.

[13] Marseglia G, Sanches M, Ribeiro APC, Moreira ALN, Moita AS. Thermofluid characterization of nanofluids in spray cooling. Appl Therm Eng 2022;210:118411. https://doi.org/10.1016/j.applthermaleng.2022.118411.

[14] Vuppaladadiyam AK, Antunes E, Vuppaladadiyam SSV, Baig ZT, Subiantoro A, Lei G, et al. Progress in the development and use of refrigerants and unintended environmental consequences. Science of The Total Environment 2022;823:153670. https://doi.org/10.1016/j.scitotenv.2022.153670.

[15] Saleem S, Bradshaw CR, Bach CK. Development of design guidelines for fin-and-tube heat exchangers with low-GWP refrigerants. International Journal of Refrigeration 2022;143:166–81. https://doi.org/10.1016/j.ijrefrig.2022.06.037.

[16] Abas N, Kalair AR, Khan N, Haider A, Saleem Z, Saleem MS. Natural and synthetic refrigerants, global warming: A review. Renewable and Sustainable Energy Reviews 2018;90:557–69. https://doi.org/10.1016/j.rser.2018.03.099.

[17] Aprea C, Greco A, Maiorino A. An experimental investigation on the substitution of HFC134a with HFO1234YF in a domestic refrigerator. Appl Therm Eng 2016;106:959–67. https://doi.org/10.1016/j.applthermaleng.2016.06.098.

[18] Ustaoglu A, Kursuncu B, Metin Kaya A, Caliskan H. Analysis of vapor compression refrigeration cycle using advanced exergetic approach with Taguchi and ANOVA optimization and refrigerant selection with enviroeconomic concerns by TOPSIS analysis. Sustainable Energy Technologies and Assessments 2022;52:102182. https://doi.org/10.1016/j.seta.2022.102182.

[19] Mota-Babiloni A, Navarro-Esbrí J, Barragán Á, Molés F, Peris B. Theoretical comparison of low GWP alternatives for different refrigeration configurations taking R404A as baseline. International Journal of Refrigeration 2014;44:81–90. https://doi.org/10.1016/j.ijrefrig.2014.04.015.

[20] Mota-Babiloni A, Navarro-Esbrí J, Peris B, Molés F, Verdú G. Experimental evaluation of R448A as R404A lower-GWP alternative in refrigeration systems. Energy Convers Manag 2015;105:756–62. https://doi.org/10.1016/j.enconman.2015.08.034.

[21] Sethi A, Pottker G, Yana Motta S. Experimental evaluation and field trial of low global warming potential R404A replacements for commercial refrigeration. Sci Technol Built Environ 2016;22:1175–84. https://doi.org/10.1080/23744731.2016.1209032.

[22] Xu X, Hwang Y, Radermacher R. Refrigerant injection for heat pumping/air conditioning systems: Literature review and challenges discussions. International Journal of Refrigeration 2011;34:402–15. https://doi.org/10.1016/j.ijrefrig.2010.09.015.

[23] Tello Oquendo FM, Navarro Peris E, Gonzálvez Macia J, Corberán JM. Performance of a scroll compressor with vapor-injection and two-stage reciprocating compressor operating under extreme conditions. International Journal of Refrigeration 2016;63:144–56. https://doi.org/10.1016/j.ijrefrig.2015.10.035.

[24] Desrosier NW, James N. D. The Technology of Food Preservation. 4th ed. Westport, Connecticut: AVI Publishing Company, Inc.; 1977.

[25] Muthukumarappan K, Marella C, Sunkesula V. Food Freezing Technology. Handbook of Farm, Dairy and Food Machinery Engineering, Elsevier; 2019, p. 389–415. https://doi.org/10.1016/B978-0-12-814803-7.00015-4.

[26] Alexandre EMC, Brandão TRS, Silva CLM. Frozen Food and Technology. Advances in Food Science and Technology, Wiley; 2013, p. 123–50. https://doi.org/10.1002/9781118659083.ch4.

[27] Chen L, Feng D-Z. Fast Implementation of the Progressive Edge-Growth Algorithm. ETRI Journal 2009;31:240–2. https://doi.org/10.4218/etrij.09.0208.0358.

[28] Sheen S, Whitney LF. Modelling heat transfer in fluidized beds of large particles and its applications in the freezing of large food items. J Food Eng 1990;12:249–65. https://doi.org/10.1016/0260-8774(90)90001-O.

[29] Salvadori VO, Mascheroni RH. Analysis of impingement freezers performance. J Food Eng 2002;54:133–40. https://doi.org/10.1016/S0260-8774(01)00198-4.

[30] Shafiur Rahman M, Velez-Ruiz JF. Food Preservation by Freezing. Handbook of Food Preservation. 3rd ed., Taylor &Francis Group; 2020.

[31] Newman MD, McCormick S. Modular apparatus for cooling and freezing of food product on a moving substrate. US6263680B1, 2001.

[32] Estrada-Flores S. Novel cryogenic technologies for the freezing of food products. The Official Journal of AIRAH 2002.

[33] Jones CD, Jones S. Cryogenic processor for liquid feed preparation of a free-flowing frozen product. US6209329B1, 2001.

[34] Lang G. Cryogenic Freezing. Industrial Refrigeration Consortium Industrial Refrigeration Consortium Research & Technology Forum, Madison, WI: Industrial Refrigeration Consortium; 2006.

[35] Agnelli ME, Mascheroni RH. Cryomechanical freezing. A model for the heat transfer process. J Food Eng 2001;47:263–70. https://doi.org/10.1016/S0260-8774(00)00126-6.

[36] ELECTROMAGNETIC FIELDS (300 Hz to 300 GHz) . Geneva: 1993.

[37] Hay N, Quang Huy L, Van Kien P. A Review of Drying Methods Assisted by Infrared Radiation, Microwave and Radio Frequency. A Comprehensive Review of the Versatile Dehydration Processes, IntechOpen; 2023. https://doi.org/10.5772/intechopen.108650.

[38] Orsat V, Raghavan GSV. Radio-Frequency Processing. Emerging Technologies for Food Processing, Elsevier; 2005, p. 445–68. https://doi.org/10.1016/B978-012676757-5/50019-0.

[39] Anese M, Manzocco L, Panozzo A, Beraldo P, Foschia M, Nicoli MC. Effect of radiofrequency assisted freezing on meat microstructure and quality. Food Research International 2012;46:50–4. https://doi.org/10.1016/j.foodres.2011.11.025.

[40] Manzocco L, Alongi M, Cortella G, Anese M. Optimizing radiofrequency assisted cryogenic freezing to improve meat microstructure and quality. J Food Eng 2022;335:111184. https://doi.org/10.1016/j.jfoodeng.2022.111184.

[41] Hafezparast-Moadab N, Hamdami N, Dalvi-Isfahan M, Farahnaky A. Effects of radiofrequency-assisted freezing on microstructure and quality of rainbow trout (Oncorhynchus mykiss) fillet. Innovative Food Science & Emerging Technologies 2018;47:81–7. https://doi.org/10.1016/j.ifset.2017.12.012.

[42] Wang J, Olsen RG, Tang J, Tang Z. Influence of Mashed Potato Dielectric Properties and Circulating Water Electric Conductivity on Radio Frequency Heating at 27 MHz. Journal of Microwave Power and Electromagnetic Energy 2007;42:31–46. https://doi.org/10.1080/08327823.2007.11688579.

[43] Garbati Pegna F, Sacchetti P, Canuti V, Trapani S, Bergesio C, Belcari A, et al. Radio frequency irradiation treatment of dates in a single layer to control Carpophilus hemipterus. Biosyst Eng 2017;155:1–11. https://doi.org/10.1016/j.biosystemseng.2016.11.011.

[44] Cui B, Fan R, Ran C, Yao Y, Wang K, Wang Y, et al. Improving radio frequency heating uniformity using a novel rotator for microorganism control and its effect on physiochemical properties of raisins. Innovative Food Science & Emerging Technologies 2021;67:102564. https://doi.org/10.1016/j.ifset.2020.102564.

[45] Wang C-Y, Huang H-W, Hsu C-P, Yang BB. Recent Advances in Food Processing Using High Hydrostatic Pressure Technology. Crit Rev Food Sci Nutr 2016;56:527–40. https://doi.org/10.1080/10408398.2012.745479.

[46] LeBail A, Chevalier D, Mussa DM, Ghoul M. High pressure freezing and thawing of foods: a review. International Journal of Refrigeration 2002;25:504–13. https://doi.org/10.1016/S0140-7007(01)00030-5.

[47] Li D, Zhu Z, Sun D-W. Effects of freezing on cell structure of fresh cellular food materials: A review. Trends Food Sci Technol 2018;75:46–55. https://doi.org/10.1016/j.tifs.2018.02.019.

[48] Mahato S, Zhu Z, Sun D-W. Glass transitions as affected by food compositions and by conventional and novel freezing technologies: A review. Trends Food Sci Technol 2019;94:1–11. https://doi.org/10.1016/j.tifs.2019.09.010.

[49] Otero L. Application of high pressure processing in freezing and thawing processes. Non-thermal Food Processing Operations, Elsevier; 2023, p. 359–405. https://doi.org/10.1016/B978-0-12-818717-3.00005-6.

[50] Fernández PP, Otero L, Guignon B, Sanz PD. High-pressure shift freezing versus high-pressure assisted freezing: Effects on the microstructure of a food model. Food Hydrocoll 2006;20:510–22. https://doi.org/10.1016/j.foodhyd.2005.04.004.

[51] Otero L, Sanz PD. High-pressure-shift freezing: Main factors implied in the phase transition time. J Food Eng 2006;72:354–63. https://doi.org/10.1016/j.jfoodeng.2004.12.015.

[52] Su G, Ramaswamy HS, Zhu S, Yu Y, Hu F, Xu M. Thermal characterization and ice crystal analysis in pressure shift freezing of different muscle (shrimp and porcine liver) versus conventional freezing method. Innovative Food Science & Emerging Technologies 2014;26:40–50. https://doi.org/10.1016/j.ifset.2014.05.006.

[53] Van Buggenhout S, Grauwet T, Van Loey A, Hendrickx M. Effect of high-pressure induced ice I/ice III-transition on the texture and microstructure of fresh and pretreated carrots and strawberries. Food Research International 2007;40:1276–85. https://doi.org/10.1016/j.foodres.2007.08.008.

[54] Urrutia Benet G, Schlüter O, Knorr D. High pressure–low temperature processing. Suggested definitions and terminology. Innovative Food Science & Emerging Technologies 2004;5:413–27. https://doi.org/10.1016/j.ifset.2004.06.001.

[55] Su G, Ramaswamy HS, Zhu S, Yu Y, Hu F, Xu M. Thermal characterization and ice crystal analysis in pressure shift freezing of different muscle (shrimp and porcine liver) versus conventional freezing method. Innovative Food Science & Emerging Technologies 2014;26:40–50. https://doi.org/10.1016/j.ifset.2014.05.006.

[56] Li M, Ling C, Ye B, Cai J, Wang W, Li J. Development of Ultra-high Pressure Cooling and Quick Freezing Device Based on Hydraulic Transmission. E3S Web of Conferences 2019;118:02032. https://doi.org/10.1051/e3sconf/201911802032.

[57] Cacace F, Bottani E, Rizzi A, Vignali G. Evaluation of the economic and environmental sustainability of high pressure processing of foods. Innovative Food Science & Emerging Technologies 2020;60:102281. https://doi.org/10.1016/j.ifset.2019.102281.

[58] Woo MW, Mujumdar AS. Effects of Electric and Magnetic Field on Freezing and Possible Relevance in Freeze Drying. Drying Technology 2010;28:433–43. https://doi.org/10.1080/07373930903202077.

[59] PANG X-F, SHEN G-F. THE CHANGES OF PHYSICAL PROPERTIES OF WATER ARISING FROM THE MAGNETIC FIELD AND ITS MECHANISM. Modern Physics Letters B 2013;27:1350228. https://doi.org/10.1142/S021798491350228X.

[60] Sun Q, Zhang H, Yang X, Hou Q, Zhang Y, Su J, et al. Insight into muscle quality of white shrimp (Litopenaeus vannamei) frozen with static magnetic-assisted freezing at different intensities. Food Chem X 2023;17:100518. https://doi.org/10.1016/j.fochx.2022.100518.

[61] Al Faruq A, Farahnaky A, Dokouhaki M, Khatun HA, Trujillo FJ, Majzoobi M. Technological Innovations in Freeze Drying: Enhancing Efficiency, Sustainability, and Food Quality. Food Engineering Reviews 2025. https://doi.org/10.1007/s12393-025-09415-8.

[62] Wei Q, Sun Q, Dong X, Kong B, Ji H, Liu S. Effect of static magnetic field-assisted freezing at different temperatures on muscle quality of pacific white shrimp (Litopenaeus vannamei). Food Chem 2024;438:138041. https://doi.org/10.1016/j.foodchem.2023.138041.

[63] Ye P, Luo K, Feng A, Zhao D, Wang D, Lin X, et al. Magnetic field improves the quality of frozen tilapia fillets by decreasing the ice crystals during freezing process. Int J Food Sci Technol 2024;59:8961–71. https://doi.org/10.1111/ijfs.17357.

[64] Tang J, Zhang H, Tian C, Shao S. Effects of different magnetic fields on the freezing parameters of cherry. J Food Eng 2020;278:109949. https://doi.org/10.1016/j.jfoodeng.2020.109949.

[65] Dalvi-Isfahan M, Havet M, Hamdami N, Le-Bail A. Recent advances of high voltage electric field technology and its application in food processing: A review with a focus on corona discharge and static electric field. J Food Eng 2023;353:111551. https://doi.org/10.1016/j.jfoodeng.2023.111551.

[66] Rahbari M, Hamdami N, Mirzaei H, Jafari SM, Kashaninejad M, Khomeiri M. Effects of high voltage electric field thawing on the characteristics of chicken breast protein. J Food Eng 2018;216:98–106. https://doi.org/10.1016/j.jfoodeng.2017.08.006.

[67] Horikoshi S, Brodie G, Takaki K, Serpone N, editors. Agritech: Innovative Agriculture Using Microwaves and Plasmas. Singapore: Springer Singapore; 2022. https://doi.org/10.1007/978-981-16-3891-6.

[68] Jia G, He X, Nirasawa S, Tatsumi E, Liu H, Liu H. Effects of high-voltage electrostatic field on the freezing behavior and quality of pork tenderloin. J Food Eng 2017;204:18–26. https://doi.org/10.1016/j.jfoodeng.2017.01.020.

[69] Hu R, Zhang M, Mujumdar AS. Novel assistive technologies for efficient freezing of pork based on high voltage electric field and static magnetic field: A comparative study. Innovative Food

Science & Emerging Technologies 2022;80:103087. https://doi.org/10.1016/j.ifset.2022.103087.

[70] Schudel S, Prawiranto K, Defraeye T. Comparison of freezing and convective dehydrofreezing of vegetables for reducing cell damage. J Food Eng 2021;293:110376. https://doi.org/10.1016/j.jfoodeng.2020.110376.

[71] Ben Haj Said L, Bellagha S, Allaf K. Dehydrofreezing of Apple Fruits: Freezing Profiles, Freezing Characteristics, and Texture Variation. Food Bioproc Tech 2016;9:252–61. https://doi.org/10.1007/s11947-015-1619-4.

[72] Ando H, Kajiwara K, Oshita S, Suzuki T. The effect of osmotic dehydrofreezing on the role of the cell membrane in carrot texture softening after freeze-thawing. J Food Eng 2012;108:473–9. https://doi.org/10.1016/j.jfoodeng.2011.08.013.

[73] Zaritzky N. Physical–Chemical Principles in Freezing, 2011, p. 3–38. https://doi.org/10.1201/b11204-3.

[74] Fu H, Huang S, Li Y, Cheng J, Guo Y, Wang K, et al. The research and application of technology and core components in commercial refrigeration and freezing Systems：A review. J Stored Prod Res 2024;108:102400. https://doi.org/10.1016/j.jspr.2024.102400.

[75] Salins SS, Reddy SVK, Kumar S. Experimental investigation of the influence of vapor compression refrigeration in a multistage reciprocating dehumidifier test rig. Appl Therm Eng 2021;199:117546. https://doi.org/10.1016/j.applthermaleng.2021.117546.

[76] Hu Y, Xu W, Ren T, Cai M, Yang B, Shi Y. Theoretical study on the application of isothermal compression technology in vapor-compression refrigeration systems with an isothermal piston. Energy Sci Eng 2021;9:2321–32. https://doi.org/10.1002/ese3.984.

[77] Kadam ST, Kyriakides A-S, Khan MS, Shehabi M, Papadopoulos AI, Hassan I, et al. Thermo-economic and environmental assessment of hybrid vapor compression-absorption refrigeration systems for district cooling. Energy 2022;243:122991. https://doi.org/10.1016/j.energy.2021.122991.

[78] Dai D, Liu Z, Yuan F, Long R, Liu W. Finite time thermodynamic analysis of a solar duplex Stirling refrigerator. Appl Therm Eng 2019;156:597–605. https://doi.org/10.1016/j.applthermaleng.2019.04.098.

[79] Doğan B. Assessment of design constraints for the Duplex Stirling Refrigerator with imperfect regeneration. J Clean Prod 2020;265:121823. https://doi.org/10.1016/j.jclepro.2020.121823.

[80] Salehi A, Mousavi S, Fasihfar A, Ravanbakhsh M. Thermo-environmental analysis of a new molten carbonate fuel cell-based tri-generation plant using stirling engine, generator absorber exchanger and vapour absorption refrigeration: A comparative study. Int J Hydrogen Energy 2021;46:38451–68. https://doi.org/10.1016/j.ijhydene.2021.09.101.

[81] Zhu H, Guo B, Geng W, Chi J, Guo S. Simulation of an improved solar absorption refrigeration system with phase change materials. Energy Reports 2022;8:3671–9. https://doi.org/10.1016/j.egyr.2022.02.306.

[82] Hafiz A. Refrigeration Engineering (New Edition). Book Rivers; 2025.

[83] Gużda A, Szmolke N. Compressors in Heat Pumps. Machine Dynamics Research 2015;39:7183–83.

[84] Jianguo Q. Study on basic parameters of scroll fluid machine based on general profile. Mech Mach Theory 2010;45:212–23. https://doi.org/10.1016/j.mechmachtheory.2009.08.005.

[85] Stosic N, Smith IK, Kovacevic A. Optimisation of screw compressors. Appl Therm Eng 2003;23:1177–95. https://doi.org/10.1016/S1359-4311(03)00059-0.

[86] Ayub S, Bush JW, Haller DK, Ayub S, Bush JW. Liquid Refrigerant Injection in Scroll Compressors Operating at High Compression Ratios. 1992.

[87] Winandy EL, Lebrun J. Scroll compressors using gas and liquid injection: experimental analysis and modelling. International Journal of Refrigeration 2002;25:1143–56. https://doi.org/10.1016/S0140-7007(02)00003-8.

[88] Cho H, Chung JT, Kim Y. Influence of liquid refrigerant injection on the performance of an inverter-driven scroll compressor. International Journal of Refrigeration 2003;26:87–94. https://doi.org/10.1016/S0140-7007(02)00017-8.

[89] Lee D, Seong KJ, Lee J. Performance investigation of vapor and liquid injection on a refrigeration system operating at high compression ratio. International Journal of Refrigeration 2015;53:115–25. https://doi.org/10.1016/J.IJREFRIG.2015.01.013.

[90] Kim D, Jeon Y, Jang DS, Kim Y. Performance comparison among two-phase, liquid, and vapor injection heat pumps with a scroll compressor using R410A. Appl Therm Eng 2018;137:193–202. https://doi.org/10.1016/J.APPLTHERMALENG.2018.03.086.

[91] Lee H, Hwang Y, Radermacher R, Chun HH. Potential benefits of saturation cycle with two-phase refrigerant injection. Appl Therm Eng 2013;56:27–37. https://doi.org/10.1016/J.APPLTHERMALENG.2013.03.030.

[92] Yang M, Wang B, Li X, Shi W, Zhang L. Evaluation of two-phase suction, liquid injection and two-phase injection for decreasing the discharge temperature of the R32 scroll compressor. International Journal of Refrigeration 2015;59:269–80. https://doi.org/10.1016/J.IJREFRIG.2015.08.004.

[93] Ding Y, Chai Q, Ma G, Jiang Y. Experimental study of an improved air source heat pump. Energy Convers Manag 2004;45:2393–403. https://doi.org/10.1016/J.ENCONMAN.2003.11.021.

[94] Ma GY, Chai QH. Characteristics of an improved heat-pump cycle for cold regions. Appl Energy 2004;77:235–47. https://doi.org/10.1016/S0306-2619(03)00123-5.

[95] Bertsch SS, Groll EA. Two-stage air-source heat pump for residential heating and cooling applications in northern U.S. climates. International Journal of Refrigeration 2008;31:1282–92. https://doi.org/10.1016/J.IJREFRIG.2008.01.006.

[96] Wang X, Hwang Y, Radermacher R. Two-stage heat pump system with vapor-injected scroll compressor using R410A as a refrigerant. International Journal of Refrigeration 2009;32:1442–51. https://doi.org/10.1016/J.IJREFRIG.2009.03.004.

[97] Heo J, Jeong MW, Baek C, Kim Y. Comparison of the heating performance of air-source heat pumps using various types of refrigerant injection. International Journal of Refrigeration 2011;34:444–53. https://doi.org/10.1016/J.IJREFRIG.2010.10.003.

[98] Roh CW, Kim MS. Effects of intermediate pressure on the heating performance of a heat pump system using R410A vapor-injection technique. International Journal of Refrigeration 2011;34:1911–21. https://doi.org/10.1016/J.IJREFRIG.2011.07.011.

[99] Navarro E, Redón A, Gonzálvez-Macia J, Martinez-Galvan IO, Corberán JM. Characterization of a vapor injection scroll compressor as a function of low, intermediate and high pressures and temperature conditions. International Journal of Refrigeration 2013;36:1821–9. https://doi.org/10.1016/J.IJREFRIG.2013.04.022.

[100] Dardenne L, Fraccari E, Maggioni A, Molinaroli L, Proserpio L, Winandy E. Semi-empirical modelling of a variable speed scroll compressor with vapour injection. International Journal of Refrigeration 2015;54:76–87. https://doi.org/10.1016/J.IJREFRIG.2015.03.004.

[101] Tello Oquendo FM, Navarro Peris E, Gonzálvez MacIa J, Corberán JM. Performance of a scroll compressor with vapor-injection and two-stage reciprocating compressor operating under extreme conditions. International Journal of Refrigeration 2016;63:144–56. https://doi.org/10.1016/J.IJREFRIG.2015.10.035.

[102] Tello-Oquendo FM, Navarro-Peris E, Gonzálvez-Maciá J. New characterization methodology for vapor-injection scroll compressors. International Journal of Refrigeration 2017;74:528–39. https://doi.org/10.1016/J.IJREFRIG.2016.11.019.

[103] Lumpkin DR, Bahman AM, Groll EA. Two-phase injected and vapor-injected compression: Experimental results and mapping correlation for a R-407C scroll compressor. International Journal of Refrigeration 2018;86:449–62. https://doi.org/10.1016/J.IJREFRIG.2017.11.009.

[104] Dechesne BJ, Tello-Oquendo FM, Gendebien S, Lemort V. Residential air-source heat pump with refrigerant injection and variable speed compressor: Experimental investigation and compressor modeling. International Journal of Refrigeration 2019;108:79–90. https://doi.org/10.1016/J.IJREFRIG.2019.08.034.

[105] Xu Q, Wu J, Guo Z, Xue X, Li X. Analysis of optimal intermediate temperature and injection pressure for refrigerant injection heat pump systems with economiser. Appl Therm Eng 2022;210:118361. https://doi.org/10.1016/J.APPLTHERMALENG.2022.118361.

[106] Tongchana Thongtip, Kittiwoot Sutthivirode. Case Stud. Therm. Eng. 2020;21:100–10.

[107] Liu C, Shang L, Yoshioka HT, Chen B, Hayashi K. Preparation of molecularly imprinted polymer nanobeads for selective sensing of carboxylic acid vapors. Anal Chim Acta 2018;1010:1–10. https://doi.org/10.1016/J.ACA.2018.01.004.

[108] Hermanucz Péter. ÉPÜLET HŐIGÉNYÉHEZ ILLESZTETT TÖBB HŐFORRÁSÚ HŐSZIVATTYÚ ELEMZÉSE. Műszaki Tudományi Doktori Iskola, Magyar Agrár és Élettudományi Egyetem, 2022.

[109] Raju GN, Kumar KD, Rao TS. Enhancement of Cop of Vapour Compression Refrigeration System by using Diffusers. International Journal of Recent Technology and Engineering (IJRTE) 2019;8:6123–9. https://doi.org/10.35940/ijrte.B3908.078219.

[110] Aziz A, Izzudin, Mainil AK. Performance comparison of a refrigerator system using R134a and hydrocarbon refrigerant (HCR134a) with different expansion devices. IOP Conf Ser Mater Sci Eng 2017;237:012008. https://doi.org/10.1088/1757-899X/237/1/012008.

[111] Pathakm SS, Shukla P, Chauhan S, Srivastava AK. An experimental study of the Effect of capillary tube diameter and configuration on the performance of a simple vapour compression refrigeration system. IOSR Journal of Mechanical and Civil Engineering (IOSR-JMCE) 2014;2:101–13.

[112] Sunu PW, Made Rasta I, Anakottapary DS, Made Suarta I, Cipta Santosa IDM. Capillary Tube and Thermostatic Expansion Valve Comparative Analysis in Water Chiller Air Conditioning. J Phys Conf Ser 2018;953:012063. https://doi.org/10.1088/1742-6596/953/1/012063.

[113] WAN H, HWANG Y, RADERMACHER R, OH S. Review of Electronic Expansion Valve Correlations for Heat Pump and Air Conditioning Systems. 17 th International Refrigeration and Air Conditioning Conference, Purdue: 2018.

[114] Sivaraman N, Muthu Vaidyanathan R, Patel M, Markos M. Performance analysis of refrigerants with various expansion valves in vapour compression refrigeration and air-conditioning system. Mater Today Proc 2021;45:2465–9. https://doi.org/10.1016/j.matpr.2020.11.025.

[115] ElSherbini AI, Maheshwari GP. Impact of shading air-cooled condensers on the efficiency of air-conditioning systems. Energy Build 2010;42:1948–51. https://doi.org/10.1016/j.enbuild.2010.05.031.

[116] Vakiloroaya V, Samali B, Pishghadam K. A comparative study on the effect of different strategies for energy saving of air-cooled vapor compression air conditioning systems. Energy Build 2014;74:163–72. https://doi.org/10.1016/j.enbuild.2014.01.042.

[117] Bari E, Noël J-Y, Comini G, Cortella G. Air-cooled condensing systems for home and industrial appliances. Appl Therm Eng 2005;25:1446–58. https://doi.org/10.1016/j.applthermaleng.2004.10.004.

[118] Hosoz M, Kilicarslan A. Performance evaluations of refrigeration systems with air-cooled, water-cooled and evaporative condensers. Int J Energy Res 2004;28:683–96. https://doi.org/10.1002/er.990.

[119] Murphy D. Cooling towers used for free cooling. ASHRAE Journal (American Society of Heating, Refrigerating and Air-Conditioning Engineers) 1991;33:6:16–26.

[120] Goshayshi H, Missenden JF, Tozer R, Maidment GG. Improving cooling tower performance for sustainable refrigeration. Proceedings of Joint CIBSE/ASHRAE Conference, Dublin: 2000, p. 344–50.

[121] De Saulles T. Free Cooling Systems. BSRIA; 2004.

[122] Chen H, Lee WL, Yik FWH. Applying water cooled air conditioners in residential buildings in Hong Kong. Energy Convers Manag 2008;49:1416–23. https://doi.org/10.1016/j.enconman.2007.12.024.

[123] Sreejith K., Sushmitha S., Vipin Das. Experimental Investigation of a Household Refrigerator using Air-cooled and Water-cooled Condenser . International Journal of Engineering And Science 2014;4:13–7.

[124] Hu SS, Huang BJ. Study of a high efficiency residential split water-cooled air conditioner. Appl Therm Eng 2005;25:1599–613. https://doi.org/10.1016/j.applthermaleng.2004.11.011.

[125] Chang Y-P, Tsai R, Hwang J-W. Condensing heat transfer characteristics of aluminum flat tube. Appl Therm Eng 1997;17:1055–65. https://doi.org/10.1016/S1359-4311(97)00011-2.

[126] Refrigerating and Air-Conditioning Engineers American Society of Heating. ASHRAE Handbook Heating, Ventilating, and Air-conditioning Systems and Equipment. SI. ASHRAE; 2020.

[127] Harby K, Gebaly DR, Koura NS, Hassan MS. Performance improvement of vapor compression cooling systems using evaporative condenser: An overview. Renewable and Sustainable Energy Reviews 2016;58:347–60. https://doi.org/10.1016/j.rser.2015.12.313.

[128] Nemati H, Ardekani MM, Mahootchi J, Meyer JP. Heat exchanger classifications. Fundamentals of Industrial Heat Exchangers, Elsevier; 2024, p. 3–5. https://doi.org/10.1016/B978-0-443-13902-4.00021-4.

[129] Jouhara H. Waste Heat Recovery in Process Industries. WILEY; 2021.

[130] Ramesh K. Shah DPS. Classification of Heat Exchangers. Fundamentals of Heat Exchanger Design, Wiley; 2003, p. 1–77. https://doi.org/10.1002/9780470172605.ch1.

[131] Malinauskaite J, Jouhara H. A theoretical analysis of waste heat recovery technologies. Sustainable Energy Technology, Business Models, and Policies, Elsevier; 2024, p. 99–144. https://doi.org/10.1016/B978-0-443-18454-3.00001-1.

[132] Pandya NS, Shah H, Molana M, Tiwari AK. Heat transfer enhancement with nanofluids in plate heat exchangers: A comprehensive review. European Journal of Mechanics - B/Fluids 2020;81:173–90. https://doi.org/10.1016/j.euromechflu.2020.02.004.

[133] Mota FAS, Carvalho EP, Ravagnani MASS. Modeling and Design of Plate Heat Exchanger. Heat Transfer Studies and Applications, InTech; 2015. https://doi.org/10.5772/60885.

[134] Picón-Núñez M, Canizalez-Dávalos L, Martínez-Rodríguez G, Polley GT. Shortcut Design Approach for Spiral Heat Exchangers. Food and Bioproducts Processing 2007;85:322–7. https://doi.org/10.1205/fbp07073.

[135] Alsouda F, Bennett NS, Saha SC, Salehi F, Islam MS. Vapor Compression Cycle: A State-of-the-Art Review on Cycle Improvements, Water and Other Natural Refrigerants. Clean Technologies 2023;5:584–608. https://doi.org/10.3390/cleantechnol5020030.

[136] Park C, Lee H, Hwang Y, Radermacher R. Recent advances in vapor compression cycle technologies. International Journal of Refrigeration 2015;60:118–34. https://doi.org/10.1016/j.ijrefrig.2015.08.005.

[137] Domanski PA, Didion DA, Doyle JP. Evaluation of suction-line/liquid-line heat exchange in the refrigeration cycle. International Journal of Refrigeration 1994;17:487–93. https://doi.org/10.1016/0140-7007(94)90010-8.

[138] Preissner Marcus, Cutler Brett, Radermacher Reinhard, Zhang ChaoA. Suction Line Heat Exchanger for R134A Automotive Air-Conditioning System. Eighth International Refrigeration and Air Conditioning Conference, West Lafayette: 2000.

[139] Klein SA, Reindl DT, Brownell K. Refrigeration system performance using liquid-suction heat exchangers. International Journal of Refrigeration 2000;23:588–96. https://doi.org/10.1016/S0140-7007(00)00008-6.

[140] Hwang Y, Huff H-J, Preissner M, Radermacher R. CO2 Transcritical Cycles for High Temperature Applications. Advanced Energy Systems, American Society of Mechanical Engineers; 2001, p. 255–60. https://doi.org/10.1115/IMECE2001/AES-23630.

[141] Cho H, Ryu C, Kim Y. Cooling performance of a variable speed CO2 cycle with an electronic expansion valve and internal heat exchanger. International Journal of Refrigeration 2007;30:664–71. https://doi.org/10.1016/j.ijrefrig.2006.10.004.

[142] Cho H, Lee H, Park C. Performance Characteristics of a Drop-in System for a Mobile Air Conditioner Using Refrigerant R1234yf. Korean Journal of Air-Conditioning and Refrigeration Engineering 2012;24:823–9. https://doi.org/10.6110/KJACR.2012.24.12.823.

[143] Navarro-Esbrí J, Molés F, Barragán-Cervera Á. Experimental analysis of the internal heat exchanger influence on a vapour compression system performance working with R1234yf as a drop-in replacement for R134a. Appl Therm Eng 2013;59:153–61. https://doi.org/10.1016/j.applthermaleng.2013.05.028.

[144] Cho H, Lee H, Park C. Performance characteristics of an automobile air conditioning system with internal heat exchanger using refrigerant R1234yf. Appl Therm Eng 2013;61:563–9. https://doi.org/10.1016/j.applthermaleng.2013.08.030.

[145] Pottker G, Hrnjak P. Experimental investigation of the effect of condenser subcooling in R134a and R1234yf air-conditioning systems with and without internal heat exchanger. International Journal of Refrigeration 2015;50:104–13. https://doi.org/10.1016/j.ijrefrig.2014.10.023.

[146] Rajendran P, Narayanaswamy GR, Dhasan ML. Tuning thermostatic expansion valve for implementing suction line heat exchanger in mobile air conditioning system. Journal of the Brazilian Society of Mechanical Sciences and Engineering 2019;41:191. https://doi.org/10.1007/s40430-019-1680-4.

[147] MAHDİ AL-OBAİDİ AS, NAİF A, AL- HARTHİ TK. OPTIMIZATION OF THE PERFORMANCE OF VAPOUR COMPRESSION CYCLE USING LIQUID SUCTION LINE HEAT EXCHANGER. Journal of Thermal Engineering 2020;6:201–10. https://doi.org/10.18186/thermal.730765.

[148] Thornton JW, Klein SA, Mitchell JW. Dedicated mechanical subcooling design strategies for supermarket applications. International Journal of Refrigeration 1994;17:508–15. https://doi.org/10.1016/0140-7007(94)90026-4.

[149] Khan J-R, Zubair SM. Design and rating of dedicated mechanical-subcooling vapour compression refrigeration systems. Proceedings of the Institution of Mechanical Engineers, Part A: Journal of Power and Energy 2000;214:455–71. https://doi.org/10.1243/0957650001538010.

[150] Qureshi BA, Zubair SM. The effect of refrigerant combinations on performance of a vapor compression refrigeration system with dedicated mechanical sub-cooling. International Journal of Refrigeration 2012;35:47–57. https://doi.org/10.1016/j.ijrefrig.2011.09.009.

[151] She X, Yin Y, Zhang X. A proposed subcooling method for vapor compression refrigeration cycle based on expansion power recovery. International Journal of Refrigeration 2014;43:50–61. https://doi.org/10.1016/j.ijrefrig.2014.03.008.

[152] Miran AZ, Nemati A, Yari M. Performance analysis and exergoeconomic evaluation of a TRC system enhanced by a dedicated mechanical subcooling. Energy Convers Manag 2019;197:111890. https://doi.org/10.1016/j.enconman.2019.111890.

[153] Chen E, Li Z, Yu J, Xu Y, Yu Y. Experimental research of increased cooling output by dedicated subcooling. Appl Therm Eng 2019;154:9–17. https://doi.org/10.1016/j.applthermaleng.2019.03.071.

[154] Winkler J, Aute V, Yang B, Radermacher R. Potential Benefits of Thermoelectric Element Used With Air-Cooled Heat Exchangers. International Refrigeration and Air Conditioning Conference, West Lafayette: 2006.

[155] Radermacher R, Yang B, Hwang Y. Integrating alternative and conventional cooling technologies. 2007.

[156] Schoenfield J, Hwang Y, Radermacher R. CO_2 transcritical vapor compression cycle with thermoelectric subcooler. HVAC&R Res 2012;18:297–311. https://doi.org/10.1080/10789669.2012.625348.

[157] Sarkar J. Exergy analysis of vortex tube expansion vapour compression refrigeration system. International Journal of Exergy 2013;13:431. https://doi.org/10.1504/IJEX.2013.058101.

[158] Kwan TH, Shen Y, Wu Z, Yao Q. Performance analysis of the thermoelectric device as the internal heat exchanger of the trans-critical carbon dioxide cycle. Energy Convers Manag 2020;208:112585. https://doi.org/10.1016/j.enconman.2020.112585.

[159] Liu X, Yu K, Wan X, Li X. Performance evaluation of CO2 supermarket refrigeration system with multi-ejector and dedicated mechanical subcooling. Energy Reports 2021;7:5214–27. https://doi.org/10.1016/j.egyr.2021.08.110.

[160] Aranguren P, Sánchez D, Casi A, Cabello R, Astrain D. Experimental assessment of a thermoelectric subcooler included in a transcritical CO2 refrigeration plant. Appl Therm Eng 2021;190:116826. https://doi.org/10.1016/j.applthermaleng.2021.116826.

[161] Sharma D, Sachdeva G, Saini DK. Optimized Refrigerant Flow Rate and Dimensions of the Ejector Employed in a Modified Ejector Vapor Compression System. International Journal of Air-Conditioning and Refrigeration 2020;28:2050038. https://doi.org/10.1142/S2010132520500388.

[162] Huff H-J, Lindsay D, Radermacher R. Positive Displacement Compressor And Expander Simulation. International Compressor Engineering Conference, West Lafayette: 2002.

[163] Nickl J, Will G, Quack H, Kraus WE. Integration of a three-stage expander into a CO2 refrigeration system. International Journal of Refrigeration 2005;28:1219–24. https://doi.org/10.1016/j.ijrefrig.2005.08.012.

[164] Wang M, Zhao Y, Cao F, Bu G, Wang Z. Simulation study on a novel vane-type expander with internal two-stage expansion process for R-410A refrigeration system. International Journal of Refrigeration 2012;35:757–71. https://doi.org/10.1016/j.ijrefrig.2011.11.014.

[165] Subiantoro A, Ooi KT. Economic analysis of the application of expanders in medium scale air-conditioners with conventional refrigerants, R1234yf and CO2. International Journal of Refrigeration 2013;36:1472–82. https://doi.org/10.1016/j.ijrefrig.2013.03.010.

[166] Hu J, Li M, Zhao L, Xia B, Ma Y. Improvement and experimental research of CO2 two-rolling piston expander. Energy 2015;93:2199–207. https://doi.org/10.1016/j.energy.2015.10.097.

[167] Disawas S, Wongwises S. Experimental investigation on the performance of the refrigeration cycle using a two-phase ejector as an expansion device. International Journal of Refrigeration 2004;27:587–94. https://doi.org/10.1016/j.ijrefrig.2004.04.002.

[168] Li D, Groll EA. Transcritical CO2 refrigeration cycle with ejector-expansion device. International Journal of Refrigeration 2005;28:766–73. https://doi.org/10.1016/j.ijrefrig.2004.10.008.

[169] Lawrence N, Elbel S. Theoretical and practical comparison of two-phase ejector refrigeration cycles including First and Second Law analysis. International Journal of Refrigeration 2013;36:1220–32. https://doi.org/10.1016/j.ijrefrig.2013.03.007.

[170] Boumaraf L, Haberschill P, Lallemand A. Investigation of a novel ejector expansion refrigeration system using the working fluid R134a and its potential substitute R1234yf. International Journal of Refrigeration 2014;45:148–59. https://doi.org/10.1016/j.ijrefrig.2014.05.021.

[171] Lawrence N, Elbel S. Experimental investigation of a two-phase ejector cycle suitable for use with low-pressure refrigerants R134a and R1234yf. International Journal of Refrigeration 2014;38:310–22. https://doi.org/10.1016/j.ijrefrig.2013.08.009.

[172] Hafner A, Försterling S, Banasiak K. Multi-ejector concept for R-744 supermarket refrigeration. International Journal of Refrigeration 2014;43:1–13. https://doi.org/10.1016/j.ijrefrig.2013.10.015.

[173] Zhang Z, Tian L. Effect of Suction Nozzle Pressure Drop on the Performance of an Ejector-Expansion Transcritical CO2 Refrigeration Cycle. Entropy 2014;16:4309–21. https://doi.org/10.3390/e16084309.

[174] Jeon Y, Kim S, Kim D, Chung HJ, Kim Y. Performance characteristics of an R600a household refrigeration cycle with a modified two-phase ejector for various ejector geometries and operating conditions. Appl Energy 2017;205:1059–67. https://doi.org/10.1016/j.apenergy.2017.08.148.

[175] Dutta AK, Yanagisawa T, Fukuta M. An investigation of the performance of a scroll compressor under liquid refrigerant injection. International Journal of Refrigeration 2001;24:577–87. https://doi.org/10.1016/S0140-7007(00)00041-4.

[176] Cho H, Chung JT, Kim Y. Influence of liquid refrigerant injection on the performance of an inverter-driven scroll compressor. International Journal of Refrigeration 2003;26:87–94. https://doi.org/10.1016/S0140-7007(02)00017-8.

[177] Winandy EL, Lebrun J. Scroll compressors using gas and liquid injection: experimental analysis and modelling. International Journal of Refrigeration 2002;25:1143–56. https://doi.org/10.1016/S0140-7007(02)00003-8.

[178] Heo J, Jeong MW, Kim Y. Effects of flash tank vapor injection on the heating performance of an inverter-driven heat pump for cold regions. International Journal of Refrigeration 2010;33:848–55. https://doi.org/10.1016/j.ijrefrig.2009.12.021.

[179] Wang X, Hwang Y, Radermacher R. Two-stage heat pump system with vapor-injected scroll compressor using R410A as a refrigerant. International Journal of Refrigeration 2009;32:1442–51. https://doi.org/10.1016/j.ijrefrig.2009.03.004.

[180] Heo J, Jeong MW, Baek C, Kim Y. Comparison of the heating performance of air-source heat pumps using various types of refrigerant injection. International Journal of Refrigeration 2011;34:444–53. https://doi.org/10.1016/j.ijrefrig.2010.10.003.

[181] Xu X, Hwang Y, Radermacher R. Transient and steady-state experimental investigation of flash tank vapor injection heat pump cycle control strategy. International Journal of Refrigeration 2011;34:1922–33. https://doi.org/10.1016/j.ijrefrig.2011.08.003.

[182] Xu X, Hwang Y, Radermacher R. Refrigerant injection for heat pumping/air conditioning systems: Literature review and challenges discussions. International Journal of Refrigeration 2011;34:402–15. https://doi.org/10.1016/j.ijrefrig.2010.09.015.

[183] Xu X, Hwang Y, Radermacher R. Performance comparison of R410A and R32 in vapor injection cycles. International Journal of Refrigeration 2013;36:892–903. https://doi.org/10.1016/j.ijrefrig.2012.12.010.

[184] Lee H, Hwang Y, Radermacher R, Chun H-H. Potential benefits of saturation cycle with two-phase refrigerant injection. Appl Therm Eng 2013;56:27–37. https://doi.org/10.1016/j.applthermaleng.2013.03.030.

[185] Lee H, Hwang Y, Radermacher R, Chun H-H. Performance investigation of multi-stage saturation cycle with natural working fluids and low GWP working fluids. International Journal of Refrigeration 2015;51:103–11. https://doi.org/10.1016/j.ijrefrig.2014.12.018.

[186] ISO/IEC 17025:2017 (General requirements for the competence of testing and calibration laboratories). The International Organization for Standardization (ISO) 2018.

[187] Service and Calibration Guidelines. Fluke 434 Power Quality Analyzer. Https://WwwFlukeCom 2023.

[188] National Institute of Standards and Technology (NIST). Thermocouples Calibrations Services. Https://WwwNistGov/Pml/Sensor-Science/Thermodynamic-Metrology/Thermocouples-Calibrations-Services n.d.

[189] Global Manufacturer DwyerOmega. Common Techniques to Calibrate Thermocouples. Https://WwwDwyeromegaCom/En-Us/Resources/Calibrating-Thermocouples n.d.

[190] Fraden J. Handbook of Modern Sensors - Physics, Designs, and Applications. Fifth. San Diego, California: Springer; 2016. https://doi.org/10.1007/978-3-319-19303-8.

[191] The Fundamentals of Pressure Calibration. Https://InfoMensorCom/Pressure-Calibration-Fundamentals n.d.

[192] https://seatemperature.net/seas/mediterranean-sea n.d.

[193] https://seatemperature.net/seas/black-sea n.d.

[194] https://seatemperature.net/seas/north-sea n.d.

[195] ISO/IEC Guide 98-3:2008. Geneva: 2010.

[196] Ndanduleni AUC, Ramathe T, Huan Z. Experimental analysis of an R134a refrigeration system using POE/CuO nanolubricant. Case Studies in Thermal Engineering 2026;78:107734. https://doi.org/10.1016/j.csite.2026.107734.

[197] Hoang HN, Agustiarini N, Oh JT. Experimental Investigation of Two-Phase Flow Boiling Heat Transfer Coefficient and Pressure Drop of R448A inside Multiport Mini-Channel Tube. Energies (Basel) 2022;15:4331. https://doi.org/10.3390/en15124331.

[198] Rodonò G, Volpes R. Fisica tecnica. vol. 1. Roma: ARACNE editrice S.r.l.; 2011.

[199] Marino F. Analisi sperimentale del processo di congelazione rapida della zucchina genovese. Università degli Studi di Palermo, 2002.

[200] ASHRAE Handbook Refrigeration . SI. ASHRAE; 2022.

[201] Paolo Schilleci. ANALISI TEORICO-SPERIMENTALE DEL PROCESSO DI SURGELAZIONE DI PRODOTTI ITTICI. Universita degli Studi di Palermo, 2025.

[202] Anderson W, Barnett M, Bensmiller D, Chong F, Christian R, Clay D, et al. Storage Temperatures and Procedures. Food Safety, Sanitation, and Personal Hygiene, Victoria: BCcampus; 2015.

[203] www.fda.gov/media/74435/download. REFRIGERATOR & FREEZER STORAGE CHART. US Food and Drug Administration 2018.

[204] Council of the European Communities. Council Directive 89/108/EEC on quick-frozen foodstuffs for human consumption. Official Journal of the European Communities 2013.

[205] Yoo M. Development of a Simulator for Household Refrigerator Using Equation-Based Optimization Control with Bayesian Calibration. Machines 2023;12:12. https://doi.org/10.3390/machines12010012.